VU VRIJE UNIVERSITEIT AMSTERDAM

VU Research Portal

Characterisation and commissioning of the LHCb VELO detector

Papadelis, E.A.

2009

document version
Publisher's PDF, also known as Version of record

Link to publication in VU Research Portal

citation for published version (APA)
Papadelis, E. A. (2009). *Characterisation and commissioning of the LHCb VELO detector*. [PhD-Thesis - Research and graduation internal, Vrije Universiteit Amsterdam].

General rights
Copyright and moral rights for the publications made accessible in the public portal are retained by the authors and/or other copyright owners and it is a condition of accessing publications that users recognise and abide by the legal requirements associated with these rights.

- Users may download and print one copy of any publication from the public portal for the purpose of private study or research.
- You may not further distribute the material or use it for any profit-making activity or commercial gain
- You may freely distribute the URL identifying the publication in the public portal ?

Take down policy
If you believe that this document breaches copyright please contact us providing details, and we will remove access to the work immediately and investigate your claim.

E-mail address:
vuresearchportal.ub@vu.nl

Download date: 04. May. 2023

Characterisation and commissioning of the LHCb VELO detector

Aras Papadelis

Front cover: One of the lead targets used in ACDC3.
Back cover: Wooden sculpture of a bike by Ilias Papadelis.

Printed in 2009 by Ipskamp Drukkers, Enschede, The Netherlands.

This work is part of the research programme of the 'Stichting voor Fundamenteel Onderzoek der Materie (FOM)', which is financially supported by the 'Nederlandse Organisatie voor Wetenschappelijk Onderzoek (NWO)'.

VRIJE UNIVERSITEIT

Characterisation and commissioning of the LHCb VELO detector

ACADEMISCH PROEFSCHRIFT

ter verkrijging van de graad Doctor aan
de Vrije Universiteit Amsterdam,
op gezag van de rector magnificus
prof.dr. L.M. Bouter,
in het openbaar te verdedigen
ten overstaan van de promotiecommissie
van de faculteit der Exacte Wetenschappen
op woensdag 17 juni 2009 om 15.45 uur
in de aula van de universiteit,
De Boelelaan 1105

door

Erik Aras Papadelis

geboren te Röke, Zweden

promotor:	prof.dr. M.H.M. Merk
copromotor:	dr. E. Jans

Contents

Introduction

The Standard Model of particle physics is one of the triumphs of physics of the past 40 years. It is a combination of the theories of electroweak and strong interactions, describing the kinematical properties and interactions of the elementary building blocks of matter: quarks and leptons. Before their discovery, the theory had successfully predicted the existence of the W^+, W^- and Z^0 bosons; the force mediators of the weak interaction. The theory identifies the force mediators of the strong force as gluons: massless, electrically neutral bosons which carry colour charge and bind quarks together in nucleons. The only particle predicted by the Standard Model that is not discovered to this day is the Higgs boson: a particle related to the mechanism in which fermions, leptons and gauge bosons acquire mass.

In the past few years, a particularly vital field of particle physics has been B-physics, in which BaBar, Belle and the LEP and Tevatron experiment have produced copious measurements and discovered new particles. B-physics, as the name implies, focuses on the study of b-quarks. The prediction of a third generation of quarks by Kobayashi and Maskawa in 1973 [1] marked the advent of the field. It was followed four years later by the discovery of the b-quark in the di-muon decay of Υ ($b\overline{b}$) mesons by the E288 experiment [2].

The existence of a third quark generation allows violation of the CP-symmetry in the weak sector of the standard model. CP-symmetry implies that a left-handed particle has identical interaction and decay properties as a right-handed antiparticle, i.e. the system is invariant under a combined charge (C) and parity (P) transformation. CP-violation in nature is therefore a manifestation of a fundamental asymmetry between matter and antimatter. It is also one of the necessary ingredients required in the process of baryogenesis as was identified by Andrei Sakharov in his seminal 1967 paper [3]. To understand the origin of CP-violation is a prerequisite to solve the mystery of the currently unexplained absence of antimatter in the visible part of our universe.

CP-violation in the decay of neutral B-mesons had been predicted long before it was first measured by the Belle and BaBar collaborations in 2001 [4, 5]. The observation was a crucial milestone for B-physics and an important test of the Standard Model. In recent years, precision measurements by BaBar, Belle, DØ and CDF have demonstrated that the results obtained in the heavy flavour sector are consistent with the Standard Model, although first hints of deviations have been reported [6]. Meanwhile, experimental evidence such as observations of the presence of an unknown, non-baryonic form of matter ("dark matter") in the universe, are indicating the Standard Model is not a final theory of fundamental interactions. Another perceived inadequacy of the theory is the presence of 19 free parameters (not including the neutrino masses), of which the values can not be predicted but have to be measured. Furthermore, the failure of the Standard Model to incorporate gravitational interactions is often interpreted as a sign that the Standard Model is a part of a bigger picture.

To investigate these and other outstanding issues in the Standard Model, as well as to directly search for new physics, a new hadron collider has been built at the European Laboratory for Particle Physics, CERN. The Large Hadron Collider (LHC) is expected to start operation in late 2009. One of the experiments at the LHC is dedicated to the study of B-mesons: the LHCb experiment is the result of a collaboration of about 550 physicists from 51 universities and laboratories in 15 countries. LHCb is specifically designed to precisely detect the wealth of B-mesons that are produced by the proton-proton collisions. With b-quarks being produced at a rate of 100 kHz in the LHCb detector, the LHC is truly a B-factory. As will be briefly discussed in chapter 1, there are reasons to believe that the B-sector will provide clear signatures and evidence of physics beyond the Standard Model.

The LHCb detector consists of a number of subdetectors, each of which is crucial for successful operation of the experiment. Chapter 1 describes the detector, gives an outline of the physics programme of LHCb and discusses the LHC accelerator facility.

Chapter 2 describes the VELO detector, which is the first subdetector traversed by a particle that is generated in a collision of the LHC beams. The VELO is a tracking device that uses silicon as active medium to detect the passage of charged particles. To maximise the performance of the detector, it is positioned at a distance of 7 mm from the pp-interactions. As a result, the VELO itself forms a part of the LHC beampipe and is integrated with the LHC vacuum. To stay clear of beam excursions during LHC injection, the VELO can be retracted from the luminous region. This feature requires a precise on-the-fly alignment procedure. To cope with the intense radiation levels close to the interaction point, the silicon sensors and readout electronics have a radiation hard design that will ensure operation over at least three years of nominal luminosity.

Due to the complexity of the VELO, its development spans over more than a decade, and has involved physicists and engineers from institutes in Germany, Great Britain, The Netherlands, Switzerland and the United States. The research on which this thesis is based has been the performance evaluation, data quality monitoring and commissioning of the VELO. Chapter 3 describes a milestone on the road to completion: a test of the performance of near-final prototype silicon sensors in a beam of charged particles. This was the last beam test in the R&D phase and the results were used as main input for the final design decisions. The chapter puts forward a selection of these results and describes their analyses.

Chapter 4 gives a detailed report of a system test in which a quarter of the final detector was placed in a charged particle beam and read out with the final data acquisition system. This test can be seen as a first step of the commissioning of the VELO. The performance of the silicon sensors was investigated and the vertex reconstruction capability of the detector was put to test with a fixed target setup specifically designed to emulate a set of conditions present during LHC operation. The chapter reviews an assortment of the analyses performed with the data acquired during this test.

Chapter 5, the final chapter, documents the commissioning of the VELO and its readout system after its installation in the experimental area of LHCb. The chapter reviews the software tools that were developed for commissioning and data quality checking and describes the most important steps of the Data Acquisition System commissioning. This is followed by a comprehensive study of the sensor noise performance. The last section of the thesis describes the first LHC-induced events to be reconstructed in the VELO.

1 The LHCb detector at the LHC

The Large Hadron Collider [7] (LHC) at CERN, the European Laboratory for Particle Physics, is a two-ring superconducting hadron accelerator and collider located near Geneva, Switzerland. It is the most powerful accelerator in the world, designed to collide protons at a total centre-of-mass energy of $\sqrt{s} = 14$ TeV at a peak luminosity of 10^{34} cm^{-2}s^{-1}. Additionally, the LHC is capable of accelerating and colliding lead ions at an energy of 2.76 TeV per nucleon, corresponding to a centre-of-mass energy of 1150 TeV. The LHC is installed in the 26.7 km tunnel that was constructed between 1984 and 1989 for the LEP machine. The LHC tunnel has eight straight sections as well as eight arcs and lies between 45 m and 170 m below the surface. The approval of the LHC project was given by the CERN Council in December 1994, but installation work in the tunnel could only commence after the LEP accelerator had been dismantled in 2001. On September 10, 2008, protons circulated in the LHC ring for the first time.

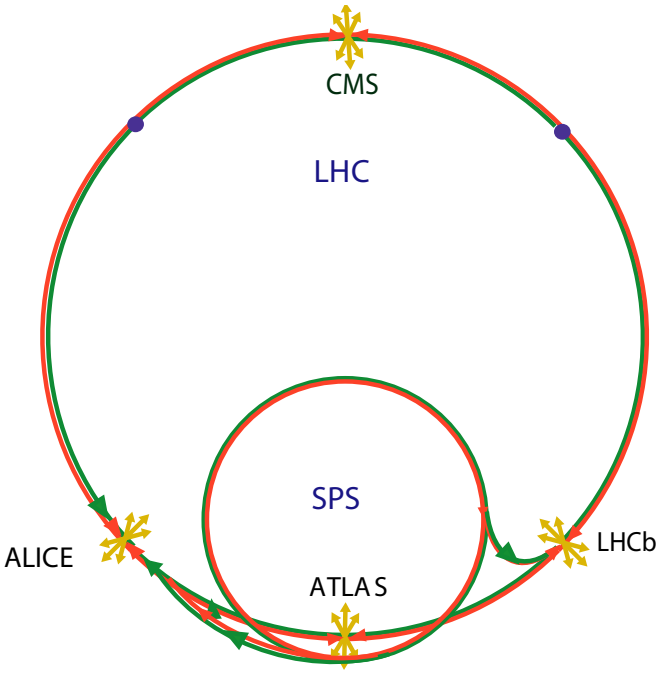

Figure 1.1: *The 26.7 km LHC accelerator ring with the four interaction points. Also shown is the SPS machine which pre-accelerates protons to an energy of 450 GeV before injecting them into the LHC.*

The protons are accelerated from rest in a series of pre-accelerators before being injected with a kinetic energy of 450 GeV into the LHC, in which they are ramped up to 7 TeV. To keep the two circulating proton beams in their orbits, a total of 1232 superconducting dipole magnets are needed. To reach the required field strength of 8.33 T the magnets are

cooled to 1.9 K using superfluid helium. At design luminosity the protons are accelerated in bunches of 1.15×10^{11} protons each, with 24.95 ns bunch spacing. Out of the 3564 possible bunches in each beam direction, 2808 are filled. This corresponds to a total beam current of 0.584 A, equivalent to a stored energy of 352 MJ.

The beams are brought to collision at four different interaction points, as illustrated in figure 1.1. Each interaction point houses a detector of the LHC: ATLAS ("A Toroidal LHC ApparatuS"), CMS ("Compact Muon Solenoid"), ALICE ("A Large Ion Collider Experiment") and LHCb ("Large Hadron Collider beauty"). ATLAS [8] and CMS [9] are general purpose detectors designed to search for new physics beyond the Standard Model (SM) at the TeV-scale, and shed light on the mechanism behind the origin of mass. ALICE [10] is a detector dedicated to heavy ion collisions, in which the physics of strongly interacting matter at high temperature is studied. The primary goal is to study the formation of a new state of matter, the quark-gluon plasma. The LHCb detector is described in the following sections.

1.1 B-physics at the LHC

B-mesons (mesons containing a b or $\overline{b}$ quark) have attracted much experimental as well as theoretical attention since the discovery of the b-quark in 1977 [2]. Their long lifetime, first measured in 1983 to be of the order of picoseconds [11, 12], makes it relatively easy to study B-mesons in the laboratory. The quark contents, lifetimes and masses of various B-mesons are listed in table 1.1. The dominant decay mode of B-mesons is through the weak transition $b \to cW$ which results in similar lifetimes to B^+, B^0 and B_s^0. The u, d and s are considered *spectator quarks*; they do not contribute to the decay at tree level. The lifetime of B_c^+ is considerably shorter due to the contribution from electroweak c decays.

Table 1.1: *World-average lifetimes and masses of various B-mesons as of January 2008 [13].*

Particle	*Lifetime [ps]*	*Mass [MeV/c^2]*
B^+ $(\overline{b}u)$	1.638 ± 0.011	5279.15 ± 0.31
B^0 $(\overline{b}d)$	1.530 ± 0.009	5279.53 ± 0.33
B_s $(\overline{b}s)$	$1.437^{+0.031}_{-0.030}$	5366.3 ± 0.6
B_c^+ $(\overline{b}c)$	0.463 ± 0.071	6276 ± 4

Apart from providing fruitful circumstances for experimental detection, the long lifetime of B-mesons gives the opportunity to observe flavour oscillations between $B^0(\overline{b}d)$ and its antiparticle $\overline{B}^0$ $(b\overline{d})$. First observed by the ARGUS collaboration in 1987 [14], the mixing is mainly mediated by a box diagram with double virtual W-boson exchange (see figure 1.2).

Decays of B-mesons carry signatures of underlying mechanisms that makes them particularly interesting to study. The two principal areas of study are CP-violation and rare decays. Both these areas contain observables that are sensitive to contributions from "New Physics" beyond the Standard Model.

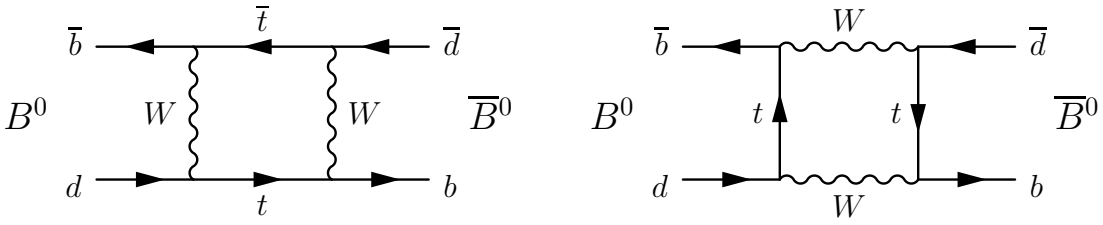

Figure 1.2: *Dominant diagrams of B^0-oscillation (mixing).*

1.1.1 CP-violation

The source of CP-violation in the Standard Model is the irreducible complex phase of the so-called Cabibbo-Kobayashi-Maskawa (CKM) matrix. This 3×3 matrix relates electroweak eigenstates of the quarks to their mass eigenstates and contains the couplings of W-bosons to up-type antiquarks and down-type quarks.

The presence of CP-asymmetry in the laws of nature was first observed in 1964 in rare weak K^0 decays [15]. In 2001, CP-violation in B-mesons decaying to the CP eigenstate $J/\psi K_S$ was observed [4, 5]. In this decay the effect is caused by quantum mechanical interference between the decays $B^0 \to J/\psi K_S$ and $B^0 \to \overline{B}^0 \to J/\psi K_S$. Later, additional measurements of CP-violation in the B^0-system have been established in a wide range of decays. See reference [13], section 12, for a comprehensive overview.

The next frontier in CP-violating B-decays is the B_s system, which is very difficult to access for e^+e^- colliders. An important difference between B^0 and B_s are their mixing properties. The particle and antiparticle states of neutral B-mesons can be expressed as linear combinations of two mass eigenstates of almost identical mass. The mass difference, Δm, which is related to the oscillation frequency of the B-meson, is larger in the B_s system than in the B^0 system. The values are $\Delta m_d = 0.507 \pm 0.005$ ps^{-1} and $\Delta m_s = 17.77 \pm 0.12$ ps^{-1} [13]. The study of CP-violation in B_s decays is considered particularly interesting due to the sensitivity of the $B_s - \overline{B}_s$ mixing phase ϕ_s to new physics, which appears for example as the relative phase between the decays $B_s \to J/\psi\phi$ and $B_s \to \overline{B}_s \to J/\psi\phi$. Particles that appear in various SM-extensions will in general introduce new CP-violating phases and cause observed CP-asymmetries to differ from Standard Model predictions. The current best individual measurement, $\phi_s = 0.35^{+0.20}_{-0.24}$ [16], has too large errors to establish a deviation from the SM-predicted value of $\phi_s = -0.037 \pm 0.002$ [17]. Hence, a precise measurement of CP-violation in the B_s system has high potential of providing evidence for new physics. A recent study [6] using combined data from CDF and DØ claims a evidence of more than 3 σ significance of new physics in B_s decays, but concludes that more experimental input are needed to avoid the use of some theoretical assumptions in the analysis.

1.1.2 Rare decays

All B-meson decays that occur through transitions other than $b \to c$ are considered rare. The SM-predictions of rare decay branching fractions are typically around 10^{-5} or smaller. The $b \to u$ transition is so strongly Cabibbo-suppressed in weak decays such that rates of $b \to s$ decays, which are not allowed at tree level in the Standard Model, are of comparable magnitude or even larger than $b \to u$ decays. These decays take place through electroweak

or gluonic loops. It is also a possibility that new, undiscovered particles contribute to these loop induced decays in a similar way as they might do in the mixing process. The result would be decay rates that differ from the Standard Model predictions. The $B_s \to \mu^+\mu^-$ decay is an example of a promising channel in which an observation of a deviating decay rate is expected in the presence of new physics. The decay is yet to be observed; the current limit on the branching fraction is less than 4.7×10^{-8} [18], while the Standard Model prediction is $(3.42 \pm 0.54) \times 10^{-9}$ [19]. Other evidence of new physics can be sought in the topological signatures of rare B-decays. An example is the asymmetry in the angular distribution of the final state muons in the flavour-changing neutral current decay $B^0 \to K^*\mu^+\mu^-$ [20] which has a branching fraction of 1.1×10^{-6} [13]. A review of the potential for observations of new physics through CP-violation and rare decays in LHCb can be found in reference [21].

1.1.3 B-production at the LHC

From experiments with air-showers [22] the total inelastic cross-section at the LHC centre-of-mass energy is known to be about 80 mb. The cross section for b-production is predicted to be 870 μb according to a PYTHIA v6.4 [23] simulation. However, the conservative number of 500 μb is conventionally used in LHCb Monte Carlo studies, such as in [24]. This translates to a one $b\overline{b}$-pair in every 160 inelastic interactions. The main production mechanisms at $\sqrt{s} = 14$ TeV are through the leading order process of gluon fusion (14.4% of the $b\overline{b}$-pairs produced) and next-to-leading order processes such as flavor excitation (60.3%) and gluon splitting (25%). Production by quark-antiquark annihilation makes a small contribution (0.2%) [25,26]. Due to the fact that the gluon processes dominate, the LHC is sometimes referred to as a gluon collider. Example Feynman diagrams of these processes are drawn in figure 1.3.

The partons participating in a pp collision typically have unequal momenta, which boosts the B-system in one of the two beam directions. As a result, the angular distribution of the b and the $\overline{b}$ peaks close to the polar angles $\theta = 0$ and $\theta = \pi$. The predicted angular distributions of produced b-quarks according to a PYTHIA Monte Carlo simulation at LHC energy are shown in figure 1.4. After production, the quarks of the $b\overline{b}$ pair hadronise separately and incoherently from each other.

The B-system has a typical boost of $\beta\gamma = 15 - 20$ with respect to the laboratory frame, which results in decay lengths of around 1 cm for the B-mesons. Such decay lengths facilitate the detection of B-mesons and allow observation of many B_s oscillation cycles. The high initial p_{T} of the b-quarks and the large mass of the B-mesons relative to the masses of the decay products, give the decay particles a higher transverse momentum distribution than that of the particles typically produced in inelastic pp collisions (so-called *minimum bias* events), see figure 1.4. Particles with high p_{T} coming from a secondary vertex that is spatially detached from the primary vertex are therefore a good experimental signature of a B-decay.

1.2 The LHCb detector

The LHCb detector [27] is a single-arm spectrometer with an angular coverage of 10–350 mrad in the bending plane of the magnet and 10–250 mrad in the non-bending

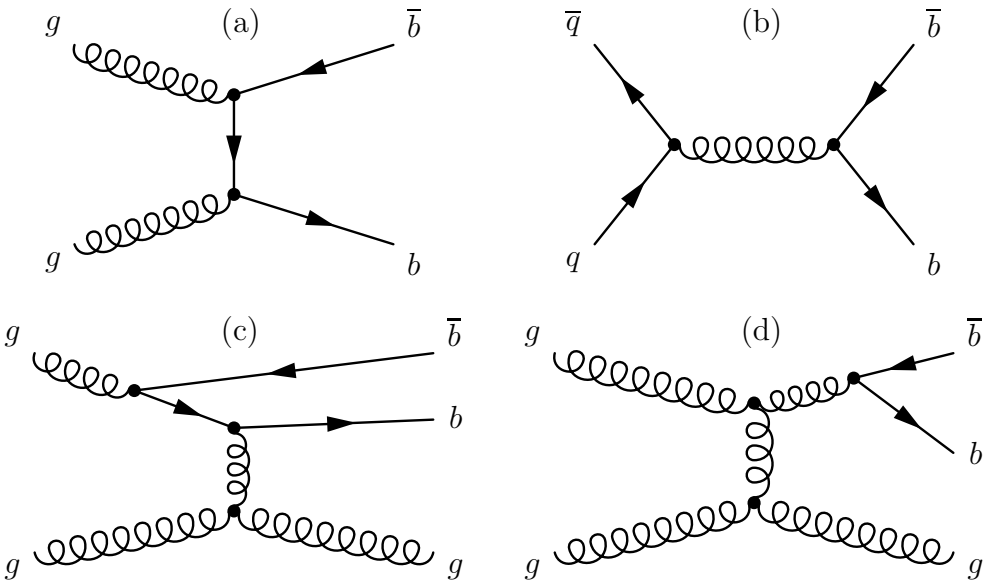

Figure 1.3: *Examples of Feynman diagrams for B-production. Two leading-order diagrams are pair creation through gluon fusion (a) and quark-antiquark annihilation (b). Examples of important higher order diagrams are flavour excitations (c) and gluon splitting (d).*

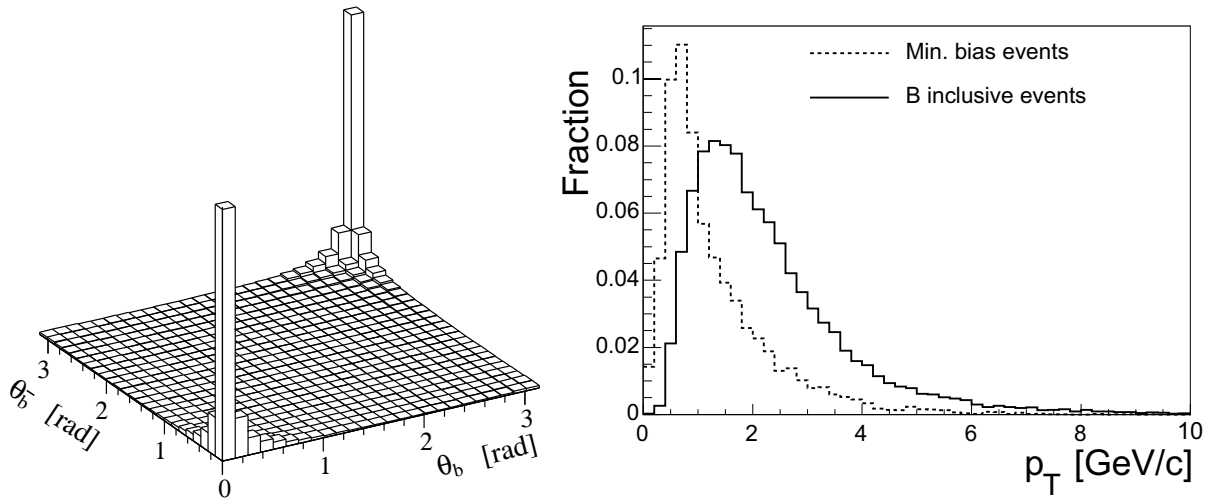

Figure 1.4: *Left: the polar angle correlation between two b-quarks produced in a pp-collision at the LHC as predicted by a Monte Carlo simulation. Right: transverse momentum (p_T) distribution of particles from B-decays compared to minimum bias events.*

plane. This corresponds to a pseudorapidity coverage of $1.7 < \eta < 5.3$ and $2.1 < \eta < 5.3$ respectively[1]. The detector layout is shown in figure 1.5. The experiment uses a right-handed coordinate system, with the z-axis pointing downstream along the beam direction and the y-axis in the upwards direction. The origin is located at the centre of the interaction region.

A warm dipole magnet [28] is used to deflect charged particles, thus providing an

[1]Pseudorapidity is defined as $\eta = -\ln\left(\tan\frac{\theta}{2}\right)$ where θ is the angle with respect to the beam axis.

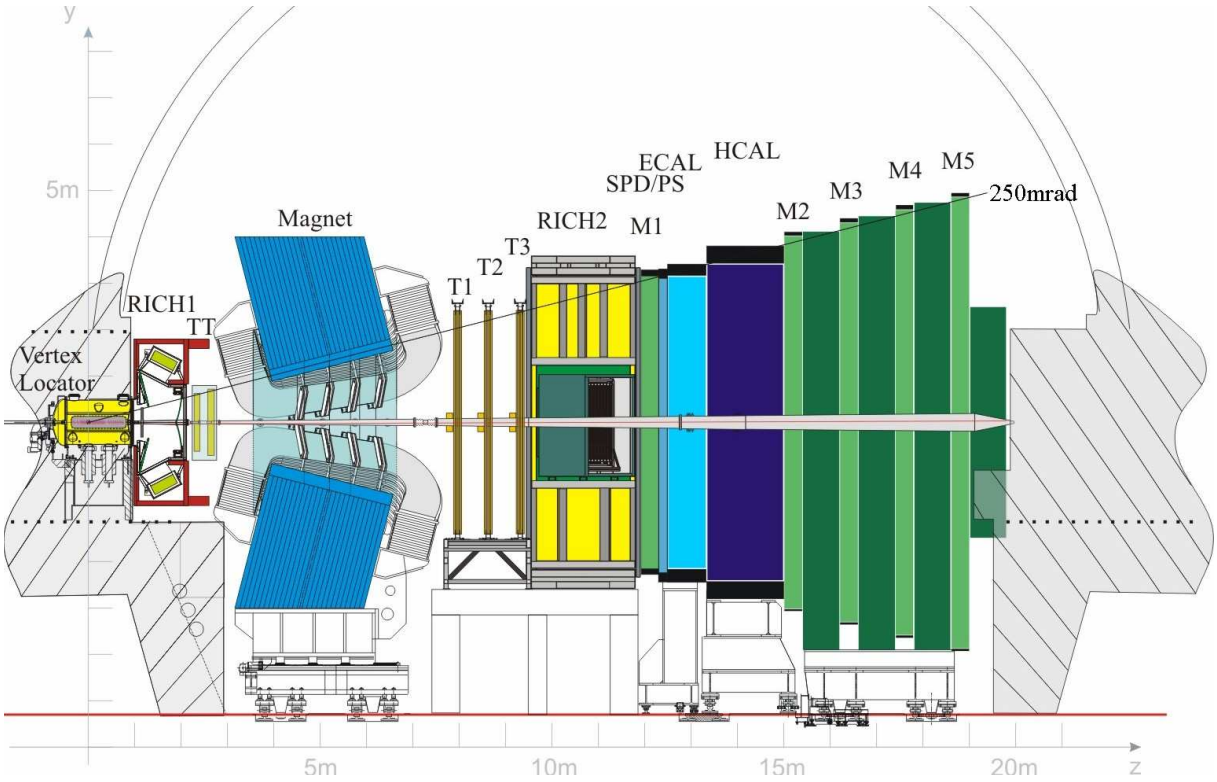

Figure 1.5: *A cross-section of the LHCb detector in the non-bending yz-plane. The interaction point is located inside the Vertex Locator.*

observable for a particle momentum measurement. The main component of the magnetic field is in the y-direction and the integrated magnetic field is 4.2 Tm. Figure 1.6 shows a perspective view of the magnet with its saddle-shaped coils. The role of the magnet in the track reconstruction is further discussed in section 1.2.2.

The angular coverage of the detector is motivated by the event topology of the produced B-mesons. As discussed in section 1.1.3, the quarks in a $b\overline{b}$-pair are either produced in the same forward or backward cone relative to the beam axis, and predominantly at high pseudorapidity ($\eta > 4.5$). At the nominal luminosity of 2×10^{32} cm^{-2}s^{-1} an estimated number of 10^{12} $b\overline{b}$-pairs will be produced and in the LHCb acceptance each year, corresponding to a rate of 100 kHz[2].

The detector is located at Interaction Point 8 (IP8), in the same cavern that was occupied by the DELPHI detector during LEP operation. To accommodate the full length of the detector in the cavern, the interaction point has been shifted 11.25 m from the centre of the cavern in the direction of IP7.

At LHC design luminosity of 10^{34} cm^{-2}s^{-1}, 27 inelastic interactions per collision occur on average. However, LHCb is not utilising the full luminosity potential of the LHC. The mean luminosity is adjusted to 2×10^{32} cm^{-2}s^{-1} by a softer focus of the beams. By operating at limited luminosity, the average number of inelastic interactions per bunch crossing at IP8 is 0.54. One inelastic interaction occurs in about 30% of the collisions and

[2]The b-production rate $\frac{\mathrm{dN}}{\mathrm{dt}}$ can be expressed in terms of the luminosity $\mathcal{L}$ and the cross-section σ_b as $\frac{\mathrm{dN}}{\mathrm{dt}} = \mathcal{L}\sigma_b$. One year is defined as 10^7 seconds.

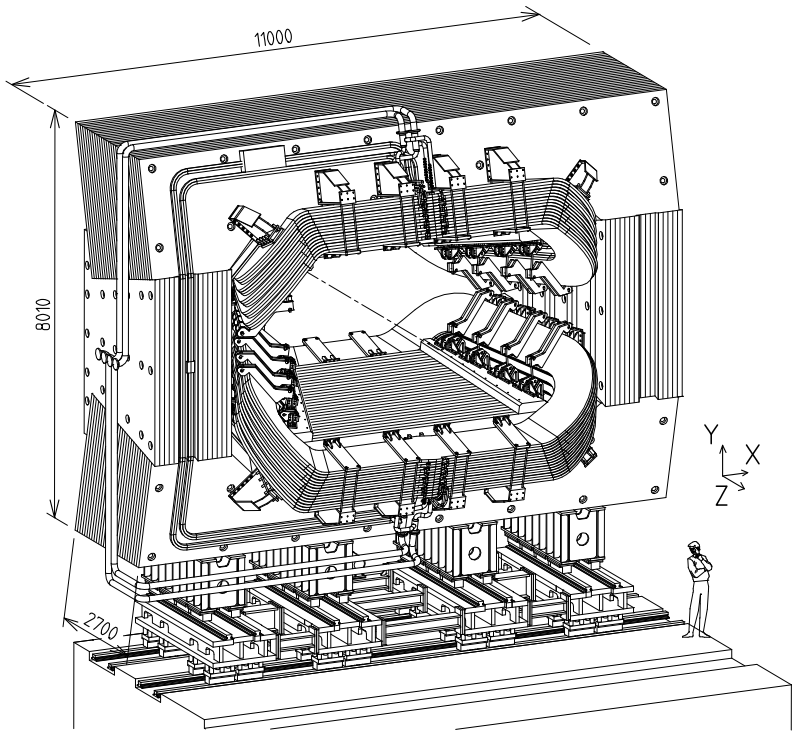

Figure 1.6:
A sketch of the warm dipole magnet in LHCb. The primary component of the field runs in the y-direction, so charged particles are mainly bent in the x-direction.

the probability of more than one interaction is less than 10%. By limiting the number of multiple interactions, it is easier to unambiguously identify the displaced vertices that are characteristic for B-meson decays and to link these vertices to the correct primary vertex. To further avoid pollution from multiple interactions in one event ("pile-up events"), a dedicated detector upstream of the interaction point vetoes bunch-crossings with more than one interaction, see section 2.6. The limited luminosity has further experimental advantages compared to LHC design luminosity operation: the detector has to withstand a lower radiation dose and the individual subdetectors get lower hit multiplicities, which is beneficial for event reconstruction.

Nevertheless, the rapidity region explored by LHCb has a high particle density. It is important to minimise the number of secondary particles created from interactions of protons incident on the beam pipe [24]. The beam pipe through LHCb is therefore of a conical design and its first 12 m (out of 19m) are made out of 1 mm thick beryllium, which has a large radiation length and a good elasticity. This makes it transparent to primary particles while withstanding the external atmospheric pressure. The design pressure in the beam pipe is 10^{-9} mbar. The LHCb detector is interfaced to the LHC beam pipe through the VELO RF-boxes surrounding the interaction point (see section 2.2). The most downstream section of the beam pipe, which is out of the critical zone of transparency, is made of stainless steel.

The subdetectors of LHCb can be divided into two main classes depending on their tasks.

The tracking system consists of the Vertex Locator (VELO), the Tracker Turicensis

(TT) and the tracking stations T1–T3. The tracking stations T1–T3 are actually two subdetectors: the Inner Tracker (IT) and the Outer Tracker (OT). The tracking system reconstructs particle trajectories across the spectrometer. By using the curvature of the tracks in conjunction with the known magnetic field provided by the dipole magnet, the momenta of the particles are reconstructed. Moreover, the tracking system provides primary and secondary vertex information.

The particle Identification (PID) system includes three detector technologies: the Ring Imaging Cherenkov detectors (RICH1 and RICH2) provide K/π separation, the electromagnetic and hadronic calorimeters (SPD, PS, ECAL and HCAL) provide e/γ separation and hadron identification, and the muon chambers (M1–M5) perform muon identification.

A short description of the individual subdetectors, the track reconstruction and the particle identification method are given in sections 1.2.1-1.2.4. The VELO is described in detail in chapter 2.

1.2.1 Tracking system

Vertex Locator

The Vertex Locator (VELO) [29], is a silicon micro-strip detector positioned around the interaction region. The sensors are arranged in 23 consecutive planes, perpendicular to the beam axis. By the use of two types of strip geometries the radial and azimuthal coordinates of traversing particles are measured. With its active area beginning at 8.2 mm from the interaction region, the VELO provides precise measurements of track coordinates which are used to reconstruct the primary collision vertex as well as displaced secondary vertices that are characteristic of B-meson decays. Two of its stations make up the so-called Pile-up Veto detector. They are used in the first level trigger (L0) to reject bunch crossings with multiple interactions. The VELO detector is described in detail in chapter 2.

Tracker Turicensis

The Tracker Turicensis (TT) [24], formerly known as the Trigger Tracker, is a silicon micro-strip detector using 500 μm thick p-in-n sensors. With a strip pitch of 183 μm its single-hit resolution is close to 50 μm. The TT is installed just upstream of the dipole magnet and covers the entire angular acceptance of the experiment. Its four planar detection layers are shown in figure 1.7. The layers are arranged in two pairs: (x, u) and (v, x), where the u and v layers are rotated around the z-axis to give the strips a stereo angle of $\mp 5^\circ$ respectively.

Inner Tracker

The Inner Tracker (IT) [30] is a silicon micro-strip detector installed in the region around the beam pipe in the tracking stations T1–T3 where the particle flux is too high to use the straw-tube technology of the OT. As in the case of the TT, single-sided p-in-n sensors are used. To satisfy the signal-to-noise requirements of the experiment, two types of sensors of 320 μm and 410 μm thickness are used. The strip pitch of 198 μm gives a single-hit

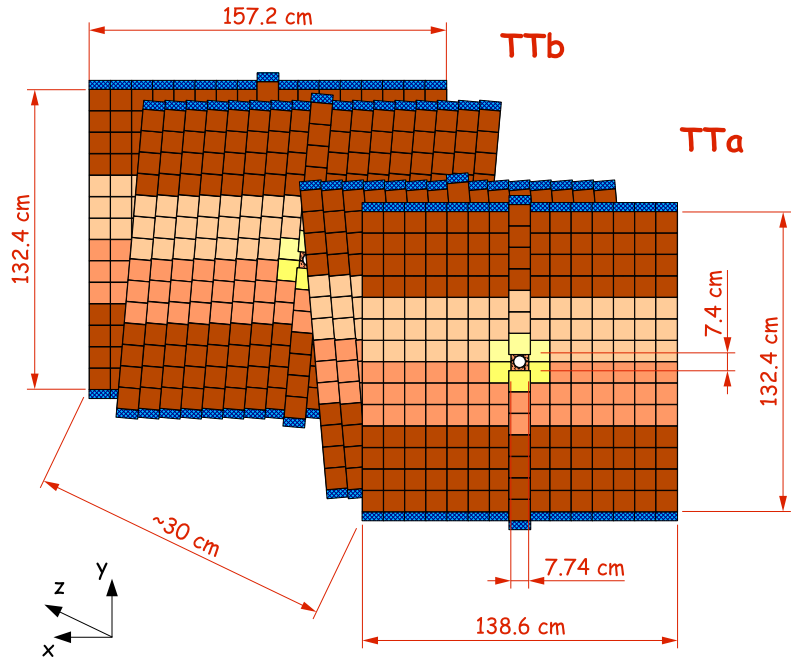

Figure 1.7: *The four layers of the TT. The two middle layers are rotated* $\pm 5°$ *around the z-axis to give the strips a stereo angle.*

resolution around 50 μm. Each of the tracking stations T1–T3 has four detection layers in the order x-u-v-x, similar to the TT. The u and v layers have a $\mp 5°$ stereo angle. Figure 1.8 shows the design and dimensions of an x and a u layer.

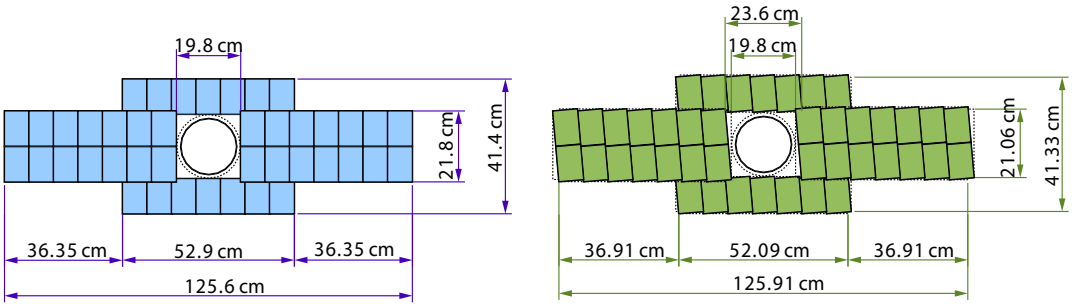

Figure 1.8: *The x (left) and u (right) layers of an IT station. The silicon sensors are arranged in a cross around the beam pipe. The detector modules consist of either one or two sensors. The one-sensor and two-sensor modules are 320* μm *and 410* μm *thick respectively. The two-sensor modules are noisier and are therefore thicker in order to maintain a sufficient Signal-to-Noise ratio.*

Outer Tracker

The Outer Tracker (OT) [31–33] is a straw-tube detector surrounding the IT in the T1–T3 tracking stations. It measures drift times in straw-tubes to determine the position of intercept of a charged particle. The maximum drift time is kept below 50 ns and the drift-coordinate resolution is about 200 μm [34].

Figure 1.9 shows a perspective view of the OT, IT and TT detection layers. Just like the IT, the OT modules are arranged in three stations. Each station consists of four layers in the same x-u-v-x orientation. The modules that make up an OT layer consist of two staggered "monolayers" with 5 mm diameter straw-tubes, illustrated in figure 1.9. The OT extends to cover the full outer angular acceptances of LHCb.

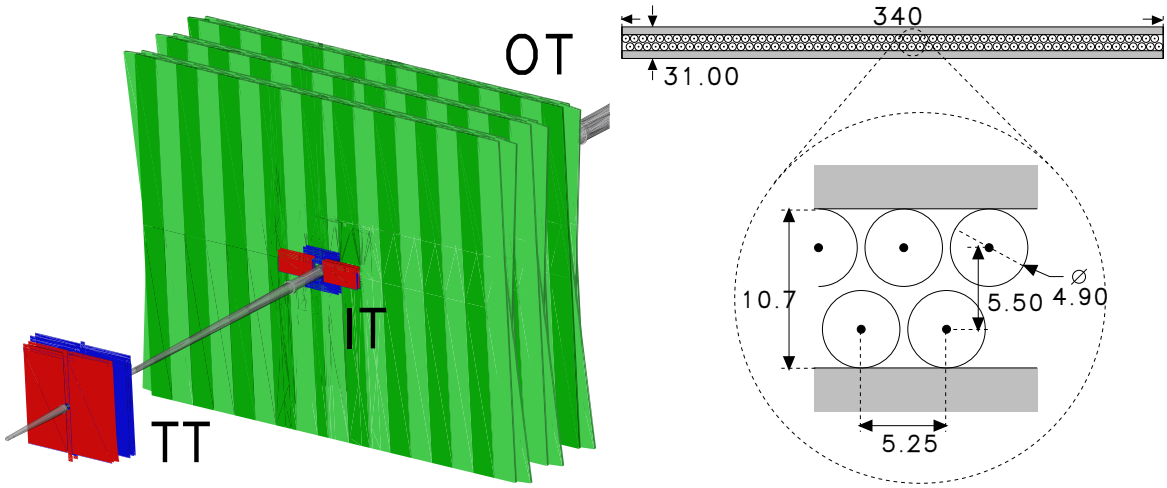

Figure 1.9: *Left: A perspective view of the TT, IT and OT detection layers. Right: Cross-section of an OT module, showing the staggered monolayers and the layout of the drift-tubes. Sizes are in millimetres.*

1.2.2 Track and vertex reconstruction

The tracking software combines hits from all the tracking detectors to find and reconstruct particle trajectories. By using the curvature of the tracks and knowledge of the magnetic field in the detector, momenta and particle charges can be deduced. The starting point of the reconstruction are pattern recognition algorithms [35, 36] that find initial track states (track seeds) in the detectors. A track state is defined by the particle charge, its momentum, and the (x, y)-position as well as tangent directions at a given z-coordinate. The track seeds are refitted using a Kalman filter method [26,37,38]. This technique uses an algorithm that progressively adds measurements in the fit to update the track state with new information. The Kalman filter is mathematically equivalent to a least squares fit but in addition it incorporates the effects of multiple scattering and energy loss.

Five classes of tracks are defined [39, 40], as illustrated in figure 1.10. The *long tracks* are reconstructed from measurements in all tracking detectors and have the best momentum resolution. *Upstream tracks* are typically low momentum tracks that only traverse the VELO and TT before being bent out of the detector acceptance by the magnetic field. *Downstream tracks* only traverse the TT and T-stations. These are typically decay products of particles decaying outside the VELO acceptance or with insufficient VELO hits to be reconstructed. *T tracks* are only measured in the T-stations. They are typically produced in secondary interactions or are low angle tracks that are bent into the acceptance by the magnetic field. Finally, *VELO tracks* only have hits in the VELO due to a large or backwards production angle. These VELO tracks are used mainly for

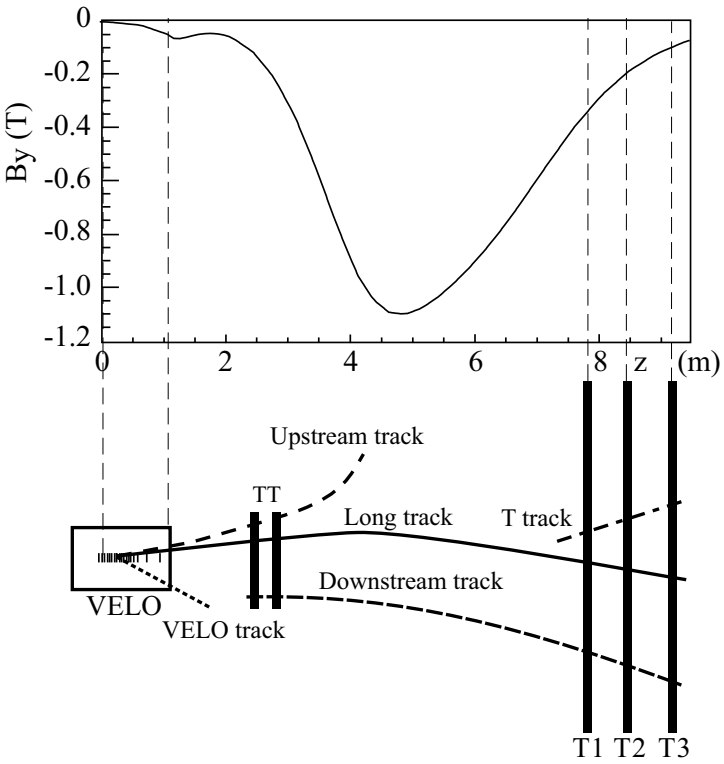

Figure 1.10: *A schematic overview of the various track types in LHCb, together with the main B-field component as a function of z.*

primary vertex reconstruction. A typical B-event has an average of 106 reconstructed tracks, of which long tracks and VELO tracks are the most common [26]. The relative resolution $\delta p/p$ of long tracks, as calculated using Monte Carlo simulations[3], is plotted versus momentum in figure 1.11a. The resolution δp is defined as the RMS of the residual distribution between the reconstructed and true track momentum. The plot immediately below shows the momentum spectrum of B-decay particles in generic B-events. The *impact parameter* resolution $\sigma_{\mathrm{d_0}}$ is plotted as a function of $1/p_{\mathrm{T}}$ in figure 1.11b, with the $1/p_{\mathrm{T}}$-distribution below. The impact parameter d_0 is the shortest distance in three dimensions between a track and the primary vertex. It is used extensively in the trigger to select B-candidates. The impact parameter resolution depends on the multiple scattering of the particles, the hit resolution and the geometry of the tracking detector. A linear fit to the data points in figure 1.11b gives the impact parameter resolution parameterisation $\sigma_{\mathrm{d_0}} = 14\mu\mathrm{m} + 35\mu\mathrm{m}/p_{\mathrm{T}}$. For the derivation of a model for the impact parameter resolution, see appendix A.

Primary vertices (PV) are reconstructed using long, upstream and VELO-tracks. The principle is to use a global least squares fit, minimising the χ^2 :

$$\chi^2 = \sum_{i=1}^{n_{tracks}} \frac{d_{0_i}^2}{\sigma_{d_{0_i}}^2} \tag{1.1}$$

where d_0^2 is the three-dimensional impact parameter between a track and the PV position.

[3]These simulations were performed for the *LHCb Reoptimized Detector Technical Design Report* [24].

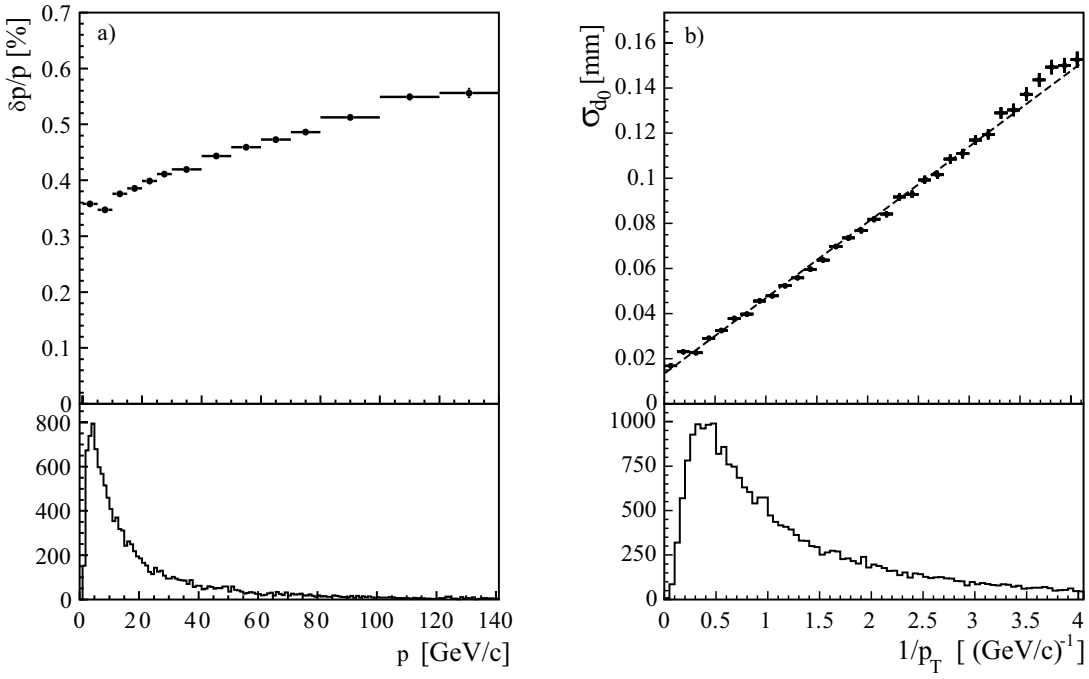

Figure 1.11: *(a) Relative momentum resolution of the reconstructed long tracks as a function of momentum, with the momentum spectrum of B-decay particles below. (b) Impact parameter resolution (σ_{d_0}) as a function of inverse transverse momentum. The dashed line is a linear fit to the data points. The $1/p_{\mathrm{T}}$ spectrum of B-decay particles is shown below.*

Monte Carlo simulations with an accurately modelled detector predict a PV resolution of 8, 10 and 59 μm in the x, y and z dimension respectively [41]. Secondary detached vertices from B-decays are reconstructed offline using a variety of techniques. If no assumptions are made about the nature of the decay, an unconstrained fit is used where tracks with a common point in space are found using an iterative minimum χ^2 procedure. Higher precision can be achieved by constraining the fit based on kinematical properties of the decay, such as the mass of the mother particle. In a mass constrained fit, the summed invariant mass of the tracks is required to be that of the mother particle. For further explanations and details, see [42].

1.2.3 Particle Identification system

RICH

Efficient separation of pions and kaons is important for the physics programme of LHCb. For this purpose, two Ring Imaging Cherenkov (RICH) detectors [43] are used. The detection principle is based on the process of Cherenkov radiation, i.e. photons are emitted when a charged particle passes through an insulator (a so-called "radiator") at a speed greater than the macroscopic speed of light in that medium. The angle of the emitted photons can be related to the velocity of the charged particle. Thus, by combining a Cherenkov angle with a momentum measurement, the mass of the particle can be calculated. In this way, pions and kaons can be separated.

The two RICH detectors in LHCb cover the full charged particle momentum range from

about 1–100 GeV/c. This is accomplished by using three different radiators: aerogel and C_4F_{10} in RICH (1–60 GeV/c) and CF_4 in RICH2 (15–100 GeV/c). Figure 1.12 shows the Cherenkov angle as a function of particle momentum for the RICH radiators. The

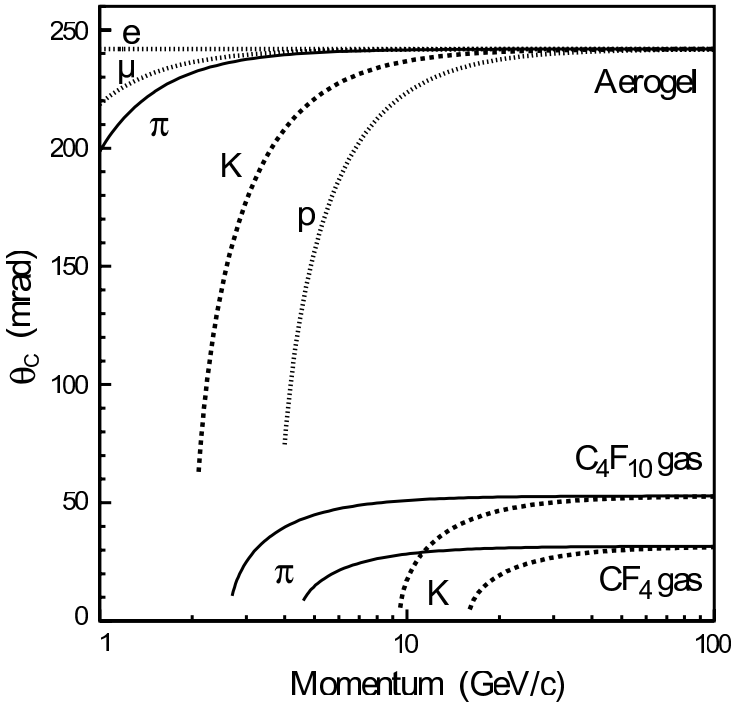

Figure 1.12: *Cherenkov angle as a function of particle momentum for the three radiators used in LHCb. The best π/K separation for low momentum particles is accomplished by RICH1 which uses aerogel and C_4F_{10}. RICH2, using CF_4 as radiator, is designed for the momentum range above 15 GeV/c.*

Cherenkov light, which is in the 200-600 nm wavelength range, is reflected out of the detector acceptance by the use of spherical and flat mirrors, and focused onto Hybrid Photon Detectors (HPDs). In the HPDs, the incident photons are converted into photoelectrons which are detected by an array of 1024 500 μm $\times$ 500 μm large silicon pixels. The measurements in the HPDs are combined to reconstruct rings, the radii of which are measures of the Cherenkov emission angles of the traversing particles.

RICH1 is situated upstream of the dipole magnet, between the TT and the VELO, while RICH2 is situated between tracking station T3 and the first muon station. The design of the two detectors is illustrated in figure 1.13.

Calorimeters

The calorimeters [44] are located between the muon stations M1 and M2. They provide particle identification as well as energy and position measurements. The first level trigger (L0) relies heavily on their ability to quickly select photon, electron and hadron candidates with high transverse energy[4] (E_T). The structure is classical: an electromagnetic calorimeter (ECAL) followed by a hadronic calorimeter (HCAL). Both ECAL and HCAL work with a similar basic principle: incident particles interact with the absorber

[4]Transverse energy is not a physical concept but defined as $E_T \equiv E \sin\theta$ where θ is the polar angle.

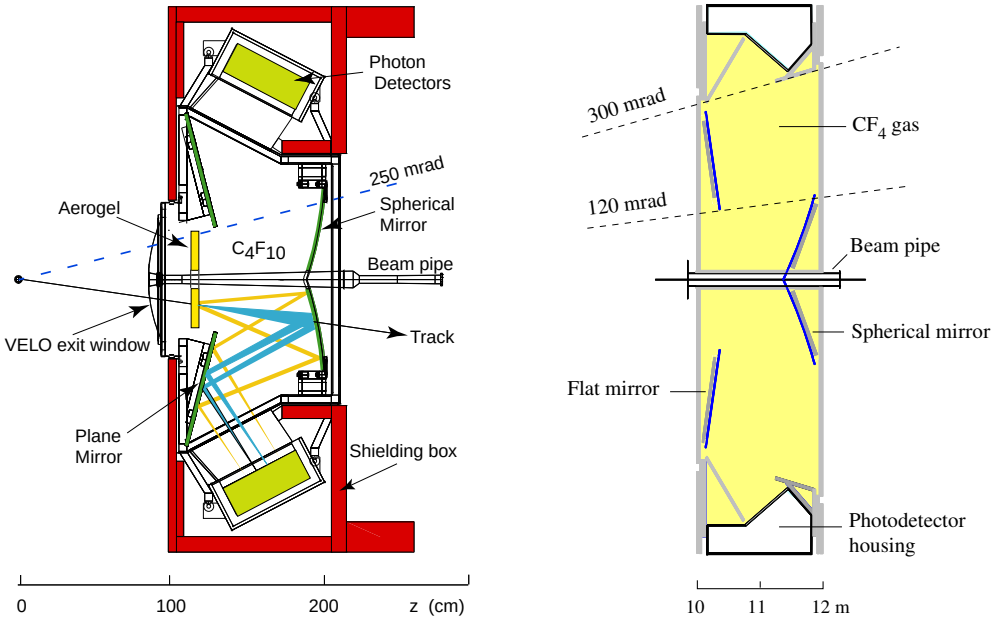

Figure 1.13: *Side-view of the RICH1 (left) and RICH2 (right) detectors. Note that the scale differs between the figures.*

material (lead in the ECAL and iron in the HCAL) of the calorimeter, creating a cascade or shower of secondary particles. These particles induce light as they pass through scintillators (polystyrene plastic) inside the calorimeter. The light is collected by photomultiplier tubes and the amount of collected light can be related to the energy of the original incident particle. The ECAL is designed to fully contain the shower of electrons and photons, while the HCAL fully absorbs the energy of hadrons. Muons are not stopped by the calorimeters but make a small energy deposition. The hit density depends on the distance to the beam pipe and varies over the calorimeter surface by two orders of magnitude. The calorimeter is therefore segmented into inner, middle and outer sections with increasing cell size. The dimensions of the calorimeters are $6.2\,\mathrm{m} \times 7.8\,\mathrm{m} \times 0.18\,\mathrm{m}$ (ECAL) and $6.8\,\mathrm{m} \times 8.4\,\mathrm{m} \times 1.2\,\mathrm{m}$ (HCAL).

Two additional detectors are located before the ECAL to provide further particle identification. The Scintillating Pad Detector (SPD) detects the passage of charged particles and is used in conjunction with the ECAL to separate electrons from photons (the latter pass the SPD undetected). Separated from the SPD by a 15 mm lead layer ($2.5\ \mathrm{X}_0$) which induces electromagnetic showers, the Preshower (PS) detector is mounted. Light hadrons, like charged pions, deposit more energy in the PS than electrons. This is exploited for e/π-separation.

Muon system

The muon system [45–47] consists of five stations (M1–M5) of rectangular shape positioned downstream of the RICH2 detector with the calorimeters located between M1 and M2. Muons are detected using radiation hard multi-wire proportional chambers with fast response time, with exception of the innermost part of M1 where the particle flux is too high and triple Gas Electron Multiplier (GEM) detectors are used instead. Iron absorbers are interleaved between stations M2–M5 and behind M5. They remove hadronic back-

grounds and shield the muon detector from particles that have strayed from the LHC beam. The muon system is used in the L0 trigger to select events with muons of high transverse momentum (p_{T}) and in the high-level trigger (HLT) and offline analysis for muon identification. In the trigger, the muon chambers are used for a stand-alone momentum measurement with a p_{T} resolution of about 20%. The momentum is obtained by assuming that a muon track originates from the nominal interaction point and using the position and slope of the track between M1 and M2 to calculate the deflection by the magnetic field. By placing M1 before the calorimeter the uncertainty in the momentum measurement due to scattering is decreased.

1.2.4 Particle Identification methods

The information from the RICH detectors, the calorimeters and the muon system is combined for the identification of charged particles ($e, \mu, \pi, \mathrm{K}, \mathrm{p}$). The ECAL, SPD and PS are used to identify neutral particles (γ, π^0).

The baseline algorithm for K/π-identification in the RICH uses a log-likelihood approach which matches the observed pattern of hit pixels in the RICH photodetectors to that expected from the reconstructed tracks under a given set of particle hypotheses [48]. The average efficiency for kaon identification is $\epsilon(K \to K) = 95\%$ with a corresponding average pion misidentification rate $\epsilon(\pi \to K) = 5\%$ [27].

Muons are identified by extrapolating reconstructed tracks with $p > 3$ GeV/c into the muon stations[5]. Hits are searched around the extrapolation point of the track in each muon station. Using a sample of $B_0 \to J/\psi K_s$ the muon identification efficiency was measured to be $\epsilon(\mu \to \mu) = 94\%$ with a corresponding misidentification $\epsilon(\mathrm{p} \to \mu) = 3\%$ [27].

The electron identification is mainly based on the balance of track momentum and energy of the charged cluster in the ECAL, and the matching between the position of the cluster with the extrapolated track impact point [49]. Further improvement in electron identification is obtained by using the track energy deposition in the Preshower detector and the deposition of the energy along the extrapolated particle trajectory in the HCAL. [27]

Photons are reconstructed and identified with the electromagnetic calorimeter, as clusters without an associated track. By matching hits in the SPD with ECAL clusters, further purity improvements in photon identification are reached [50].

1.2.5 Trigger

LHCb will operate at a luminosity of 2×10^{32} cm^{-2}s^{-1}, a factor 50 lower than the LHC design luminosity. The reasons for this were discussed in section 1.2. The purpose of the trigger is to reduce the 40 MHz bunch crossing rate to about 2 kHz which is the rate at which the events can be stored for offline analysis. This is achieved in two trigger levels: Level 0 (L0) and the High Level Trigger (HLT). The trigger scheme is illustrated in figure 1.14 and described in the following section.

[5] Particles with $p < 3$ GeV/c do not reach the muon system.

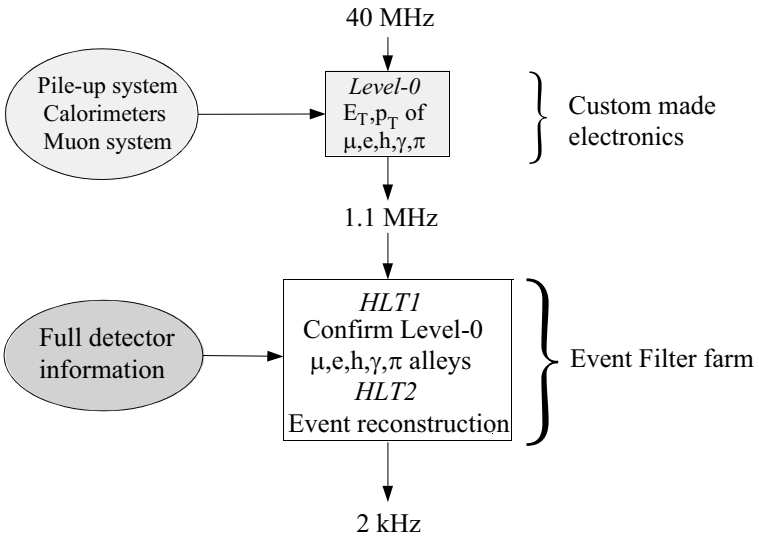

L0 criteria

μ_1	p_T	> 1.3 GeV/c
$\mu_1+\mu_2$	p_T^{total}	> 1.5 GeV/c
h	E_T	> 3.5 GeV
e	E_T	> 2.6 GeV
γ	E_T	> 2.3 GeV
π^0	E_T	> 4.3 GeV

Figure 1.14: *Left: Schematic overview of the Trigger system which reduces the 40 MHz bunch crossing rate to a storage rate of 2 kHz. Right: L0 trigger criteria for nominal luminosity (as used in the simulated "DC06" dataset).*

Level 0

The L0 trigger operates at 40 MHz synchronous with the LHC clock. It uses custom made electronics to form the trigger decision using information from the calorimeters, the muon system and the pile-up veto detector. Due to the large mass of B-mesons, the decay products often have large p_T and E_T. The L0 decision is based on the observed values of the two highest p_T muons and highest E_T hadron, electron and/or photon clusters. Additionally, the pile-up detector in the VELO is used to reject bunch crossings with multiple interactions. The information from these subdetectors is collected by the L0 Decision Unit which evaluates the data. If they match one or more of the required criteria (see the table in figure 1.14), a signal is sent to the front-end electronics of all subdetector systems, triggering them to be read out. The latency, i.e. the total time between bunch crossing and the arrival of the trigger decision at the subdetectors, is fixed to 4 μs. The allowed output bandwidth of L0 is 1.1 MHz.

High Level Trigger

The High Level Trigger (HLT) is a computer program that runs on a farm of 2000 CPUs. It has access to the full event information from all subdetectors and its purpose is to reduce the 1.1 MHz input rate from L0 to a 2 kHz output rate at which events are stored for offline analysis. To meet the time limitations imposed by this requirement, the HLT has two stages. In the first stage (HLT1) the events are sorted into different "alleys" that each address one of the L0 trigger types. Depending on the L0 trigger type, events may enter multiple trigger alleys. The events are partially reconstructed to such an extent that the majority of the uninteresting events is rejected. The primary vertex position is reconstructed using 2D Rz-tracks in the VELO. The impact parameter of a track with respect to the primary vertex is a powerful discriminator for B-events and used in many of the alleys.

The second stage (HLT2), which operates at an event rate of approximately 30 kHz, performs a full reconstruction with information from all subdetectors and makes the final trigger selection. Figure 1.15 illustrates the trigger flow from L0 via HLT1 and HLT2 to storage.

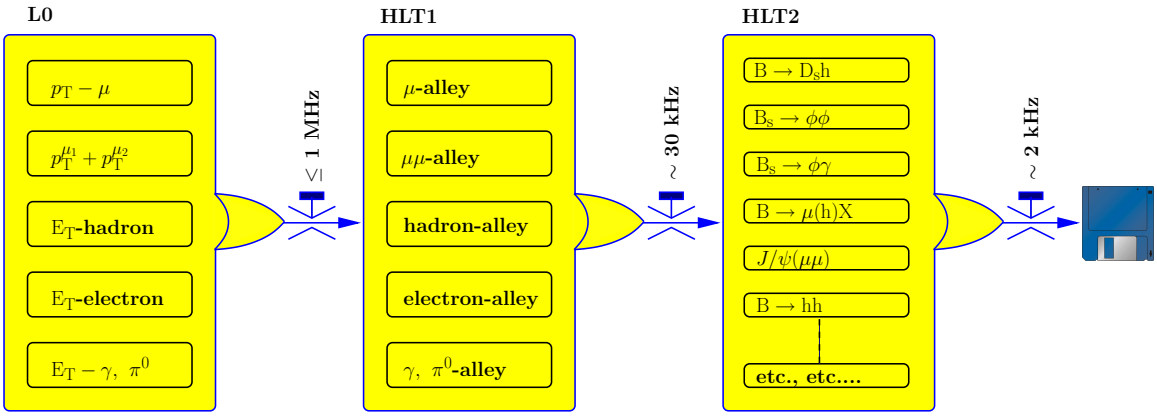

Figure 1.15: *Flow diagram of the various sequences in the trigger.*

2 The VELO detector

The LHCb physics programme relies on the ability to successfully select B-events at the trigger level and to accurately reconstruct them offline while rejecting the abundantly produced background events efficiently. A "smoking gun" signature of a b- or c-hadron decay is the presence of a secondary vertex, spatially detached from the interaction point. The Vertex Locator (VELO) detector is a silicon micro-strip detector specially designed for vertex detection. To optimise the vertex reconstruction resolution the sensitive area of the detection layers starts at 8 mm from the beam axis. This design has many consequences which will be discussed here. The chapter begins with an introduction to the principles of silicon detectors (section 2.1). An overview of the VELO detector (section 2.2) is followed by a description of the silicon sensors (section 2.3), the front-end readout chip (section 2.4) and detector readout (section 2.5). The two last sections give brief overviews of the Pile-Up detector (section 2.6) and the VELO alignment (section 2.7).

2.1 Charged particle detection with silicon detectors

Semiconductors, such as silicon, have electrical properties that fall between those of insulators and metals. In crystalline silicon, the atoms are packed together in a diamond lattice structure with four valence electrons. These electrons occupy a near continuous band of energy levels, forming a so-called *valence band*. If the electrons are given sufficient energy, they can break the covalent bonds of the lattice and become liberated. Via this process the electron is said to be promoted to the *conduction band*, leaving a "hole" in the valence band. Electrons in the conduction band can be treated as free charge carriers and likewise, the holes can be treated as positive charge carriers that move freely in the valence band.

The difference between a metal (conductor), a semiconductor and an insulator lies in the size of the smallest energy difference, the so-called band gap, between the valence and conduction band. The band gap of silicon is 1.12 eV at room temperature and atmospheric pressure. In comparison, insulators typically have band gaps exceeding 9 eV while the bands overlap in conductors. The conductive properties of a semiconductor can be modified by the introduction of a *dopant* in the silicon lattice. The dopant is typically a *donor* atom from group V (e.g. phosphorus) or an *acceptor* atom from group III (e.g. boron). The introduction of a donor atom adds an extra valence electron to the silicon lattice and results in a new discrete energy level just below the conduction band. The silicon is said to be of *n-type*. With the addition of an *acceptor* atom, which has one valence electron less than silicon, a discrete energy level is created just above the valence band. Electrons from the silicon fill up the new energy level, leaving holes in the valence band. This type of silicon is called *p-type*. With this method, called doping, silicon can be made conductive at room temperature.

The introduced valence electrons or holes take the role of charge carriers in the doped

material. If an external electric field is applied to the silicon, the charge carriers start to drift in the direction of the field. The drift velocities of electrons and holes are determined by their *mobility*, which is about three times larger for electrons than for holes.

The basic working principle of all silicon sensors is the presence of a pn-junction, which occurs when p-type and n-type silicon are brought into contact. The holes in the p-type silicon and electrons in the n-type silicon will diffuse across the junction and recombine with each other. At equilibrium a *depletion zone* devoid of free charge carriers has been formed, with a built-in electric field over the zone. The two pieces of silicon together form a diode, in which current can only flow in one direction. The size of the depletion zone can be increased by applying a reverse bias to the silicon. The voltage at which the depletion region extends across the entire depth of the sensor is called the *depletion voltage*.

2.1.1 Energy loss in silicon

As charged particles pass through silicon, they lose energy through inelastic and elastic scattering with nuclei and atomic electrons. The energy transferred during scattering causes the atoms to ionise and induces electron-hole pairs in the depletion zone. The electric field across the pn-junction prevents immediate recombination and the electrons and holes drift to the n- and p-side respectively. At room temperature, the average energy needed for electron-hole pair creation is 3.6 eV, and the most probable energy deposition in silicon is about 264 eV/μm. For a 300 μm thick sensor, which is used in the VELO, this results in about 22000 electron-hole pairs. These electron-hole pairs will drift through the diode and induce charge on the electrodes.

The average energy loss dE/dx of highly energetic charged particles in matter can be described by the Bethe-Bloch formula (see e.g. reference [51] for details). At typical momenta of decay products from pp-interactions in the LHC, the relativistic charged particles are *minimum ionising*, i.e. their energy loss in matter is the minimum loss predicted by the Bethe-Bloch formula. Such particles are referred to as MIPs (minimum ionising particles). As was shown by Landau [52], the energy loss (ϵ) distribution of a MIP in a thin absorber of thickness d can be described by

$$f_L(\epsilon, d) = \frac{\phi(\lambda)}{\xi} \tag{2.1}$$

where ξ is proportional to d and depends on the material properties, and the Landau distribution $\phi(\lambda)$ can be formulated as

$$\phi(\lambda) = \frac{1}{\pi} \int_0^\infty e^{-u(\lambda + \ln u)} \sin(\pi u) \mathrm{d}u \tag{2.2}$$

where λ is a dimensionless number that depends on the energy loss ϵ [51]. The energy at which the Landau distribution peaks is referred to as the *most probable value* (MPV). For a 300 μm thick sensor, the average energy loss is about 16% higher than the most probable energy loss [53]. Although silicon sensors used in high-energy physics experiments can be viewed as thin absorbers, the Landau distribution fails to accurately describe the energy loss distribution of a MIP. This is mainly due to simplifications with regards to the binding of atomic electrons in the derivation of the distribution function. A practical solution to

the problem is to use a Landau distribution convoluted with a Gaussian distribution [54]:

$$f(\epsilon, d) = \frac{1}{\sigma\sqrt{2\pi}} \int_{-\infty}^{\infty} f_L(\epsilon', d)\, e^{-(\epsilon-\epsilon')^2/2\sigma^2} \mathrm{d}\epsilon'. \tag{2.3}$$

When evaluating experimental data, the Gaussian component also serves the purpose of accounting for system noise, like Gaussian noise in the detector and front-end electronics.

Figure 2.1 shows an authentic example of this: the distribution of collected charge in a VELO silicon sensor fitted with a pure Landau and with a convoluted Landau⊗Gaussian distribution[1].

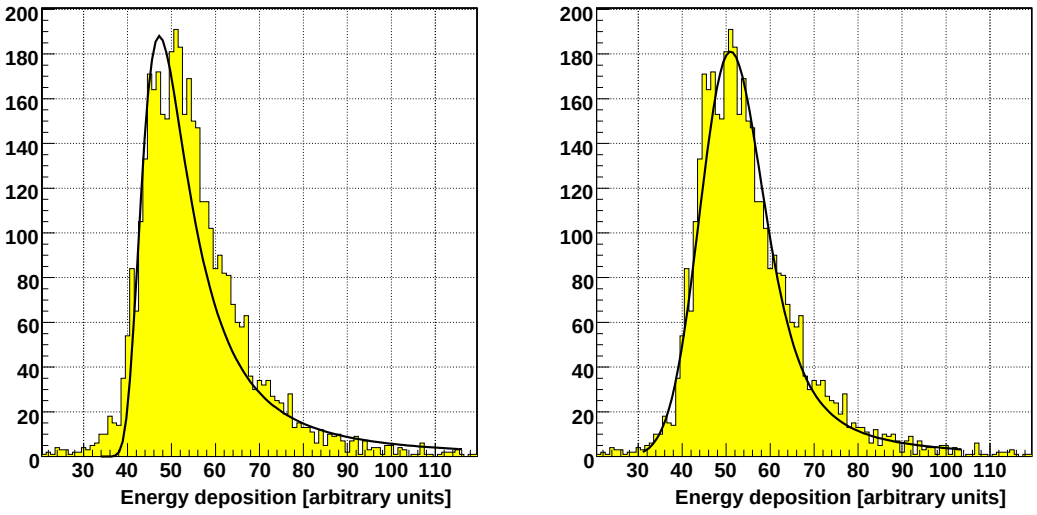

Figure 2.1: *Collected charge distribution in a VELO sensor, fitted with a pure Landau (left) and with a convoluted Landau⊗Gaussian distribution (right). The normalised χ^2 of the two fits are 6.45 and 2.28 respectively.*

The pure Landau will underestimate the most probable value (MPV) of the energy deposition and fail to fit the distribution over the full range. The convoluted fit function performs better. Equation 2.3 will be used in chapters 3 and 4 to extract the MPV of the Landau component in VELO sensor energy loss distributions much like that in figure 2.1. The MPV will be quoted as the signal level of the sensors.

2.1.2 Silicon strip detectors

The concept of reverse biased pn-junctions is put into use in *silicon micro-strip detectors*. The main components of such a detector are the backplane, the bulk and the strip implants (see figure 2.2).

In the VELO sensors, the bulk consists of lightly doped n-type silicon. Acceptor atoms are diffused into one edge of the bulk, resulting in a thin layer of heavily p-doped silicon which forms the p^+-type backplane. On top of the bulk shallow strips of n^+-type silicon

[1] For the convolution, the implementation of Früwirth, Pernegger and Friedl is used, see http://root.cern.ch/root/html/tutorials/fit/langaus.C.html.

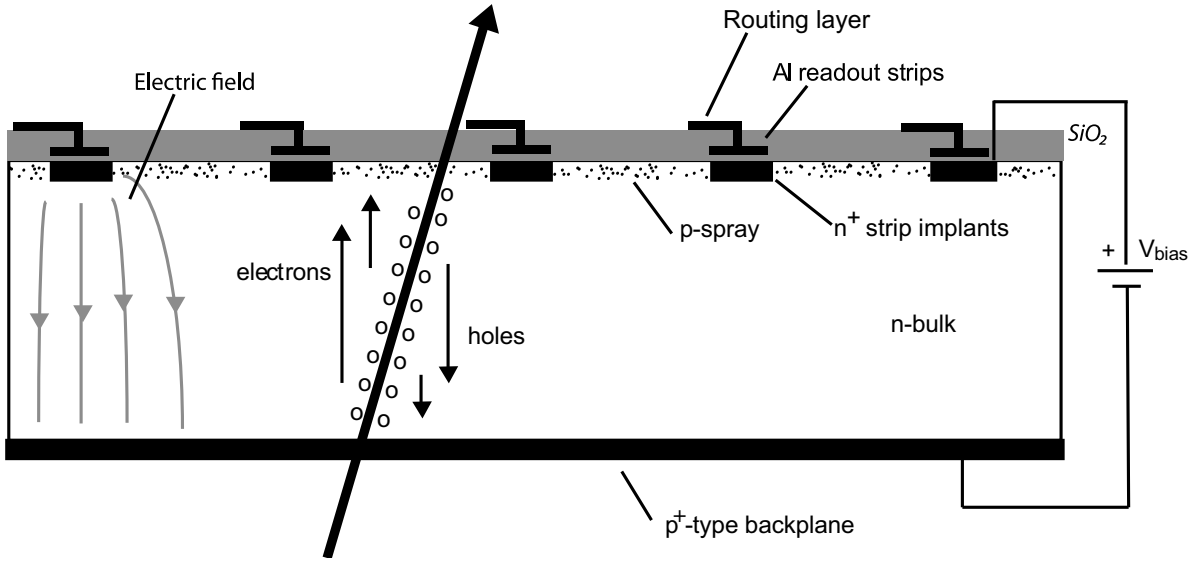

Figure 2.2: *Cross-section of a VELO silicon sensor of type n-in-n. The pn-junction is formed at the interface of the backplane and the bulk. A reverse bias is applied to the sensor, creating an electric field between the backplane and the implants. If an ionising particle traverses the bulk while the sensor is depleted, electrons will drift towards the implant side, inducing a signal on the strips. The holes drift towards the backplane. A SiO_2 layer isolates the silicon from direct contact with the Al readout strips, and thus forms an AC coupling to the strip implants. The Al readout strips are connected to a routing layer which transports the strip signals to the front-end electronics.*

(heavily n-doped) are implanted. This design is called *n-in-n* and one of its features is its radiation hardness in comparison to p-in-n type silicon, another design commonly used in micro-strip detectors (n^+-type backplane, n-type bulk and p-type strips). Under irradiation, the relative dopant concentration in n-type silicon decreases and the silicon effectively becomes p-type. After this so-called type inversion, the voltage required to fully deplete the sensor increases with the received radiation dose. Above a certain voltage, the silicon experiences an electrical breakdown. This limits the operational lifetime of the sensor. At type inversion, the junction of a n-in-n sensor moves to the strip side of the sensor while the junction of a p-in-n sensor moves to the backplane. The n-in-n sensor can therefore be operated without being fully depleted while the p-in-n sensor has to be operated fully depleted, making it more vulnerable to breakdown.

To maintain isolation between the implants, a shallow layer of p-type silicon, *p-spray*, is introduced between the strips. The signal from the strips are extracted by AC coupling to aluminium metal strips which are read out through contacts. Due to the strip geometry of the VELO sensors, a routing layer (the *double metal layer*) is required to transfer the charge from the strips to the read-out electronics at the outer radius. A 3.5 μm thick oxide (SiO_2) layer isolates the implants from direct contact with the Al strips and the double metal layer. The strips are biased using 1.8 MΩ polysilicon resistors.

2.2 Detector overview

The VELO design is mainly driven by the requirement of high spatial resolution on the reconstructed track parameters close to the interaction region. Figure 2.3 shows an overview of the detector. The silicon sensors are mounted in two separate detector

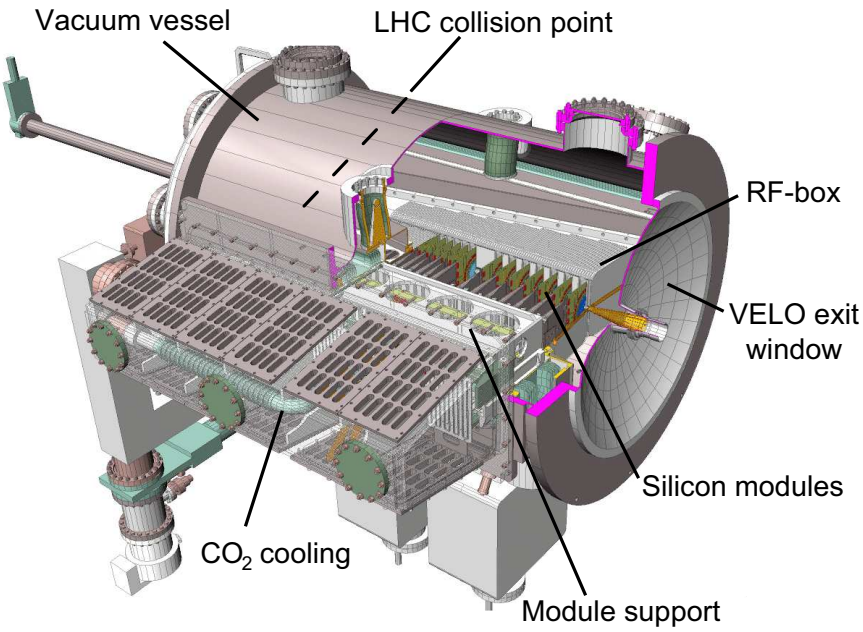

Figure 2.3: *Overview of the VELO vacuum vessel.*

halves and are arranged in planes perpendicular to the beam to cover the full angular acceptance of the spectrometer. To minimise the extrapolation distance between the beam interaction region and the sensors, the latter are placed at a radial distance of 7 mm from the beam axis, with the active area starting at a radius of 8.2 mm. As this is smaller than the aperture required by the LHC beams during injection[2], the detector will be retracted by 30 mm. The proximity of the sensors to the interaction region also implies that the detector has to be integrated in the LHC vacuum system, and shielded against RF-pickup from the beams. For this purpose as well as to protect the LHC vacuum from outgassing of detector modules, the sensors are separated from the machine (primary) vacuum by 300 μm thick aluminium boxes (the RF-boxes). As the RF-boxes are expected to deform non-elastically at a differential pressure of 20 mbar or more, the pressure difference between the primary vacuum and the detector volume (secondary vacuum) needs to be kept small during evacuation, operation and venting[3]. The primary and secondary vacuum pressures are 10^{-9} mbar and 10^{-6} mbar respectively during nominal operation.

The sensors are mounted in two detector halves in a vacuum vessel in such a way that the sensors overlap slightly in the closed position. The RF-boxes are corrugated to accommodate the overlapping sensors and the passing beams. The nominal clearance

[2]The LHC beam pipe has a radius of 27 mm.

[3]The pressure difference between beam and detector vacuum never exceeds 5 mbar overpressure in the detector vacuum and 2 mbar overpressure in the beam vacuum.

between the sensors and RF-foil is 1 mm. Figure 2.4 shows an exploded view of the module support with the detector modules and the accompanying RF-box.

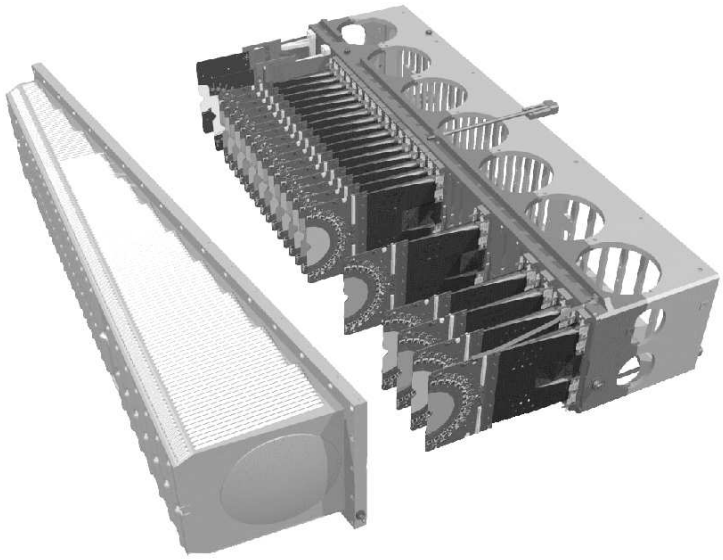

Figure 2.4: *Exploded view of the modules on a module support and the RF-box that surrounds them.*

Since the sensors are operated in vacuum, the heat load must be removed via a liquid cooling system. Furthermore, permanent cooling is required to limit the effects of radiation damage to the sensors. A two-phase CO_2 system [55] with the capacity of keeping the sensors always below $-5°$ C is used. Liquid CO_2 is distributed to cooling capillaries that are thermally connected to cooling blocks. These are screwed against the detector modules during assembly.

Two sensor types with different strip geometry are used, measuring the r (R-sensors) and ϕ (Φ-sensors) coordinates of incident particles. The sensors are arranged in 21 VELO *stations* with 4 sensors each and 2 Pile-Up stations with 2 R-sensors each. A VELO station consists of two *modules*, staggered in z, mounted opposite to each other in their respective detector halves. A module has one R- and one Φ-sensor glued back to back. Figure 2.5 shows a schematic top-view of the sensors in the detector. It also shows the relative positions of two sensors in a station when the VELO is closed and open.

The size of the detector in z is dictated by the requirement of matching the angular coverage of the spectrometer and the length of the interaction region, which is $\sigma_z = 5.3$ cm. At least three hits in different stations are required to reconstruct a track. The arrangement of the sensors matches this requirement for primary vertices as far as $2\sigma_z$ from the nominal interaction point. As a consequence of the wide interaction region, six of the VELO stations are located upstream from the nominal interaction point. Additionally, these upstream stations increase the primary vertex position reconstruction performance.

A detailed figure of the layout and the individual module positions can be found in appendix B and reference [56]. The module and sensor design is further explained in section 2.3.

The performance of the VELO has been evaluated in multiple beam tests, see for example references‘ [27, 57–63]. Studies of the Signal-to-Noise ratio, single hit resolution

and vertex reconstruction using beam data are presented in chapters 3 and 4.

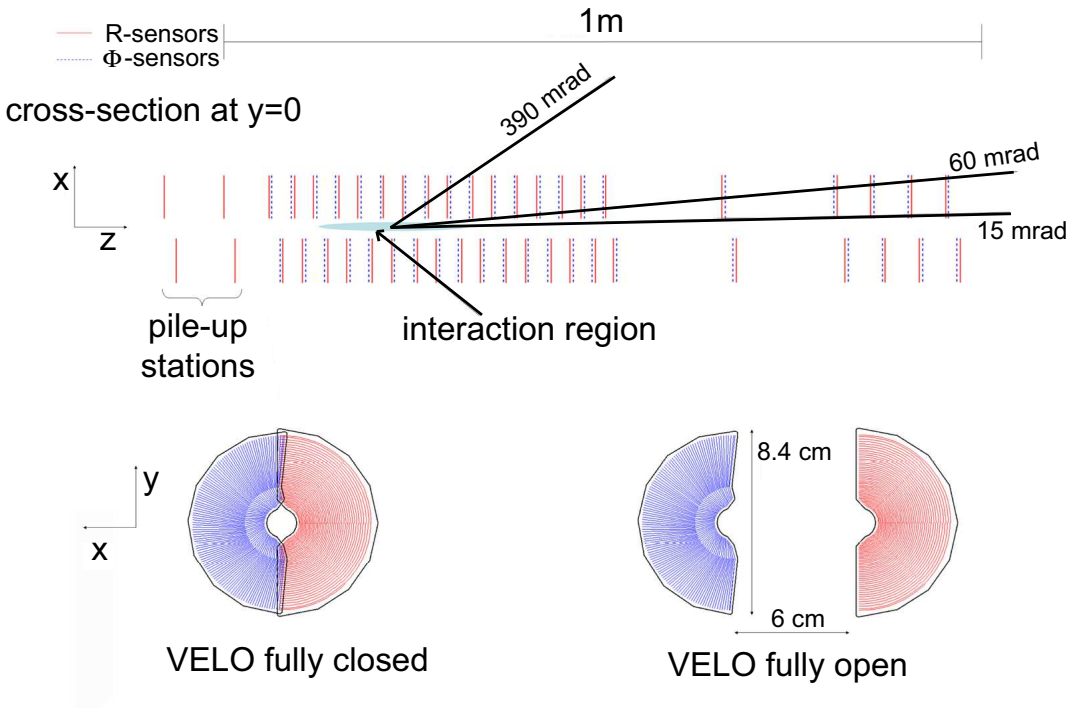

Figure 2.5: *Top: Cross-section of the VELO sensors in the xz-plane, indicating the angular acceptance of the detector and relative arrangement of the stations. The drawing shows the VELO in open position. The distance from first to last station is 106.5 cm. Bottom: Sketch of a VELO station in closed and in fully open position.*

2.3 Detector modules

The main parts of a VELO module are the paddle, the hybrid and the sensors, but as figure 2.6 shows, a module has a complex design with many components. It consists of two sensors that need to stay in a fixed, well-defined position with respect to the module support while moving and experiencing large temperature differences. The modules provide thermal management (cooling), electrical readout of the sensors and routing of signals to the detector Data Acquisition System (DAQ). The two sensors are glued back-to-back on the double-sided hybrid. The hybrid substrate, which has a semi-circular hole where the sensors are located, has a core of TPG[4] (for heat conduction) encapsulated in a carbon fibre (CF) cladding onto which two circuits are laminated. Each circuit has 16 front-end chips (Beetles) that are connected to the sensors through double-layer kapton pitch adaptors. The temperatures of the hybrids are measured with NTC[5] sensors. The paddle is a low mass CF construction designed to hold the hybrid steadily in place. The paddle is glued to a CF base with invar feet that are used to mount the module to the detector base plate. Invar is a nickel steel alloy with a particularly low coefficient of thermal expansion.

[4]Thermal Pyrolitic Graphite
[5]Negative Temperature Coefficient

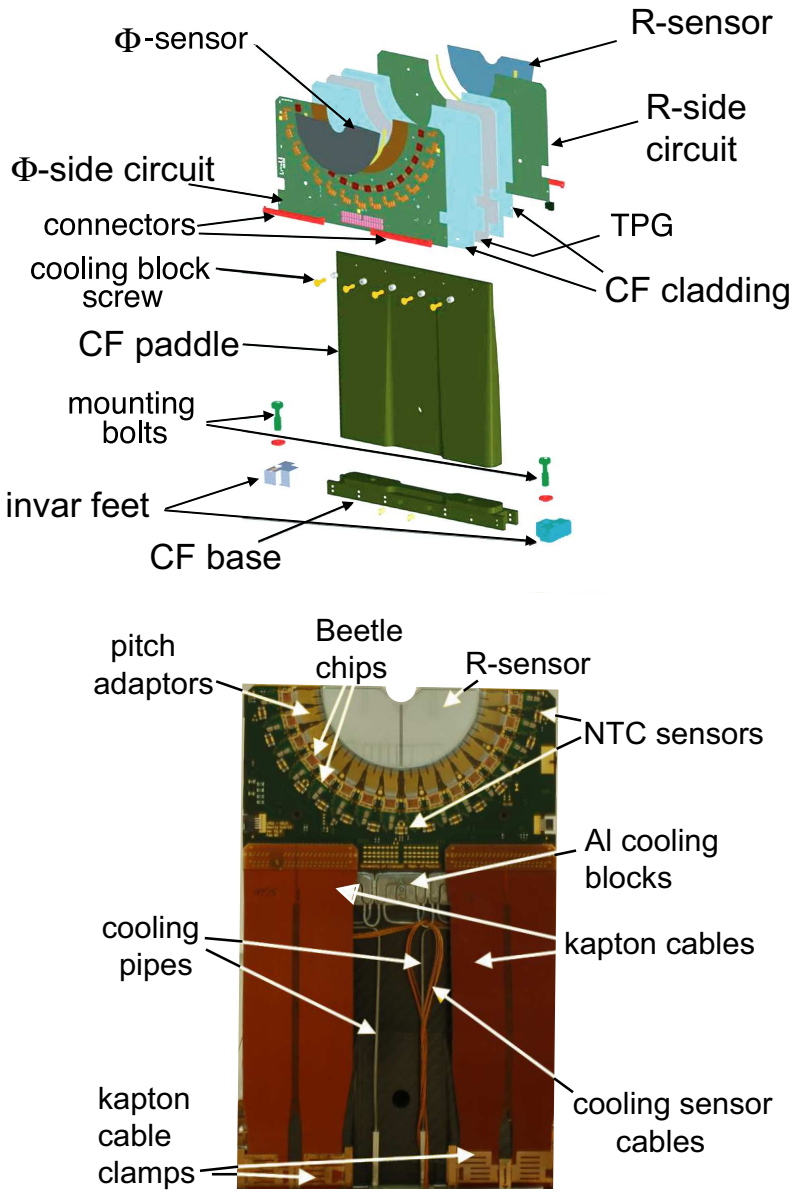

Figure 2.6: *Top: An exploded view of a VELO module. Bottom: Photograph of a module with kapton cables connected to it.*

2.3.1 Silicon sensors

The VELO silicon sensors are single-sided 300 μm thick n-in-n type detectors with a half-circular shape covering a 182° angle, including a 2° overlap area with the opposite sensor. The module production process is described in reference [64]. Figure 2.7 shows an R- and a Φ-sensor adjacent to each other. They are centred around the beam-axis and their active area extends from a radius of 8.2 mm to 42.0 mm.

The strips in the R-sensor are concentric semi-circles segmented into four 45°-sectors. Each sector has 512 strips. The segmentation has beneficial effects on hit occupancy and strip capacitance (shorter strips). The strip pitch increases linearly as a function of radius, from 38 μm at the inner edge to about 102 μm at the outer edge.

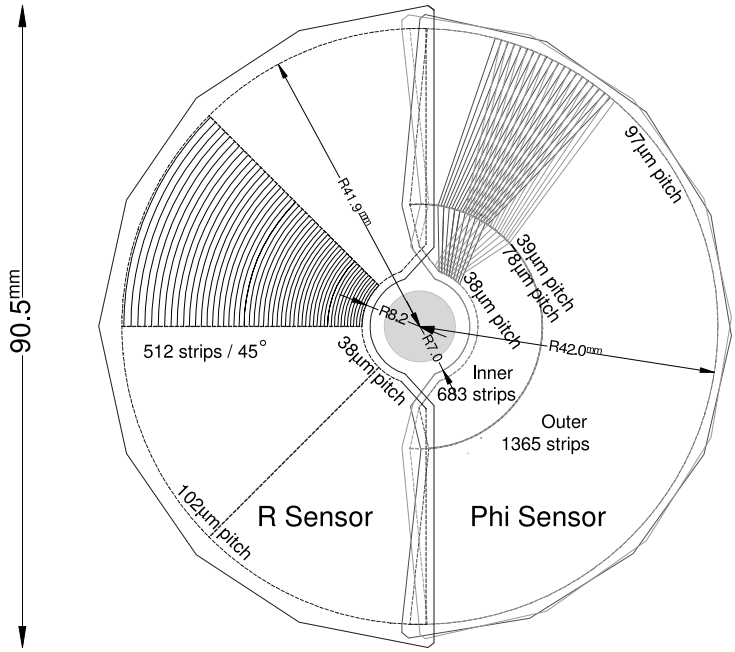

Figure 2.7: *View of the R- and Φ-sensors in the xy-plane. The rϕ strip geometries are illustrated. An additional Φ-sensor of a neighbouring station with the strip side facing the opposite way is drawn in the background to highlight the effect of the stereo angle of the ϕ-strips.*

The strip orientation in the Φ-sensor is semi-radial. The sensor is divided into an inner and an outer region in which the strips are skewed in opposite directions to form a dog-leg shape. At 8 mm the inner strips have an angle of 20° with respect to the radial and the outer strips are at a 10° angle to the radial at 17 mm. By alternating the direction that the Φ-sensors face, the strips in adjacent sensors have a stereo angle with respect to each other. This measure reduces the combinatoric background in the pattern recognition.

Analogously to the R-sensor, the strip pitch of the Φ-sensor increases linearly with radius. The pitch ranges from 38 μm – 78 μm in the inner region and 39 μm – 97 μm in the outer region. Table 2.1 summarises the principal characteristics of the VELO sensors.

2.4 The Beetle front-end readout chip

The Beetle chip [65] is the front-end chip used to read out the VELO. It was designed to withstand the high radiation levels expected in the harsh LHC environment. The development of the chip has been described in references [66, 67]. The Beetle chip has a sampling rate of 40 MHz and can accept trigger rates up to 1.1 MHz. The signals of the 128 strips connected to each chip are read out via AC coupling to charge sensitive amplifiers. The collected charge is converted into a voltage pulse which is shaped in consecutive steps of differentiators and integrators. To satisfy LHCb requirements, the resulting pulse must have a rise time[6] of less than 25 ns and spillover[7] less than 30% of

[6]The time it takes for the pulse to rise from 10% to 90% of the peak amplitude.
[7]The pulse value 25 ns after the time of peak amplitude.

Table 2.1: *Characteristics of the VELO sensors*

	R-sensor	Φ-sensor
number of sensors	42 + 4 (Pile-Up)	42
readout channels per sensor	2048	2048
sensor thickness	300 μm	300 μm
depletion voltage (unirradiated)	20-70 V	20-70 V
smallest pitch	38 μm	38 μm
largest pitch	102 μm	97 μm
length of shortest strip	3.8 mm	5.9 mm
length of longest strip	33.8 mm	24.9 mm
strip width	0.4×pitch	0.4×pitch
inner radius of active area	8.2 mm	8.2 mm
outer radius of active area	42 mm	42 mm
angular coverage	182 deg	≈ 182 deg
stereo angle	-	10-20 deg
bias resistors	1.8 MΩ	1.8 MΩ

the peak amplitude [68]. A set of currents and voltages of the preamplifier and shaper are used to optimise the properties of the pulse, such as peaking time, peak amplitude, spillover and undershoot (see table 3.2 for details). The relationship between the Beetle parameters and the pulse shape has been studied in depth in test beam experiments [59] and shown to fulfill the requirements.

After shaping, the pulse is sampled and its analogue value stored in a 160 event deep pipeline buffer that can store events for 4 μs awaiting a trigger decision. After receiving a L0 trigger, the pipeline value is multiplexed at 40 MHz onto 4 output ports with 32 channels and 4 header bits per port. In this way the 128 Beetle channels can be read out at a trigger rate of 1.1 MHz, corresponding to a read-out time of 900 ns[8]. Comparators connected to the front-end provide the binary interface used for the Pile-Up Veto detectors. The parameters of the chip are programmable using a standard I^2C interface, and a charge injector is available for creating test pulses with adjustable pulse height.

2.5 Detector readout

The low and high voltage, data, monitoring and fast control signals to and from the Beetle chips are transmitted over flexible kapton cables. Flexibility is necessary as the detector is retracted by 30 mm during LHC beam injection. The analogue data signals are transmitted via *repeater boards* (one board per sensor) and 60 m twisted-pair cables to analogue receiver (*ARx*) cards on *TELL1 boards* [69]. A TELL1 board is equipped with four ARx-cards, each with an input capacity of 16 analogue links. Consequently, one TELL1 board is needed per sensor (64 links with 32 channels per link). In total, 88 TELL1 boards are used to read out the 21 VELO stations and 2 Pile-Up stations. The readout path between the sensors and TELL1s is schematically illustrated in figure 2.8 and the full VELO electronics chain is illustrated in figure 2.9.

The analogue data is digitised with 10-bit precision and then processed on four Field

[8] $(32 + 4)$ channels $\times$ 25 ns/channel = 900 ns

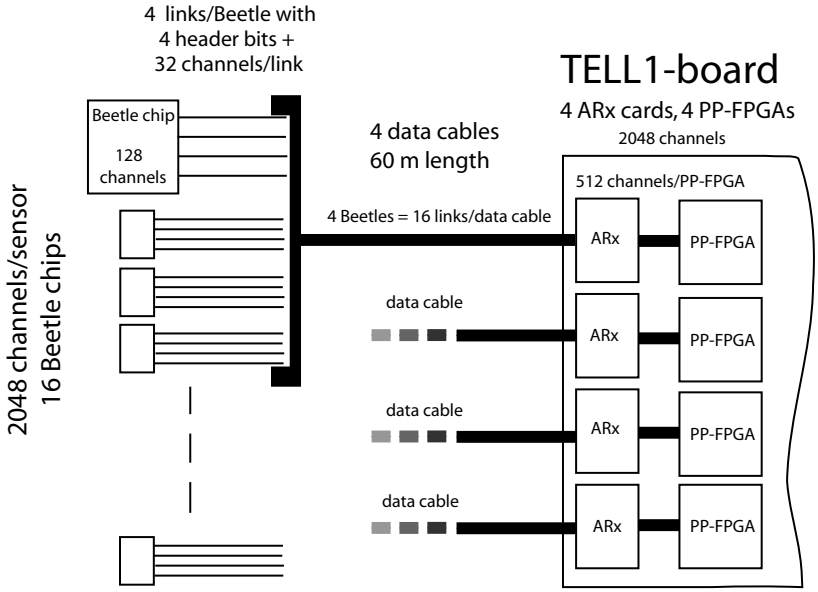

Figure 2.8: *The readout path between a VELO sensor and a TELL1. The repeater boards between the detector and the TELL1 boards have been omitted in the figure.*

Programmable Gate Arrays (FPGA) serving 512 VELO channels each. The processing is described in greater detail in section 2.5.1. After processing, the data is transmitted to the HLT computer farm through Gigabit Ethernet (GBE) boards.

Timing and fast control signals from the *Readout Supervisor* are distributed to the system through the *Control boards*. Moreover, they distribute commands via I^2C from the Experimental Control System (ECS) to configurable components (e.g. Beetle chips and low voltage). Each control board serves six repeater boards.

The temperatures on the hybrids and repeater boards are monitored by *temperature boards* which distribute it to ECS and the VELO hardware interlock system. ECS controls and monitors high and low voltages, cooling, pressures, the VELO motion system, etc. The graphical user interface, alarm system and communication between components in the system is done in PVSS, a commercial software package[9].

2.5.1 TELL1 processing and zero-suppression

The TELL1 is the common readout board in LHCb, used by all subdetectors except the RICH. In the VELO, the TELL1 is used for complex processing of raw data and zero-suppression. The processing, explained in detail in e.g. reference [70], is done on the PP-FPGAs (Pre-processing FPGA). The main steps of the processing are:

Pedestal calculation The 10-bit digitisation in the ARx cards converts the analogue value of each Beetle channel to a value in the range 0–1023 *ADC counts*. The pedestal (baseline) of the digitised output is around 512 ADC counts but can drift as external conditions, such as temperature, change. The first step in the TELL1 processing is subtraction of these pedestals on an individual channel basis. The

[9]By ETM Professional Control, see http://www.pvss.com.

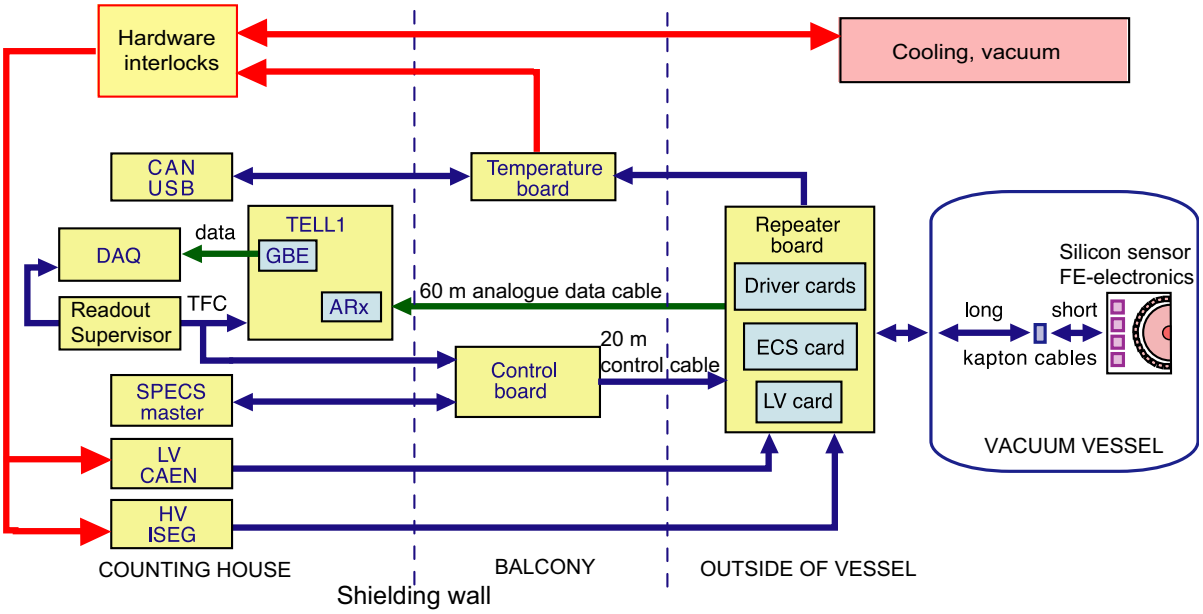

Figure 2.9: *The VELO electronics chain for one sensor.*

pedestal value to subtract is either loaded at the beginning of the run from a configuration database, or calculated from an average over the first 4000 events. During data taking, a pedestal following algorithm based on a running average can track changes and update the pedestal values. The pedestal following is not used in the default operation mode.

Header cross-talk correction The last two header bits of each analogue link are used to encode the *pipeline column number*, i.e. the position of the event in the Beetle pipeline buffer. Due to cross-talk, a fraction of the signal in the last header bit spills over into the first Beetle channel of the link. As the cross-talk level and pulse height of the header bit are known, the spillover can be corrected for. If no correction is applied, the first channel of each analogue link (every 32nd Beetle channel) appears noisy.

FIR filter The Finite Impulse Response filter is a digital filter which corrects for cross-talk, primarily from signal distortions in the 60 m data cables of the analogue links. For details on the filter and its implementation, see [70].

Channel reordering Due to the scheme with which sensor strips are bonded to the FE-electronics, scrambling occurs such that consecutive Beetle channels are not connected to adjacent strips. This is particularly prominent in the Φ-sensor, where inner and outer strips are mixed in the analogue links. The reordering algorithm accounts for this by unscrambling the Beetle channel order.

Common mode suppression The VELO operates in a noisy environment where common-mode (CM) noise pickup can occur. The source of the CM noise is for example RF pickup on the sensor (for instance from the LHC beam which passes very close). Due to the resource limitations in an FPGA, the correction algorithm can not be

too complex. The implemented algorithm is based on a linear fit to the strip charge in groups of 32 channels, performed on an event-by-event basis. The details are explained in reference [70], chapter 3. Figure 2.10 shows the noise spectrum of a 45°-sector in an R-sensor, before and after common mode subtraction. Noise is defined as the RMS value of the distribution of $\mathcal{O}(5000)$ ADC-values of a channel. The header cross-talk correction was not applied to these data, resulting in the spikes in the noise spectrum at every 32nd channel.

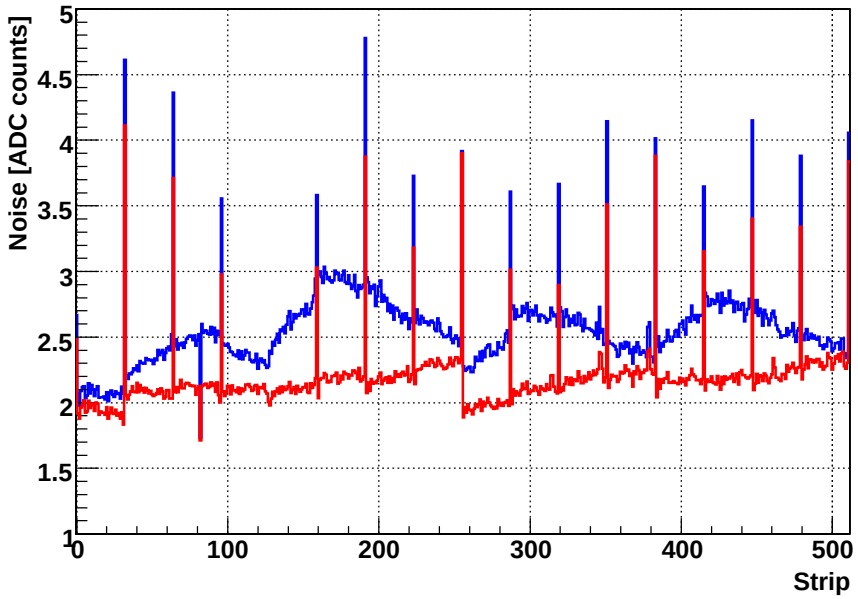

Figure 2.10: *Noise spectrum of the strips in a 45°-sector of an R-sensor. The upper curve shows the raw noise and the lower curve shows the common-mode corrected noise. The regular spikes in the spectrum are due to cross-talk in the analogue chain from the last Beetle header bit.*

Clustering The last step of the processing is the clustering [71]. A cluster is formed by a seeding strip which is selected by passing a signal threshold. Up to three additional adjacent strips are added to the cluster if their signal values are above an inclusion threshold. Thresholds can be set individually for each strip depending on their Signal-to-Noise ratio. The default values are 10 and 4 ADC counts as signal and inclusion threshold. One ADC count corresponds to the charge of 440 electrons.

In default operation mode, the processed data is sent to the HLT computer farm in a light, zero-suppressed (ZS) format that allows high data output rates and fast access to cluster information. For monitoring and test purposes, the output can also include a non-zero-suppressed (NZS) data bank containing the full, unprocessed strip information.

The processing on the TELL1 board can be emulated bit-perfectly in offline software. This functionality has been widely used during testing and commissioning and is known as the *TELL1 emulator*. The analyses presented in chapter 4 rely on the TELL1 emulator.

2.6 Pile-Up detector

The Pile-Up system consists of two stations of R-sensors integrated in the VELO detector upstream of the interaction point. The detector is used in the L0 trigger to veto bunch crossings with multiple inelastic interactions. Multiple vertices are detected using a simple histogramming technique. The resulting vertex z-position resolution has been estimated from beam tests to be $\sigma_z = 2.8$ mm. For further details, see [72, 73].

The digital signals from the Pile-Up sensors are read out using comparators on the Beetle chips and carried off the hybrid over 80 Mbit/s copper links and 1.6 Gbit/s optical links to Vertex Processing Boards where the multiple vertex search algorithm is executed. The result is sent to the L0 electronics where a trigger decision is formed. In parallel, the sensors are read out analogue, similar to the VELO, which adds four upstream R-sensors to the 84 standard VELO sensors.

2.7 Detector alignment

As mentioned previously in this chapter, the VELO design is driven by the requirement of high spatial resolution. Precise knowledge of the positions of the sensors, i.e. alignment, is key to achieving this. The core of the alignment strategy is a high precision assembly and detailed metrology, however the requirement of the VELO to open during LHC fills introduces the need for a fast track-based software alignment procedure. It is expected that the position of the detector halves will be known within an accuracy of 10 μm through the position measurement of the motion system. The software alignment, presented in reference [74], uses track residuals to determine the relative positions of the R- and Φ-sensors in each module, the module alignment within a detector half and also the alignment of the detector halves relative to each other.

The relative alignment of the R- and Φ-sensors uses an iterative fit of the distribution of track residuals across the surface of the silicon sensor. Simulations show that an accuracy of 1.3 μm in x and y can be achieved [74].

The relative alignment of the 21 VELO modules in one detector half is based on a non-iterative method using a matrix inversion technique to minimise a χ^2. The matrix inversion is based on the Millipede algorithm [75]. The feasibility of this approach was demonstrated in the ACDC3 test beam experiment (section 4) and the results are presented in reference [57]. Simulation studies show that an accuracy of 1.1 μm in x and y can be achieved in this step [74].

Two methods are used for the alignment of the detector halves relative to each other. In closed position, the same technique is used as for the module alignment, based on tracks with hits in the small overlap region of the detector halves. Simulations show that an accuracy of 12 μm in x and y can be reached with this method [74]. The sensor overlap between the halves corresponds to 2% of the active area. When the detector is not in closed position, an alternative method is used where the position of the primary vertex is reconstructed in the two halves separately. The relative alignment between the halves is calculated by comparing the reconstructed vertex positions. The alignment precision reached with this method is estimated to 35 μm in x and y from simulations [76].

The alignment of the VELO with respect to the other subdetectors is described in reference [77].

3 Prototype sensor performance

At the end of the R&D for the VELO detector in 2004, the R-Φ strip geometry and n-in-n silicon technology had been decided. One of the remaining issues was the sensor thickness, with the alternatives of using 200 μm or 300 μm thickness. For the readout, it had been decided in 2003 to use the Beetle as a common front-end chip for the VELO and Silicon Tracker detectors. Studies of a Beetle1.2 chip reading out a 200 μm thick R-sensor were presented in references [61] and [78]. The studies demonstrated problems simultaneously fulfilling the LHCb requirements for Signal-to-Noise ratio and for signal spillover to the next bunch crossing. In further test beam measurements in May 2004, using a Beetle1.3 chip reading out a 300 μm thick sensor [59], various characteristics of the chip were systematically investigated. These studies showed that the pulse shape and Signal-to-Noise ratio of the Beetle1.3, in combination with the thicker sensor, complied with the requirements set by the LHCb-experiment. Further improvements to the Beetle1.3 chip resulted in the 1.4 and 1.5 versions.

A second remaining design decision was which version of the Beetle to use. Prototype sensors and front-end read out electronics were extensively evaluated in a beam test in November 2004. The goal of these tests was to provide data for a final decision on sensor thickness and Beetle version.

This chapter reviews part of the studies performed using data collected in the beam test of November 2004. Section 3.1 introduces the setup and section 3.2 discusses the event reconstruction. Section 3.3 consists of a performance comparison study between the different front-end chip versions. The results have also been published in [58]. With the results of these studies as a basis for decision, the VELO group decided to use the Beetle1.5 chip, while the Silicon Tracker group opted for the Beetle1.3 chip. It was also decided to use 300 μm thick sensors in the VELO.

Section 3.4 describes an investigation of an observed bias-dependent cluster centroid shift in the VELO [63]. This study suggests the presence of processes in the silicon sensors that are currently not fully understood and modelled.

3.1 Experimental setup

During the beam test in November 2004, two unirradiated R-measuring prototype sensors[1] of 200 μm and 300 μm thickness (hereafter referred to as R200 and R300) were placed in the SPS 120 GeV pion beam in the X7 area at CERN. A separate beam telescope [79] with 8 silicon strip sensors provided reference tracks. A scintillator trigger asynchronous to the Beetle sampling clock was used to trigger the passage of beam particles. When triggered, 14 consecutive samples from the Beetle pipeline were recorded, corresponding to a time window of 350 ns. By using a time to digital converter (TDC), the particle arrival time with respect to the 40 MHz Beetle clock could be determined. As the particles, and

[1] Type Micron PR-04, mounted on hybrids of type K04.

consequently the triggers, are not synchronous to the Beetle clock, the events contain sampled values of the Beetle output pulse at random times of the pulse. By associating a TDC time stamp to each event and combining sufficiently many events, the complete pulse shape of the Beetle chip can thus be deduced offline, as described in section 3.3.1.

The prototype sensors were positioned either perpendicular to the beam or at a 10° incidence angle. The strip side of the sensors faced the downstream direction. A photograph and a schematic drawing of the experimental setup are shown in figure 3.1. The

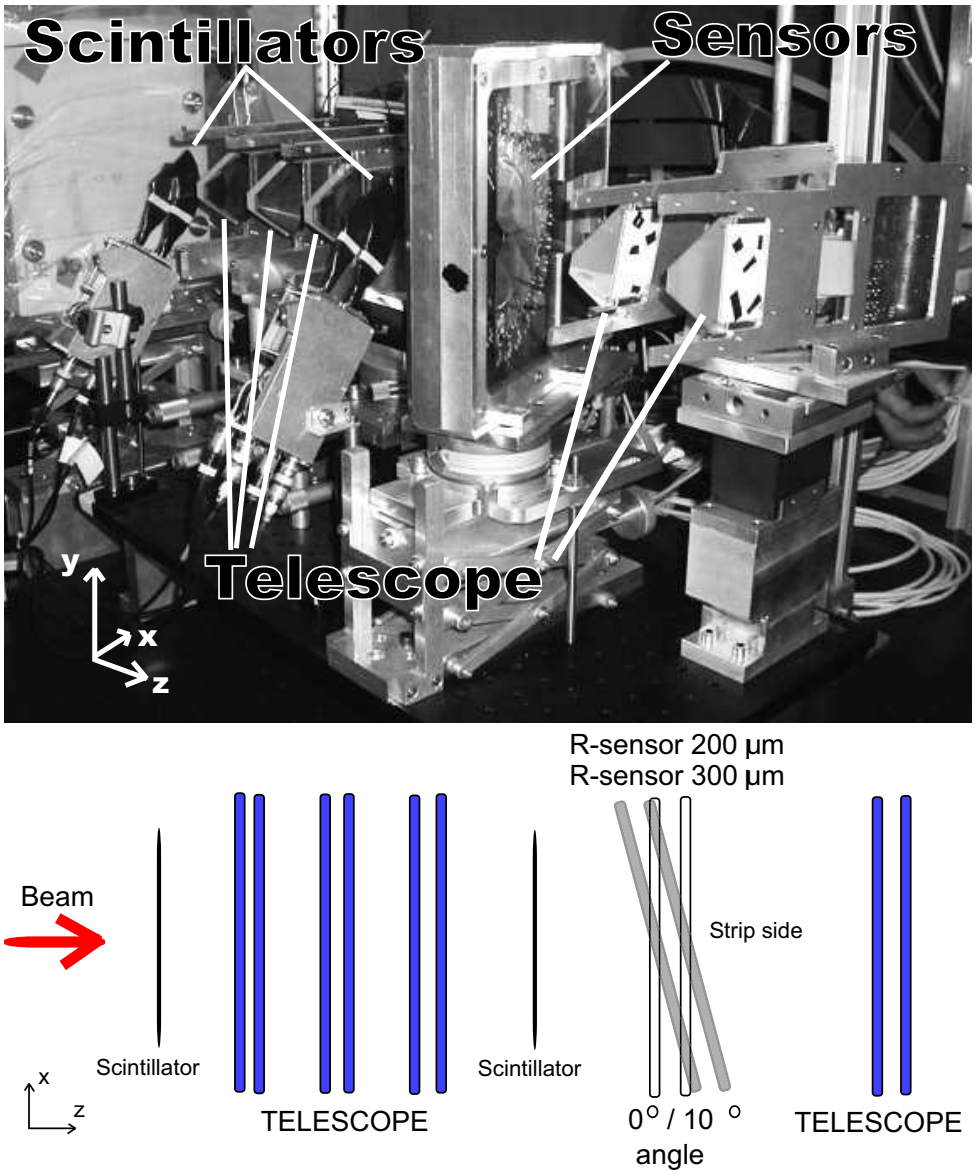

Figure 3.1: *Photograph and schematic overview of the experimental setup in the VELO beam test of November 2004. A set of scintillators in coincidence provided the trigger signal and a beam telescope of eight silicon strip sensors provided reference tracks. The two prototype VELO sensors were positioned either perpendicular to the beam or at a 10° incidence angle (the situation shown in the photograph). The two VELO sensors were oriented with their strips on the downstream side.*

depletion voltage of the 200 μm (300 μm) sensor was 34 V (55 V) and the sensors were

operated in the 100–300 V range.

For the DAQ, an "LHCb like" analogue readout chain was used; from Beetle chips mounted on a hybrid, through kapton interconnects, repeater boards and 60 m cables to ADC cards. The R300 sensor was read out with Beetle1.3 chips, while the hybrid of the R200 sensor was populated with three different versions of the chip. The hybrid contained 16 chips, enumerated from 0 to 15. Chips 0-7 were Beetle1.3, chips 8-11 were Beetle1.4 and chips 12-15 were Beetle1.5, see figure 3.2. Each set of 4 chips read out a 45 degree region of the sensor. Table 3.1 shows which chips were connected to which pitch region, ranging from fine pitch (40 μm) to large pitch (101 μm).

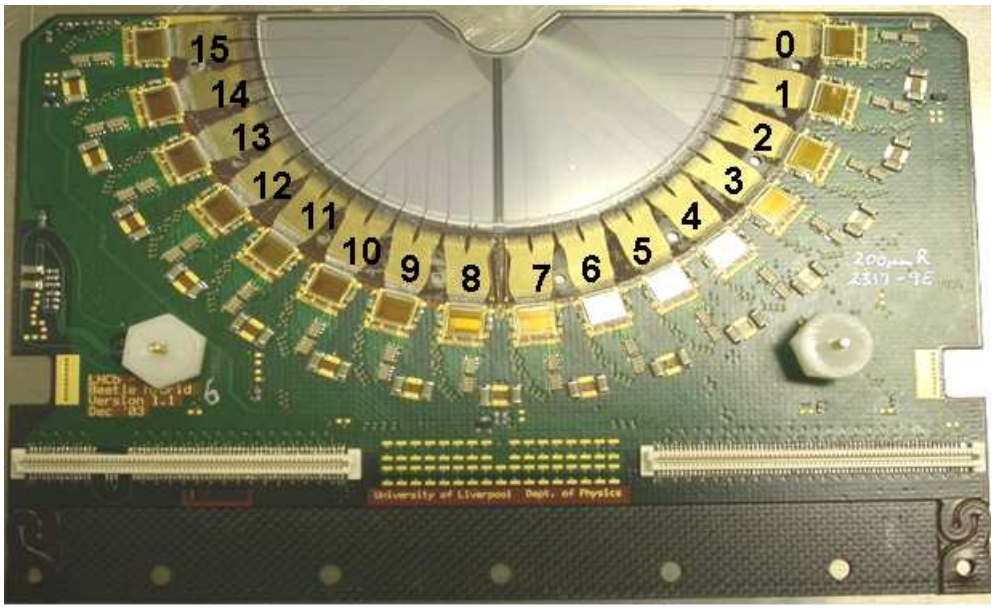

Figure 3.2: *Hybrid with sensor. The 16 Beetle chips are labelled from 0-15, where chips 0-7, 8-11 and 12-15 are of type Beetle1.3, 1.4 and 1.5 respectively. Chips 6-9 and 12-15 were included in the Beetle performance study in this chapter.*

Table 3.1: *The pitch regions of the R200 sensor and the Beetle chips that are connected to them. The parentheses indicate chips that are not included in this study due to limitations in the capacity of the Data Acquisition.*

Pitch region	Beetle1.3	Beetle1.4	Beetle1.5
40-50 μm	(3, 4)	11	12
50-64 μm	(0), 7	(8)	15
64-80 μm	(1), 6	(9)	14
80-101 μm	(2, 5)	10	13

All Beetles were configured to use the default settings as given in table 3.2. These settings were chosen based on previous beam test studies [59] and result in a peaking

time of about 25 ns.

Table 3.2: *The default Beetle settings used in all measurements.*

Parameter	Description	Value
I_{pre}	Preamplifier current	600 μA
I_{sha}	Shaper current	80 μA
I_{buf}	Front-end buffer current	80 μA
V_{fp}	Preamplifier feedback voltage	0 mV
V_{fs}	Shaper feedback voltage	700 mV

The main differences between the Beetle1.3 and later versions are a modified comparator, only affecting the digital part of the chip, and improved cross-talk performance. The Beetle1.5 chip contains a modified pipeline readout amplifier and improved power routing.

3.2 Event reconstruction

The analysis is performed within the framework of VeloTB[2], a software package developed for VELO beam tests. VeloTB performs TDC time calibration, pedestal subtraction and common mode noise correction. Clusters are seeded by strips that pass a Signal-to-Noise (S/N) threshold of 6. Neighbouring strips passing a threshold of 10% of the seeding strip S/N value are added to the cluster. The cluster size is limited to 5 strips but the vast majority of the clusters are 1 or 2 strip clusters. The cluster position x of a cluster of size N is calculated using the weighted mean of the strip positions x_i with respect to their charge Q_i:

$$x = \frac{\sum_{i=1}^{\mathrm{N}} Q_i \cdot x_i}{\sum_{i=1}^{\mathrm{N}} Q_i} \ . \tag{3.1}$$

Furthermore, VeloTB performs track reconstruction, detector alignment, and histogram generation in ROOT format [80]. The track fitting algorithms are described in detail in reference [81]. The alignment for this test setup is done by a dedicated algorithm by minimising a χ^2 built from the residuals between track intercept points and clusters. The χ^2 is minimised using an iterative technique implemented using the Minuit [82] minimisation package.

3.3 Beetle performance comparison

The hybrid with three Beetle "flavours" (reading out a 200 μm thick sensor) presented a good opportunity to study the performance differences between the various chip versions. For the purpose of comparing the Beetles, data were recorded with a broad beam illuminating a large part of the sensor. These data contain events with hits over the entire strip pitch range, read out with Beetles of all versions. The sensor was operated at 100 V bias. This section describes a comparative study of pulse shape, S/N ratio, and baseline stability.

[2] http://jpalac.home.cern.ch/jpalac/doc/VeloTB/VeloTB_User_Guide.html

3.3.1 Pulse shape and S/N

To comply with the experimental requirements, the S/N ratio at the peak of the Beetle output pulse should be maximised under the constraint that the signal remainder 25 ns after the peak (the so-called spillover) is less than 30% of the peak value. To extract these parameters from the data, the pulse shapes of the Beetle chips are reconstructed. As already described in section 3.1, 14 consecutive samples from the Beetle pipeline are recorded for each trigger, corresponding to a time window of 350 ns. The particle arrival time with respect to the 40 MHz Beetle clock is determined offline using the TDC time stamp. An alternative to the default clustering algorithm is used in this study: the strip with highest signal value of the combined data of all time samples is found and the signal of the this strip is subsequently determined for each time sample individually. The S/N ratio per time sample is calculated by summing the signal of that strip and the signal in the two surrounding strips. The signal sum is divided by the average noise in those strips. The noise per strip is extracted by calculating the RMS of the strip charge in the first time sample, where no signal is present.

A 2D histogram of S/N versus TDC time is filled (figure 3.3). The resulting plot visualises the Beetle pulse shape. The plot has been truncated to show the first 220 ns (nearly 9 complete time samples). The 2D distribution is split into 1 ns time slices. A

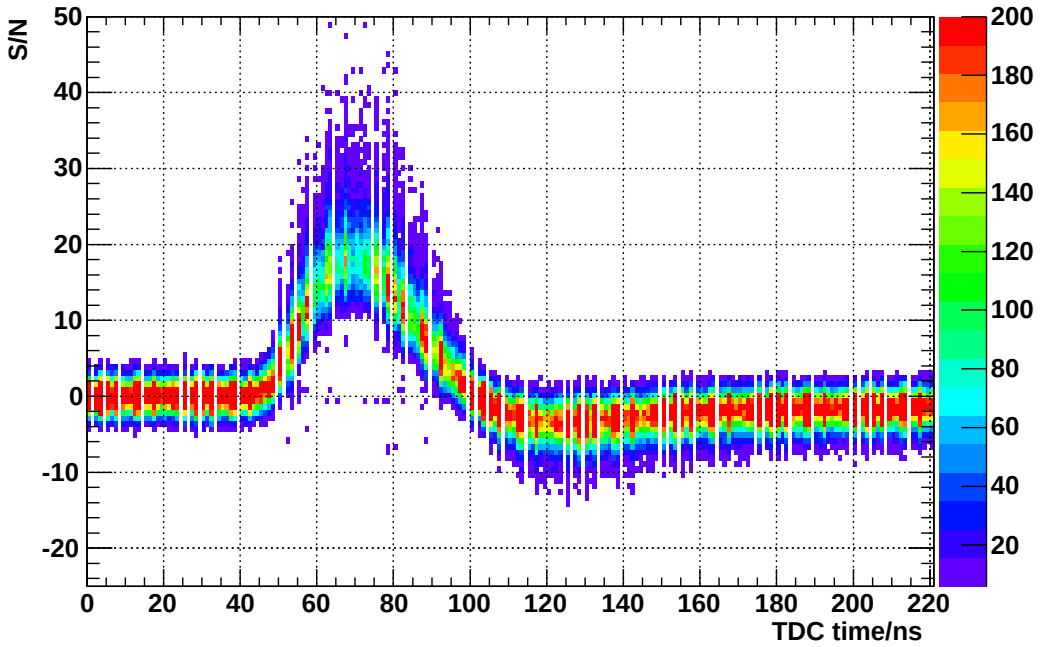

Figure 3.3: *S/N distribution versus TDC time in 1 ns bins. The Beetle pulse shape can clearly be seen .*

projection of one the time slices around the peak of the pulse shows the distribution that is characteristic for energy loss of charged particles in a thin silicon detector (figure 3.4). As discussed in section 2.1.1, the distribution is best described by a Landau convoluted with a Gaussian (equation 2.3) of which the most probable value (MPV) parameter is the peak of the Landau component (see section 2.1.1). A Landau⊗Gaussian is therefore fitted to each slice and by plotting the MPV as a function of TDC time, the pulse shapes of the chips are extracted.

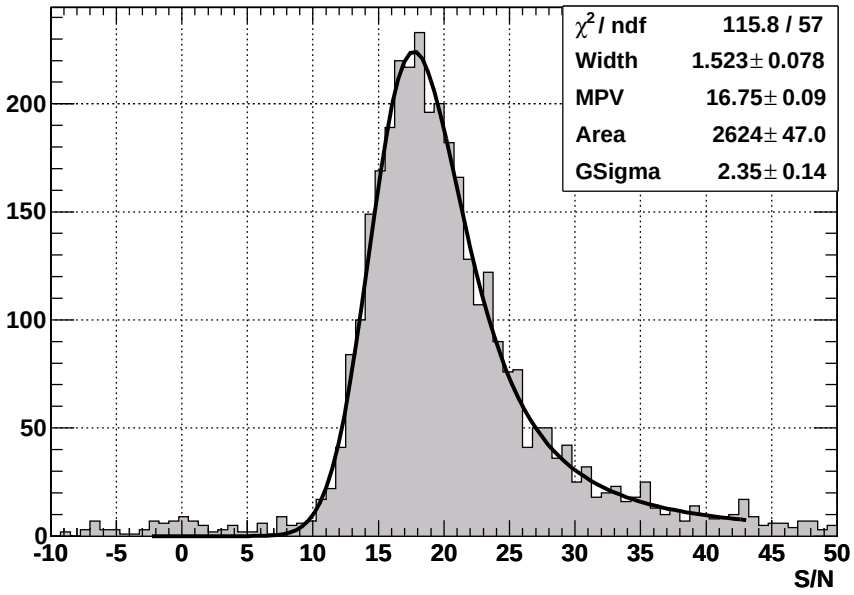

Figure 3.4: *An example of a Landau⊗Gaussian fit to a 3 ns TDC-slice around the peak of the pulse.*

Figure 3.5 shows the pulse shapes for the chips involved in the study for the pitch regions indicated in table 3.1. The pulse shape curves in figure 3.5 are fitted with a sixth degree polynomial (not shown here), from which the peak S/N and spillover values are determined. Using the same procedure, but only plotting the signal S and not taking the strip noise into account, the peak signal value (measured in ADC counts) is extracted. The error of the peak S/N and signal values are given by the statistical error of the MPV of the Landau⊗Gaussian fit. The error of the spillover value is estimated by propagating the errors in the polynomial fit parameters. To account for varying strip noise in different parts of the sensor, the results are separated into different pitch regions and presented in table 3.3.

Table 3.3: *Signal, S/N and spillover for different Beetle versions and different pitch regions (and hence different strips lengths) of a PR04 R-sensor of 200 µm thickness. The statistical errors are given.*

Pitch region	Beetle version	Signal (ADC counts)	S/N	Spillover (%)
40-50 µm	B1.4	31.7 ± 0.2	16.6 ± 0.1	18.4 ± 0.1
	B1.5	32.5 ± 0.2	17.0 ± 0.1	19.3 ± 0.1
50-64 µm	B1.3	31.3 ± 0.2	16.1 ± 0.1	19.6 ± 0.1
	B1.5	32.6 ± 0.2	16.9 ± 0.1	21.4 ± 0.1
64-80 µm	B1.3	31.5 ± 0.2	15.7 ± 0.1	20.4 ± 0.1
	B1.5	34.0 ± 0.2	17.1 ± 0.1	23.2 ± 0.2
80-101 µm	B1.4	31.9 ± 0.2	16.0 ± 0.1	22.1 ± 0.1
	B1.5	32.9 ± 0.2	16.2 ± 0.2	24.0 ± 0.2

As figure 3.5 shows, the different Beetle versions give similar pulse shapes but the

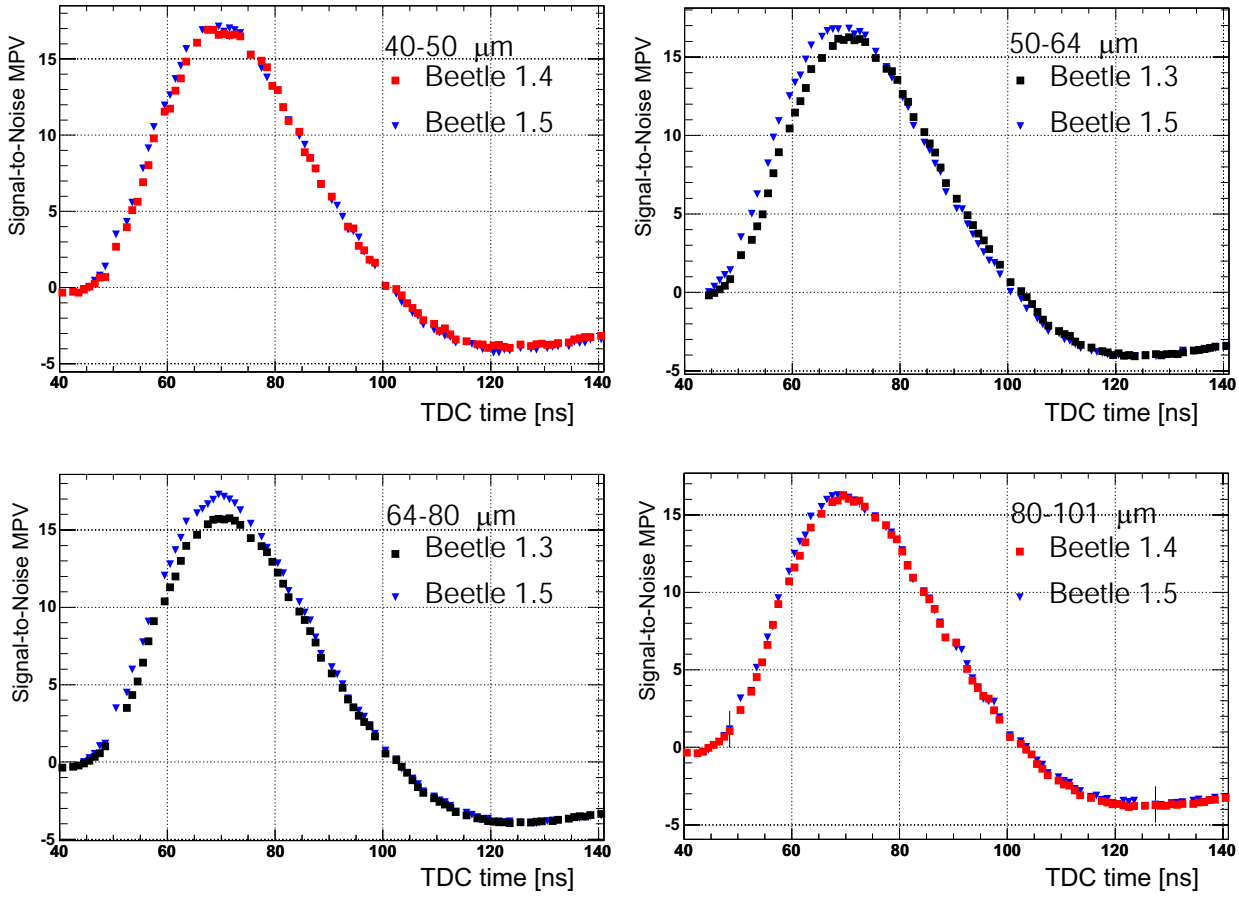

Figure 3.5: *Distribution of S/N MPVs from the Landau ⊗ Gaussian fits, in bins of 1 ns. Each plot shows a different pitch region, ranging from finest pitch (upper left plot), to largest pitch (lower right plot).*

Beetle1.5 chip has a higher S/N ratio in all pitch regions. The spillover is well within the 30% requirement. The peak signal differs little between the different pitch regions read out with the same chip type. The relation between strip length and increasing strip noise predicts the observed drop in S/N ratio at large pitch, where the strips are longer[3]. As demonstrated in the Beetle reference manual [65], the total strip and routing line length affects the spillover, implying that the outer pitch regions should have higher spillover. This is in agreement with the results of this study.

It should be noted that the S/N noise values quoted in table 3.3 are for a 200 μm thick sensor while the final VELO modules contain sensors of 300 μm thickness. These modules are therefore expected to have a better S/N performance. A S/N study using these final modules is presented in section 4.7.

[3]The noise increases as a function of the capacitance of strip and routing line, which depends on their total length. The largest noise contribution comes from the strips. As the strip length increases with radius, strips at large pitch are noisier.

3.3.2 Baseline stability

For the Beetle1.3, it has been observed that the baseline (pedestal) depends on whether the chip was read out in consecutive or non-consecutive mode [83]. Non-consecutive mode occurs when the Beetle is triggered for read out after having been idle for some time. If a readout immediately follows the previous one, it is called consecutive. Depending on the size of the difference in baseline between readout modes, there is a risk that this effect limits the dynamic range of the digitisation cards on the TELL1s. Furthermore, if the difference varies too much between the channels of an analogue link (32 channels) it can deteriorate the quality of the linear common-mode (CM) suppression algorithm. The data from the beam test provided a good opportunity to measure this effect and compare the different Beetle versions.

The DAQ of the beam test setup recorded 14 consecutive time samples when receiving a trigger. The data were taken with random triggers without beam. The first time sample is considered as read out in non-consecutive mode, while the next 13 time samples by definition are consecutive. Hence, differences between the baselines should be seen when comparing the two first time samples. In figure 3.6a, this *baseline difference* per Beetle channel is plotted, while no CM correction was applied to the data. The largest

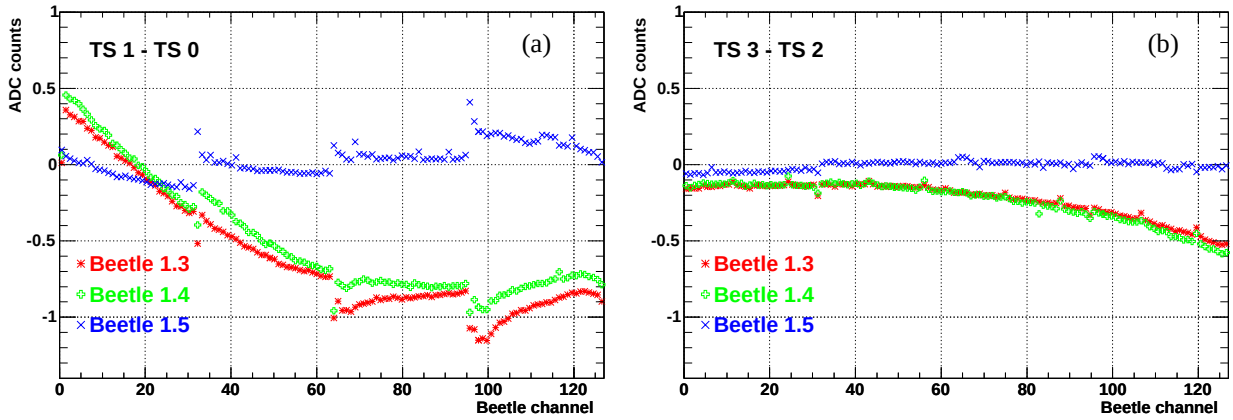

Figure 3.6: *Baseline difference between time samples expressed in ADC counts versus Beetle channel. No CM correction was applied.*
a) Time sample 1 - time sample 0 (consecutive and non-consecutive).
b) Time sample 3 - time sample 2 (consecutive and consecutive).

difference between the baselines of a consecutive and non-consecutive readout for the Beetle1.3 is about 1 ADC count (to be compared with a noise level of about 2–3 ADC counts). The Beetle1.4 gives a result very similar to that of the 1.3. The Beetle1.5 chip has a considerably smaller difference between a consecutive and a non-consecutive readout than that of the 1.3 and 1.4.

Figure 3.6b shows an example of the baseline difference between two consecutively read out time samples 2 and 3. A difference in baseline between the readouts can be seen for the Beetle1.3 and 1.4, but it is of smaller size than in figure 3.6a. The baseline of the Beetle1.5 shows only very small changes between consecutively read out time samples.

Although the Beetle1.5 behaves better than the previous chip versions, the size of the baseline shifts is small in all versions and would not limit the dynamic range of the ADCs. Moreover, such small shifts can be absorbed by the a correction algorithm. However, for the linear CM correction to work correctly, the overall shape of the shift per analogue link (32 channels) should be well described by a straight line. The shift shape of the Beetle1.5 is most consistent with this condition.

3.3.3 Conclusions

The comparison between Beetle chip versions is concluded and summarised as:

- **S/N and pulse shape.** All three Beetle versions perform well in terms of S/N and spillover. Their pulse shapes are very similar to each other. The S/N of the Beetle1.5 was found to be the highest, in the range 16.2 – 17.1, without breaking the requirement of having less than 30% spillover.

- **Baseline stability.** Differences in baseline between non-consecutively and consecutively read out samples are observed for the Beetle1.3 and 1.4. The shifts are small, about 1 ADC count, which is of similar magnitude as the noise. The Beetle1.5 shows smaller differences between consecutive and non-consecutive readouts than the Beetle1.3 and 1.4 chips. The shape of the shift per analogue link in the Beetle1.5 best fits a straight line, a feature that is beneficial for the linear CM correction algorithm.

As a conclusion from these studies it was decided to use the Beetle1.5 for the VELO detector.

3.4 Sensor bias dependence of cluster positions

Ballistic deficit is a phenomenon that occurs in semiconductor detectors when the charge carrier drift time can not be considered small compared to the peaking time of the shaper circuit in the front-end electronics. The result is a loss of signal, despite the detector being fully depleted. To collect the full signal, the drift velocity of the charge carriers has to be increased by raising the bias voltage on the sensor[4]

Ballistic deficit have been observed in unirradiated ATLAS Semiconductor Tracker (SCT) sensors, which are of p-in-n type [84, 85] and read out on the p-side. The VELO sensors, that are read out on the n-side, are of comparable thickness and the Beetle chip has a similar shaping time. At 100 V bias the average drift time in the R200 (R300) sensor is estimated to be 4 ns (8 ns) for electrons and 12 ns (24 ns) for holes , to be compared with the Beetle shaping time of 25 ns. The induced signal on the n-side is a combination of the contribution from the electrons and the holes. Due to the configuration of the electric and weighting fields[5] inside the sensor, the electrons and holes make their main contribution to the induced signal when they are in vicinity of the n-strips. Holes will move towards

[4]The drift velocity saturates when the applied electric field is of the order of 10^5 V/cm. This is never reached in the VELO.

[5]The electric field determines the speed of the charge carriers while the so-called weighting field, which depends on the sensor geometry, determines how large the induction is on a strip from a charge at a certain distance from the strip.

the p-side backplane so the hole contribution to the induced signal decreases during the period of charge collection. Electrons will move towards the read-out side and make their main signal contribution as they approach the strips, inducing a square pulse current. If the electrons do not arrive fast enough to the strips the result is a loss of detected signal.

Ballistic deficit can become a problem when reconstructing the intercept position of particles with a non-zero incidence angle. Figure 3.7 illustrates the problem. The simplified case in the figure shows how the loss of signal may cause the cluster centroid to shift, causing a wrongly reconstructed intercept position. The study described in this section

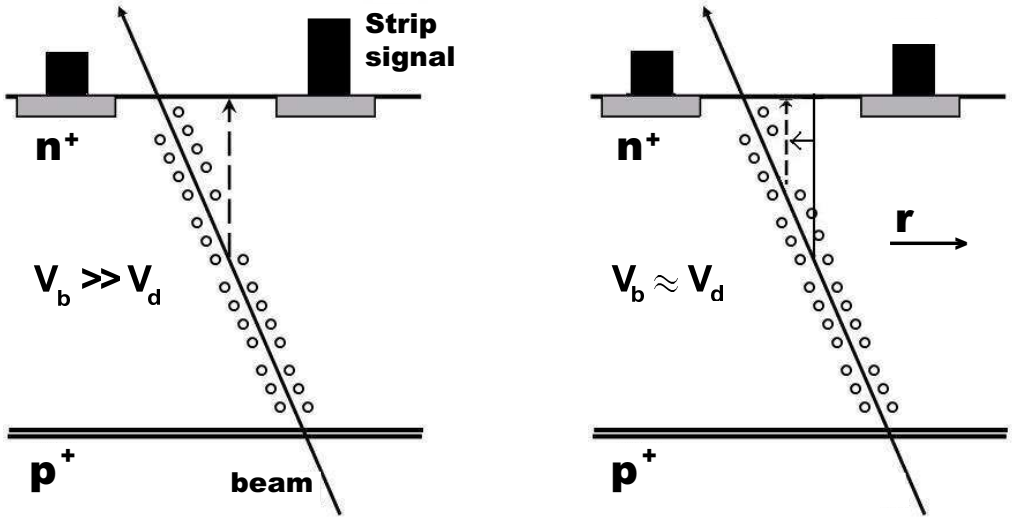

Figure 3.7: *A simplified view of the effect of ballistic deficit for an angled track. Note that the sensor is not drawn to scale. The directions of the beam and the radial coordinate axis in the experimental setup are indicated. The signal measured in the individual strips is drawn as black bars on top of the strips. The dashed arrow marks the detected cluster centroid. In the left figure, the applied bias voltage V_b is well above the depletion voltage V_d and all the charge is collected fast enough on the strips. In the right figure, however, V_b is close to V_d and the electrons close to the p-side do not reach the strips in time to contribute to the detected signal. Hence, the signal on the right strips decreases (marked by a smaller signal bar on the right strip), which changes the relative charge distribution between the strips and shifts the reconstructed cluster centroid towards the left strip.*

investigates ballistic deficit and its influence on the cluster centroids in the VELO. To do that, tracks with a non-zero angle of incidence are required. The R200 and R300 sensors were therefore rotated 10° around the y-axis (see figure 3.1). As the drift velocity of the charge carriers is proportional to the E-field in the sensor, and hence to the bias over the sensor, data were taken at different bias settings. The data with the lowest bias, 100 V, is most likely to suffer from ballistic deficit. With large drift times, the electrons close to the p-side might not contribute fully to the generated strip signal. Under this hypothesis, differences between 100, 200 and 300 V data should be observable. If differences are seen, a dependence on strip pitch and sensor thickness is to be expected.

3.4.1 Analysis

The full datasets contain about 310k, 410k and 470k events at 100, 200 and 300 V, respectively. To minimise the presence of noise clusters in the analysis only events passing a ±5 ns TDC-cut around the peak of the pulse are included. Clusters with or adjacent to dead or noisy strips are excluded. Only events with tracks that point to a fiducial region of the sensors are included. To correct for cross-talk in the setup a digital signal filter is applied to the data offline. The filter is a so-called Finite Impulse Response filter (see section 2.5.1), calibrated with measurements of cross-talk in the beam data [86].

The positions of the telescope and the sensors were kept unchanged during the entire data taking period. The sensor alignment is performed with the 100 V data and then used in the analysis of the 200 V and 300 V data since any shifts in the reconstructed cluster positions between voltages would disappear with individually aligned data sets. Due to performance problems of the alignment procedure in the innermost region of the sensors, likely due to edge effects, the strips at $r < 1.4\ cm$ (pitch region $40 - 50\ \mu$m) are excluded from the analysis.

To investigate differences in collected charge between the different bias settings, the signal values at the peak of the Beetle pulse are compared in figure 3.8. In the figure, the ratio between collected charge Q and the charge at the reference voltage 300 V, Q_0, is plotted as a function of sensor bias. It indeed shows that the charge collection efficiency degrades with reduced sensor bias for both sensors. In a study of unirradiated ATLAS sensors [84] it is demonstrated that this is an indication of the ballistic deficit at work[6].

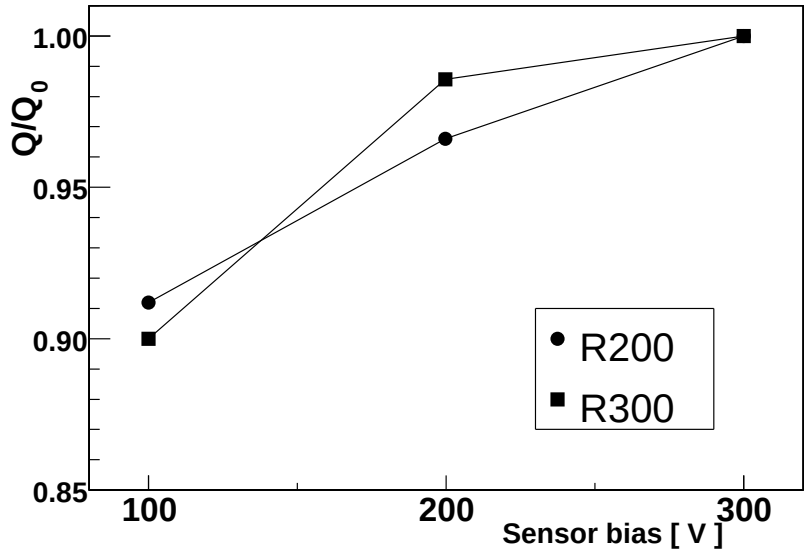

Figure 3.8: *Ratio between collected charge Q and charge at 300 V, Q_0, plotted as a function of sensor bias.*

As the effect of ballistic deficit on angled tracks is to move the reconstructed cluster centre with respect to its true position, the so-called track residual distribution between clusters and reference tracks from the beam telescope is used to study this effect. The

[6]The ATLAS study additionally uses variable front-end chip shaping time to prove ballistic deficit, an option not available for the VELO in this test beam experiment

track residual Δ is defined as the distance between a cluster centre $x_{cluster}$ and the track intercept point x_{track} on the sensor as determined by the beam telescope,

$$\Delta \equiv x_{track} - x_{cluster} \ . \tag{3.2}$$

The track intercept point is defined at half the sensor thickness.

A Gaussian function is fitted to the track residual distribution and the fitted mean value is plotted versus the radius of the strips. Figures 3.9a and b show this for the different bias voltages and two sensor thicknesses.

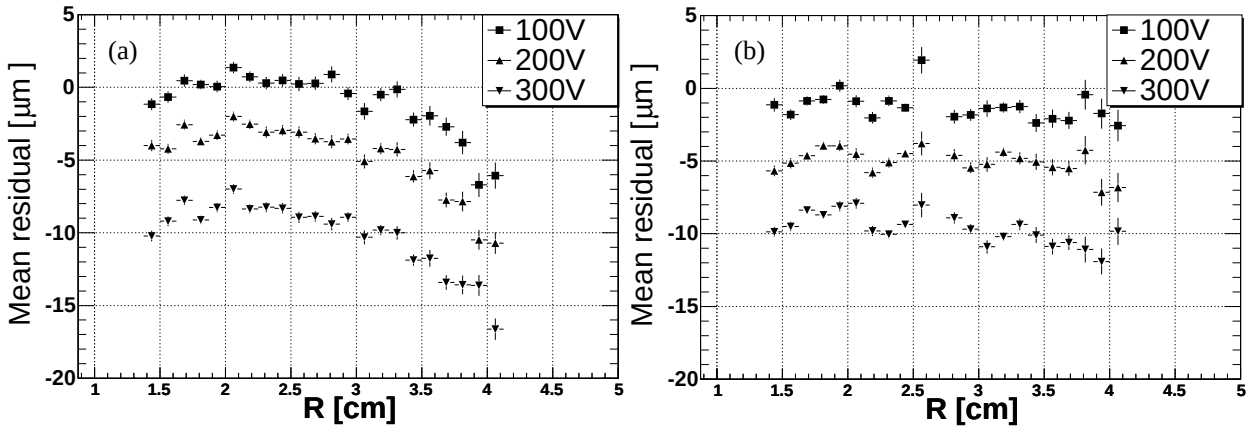

Figure 3.9: *The mean residual versus strip radius for the R200 (a) and R300 (b) sensors. The error bars represent the statistical error on the fitted mean. The lack of data points around 2.7 cm radius in (b) is due to a dead chip.*

The fitted mean of a perfectly aligned sensor should be 0. The "banana" shape in the R200 sensor plot is likely to be due to a non-flat sensor. It is observed that the 200 V and 300 V data are shifted towards progressively negative values. The residual mean shift relative to the 100 V data is shown in figure 3.10. The average shift at 200 V bias for a R200 (R300) sensor is 3.6±0.1 (3.6±0.1) μm, and at 300 V 8.1±0.1 (8.9±0.1). From first order polynomial fits to the data points of figure 3.10 no significant pitch dependence can be deduced. The standard deviation of the residual distributions (not plotted here) does not change between the sensor bias settings.

In light of the observation in figure 3.8, a possible explanation for the shift is the effect of ballistic deficit on the cluster centroids associated with angled tracks. The direction of the observed shift agrees with the hypothesis[7] .

The effects of ballistic deficit are expected to be sensor thickness dependent. However, the shifts observed in the data show no such dependence. Likewise, a pitch dependence is expected, but not observed. These are serious arguments against the ballistic deficit explanation as the cause for the observed systematic shift.

To investigate whether the shift could come from gradual movements of the sensors during data taking, the mean residual as a function of time is plotted (figure 3.11). It shows that the observed shift does not develop gradually between data sets, but changes step-wise between sensor bias settings. From this, the possibility that slow sensor displacement is the source of the apparent shift can be excluded; the shift is directly related

[7]The ballistic deficit as modelled in figure 3.7 predicts an observed shift of the cluster centroid towards smaller radius. This is consistent with the definition of the residual and the observed shifts.

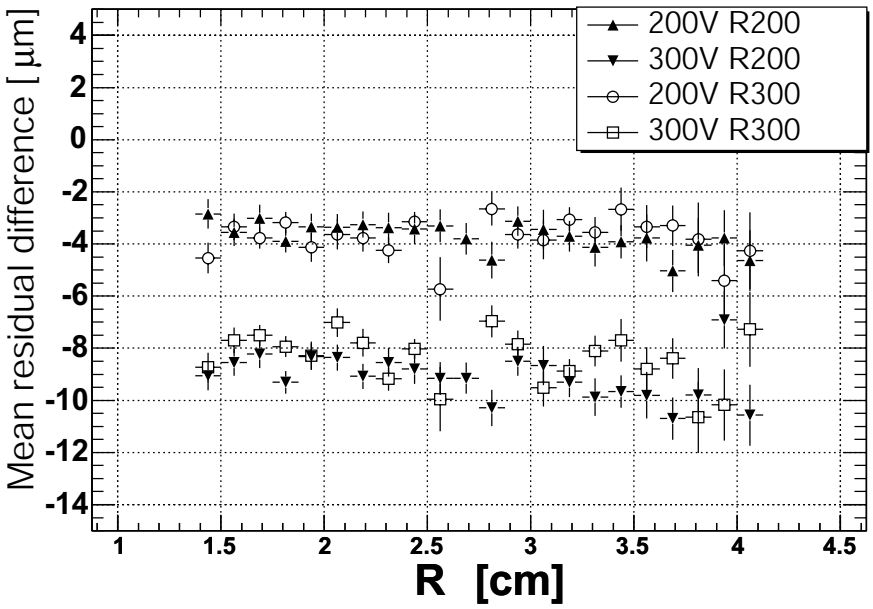

Figure 3.10: *The mean residual shift relative to the 100 V data for both thicknesses.*

to the change in sensor bias. In the simplest scenario, the sensors would attract each other when biased due to an electrostatic force between them. This kind of displacement would however be observed as a residual shift with a difference in sign between the R200 and R300 sensors. This scenario is therefore ruled out.

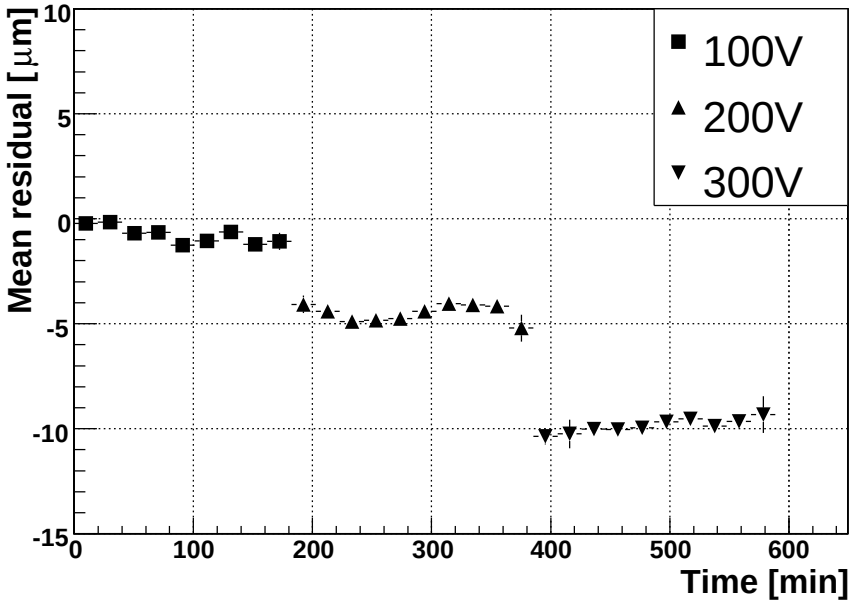

Figure 3.11: *The mean residual of the R200 sensor for the three different bias settings as a function of time elapsed since the start of data taking. The shifts clearly develop step-wise and not gradually.*

Another explanation that has been put forward, but is not further explored here, is that the shift is caused by a distorted shape of the signal distribution. The distortion would occur for tracks with a non-zero angle of incidence [87]. That hypothesis however predicts both a pitch- and a thickness-dependence, which clearly is not seen in the present data.

3.4.2 Recent developments

A study [62] aiming to reproduce this measurement was performed using ACDC3 beam test data (for details on ACDC3, see chapter 4) taken in 2006. The mean residual as a function of sensor bias in the range 100 V – 250 V was investigated using data from a 300 μm thick R-sensor that was illuminated by a beam at an 8° incidence angle. The differences between the sensors in this study (2004 data) and the 2006 data are negligible.

The 2006 study observes a shift of less than 1 μm between 100 V and 200 V (see figure 3.12), compared to the 3.6 μm shift observed in 2004 for the same bias difference.

Possible explanations for the failure to reproduce the result are:

- The 3.6 μm shift observed in the 2004 data is specific to that setup and not visible in the test setup of the 2006 study.
- There is a shift in the 2006 data, but is not as big as in the 2004 data due to differences in the experimental method. For example, no external beam telescope was used in the 2006 data, instead the VELO sensors surrounding the sensor under test provided the reference tracks and were kept at constant bias. Moreover, these sensors were also rotated with 8° relative to the beam.

Given these circumstances, a third study would be needed to settle the issue. Such a study can be envisaged using the VELO with particles produced by the colliding LHC beams. With the requirement of a 10° θ-angle and considering the geometry of the detector, 7 adjacent modules close to the interaction point (e.g. the modules in slots VL08C – VL14C) can be used, with the R-sensor in the middle module as test sensor and the remaining 13 sensors as beam telescope. Angles as high as 22.2° can be accessed while satisfying the requirement of 3 modules as telescope. With a calibrated and well-aligned detector, the final answer to whether the shift is reproducible or not should be straight-forward to obtain.

If the presence of a shift is established in such a study, the measurements can be used to parameterise the effect. This can then be used to recalibrate the cluster positions offline.

3.4.3 Conclusions

A non-flat charge collection efficiency profile for over-depleted VELO sensors was observed. This indicates the presence of ballistic deficit. Furthermore, step-wise shifts in the mean value of the track residual distribution as a function of sensor bias were observed. The shift shows no dependence on the sensor thickness and strip pitch. Due to this, the hypothesis of ballistic deficit as a possible explanation for the shifts is disfavoured. The shift can not be explained by gradual movements of the sensors during data taking. Alternative explanations based on the distortions to the shape of the signal distribution have been suggested by other authors [87] but are not pursued further here.

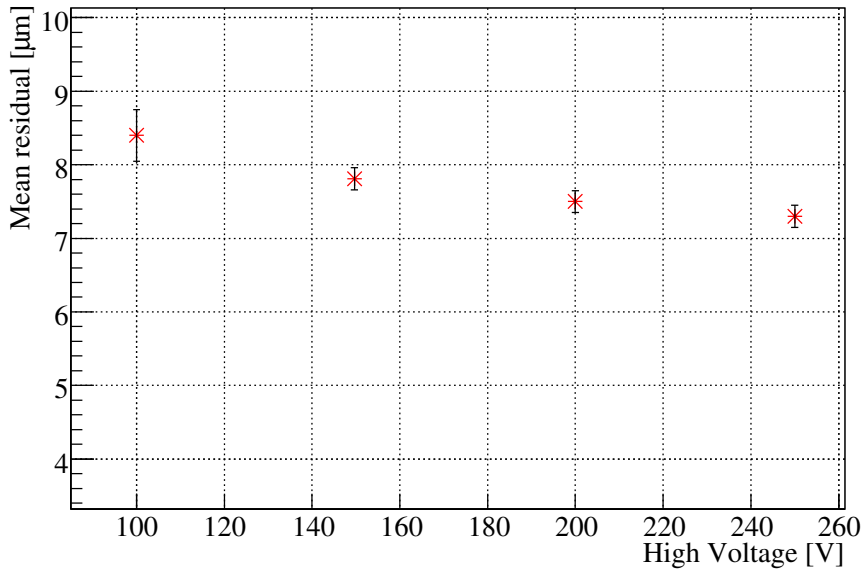

Figure 3.12: *Mean residual as a function of high voltage in the 2006 study. Plot taken from [62].*

The observations could be the effect of varying contributions from charges at different depths in the sensor but no standard simulations predict such large shifts for unirradiated sensors [88].

A recent study has tried to reproduce the results without success. Only very small shifts, $0.5 - 1$ μm are observed. A third measurement is necessary to bring full clarity to the issue.

4 The ACDC3 test beam experiment

The beam test of November 2004 and the performance of the sensors demonstrated in the subsequent analyses (see e.g. chapter 3) marked the end of the research and development phase of the VELO group. It was followed by the production, burn-in, assembly and commissioning phases of the VELO detector. As an early part of the commissioning of the VELO halves and the Data Acquisition System (DAQ), a partial system test was carried out in 2006. The main goals of this system test, referred to as ACDC (Alignment Challenge and Detector Commissioning), were:

- to commission a VELO detector half using a charged particle beam of the CERN SPS facility. This included reading out the powered and cooled detector placed under vacuum using mostly final components: sensor modules, long and short kapton cables, control boards, temperature boards, repeater boards, low-voltage supplies, data acquisition boards (TELL1s), read-out supervisor board (ODIN) as well as the standard LHCb reconstruction software.
- to use the collected beam data to demonstrate that the VELO alignment software [74] can extract the correct alignment parameters of the VELO.
- to use the collected beam data to characterise the performance of the detector.

The ACDC proved indeed to be a successful test and a useful exercise. Problems in the read-out chain and TELL1 firmware were solved and for the software it was the first time that the decoding and reconstruction algorithms were tested extensively on real data.

The road to the successful test beam experiment was paved by two small-scale tests, the ACDC1 and ACDC2, which respectively took place in April and August 2006, in which mainly the DAQ and software were evaluated and debugged. In the final phase, ACDC3, 90 million events were collected during the a two week test beam period in November 2006. This chapter covers the ACDC3 experiment and subsequent data analyses. The experimental setup and DAQ are described (sections 4.1-4.3), followed by a dataset inventory (section 4.4), event reconstruction (section 4.5) and alignment (section 4.6). The last part of the chapter treats the analyses: a Signal-to-Noise study (section 4.7), a single hit resolution study (section 4.8), and a vertexing performance study (section 4.9).

4.1 Experimental setup

For the ACDC3, the C-half was used with nine baseline modules with n-in-n sensors mounted on it. This was the number of modules that had been produced, mounted and electrically tested at the time of the test beam. Additionally, one R&D module with sensors of type n-in-p was installed in the most upstream VELO slot, making up a total of 10 modules in the detector half. Due to the order with which modules were mounted in the detector half, the baseline modules were placed in their final position in the nine most

downstream slots. The four most downstream modules are located with 50 mm spacing, the next module is 150 mm further upstream followed by a 160 mm gap. The remaining 4 baseline modules are positioned with 30 mm spacing, giving a total distance of 550 mm from first to last module. The R&D module M26 was mounted in the most upstream VELO slot. Two of the unoccupied slots were used for target holders. Figure 4.1 gives a schematic overview of the setup, showing the ten modules, the scintillators used for the trigger, and the targets. The trigger and targets are further described in sections 4.2 and 4.3, respectively.

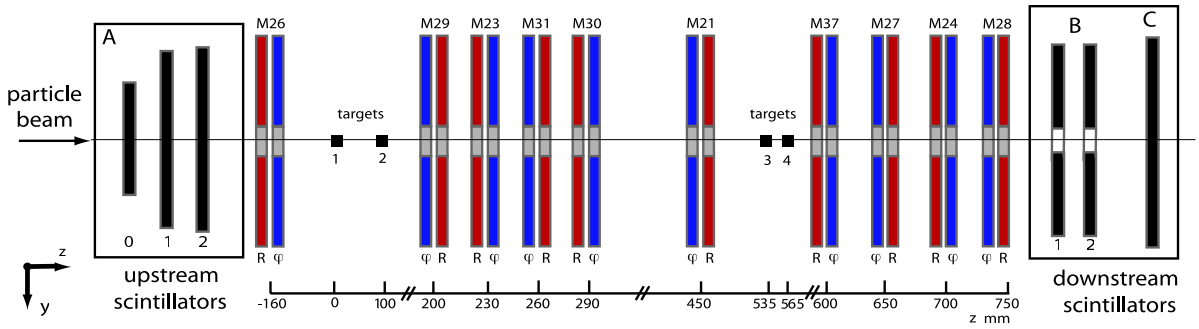

Figure 4.1: *A schematic top-view of the experimental setup in ACDC3. The most upstream module (M26) is the R&D module with sensors of n-in-p type, while the other nine modules are of baseline design with n-in-n sensors. The figure is not to scale.*

The C-half was placed in the H8 beam line[1] in the North Area at the CERN Prevessin site. The conditions of the SPS beam varied over the course of the experimental period, the two main modes being 400 GeV/c protons and 180 GeV/c hadrons (mostly protons and pions). The detector was placed on a support structure which could move vertically and horizontally in the plane perpendicular to the beam. For practical purposes, the detector was rotated 90 degrees clock-wise around the beam axis compared to its intended orientation in the LHCb detector. It was positioned in such a way that the beam would hit the R&D module first. A right-handed coordinate system identical to that of LHCb was used, with the z-axis defined along the beam axis and pointing downstream. Figure 4.1 illustrates this. By using the LHCb coordinate system, the collected data could consistently be analysed using LHCb reconstruction software.

The detector half was operated both in air and in vacuum. It was sealed with the "lid" from the so-called transport trolley. During operation in air, the detector volume was constantly flushed with dry air to avoid condensation around the cooling "cookies" that keep the hybrids and sensors at the required temperature. During vacuum operation, the pressure in the detector volume was close to 10^{-4} mbar. The modules were cooled at all times, using a CO_2 "blow" system that was custom-developed for the detector assembly[2]. The set point temperature on the blow system regulator was between -20°C and -30°C, resulting in silicon sensor temperatures just below 0°C.

The control voltages and Beetle bias voltage were supplied by two CAEN LV modules of the same type that is used for the VELO in LHCb. The silicon sensors were biased

[1] For a description of the H8 beam line, see http://nahandbook.web.cern.ch.
[2] For further information about the blow system, see https://twiki.cern.ch/twiki/pub/LHCb/VELOTestbeam/Blow_cooling_v121106.doc.

by a 16-channel High Voltage module from ISEG, located in the beam area and remotely controlled by a computer in the control room. The LV modules were mounted in racks outside the beam area, together with the control boards and TELL1 boards. The analogue data from the repeater boards were transmitted from the detector to the TELL1s using 15 m long CAT7 cables[3]. The communication between control boards and repeater boards was done with 20 m CAT7 cables. The Beetle chips were configured with the "default" parameters already listed in table 3.2. In many respects the setup was similar to the one used in ACDC2, which is described in detail in [89]. Figure 4.2 shows an overview of the DAQ in ACDC3.

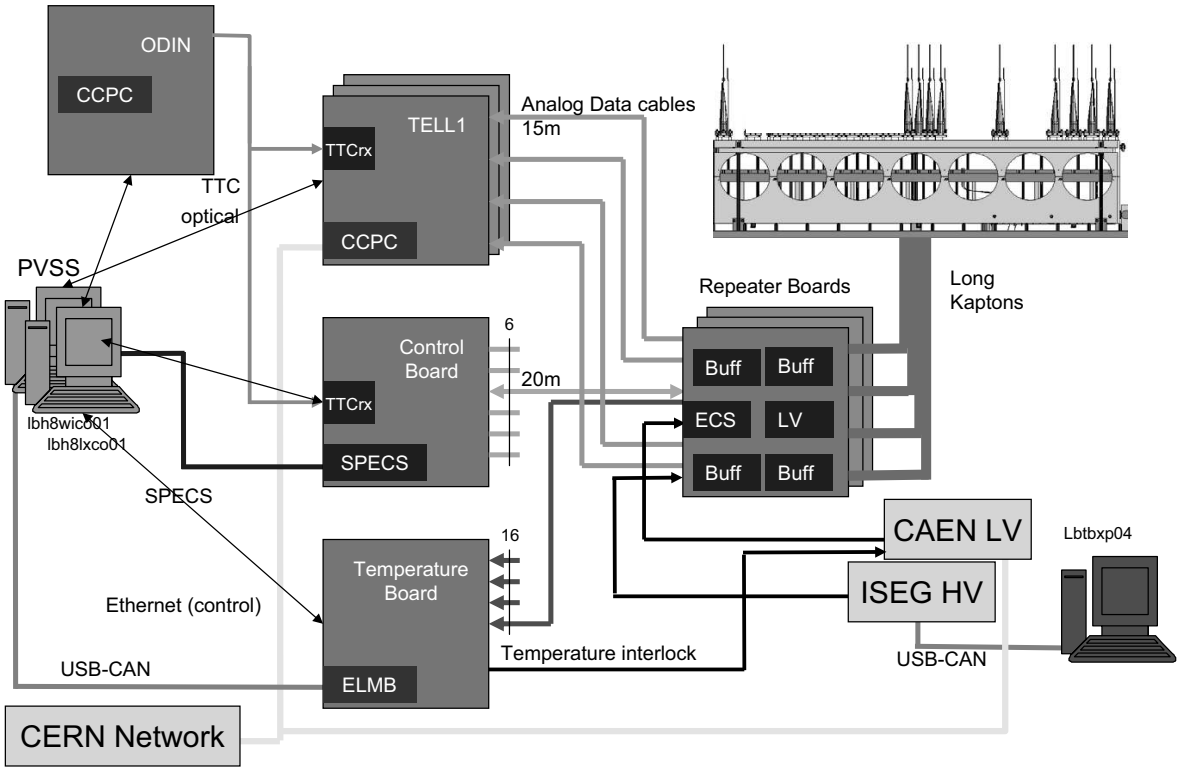

Figure 4.2: *An overview of the partially equipped C-half, the DAQ and the controls in ACDC3. The individual components are explained in section 2.5.*

4.2 Data Acquisition

Data Acquisition hardware components to read out only 6 out of 10 full modules were available at the time of the ACDC3. Therefore, four cable configurations were used in which different combinations of the modules were read out. The configurations were labelled as HP1, HP2, HP3 and HP4 (where HP is an abbreviation of "Happy pion").

[3]The DAQ is tuned to operate with 60 m cables, but due to a shortage at the time of the experiment, the existing cables had to be cut into four 15 m pieces each to cover the needs of the read out. The consequence of this was unfortunately an impedance mismatch between the cables and the analogue receiver (ARx) cards which led to higher levels of cross-talk than anticipated.

The change between different cable configurations was done by moving the repeater cards between the slots on the detector hood. The studies presented here use data only from the HP2 and HP4 configurations but the full details of the cable configurations can be found in Appendix C.

Initially, the TELL1 PP-FPGAs were running firmware version 1.8, but were upgraded to v1.9 during the experimental period[4]. All data that are used for the analysis described in this chapter were either collected with the newer version of the firmware or reprocessed offline by running the TELL1 emulator over the raw data. The processing and zero-suppression of the raw data in the PP-FPGAs and the TELL1 emulator are described more in-depth in section 2.5.1.

The readout of an event was triggered by a signal from a scintillator-based trigger setup. As can be seen in figure 4.1, six scintillation counters were used, three upstream (A0, A1, A2) from the detector and three downstream (B1, B2, C). Figure 4.3 shows the shapes and sizes of the scintillators and their position in the beam line.

After passage of a charged particle through a scintillator, the light that reaches the photo cathode of the photomultiplier tube generates an analogue signal. This signal was shaped into a digital signal of 10 ns length with a preamplifier and a discriminator circuit. The signals from the different counters were then time aligned and used in coincidence with each other. Different kinds of trigger logic for the coincidence circuit were used, depending on the run type:

- **Straight-through track runs** in which the beam was aimed at the sensors.

  Trigger logic: $A = A_0 \otimes A_1 \otimes A_2$.

- **Interaction runs** in which the beam was aimed at the sensors but only events with beam-sensor interactions were of interest.

  Trigger logic: $A \otimes (B_1 \oplus B_2)$

- **Target runs** in which the beam was aimed at the targets.

  Trigger logic: $A \otimes (B_2 \oplus C)$ Due to the higher angle tracks from the targets, the large area counter C was used specifically to increase the trigger acceptance. The target design is described in section 4.3.

- **Random trigger runs** in which data were recorded for noise and calibration studies.

To emulate the bunch frequency of the LHC, the output of the trigger logic was required to arrive in coincidence with a pulse from the internal clock of the readout supervisor (ODIN) running at 40 MHz. To further throttle the trigger input to the event builder, an additional dead time was introduced in the system to keep the trigger rate below 1 kHz.

4.3 Target design and setup

A total of 8 lead targets were mounted in the detector half, in groups of two at four different z-positions. Figure 4.4 shows the layout of one of the two holders that was used for this purpose. The base of the holder, which was machined to fit in the empty

[4]Due to an error in the channel reordering of the Φ-sensors.

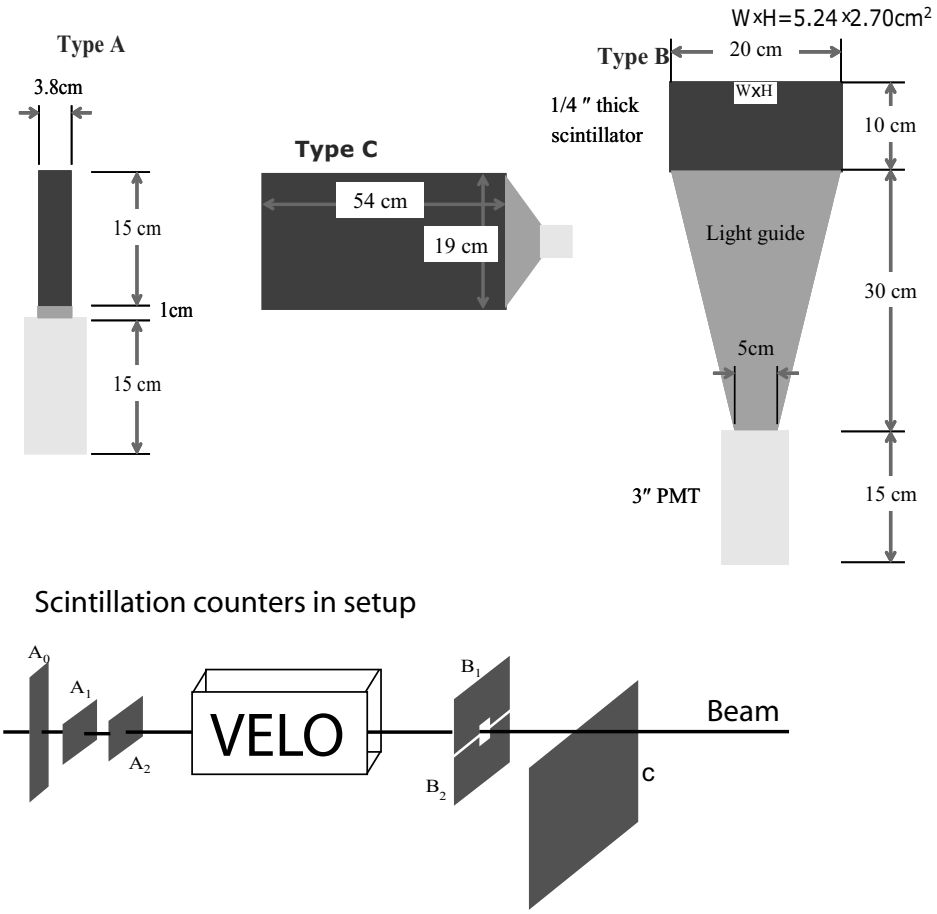

Figure 4.3: *The three types of scintillation counters that were used for the trigger, and their respective position in the beam line. The A type counters are positioned upstream from the detector, and the B and C types downstream. The B and C counters are only used for the "target" and "interaction" runs (as defined in the text). Due to the rectangular hole, the B counters are not illuminated directly by the beam, and the C counter is positioned below the beam. The figure is not to scale.*

slots of the VELO half, held an aluminium cylinder. Its orientation in the detector is indicated in figure 4.4. At each of the open edges of the cylinder, a ring with a stretched mylar foil was mounted and on each mylar foil, two coin-shaped lead targets were glued. One target of 1 mm radius was located at position $(x, y) = (0, 0)$ in the test beam (and of LHCb) coordinate system, while at $(x, y) = (15, 0)$ mm a second, bigger target with radius 2.5 mm was glued. The two targets are referred to as the *Inner* and *Outer* targets, respectively. Two target holders were used, one with $\Delta z = 100$ mm between the two rings and the other with $\Delta z = 30$ mm. The target rings were numbered 1-4, counting from upstream to downstream (towards higher z). The nomenclature for what follows will be "Inner/Outer target n, HP i" where n is the number of the ring and i is the number of the cable configuration that was used during data taking. All targets were 300 μm thick except the targets on ring 2 which were 200 μm thick. Table 4.1 shows the full target configuration.

Figure 4.5 shows a photograph of the test beam setup, where the two target holders can

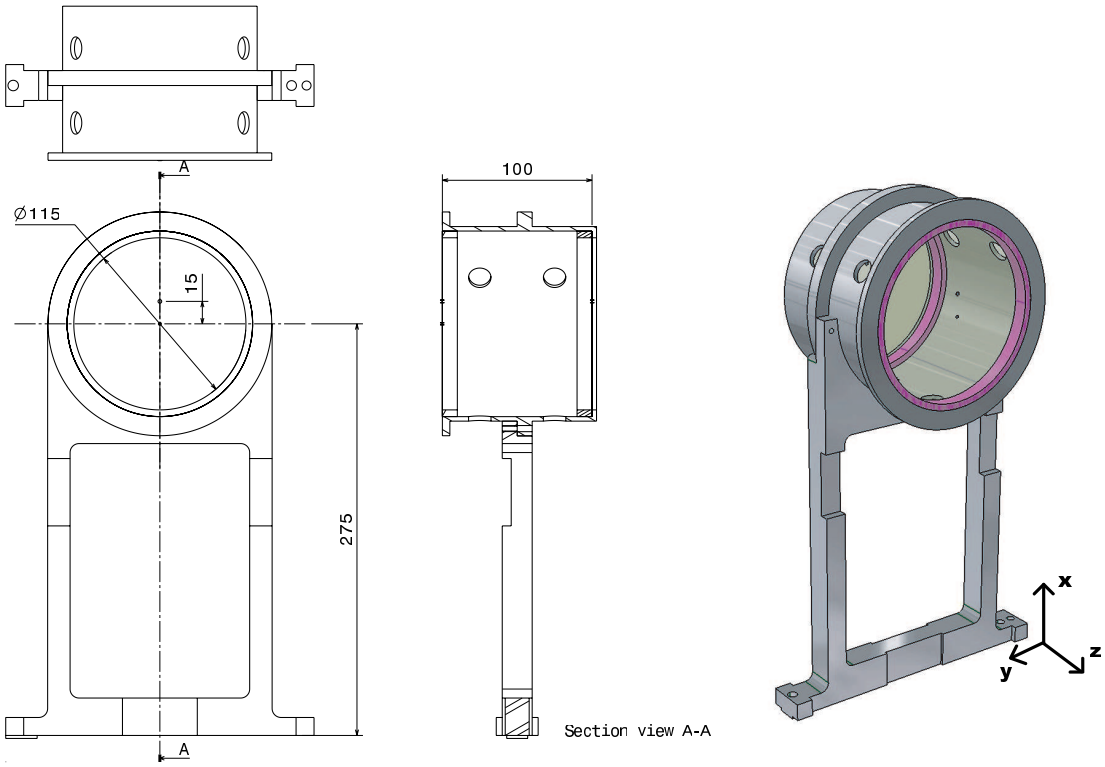

Figure 4.4: *The schematics of target holder I, which holds rings 1 and 2. Two targets can be seen as black dots on the rightmost figure.*

be seen. By aiming the beam at the targets, interactions between the beam particles and the lead nuclei could occur. If an interaction produced at least two secondary particles ("secondaries") in the acceptance of the detector, and the event was recorded, the data can be used offline to reconstruct the interaction vertex. By using the configuration of Inner and Outer targets, the difference between a closed (target position at the LHCb interaction point) and a half open (interaction point 15 mm away from detector) VELO could be emulated.

The primary concerns when designing the target system were *interaction rate*, *recon-*

Table 4.1: *Target configuration*

Holder	*Slot*	*Ring*	*Type*	*Thickness[μm]*	*Radius[mm]*	x	y	z
I	VL08R	1	Inner	300	1	0	0	0
		1	Outer	300	2.5	15	0	0
		2	Inner	200	1	0	0	100
		2	Outer	200	2.5	15	0	100
II	VL21R	3	Inner	300	1	0	0	535
		3	Outer	300	2.5	15	0	535
		4	Inner	300	1	0	0	565
		4	Outer	300	2.5	15	0	565

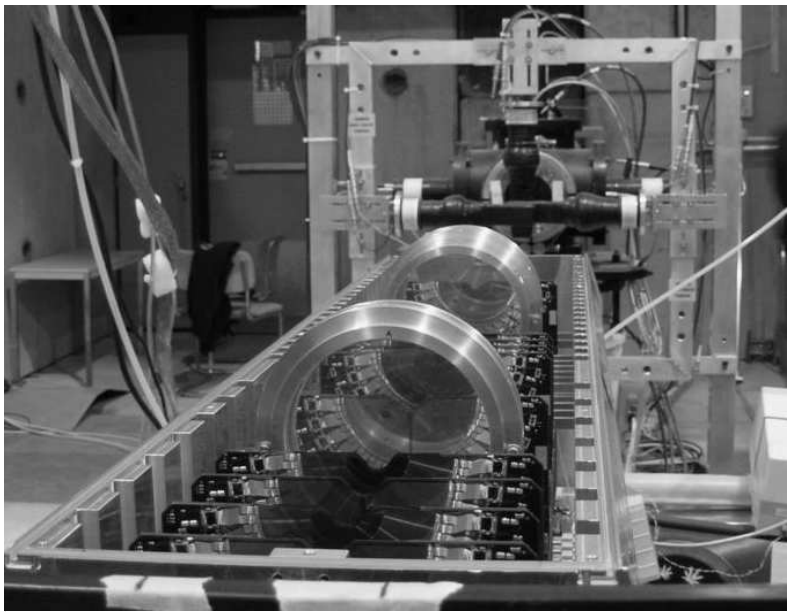

Figure 4.5: *Photograph from the test beam area, showing the opened detector half, with the 10 modules and the two target holders, with two rings each. Target ring 4 is the one closest to the camera.*

struction resolution and *detection efficiency*. As it is difficult to satisfy the three simultaneously, the final design reflects a compromise between these considerations.

Interaction rate In order to maximise the target interaction rate a material with high atomic number and density, Pb, was chosen. On the other hand, targets must be thin to minimise the amount of material between the interaction vertex and the detector. By using four targets the total interaction probability is quadrupled[5]. However, the drawback of using multiple consecutive targets is the risk of *shadowing*, i.e. that particles produced in target 1 are stopped or scattered by one of the next targets. As is discussed below, this deteriorates the reconstruction resolution and lowers the detection efficiency.

Reconstruction resolution The precision of the reconstructed track parameters at the vertex depends on the distance between the vertex and the first track measurement, which implies that the targets should be positioned as close to the sensors as possible. However, due to the beam-target interaction topology and the sensor geometry, this would have negative effects on the detection acceptance.

Detection efficiency Simulations of beam-target interactions show that the angular distribution of the secondary particles peaks at low angles, as can be seen in figure 4.6. This means that, with secondaries concentrated predominantly in a forward cone, there has to be a minimal distance between a target and a sensor to allow for particle detection. On the other hand, a large distance gives worse resolution.

The compromise was the following:

[5]Not exactly, since the targets on ring 2 only have 2/3rds thickness of the other targets.

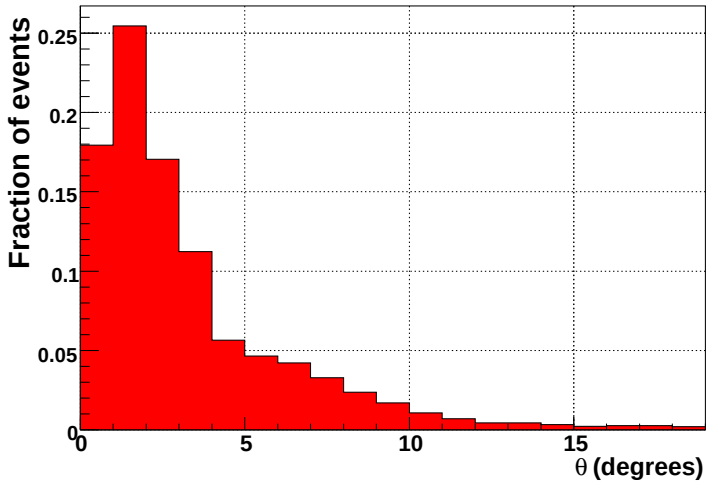

Figure 4.6: *Angular distribution of secondary particles from simulated beam-target interactions. The plot has been normalised.*

- To avoid shadowing, target rings 1 and 2 were placed 100 mm apart in the space between modules M26 and M29 (see figure 4.1) and target rings 3 and 4 are placed 30 mm apart between M21 and M37.

- To keep high reconstruction resolution, the distance from ring 3 and 4 to the closest downstream sensor was 65 and 35 mm respectively. Although less tracks were reconstructed from interactions in those targets, the accuracy of the reconstruction benefited due to the shorter distance between the vertex and the first sensor.

- To exploit the angular distribution of the secondaries, target 2 was placed at 100 mm from the first downstream sensor, M29. In this way, the probability to reconstruct many tracks with many hits per track remained high: the large distance between target and detector decreased the total solid angle of the reconstruction acceptance but actually increased the number of reconstructed vertices since a typical particle with low θ would "see" more sensor planes of the detector.

The target rings were optically surveyed by the CERN metrology department. During the survey the target holders were mounted on a mock-up base, identical in design to the real detector base but with less slots. The base provided accurate reference points and an easy way to translate the measurements to the coordinate system of the experiment. However, it was later found that the real C-half detector base plate used in the test beam setup, was not perfectly flat [90]. This causes systematic differences between the target positions as measured by metrology, and their actual value. Using the metrology of the C-half base, corrections to the target metrology measurement data are calculated. The corrections are described by

$$\Delta x = (3 \cdot 10^{-5} z - 0.0119)\,\text{mm} \tag{4.1}$$
$$\Delta y = (1 \cdot 10^{-4} z - 0.0072)\,\text{mm} \tag{4.2}$$

where z is the target z-position. The size of the correction is in the range of 10 μm$-$50 μm.

The accuracy of the target measurements was not limited by the survey instrument but by the irregular shapes of the targets which made it difficult to find well-defined measurement points. In the cases where the target shape was sufficiently close to circular, a measurement of target centre and radius could be done. However, in the majority of the cases the survey only produced a measurement of the target centre. The full report is available in [91]. As can be seen in the close-up photographs of the targets in Appendix D, it is difficult to accurately determine the centre of a target. Two individual metrology measurements of the target positions were made. The standard deviation of the difference between the measurements can be used as measure of the metrology uncertainty. By combining the x and y differences from the remeasured targets, the standard deviation is calculated to be 109 μm.

4.4 Datasets

During the nearly two weeks of data taking, a total of 90 million events were written to tape. With each TELL1 producing about 4 kB of data per event and 12 TELL1s taking data simultaneously, this resulted in 4.3 TB of data. The data of interest to the analyses presented here are:

Straight-through track runs. For the study of Signal-to-Noise and sensor resolution a dataset of about 350.000 events in configuration HP4 was used, with a wide beam illuminating a large enough region of the sensors to provide data at all strip pitches.

Target runs. For the target studies, seven datasets were used. They are listed in table 4.2.

Random trigger runs. Noise values of individual strips were extracted from a random trigger run of 5000 events in configuration HP4.

Table 4.2: *Datasets of real data (Data) and simulated data (Sim.) used in the target analysis. The "Wide beam" run is used for beam profile studies.*

Data/Sim.	*Target*	*Cable config.*	*#Events*	*#Rec. vertices*	*Comments*
Data	Inner	HP2	2.8M	21k	Vertices in targets
	Inner	HP4	15.4M	20k	
	Outer	HP4	10M	18k	
Sim.	Inner	HP2	53k	53k	(3×3) cm^2 beam around target.
	Inner	HP4	95k	95k	Same as above.
	Outer	HP4	45k	45k	(6×6) cm^2 beam around target.
Sim.	Wide beam	HP4	58k	58k	Vertices in vacuum vessel. Beam in $-2 < x < 25$ mm, $-1 < y < 1$ mm

Each of the datasets from the target runs are complemented with a Monte Carlo simulation produced with the LHCb simulation Gauss[6] and digitisation software Boole[7]. A 180 GeV charged pion beam was simulated using the "ParticleGun" feature of the simulation software. The beam profile was uniform and square shaped; the parameters are listed in table 4.2. To allow studies of systematic errors related to the beam profile, a separate dataset ("Wide beam") was generated. This is further discussed in section 4.9.2.

The simulation uses a detailed software description of the experimental setup which takes the sensor alignment results into account to ensure agreement between simulation and reality. The main difference between data and simulation is that the targets are modelled as perfect coins in contrast to the rough edges and surfaces of the real targets.

4.5 Event reconstruction

The real and simulated data are reconstructed using the Vetra program [92], a Gaudi based "project" in the LHCb software framework [93]. Vetra's capability to process zero-suppressed as well as non-zero suppressed data makes it suitable for test beam data, and with its bit-perfect TELL1 emulator it can perform zero-suppression offline. Due to the modularity of Gaudi, most of the general LHCb reconstruction software can run in Vetra.

The raw, non-zero suppressed data undergoes pedestal subtraction, strip reordering, linear common mode suppression and clustering in the TELL1 emulator. A cluster seed threshold of 10 ADC counts and a strip inclusion threshold of 4 ADC counts is used for all sensors. Since the TELL1 has a 3 bit limit on the precision of the cluster inter-strip position, the clusters positions are recalculated offline with floating point precision before the event reconstruction begins.

The first step in the track reconstruction deploys a generic 3D pattern recognition, implemented in the algorithm *PatVeloGeneric* [36]. The pattern recognition makes no a priori assumptions on the origin and direction of the track and is therefore more suitable for the ACDC3 data than the default VELO pattern recognition algorithm, which is optimised for tracks originating in the LHCb interaction region.

For the resolution study described in section 4.8 this is the starting point for a global least squares straight-line fit in two dimensions. The fit neglects the effects of multiple scattering which is possible due to the high momentum of the particles (180 GeV/c) where the effects of multiple scattering are small. The fitting procedure is described in detail in section 4.8.

The particles of interest for the vertex study (section 4.9) come from interactions between beam particles and the targets and are therefore of lower momentum. They are predominantly light (electrons, kaons, pions) and have kinetic energies of a few hundred MeV. A plot of their energy distribution is shown in figure 4.7. To account for the effects of multiple scattering on these secondary particles, the LHCb track fitter based on the Kalman filtering technique [38] is used instead, see section 1.2.2. In the LHCb software, it is implemented in the *TrackKalmanFitter* algorithm in the package *TrackFitter*. The fitter uses a detailed model of the experimental setup to propagate the track state through the detector, taking momentum dependent multiple scattering in the detector into account. However, in the test beam the individual particle momenta are not measured and

[6] http://lhcb-release-area.web.cern.ch/LHCb-release-area/DOC/gauss
[7] http://lhcb-release-area.web.cern.ch/LHCb-release-area/DOC/boole

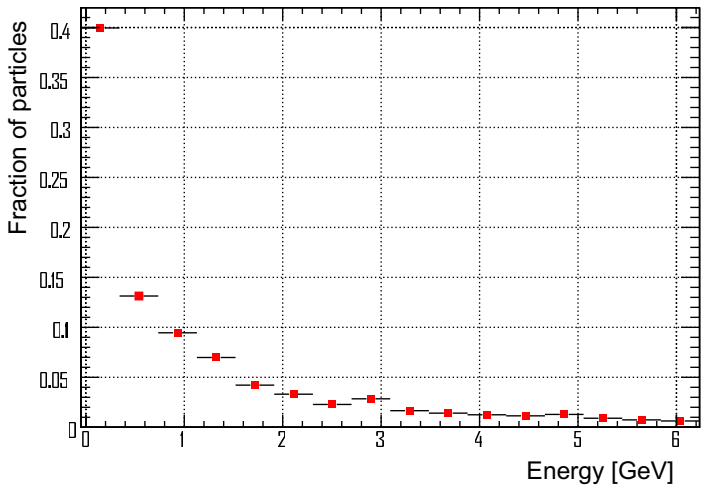

Figure 4.7: *Kinetic energy distribution of secondary particles in simulated data.*

an estimate of the momentum of 100 MeV/c is used.

For the data from the target runs, the last step of the reconstruction is the vertex fitting, i.e. the procedure to combine a set of tracks under the constraint that they originate from a common point in space. In the software, this is done by the *VertexGeneric* package which employs a so-called unconstrained progressive vertex fit [38], in which the reconstructed tracks are combined sequentially on the basis of their χ^2 contribution to the vertex.

Figure 4.8 shows an event display produced with the LHCb data visualisation program Panoramix[8]. The ten modules and the eight targets of the ACDC3 setup can be seen. In this event, three tracks were reconstructed and fitted to a vertex originating in inner target 2.

4.6 Alignment

The alignment of the silicon sensors is done using a combination of detector metrology data and a software procedure described in section 2.7 and in [57, 74]. For each cable configuration, data were recorded in a dedicated alignment run, providing 10.000 reconstructed tracks for the alignment procedure. Appendix F contains the residual distributions of all the sensors after software alignment. The R-sensors are well-aligned, while the Φ-sensors show the "banana shape" that comes from relative misalignments between the sensors of a module. As the alignment software uses so-called space points (the combination of an R and Φ-measurements of a module) these sensor-sensor misalignments cannot be easily corrected for. A method has however subsequently been demonstrated [57] in which the"banana shapes" can be used to extract the relative sensor misalignment.

[8] http://lhcb-release-area.web.cern.ch/LHCb-release-area/DOC/panoramix

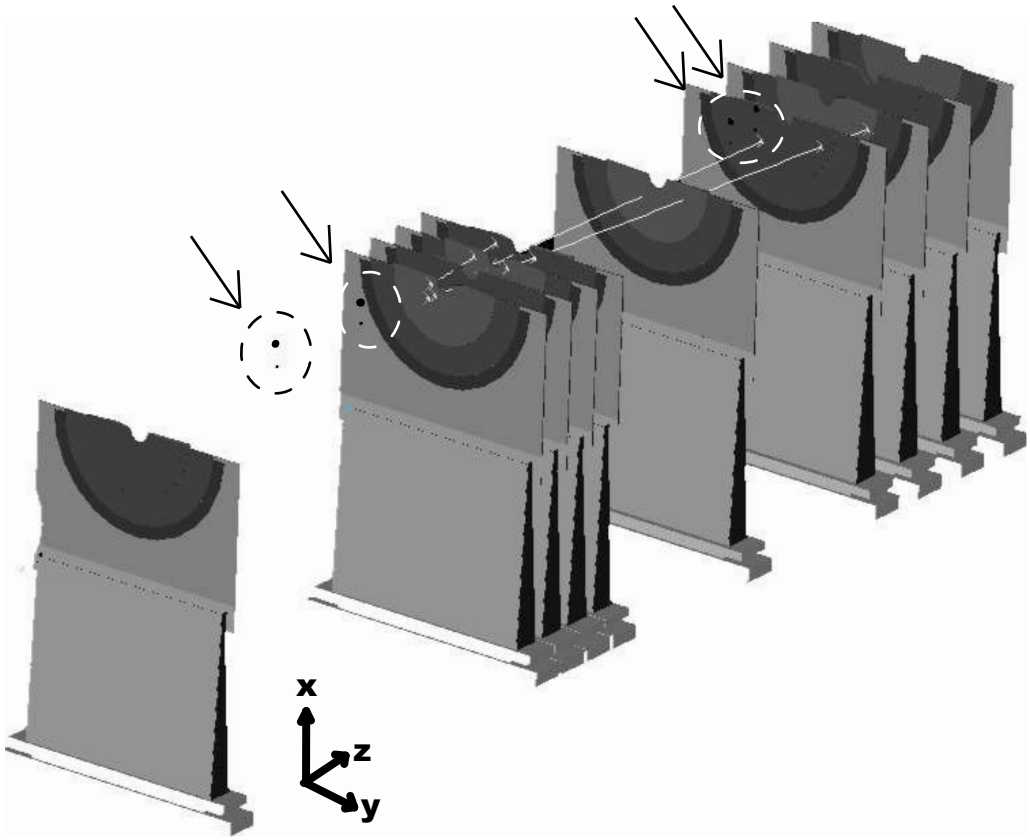

Figure 4.8: *Event display of three reconstructed tracks from an interaction in inner target 2. The targets are the black dots located within the dashed circles and indicated by arrows, The figure shows the orientation of the sensors and targets as they were mounted in the experimental setup. Since the coordinate system is identical to that of LHCb, the x-axis is pointing upwards in the setup. The coordinate system indicated in the figure only shows the orientation of the axis; the origin of the coordinate system is located at the position of inner target 1.*

4.7 Signal-to-Noise

The Signal-to-Noise (S/N) ratios of the VELO sensors are of great importance to the detector performance. As the detector gets progressively irradiated, the charge collection efficiency drops which lowers the S/N ratio [94]. This section covers S/N measurement using the data collected in ACDC3.

4.7.1 Event selection

As mentioned in section 4.4, the Signal-to-Noise (S/N) study is performed with data from straight-through track runs, where a region of the sensors in which strips of nearly all lengths were present was illuminated by the beam. Since HP4 data were used, the study includes the modules M24, M27, M29, M30, M31 and M37. Figure 4.9 shows a "hitmap" of one of the sensors, visualising the area of sensor M24-Φ under beam illumination. The vast majority of all the hits recorded in the sensor are located in a 45° slice (an octant).

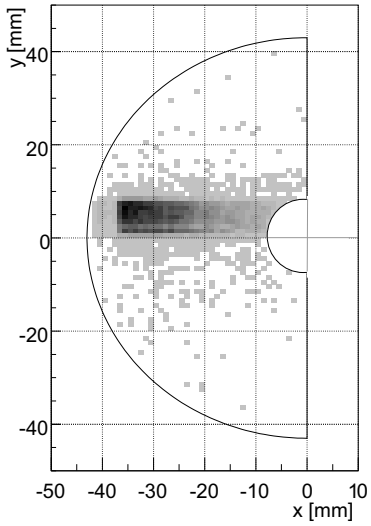

Figure 4.9: *A "hitmap" of sensor M24-Φ shows the area that was illuminated by the beam. The half circle indicates the approximate edge of the sensor. The shaded region indicates the beam spot, where black means the highest and white the lowest density of hits.*

A pure signal cluster sample is selected by only using clusters on tracks with 8 clusters or more, out of a maximum of 12. Additionally, to avoid clusters created by particles that have scattered in the vacuum vessel before traversing the detector, the tracks are required to have a polar angle $|\theta| < 2$ mrad. Clusters with a strip that is read out by the first channel of an analogue Beetle link are excluded. The reason for this is that those channels suffer from high noise due to cross-talk from the Beetle header, as explained in section 2.5.1. This is not sensor intrinsic noise since it contains an artificial component which can be removed with the header suppression algorithm in the TELL1. Finally, due to the Φ-sensor design, only one-strip Φ-clusters are considered. The reasons for this are explained in the following section.

4.7.2 Noise

The noise is determined from a dataset of 5000 events recorded with random triggers while there was no beam. It is calculated for each strip individually and is defined as the RMS of the ADC values of a strip after pedestal subtraction and common mode correction. For multi-strip clusters the total noise is defined as the arithmetic mean of the noise of the individual strips. Clusters that contain a dead or noisy strip are removed from the analysis. Dead and noisy strips are characterised by the fact that their RMS value falls outside the distribution of RMS values, which has well-defined edges. The criterion of $1.1 \leq \text{RMS} \leq 3.1$ is used.

The noise of a strip depends linearly on the total capacitance of the strip and its routing line. In the case of R-sensors, the strips at low radius are the shortest and therefore have the smallest capacitance, but they also have the longest routing lines. This decreases the difference in noise between the innermost and outermost strips. Figure 4.10 shows the noise for all R-sensors versus radius. Only the strips illuminated by the beam are included in the plot. As can be seen, the noise grows with increasing radius and varies by $10\% - 15\%$ over the strip range. As figure 4.9 shows, nearly all illuminated strips were located in the same octant, implying that only data from one ARx card per sensor is present. The differences in gain between ARx cards contribute to the systematic differences in noise levels that are observed between the sensors.

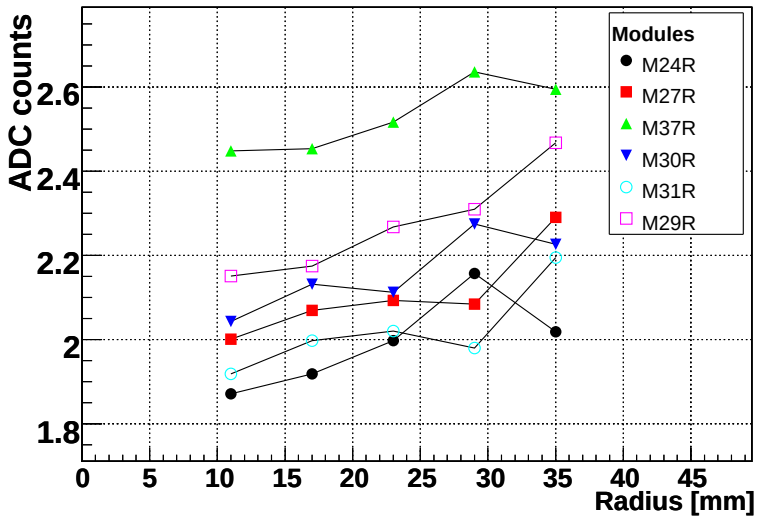

Figure 4.10: *Common mode corrected noise versus strip radius for all R-sensors read out in HP4. Only the strips illuminated by the beam are included in the plot.*

For the Φ-sensors there are two kinds of strips: inner and outer. Since they have very different lengths they are expected to have considerably different noise levels. The inner strips are read out through routing lines via a double metal layer on top of the outer strips. Since the ratio of number of inner to outer strips is 1:2, only every second outer strip has a routing line on top of it. Through capacitive coupling, these routing lines will give an extra noise contribution to the outer strips, effectively rendering three categories of strips with a distinct noise profile each: inner strips, outer strips without a routing line and outer strips with a routing line. The two categories of outer strips are identified

by their assigned strip number; an odd number means a strip with a routing line on top of it. Figure 4.11 shows an example (sensor M24Φ) of the noise distributions of each of the three categories: inner, outer odd, and outer even. The noise differences are clearly visible: the outer even strips have the lowest noise (average 1.6 ADC counts), followed by the inner strips (1.8 ADC counts) and the outer odd strips (1.9 ADC counts). Due to

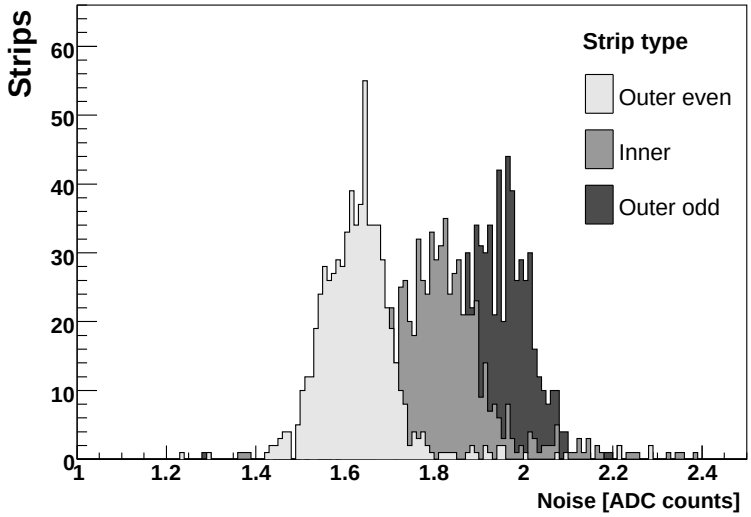

Figure 4.11: *Common mode corrected noise for all strips in M24Φ. The strips are split into three categories whose distributions are superimposed: Inner, Outer even, and Outer odd, where "even" and "odd" is related to the strip number.*

this behaviour, the S/N study of the Φ-sensor is limited to one-strip clusters. This makes it easier to disentangle the true S/N value from secondary effects caused by combining strips with different noise.

4.7.3 S/N calculation

The signal, noise and S/N are calculated analogously to the method described in section 3.3.1. The same fit procedure, using a Landau ⊗ Gauss function (equation 2.3), is also used.

The R-sensors are split into five zones with different strip lengths. The zones range from 8 mm $< R <$ 38 mm and the size of each zone is $\Delta R = 6$ mm. The signal and S/N values are calculated for each cluster, taking the individual noise values of the strips into account. The result is five distributions of signal and S/N values per R-sensor. Each of the distributions is fitted with a convolved Landau ⊗ Gauss function. The fits to the S/N distributions are shown in figures 4.12 and 4.13. For each of the fits, the most probable value (MPV) of the Landau function is taken to be the S/N value.

For the Φ-sensors, the clusters are divided into the before mentioned three different strip categories. Analogous to the R-sensor, the S/N distributions are fitted with a Landau ⊗ Gauss function (figure 4.14).

The results of the fits are summarised in figure 4.15a (R, Signal), figure 4.15b (R, S/N), and figure 4.15c (Φ, S/N).

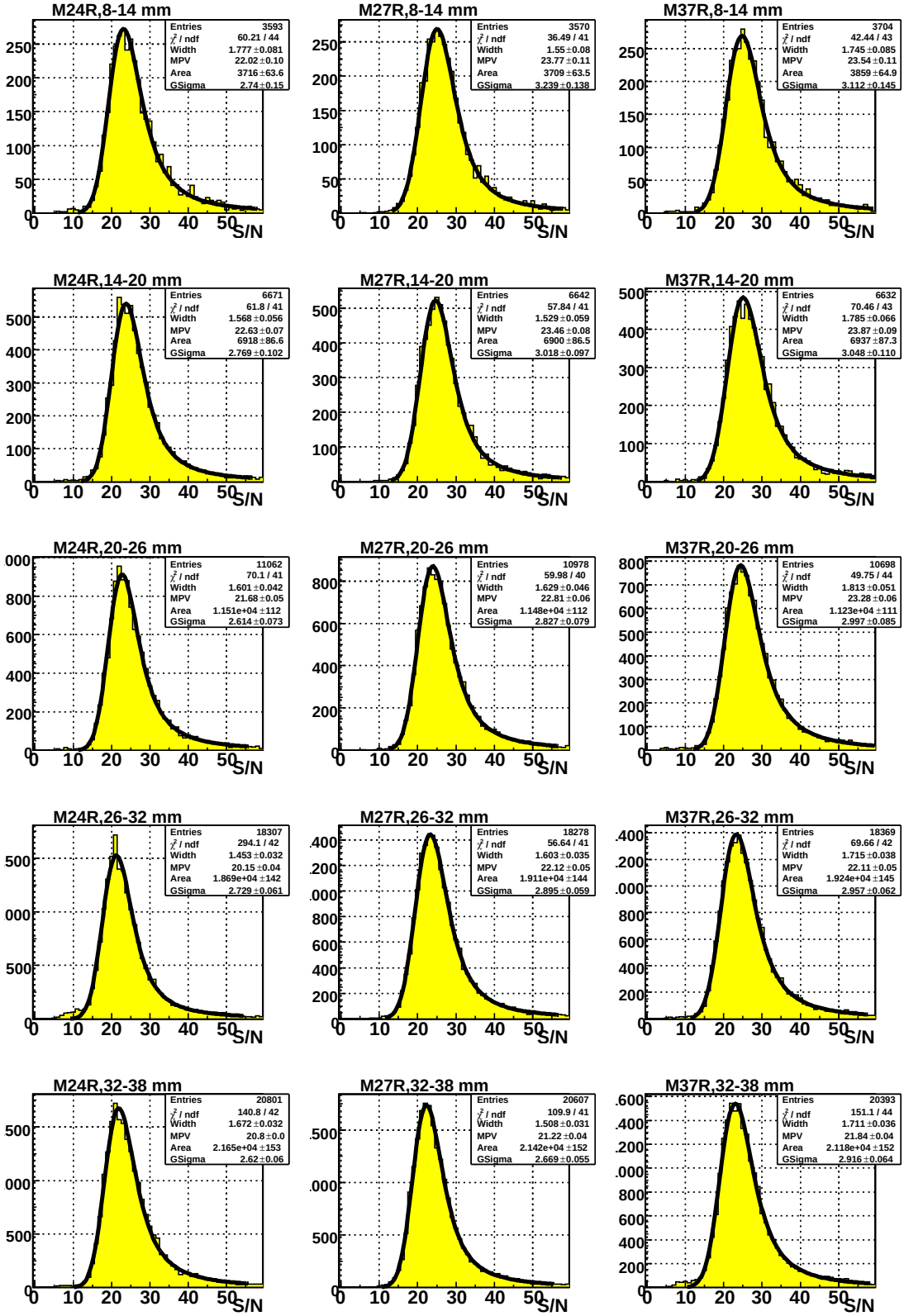

Figure 4.12: *S/N distributions for M24R, M27R and M37R split into five ranges of different radius, with a Landau ⊗ Gauss function fitted to each. The Width and Most Probable Value (MPV) are parameters of the Landau component, and GSigma is the width of the Gaussian component. The Area parameter is the normalisation factor.*

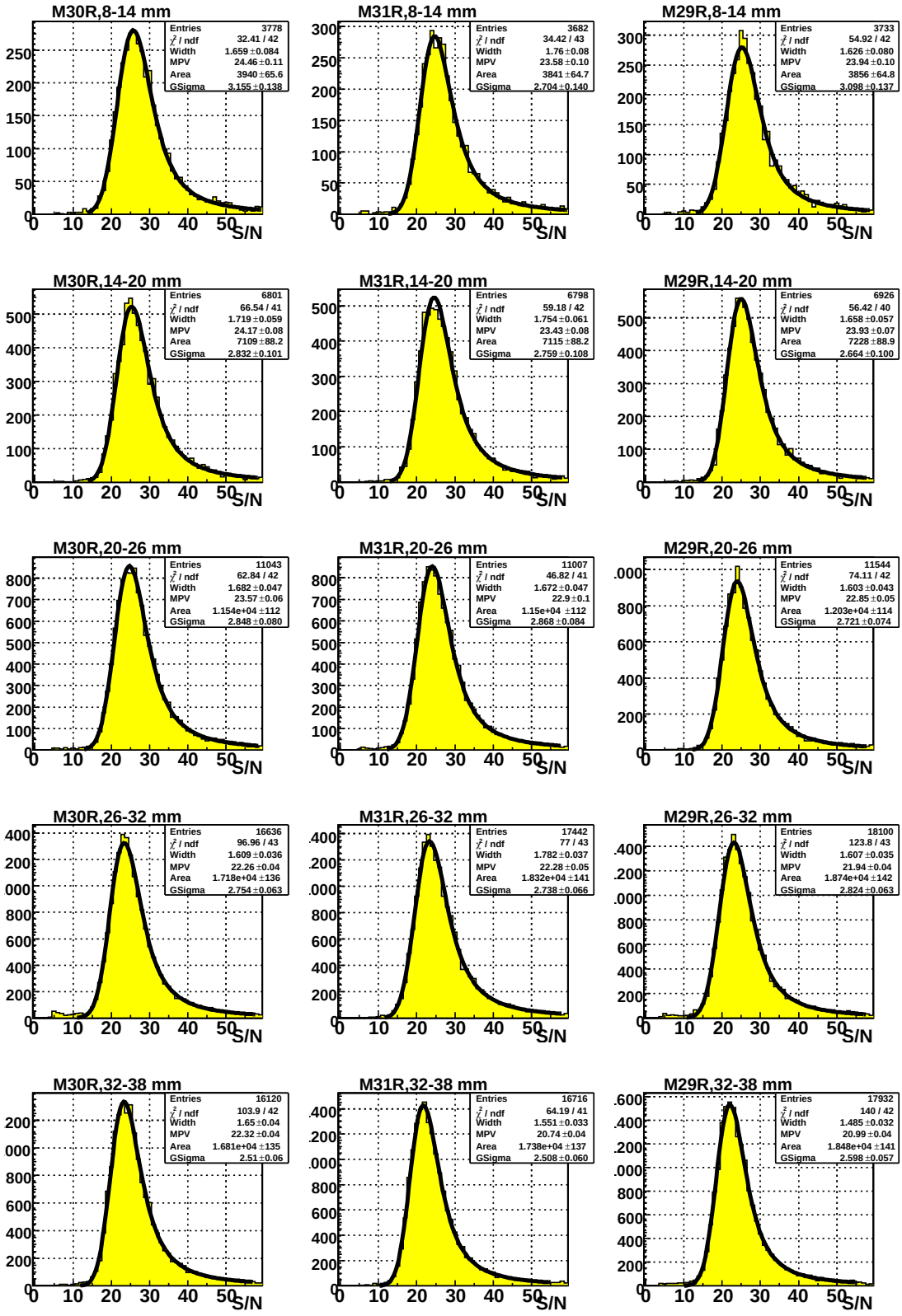

Figure 4.13: *Same as figure 4.12, for sensors M30R, M31R and M29R.*

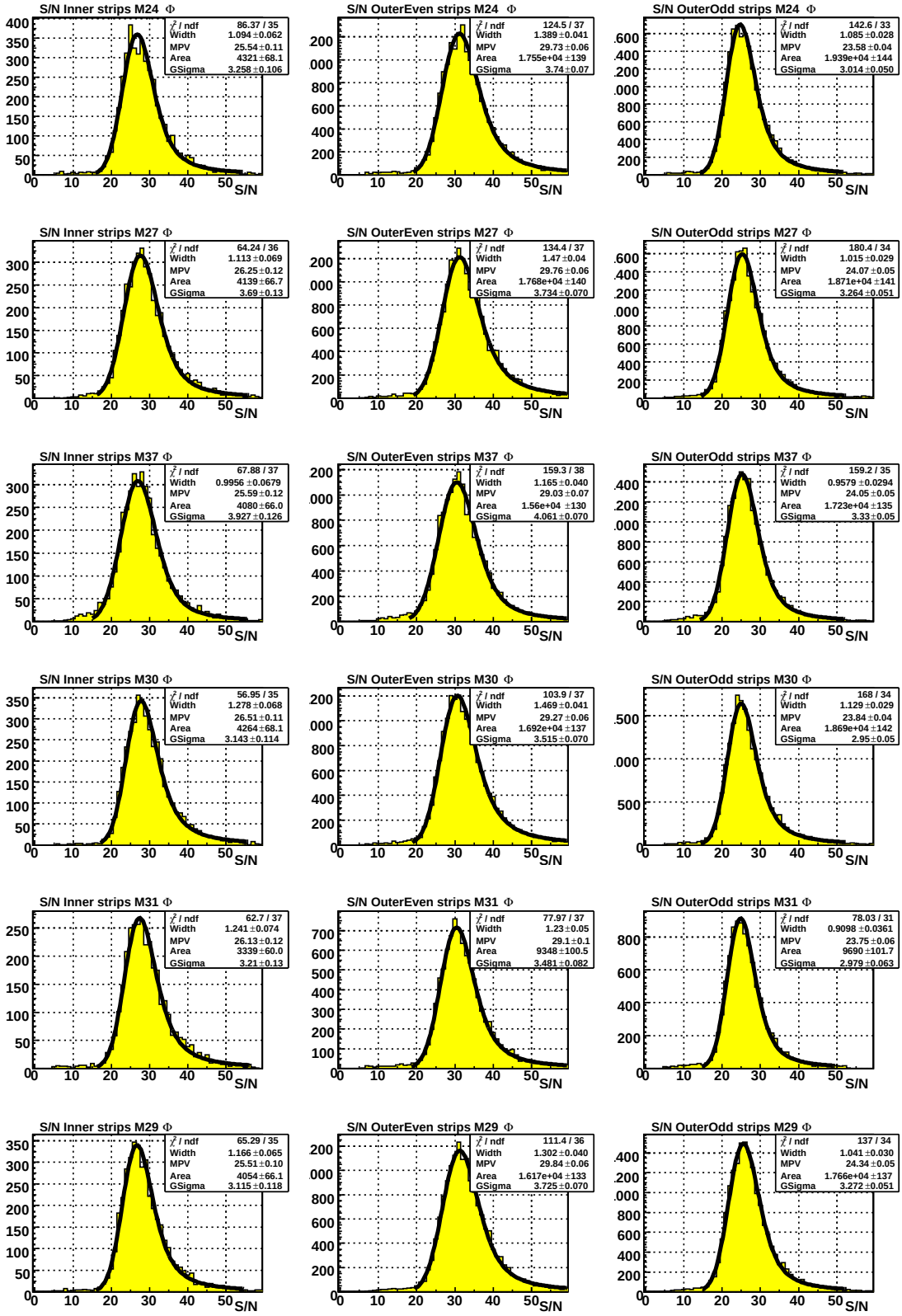

Figure 4.14: *S/N distributions for all Φ-sensors, split into the three strip categories: Inner (left column), Outer even (middle), and Outer odd (right).*

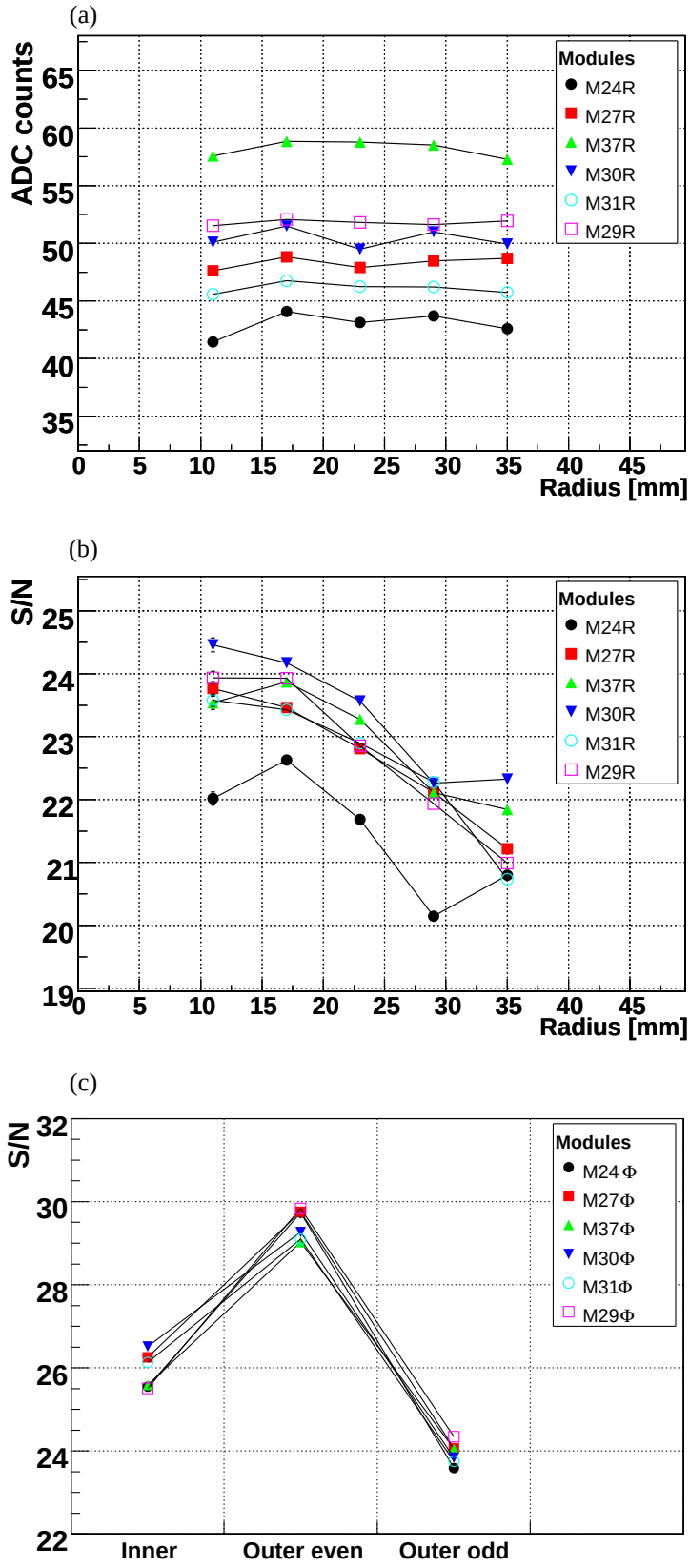

Figure 4.15: *MPVs of the Landau ⊗ Gauss fits to the*
(a) Signal (R-sensors)
(b) S/N (R-sensors)
(c) S/N (Φ-sensors).
The noise spectra of the R-sensors are shown in figure 4.10.

4.7.4 Conclusion

As figure 4.15a shows, the signal level stays constant over the entire radius of the R-sensors, and the overall difference in signal between sensors, which is caused by gain differences, matches the difference observed for the noise in figure 4.10. As expected, the S/N of the R-sensors drops with increasing radius of the strips. The bulk of the measurements fall in a band of $21 < S/N < 24.5$ for almost all measurements except those of M24R, which are systematically lower. As it turns out, M24R is the only R-sensor of HP4 which received a"B-grading" during module production [95], due to its relatively high leakage current (25 μA at 18.6°C). The noise levels in ACDC3 should however remain largely unaffected by this; the operational temperature in ACDC3 was around 0°C and the leakage current depends strongly on temperature [96]. Furthermore, the measured leakage current is too small to account for the discrepancies observed between sensor M24R and the others. Therefore, this can not be the source of the discrepancy. The observation is however consistent with what would be observed with a sub-optimally tuned ADC digitisation delay (see section 5.1.3 for description). Such a situation would lead to lower observed signal but unchanged noise levels. For the Φ-sensors, the S/N clearly follows the noise levels of the three strip types, and it is in general higher than for the R-sensors. This is attributed to the lower noise of the Φ-sensor.

Table 4.3 shows the average S/N for the R and Φ sensors. To get an average that is representative for the R-sensors, sensor M24R was removed from the calculation. When comparing these results with the older measurements presented in section 3.3.1 it is necessary to take into account the 100 μm difference in sensor thickness, which translates to a 50% more charge collection in ACDC3. This in combination with about 10% higher noise levels in ACDC3 gives an expected S/N increase of $30-40\%$ between the older data and the newer data. The ACDC3 data are consistent with this estimate.

Table 4.3: *Average S/N values for the R and Φ sensors.*

Sensor type	*Radius [mm]*	*Pitch [µm]*	*Average S/N*
R	8-14	40-51	23.9±0.1
	14-20	51-62	23.8±0.1
	20-26	62-73	23.1±0.1
	26-32	73-84	22.1±0.1
	32-38	84-94	21.4±0.1
Sensor type	*Region*		*Average S/N*
Φ	Inner		25.9±0.1
	Outer even		29.5±0.1
	Outer odd		23.9±0.1

The good sensor performance gives leeway for reducing the pulse pre-spill and spill-over[9] by sacrificing some S/N. This can mainly be accomplished by adjusting the shaper feedback voltage (Vfs) on the Beetle chip [59, 78] and/or by sampling the Beetle pulse a few nanoseconds off-peak. At the time of writing the decision has been made to use Vfs = 500 mV but this will be subject to revision when the detector is calibrated with the LHC beams.

[9]The amplitude of the pulse 25 ns before and after the time of sampling.

4.8 Sensor resolution

The single hit resolution of the sensors is calculated for HP4 using the same dataset as for the S/N analysis in the previous section. The definition of single hit resolution, based on the RMS of the track-cluster residual distribution, is the same as the one used in the November 2004 test beam experiment (chapter 3). The November 2004 analysis used unbiased residuals supplied by a beam telescope with known resolution. However, in ACDC3 no external beam telescope was available, such that the VELO detector had to provide its own reference tracks. This requires a different approach to measuring the resolution.

4.8.1 Analysis

Due to the high momentum of the particles (180 GeV/c) in the run, the effects of multiple scattering between modules are at the sub-micron level and can be neglected. This allows for the use of a global least squares minimisation of a straight line track model from which it is straight-forward to extract the single hit resolution. The results of the pattern recognition program (a set of clusters) are used as input to the track fit.

The analysis uses only events where six R-clusters, one per R-sensor, were connected to each other by the pattern recognition. To eliminate the risk of including fake hits due to noise, all the clusters are required to have a charge greater than 20 ADC counts. The polar angle θ of the track state provided by the pattern recognition program is used to select tracks that are parallel to the z-axis; the cut is set to $|\theta| < 2$ mrad. In total, about 65000 tracks satisfy these conditions. Due to the remaining misalignments of the Φ-sensors discussed in section 4.6, only data from the well-aligned R-sensors are used in this analysis. This implies that a two-dimensional $R - z$ fit can be used.

By selecting tracks with very low θ the assumption can be made that the measurement in each sensor was made with strips of the same pitch, such that all measurements on the track can be assumed to have the same resolution. The position of a cluster is calculated from the individual strip charges using the centre-of-gravity method.

The data is fitted with a straight line described by

$$f(z; k, m) = kz + m\,. \tag{4.3}$$

For a given sensor at position z_i $(1 \leq i \leq N)$, the difference between the fitted line and a cluster position r_i, the residual, is defined as

$$\Delta_i \equiv r_i - f(z_i; k, m)\,. \tag{4.4}$$

To find the values of the slope k and intercept m that best fit the measurements, the least squares method is used in which the sum of the squared residuals

$$S = \sum_{i=1}^{N} \Delta_i^2 = \sum_{i=1}^{N} (r_i - f(z_i; k, m))^2 \tag{4.5}$$

is minimised. The minimisation conditions

$$\frac{\partial S}{\partial k} = 0 \tag{4.6}$$

$$\frac{\partial S}{\partial m} = 0 \tag{4.7}$$

lead to the expressions for k and m:

$$k = \frac{N\sum zr - \sum z \sum r}{N\sum z^2 - (\sum z)^2}\,, \tag{4.8}$$

$$m = \frac{\sum r \sum z^2 - \sum zr \sum z}{N\sum z^2 - (\sum z)^2} \tag{4.9}$$

with which a straight line is fitted to the clusters selected by the pattern recognition in each event.

The single hit resolution of a sensor j can be accessed through the width of its residual distribution, which by error propagation becomes

$$\sigma_{\Delta j} = \sqrt{\sum_{i=1}^{N}\left(\frac{\partial \Delta_j}{\partial r_i}\sigma_{r_i}\right)^2 + \sum_{i=1}^{N}\left(\frac{\partial \Delta_j}{\partial z_i}\sigma_{z_i}\right)^2} \tag{4.10}$$

It will be assumed that $\sigma_{z_i} = 0$, i.e. that the errors on the z-coordinates are negligible. Furthermore, since only tracks with very low θ are used, the assumption can be made that all the clusters are measured with the same resolution ($\sigma_r = \sigma_{r_1} = \sigma_{r_2} = ... = \sigma_{r_N}$). This leads to the simplified expression

$$\sigma_{\Delta j} = \sigma_r \sqrt{\sum_{i=1}^{N}\left(\frac{\partial \Delta_j}{\partial r_i}\right)^2} \equiv \sigma_r T_j \tag{4.11}$$

with

$$\frac{\partial \Delta_j}{\partial r_i} = \delta_{ij} - \frac{\partial k}{\partial r_i} z_j - \frac{\partial m}{\partial r_i}\,. \tag{4.12}$$

After inserting equations 4.8 and 4.9 into equation 4.12 the dependence on r disappears. The transformation factor T_j becomes

$$T_j = \sqrt{\sum_{i=1}^{N}\left(\delta_{ij} - \frac{N z_i z_j - z_j \sum z + \sum z^2 - z_i \sum z}{N\sum z^2 - (\sum z)^2}\right)^2}\,. \tag{4.13}$$

The transformation factor depends on which sensor is studied (j), how many sensors are present ($N = 6$), and the positions of the sensors (z_i), i.e. it becomes a property of the detector. The z-positions of the sensors can be found in Appendix C. By inserting them into equation 4.13 the transformation factors of the six modules in HP4 are calculated. Their values are shown in table 4.4.

Table 4.4: *Transformation factor between residual width ($\sigma_{\Delta j}$) and sensor resolution (σ_r).*

Module	T_j
M29	0.76
M31	0.83
M30	0.85
M37	0.86
M27	0.82
M24	0.76

4.8.2 Results

The residuals are plotted versus strip pitch and sliced into 2 μm wide pitch intervals in the range 40-92 μm[10] after which each of the slices is fitted with a Gaussian function. The widths of the Gaussians are translated to sensor resolution by the use of the transformation factors in table 4.4 and equation 4.11. The obtained resolution values are then plotted versus strip pitch for each of the six R-sensors, see figure 4.16. The plot includes a dashed line that indicates the binary resolution at $\sigma = pitch/\sqrt{12}$.

The data points for the sensors M24R, M27R and M37R look very similar. For M30R and M29R the resolution does not worsen as quickly with pitch as for the other sensors. Sensor M31R shows the poorest resolution of all sensors, at high pitch it is comparable to binary resolution. The values from the six sensors are averaged with equal weight and plotted in figure 4.17. A linear fit to the data points gives a parameterisation of the single hit precision as a function of the pitch: $8.5 + 0.26 \times (pitch - 40)\mu$m. The result is comparable to that of a different study [57] in which the resolution was found to be about $9.5 + 0.3 \times (pitch - 40)\mu$m.

[10] There are not sufficient data at higher pitch.

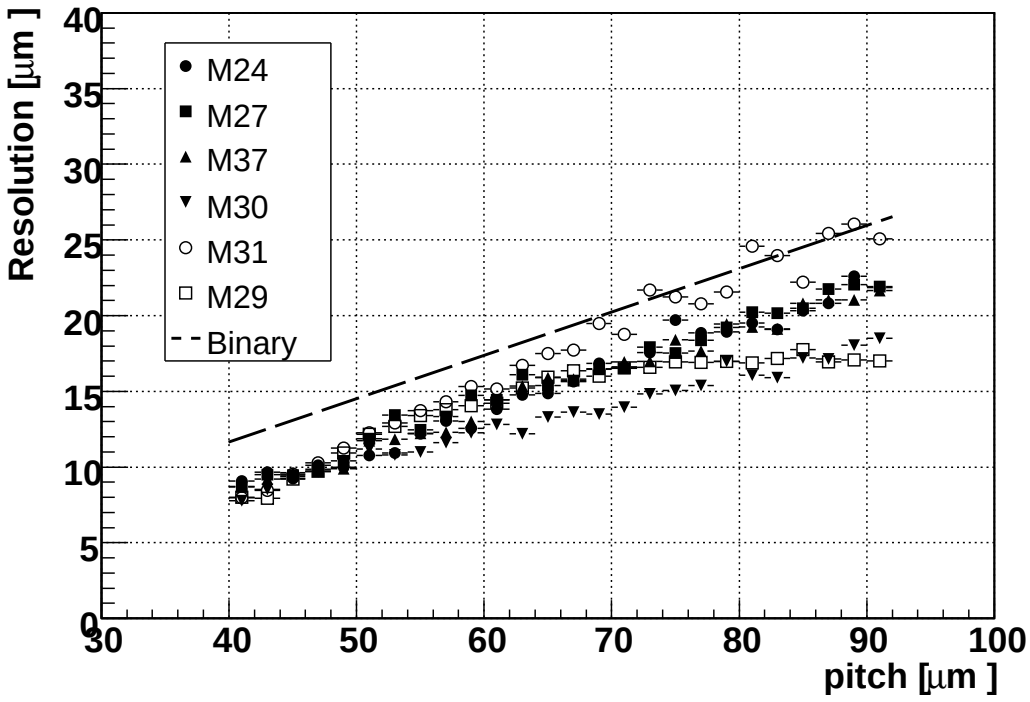

Figure 4.16: *Single hit resolution (σ_r) versus strip pitch for the six R-sensors read out in HP4. The dashed line indicates binary hit resolution.*

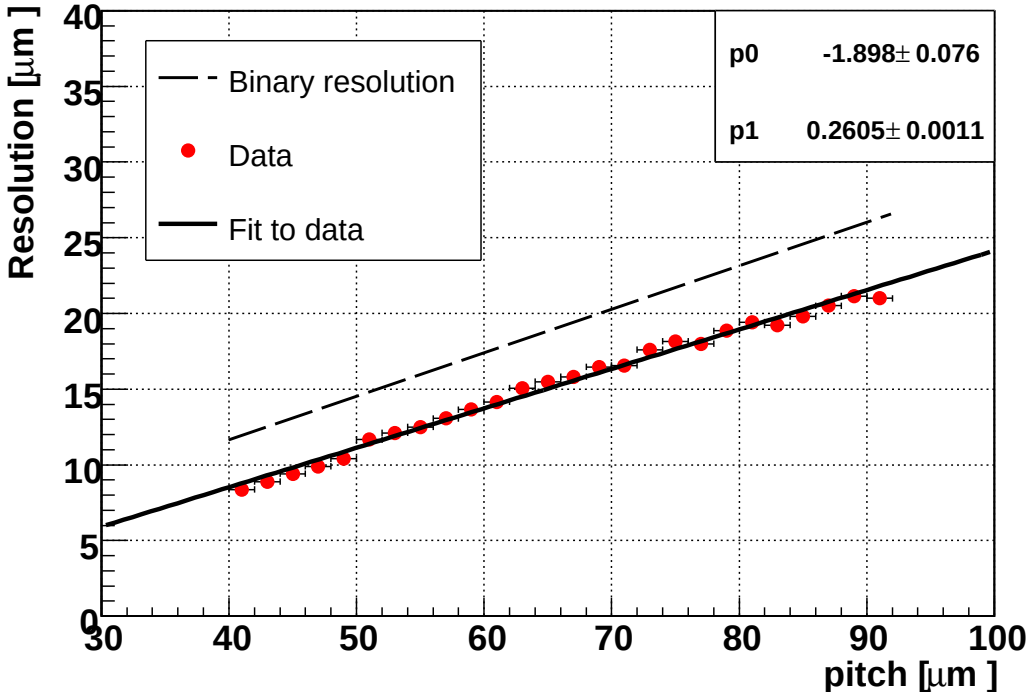

Figure 4.17: *Single hit resolution versus strip pitch averaged over six R-sensors.*

4.9 Vertex analysis

The VELO detector is used to measure the production (primary) and decay (secondary) vertices in $b\overline{b}$ events in the LHCb interaction region. Due to its design it is required to "open", i.e. to move out in the x-direction from its "physics position", during an LHC injection, and to "close", move back in, once the beams are stable. As the VELO closes, the detector has to be centred around the beam axis, an operation which requires knowledge of the position of the interaction region. The position can be measured by the VELO itself using reconstructed primary vertices. Evidently, it is important that the reconstructed vertex position is correct and free of bias. To validate this the targets were included in the ACDC3 setup. Although there are differences between the LHC conditions and the test beam setup, a study of the vertex reconstruction performance in ACDC3 gives useful insights into potential problems, gives a handle on the accuracy of the VELO simulation and acts as a proof of principle. This section discusses the analysis of the data from the target runs and compares them to data from the LHCb simulation. The main questions addressed are:

- are the reconstructed target positions in agreement with their true position and to what precision?
- are data from the LHCb simulation software consistent with real data?

A model is developed to determine the positions (edges) of the targets and the vertex resolution, based on the distributions of reconstructed vertices from the targets.

4.9.1 Event selection

The reconstruction described in section 4.5 produces a collection of events with one or more vertices per event. To keep the data clean, events with more than one reconstructed vertex are discarded. The data sample is reduced further by applying a z-criterion to the vertices. Figure 4.18 shows the z-distribution of the vertices in the Inner HP2 dataset. Twelve distinct peaks can be seen. The broad peak in the region around $z = -1700$ mm is due to vertices from interactions in the filament counters XFFV476 and XFFV477 of the H8 beam line. At $z = -375$ mm vertices from the 4 mm thick aluminium detector cover form a high peak. As described in section 4.9.2, these vertices are used to determine the beam profile. Towards higher z, vertices from the following objects can be seen: module M26 ($z = -160$ mm); targets 1 and 2 (0 mm and 100 mm); modules M29, M23, M31, M30 and M37 (200-450 mm) and targets 3 and 4 (535 mm and 565 mm). To select the target vertices, a z-cut of ± 15 mm around the nominal target centres is applied.

By applying a cut $\chi^2/DoF > 20$ the vertices with the worst quality are eliminated. This translates to rejecting 5% of the data. The cut is empirically motivated: the value 20 is trade-off between rejecting too many vertices and including too many low quality vertices.

The final cut is based on the number of tracks/vertex. Ideally, the best possible resolution is obtained from vertices with many tracks. By cutting hard on this parameter, however, one loses a large fraction of the accumulated statistics. The compromise is to demand at least 3 tracks/vertex for the targets with sufficiently many[11] vertices to maintain sufficient statistics, and accept 2-track vertices in the other cases. Table 4.5 contains

[11] "Sufficiently many" vertices is not a well-defined number but a result of a trial-and-error procedure.

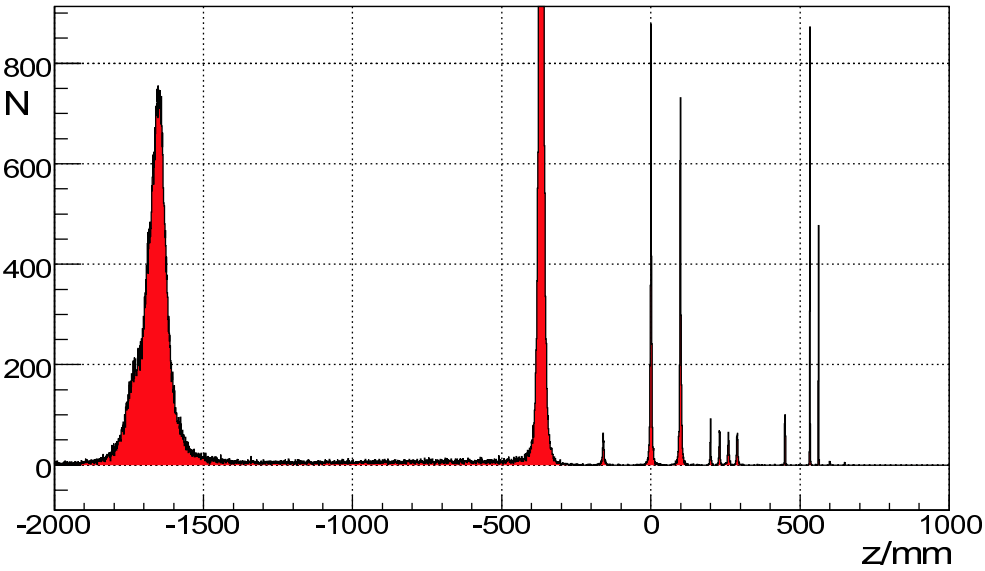

Figure 4.18: *The z-distribution of the vertices in the Inner HP2 dataset.*

the details of this cut for the various datasets. To allow fair comparisons between real and simulated data the same cuts were applied on both data types.

Table 4.5: *Summary of the #tracks/vertex cut applied to the real and simulated datasets. For the datasets that are missing from the list (Inner target 4, HP4, Outer targets HP2 and Outer targets 3-4, HP4), not enough events were accumulated.*

Cable Config	*Inner/Outer*	*Target*	*#tracks/vertex cut*
HP2	Inner	1	≥ 3
		2	≥ 3
		3	≥ 2
		4	≥ 2
HP4	Inner	1	≥ 3
		2	≥ 3
		3	≥ 2
HP4	Outer	1	≥ 3
		2	≥ 2

4.9.2 Modelling the vertex distribution

By plotting the vertex position in the xy-plane the circular shapes of the targets appear. Figure 4.19 shows an example: a photograph of inner target 2 is compared to the distribution of reconstructed vertices for the same target. The unsmooth edge of the circle is mainly a consequence of limited statistics and the uneven edges of the targets (an example of which is clearly visible in figure 4.19a). In addition, the non-uniform distribution of

vertices over the target surface is caused by statistical fluctuations and actual differences in thickness, but also by the beam profile and a varying reconstruction efficiency as will be shown below. The full set of plots for all targets can be found in Appendix E.

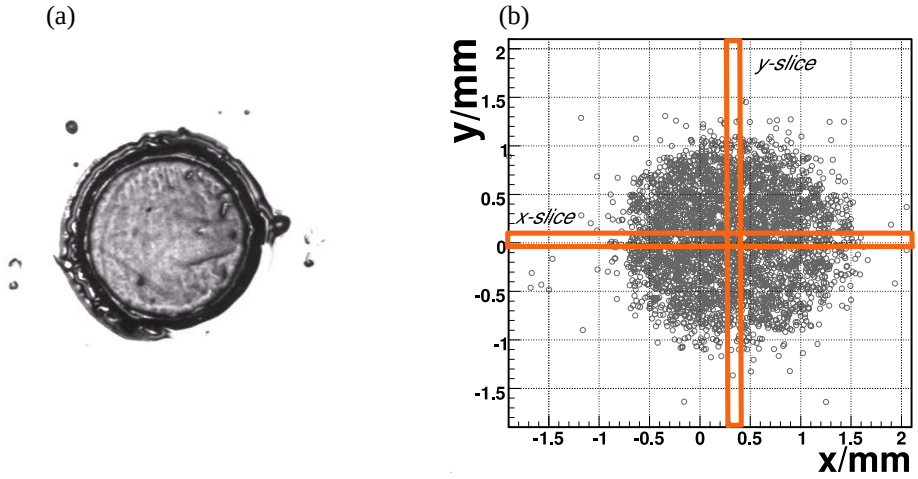

Figure 4.19: *Two views of Inner target 2.*
(a) A close-up photograph of the target. The rough edges and the uneven surface can clearly be seen.
(b) The distribution of reconstructed vertices in the xy-plane, HP2. About 3500 vertices are included in the plot. The pairs of parallel lines illustrate the principle of taking slices along the central axes (see text).

As mentioned earlier, it are the reconstructed positions of the targets and the vertex resolution that are of interest. Two approaches have been considered for the analysis of the reconstructed vertex ensemble: a single two-dimensional (2D) analysis in (r, Φ)-space and two separate one-dimensional (1D) analyses using the x- and y-projections of the vertex positions. The two-dimensional approach has the benefit that it utilises the full statistics of the dataset by taking every vertex into account when reconstructing the shape and position of each target. However, the problems associated with the above-mentioned issues of beam profile, unsmooth targets, etc, lead to an overly complicated model for the purpose of this analysis.
Matters get significantly simpler by using a 1D model in which x and y are treated separately. If the analysis in the $x(y)$-dimension is limited to vertices in a slice around the central $x(y)$-axis of the target the problems from the imperfections of the targets are largely suppressed. For this reason the 1D approach is used in this study.

The target model

The first building block in modelling the vertex distribution is the assumption that each vertex at coordinate x_i can be treated as a measurement sampled from a Gaussian distribution with mean μ_i and standard deviation σ_i. Since the measurements come from interactions within a target with edges it follows that the measurements are sampled from a set of Gaussian distributions with the property $x_{low} \leq \mu_i \leq x_{high}$, where x_{low} and x_{high} represent the edges of the target. The standard deviations σ_i of a Gaussian distribution are interpreted as the vertex resolution of the corresponding measurement x_i.

With an initial assumption of equal interaction probability over the entire target, the probability density function(PDF) that describes the distribution of the measurements becomes

$$F(x) = N \int_{x_{low}}^{x_{high}} e^{-\left(\frac{x-\mu}{\sqrt{2}\sigma}\right)^2} d\mu \,, \tag{4.14}$$

where N is a normalisation factor. For now it is assumed that the vertex resolution is constant over the entire target, i.e. $\sigma = \sigma_1 = \sigma_2 = \cdots = \sigma_n$. Variable resolution will be introduced at a later stage.

By making the variable substitution $t = (x-\mu)/(\sqrt{2}\sigma)$, equation 4.14 can be rewritten as

$$F(x) = -\sqrt{2}\sigma N \int_{\frac{x-x_{low}}{\sqrt{2}\sigma}}^{\frac{x-x_{high}}{\sqrt{2}\sigma}} e^{-t^2} dt \; = \tag{4.15}$$

$$N' \left(\int_0^{\frac{x-x_{low}}{\sqrt{2}\sigma}} e^{-t^2} dt - \int_0^{\frac{x-x_{high}}{\sqrt{2}\sigma}} e^{-t^2} dt \right) \; = \tag{4.16}$$

$$N' \left(Erf\left(\frac{x-x_{low}}{\sqrt{2}\sigma}\right) - Erf\left(\frac{x-x_{high}}{\sqrt{2}\sigma}\right) \right) \tag{4.17}$$

where the unnormalised *Error function*

$$Erf(z) = \int_0^z e^{-t^2} dt \tag{4.18}$$

is identified in the last step. The normalisation factor N' is not used in what follows and will be neglected from now on.

To visualise the model, 750 data points are randomly sampled from a set of Gaussian distributions with $-1 \leq \mu \leq 1$ and $\sigma = 0.2$ and plotted in figure 4.20. These toy data are fitted with equation 4.17. The number of data points and the parameters of the distributions are representative for the real data samples used in this analysis.

From this toy study it is concluded that the target edges and vertex resolution can be extracted by a fit using equation 4.17, under the assumption that the reconstructed vertices are uniformly distributed over the target with Gaussian errors. This is the basis of the target model. It will be refined in the remainder of this section.

By splitting the PDF into two terms in Equation 4.17, the separation between the low and high edge of the target distribution can be more easily seen. In the case that the distance between x_{low} and x_{high} is sufficiently large while σ is sufficiently small, the two terms are effectively decoupled from each other when the PDF is fitted to a target distribution. This condition is fulfilled by the data in this analysis. As a consequence of this behaviour of the error function, a change of the resolution σ in the low edge term will leave the values of the high edge term from a fit largely unaffected. The constraint that the resolution is the same everywhere is dropped, and two separate edge resolutions,

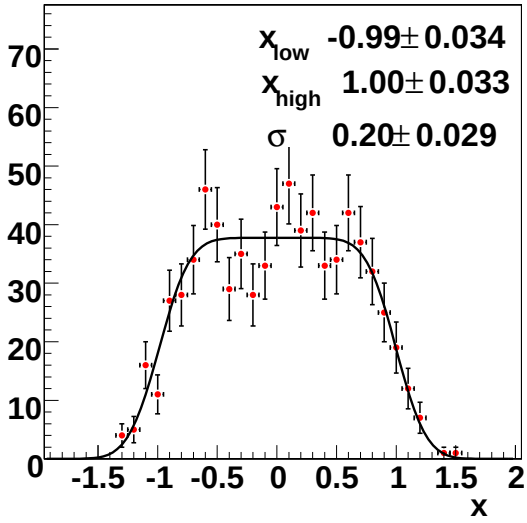

Figure 4.20: *Distributions of 750 data points randomly sampled from a set of Gaussian distributions with* $-1 \leq \mu \leq 1$ *and* $\sigma = 0.2$*. The line shows a fit to the data points using equation 4.17.*

σ_{low} and σ_{high} are introduced:

$$F\left(x, x_{low}, \sigma_{low}, x_{high}, \sigma_{high}\right) = Erf\left(\frac{x - x_{low}}{\sqrt{2}\sigma_{low}}\right) - Erf\left(\frac{x - x_{high}}{\sqrt{2}\sigma_{high}}\right). \tag{4.19}$$

Beam profile and varying vertex reconstruction efficiency

The final building block in the model is the component that accounts for beam profile variations, reconstruction efficiency, and target imperfections. The beam profile can be studied indirectly using vertices reconstructed in the vacuum vessel wall upstream of the detector. They are selected by their reconstructed z-position around $z = -375$ mm. Figure 4.21 shows the vertex distribution in x and y for the Outer HP4 dataset, when the beam was centred at $(x, y) = (15, 0)$.

While the y-profile of the beam looks like a smeared uniform distribution , the x-profile is asymmetric. As will be shown, the reason for this is that the profile is a convolution between a uniform distribution, and the geometrical acceptance functions of the detector and of the scintillator trigger. The experimental layout is such that all active sensor material is positioned at $x < 0$. This means that secondary particles from vertices at $x = 15$ mm are less likely to be in the acceptance of the detector than particles from a vertex at $x = 10$ mm for example. Less particles in the acceptance means less reconstructed tracks which leads to less observed vertices. In other words, the number of reconstructed vertices drops with increasing x. For y, this is not an issue, as the active sensor material is positioned symmetrically around $y = 0$.

Figure 4.22 shows a way to visualise the detector acceptance function and its connection to the beam x-profile. A simulated HP4 dataset with a uniform beam generated in the range $-2 \leq x \leq 25$ mm was used (the "Wide beam" dataset mentioned in table 4.2), together with the beam x-profiles of the Inner and Outer HP4 datasets. The x-distribution

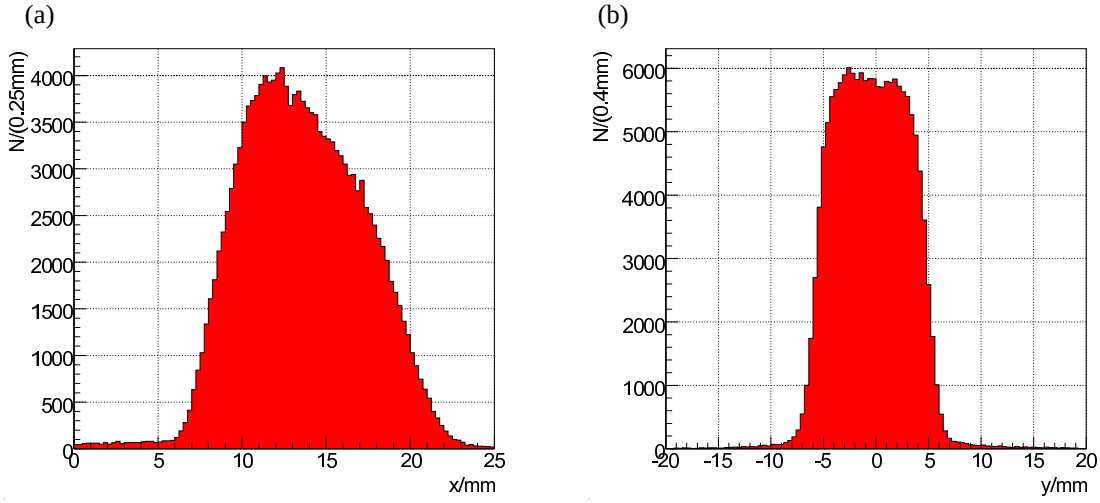

Figure 4.21: *Reconstructed vertices from interactions in the vacuum vessel in the Outer HP4 dataset. The x-distribution (a) is not symmetric, while the y-distribution (b) looks like a smeared uniform distribution.*

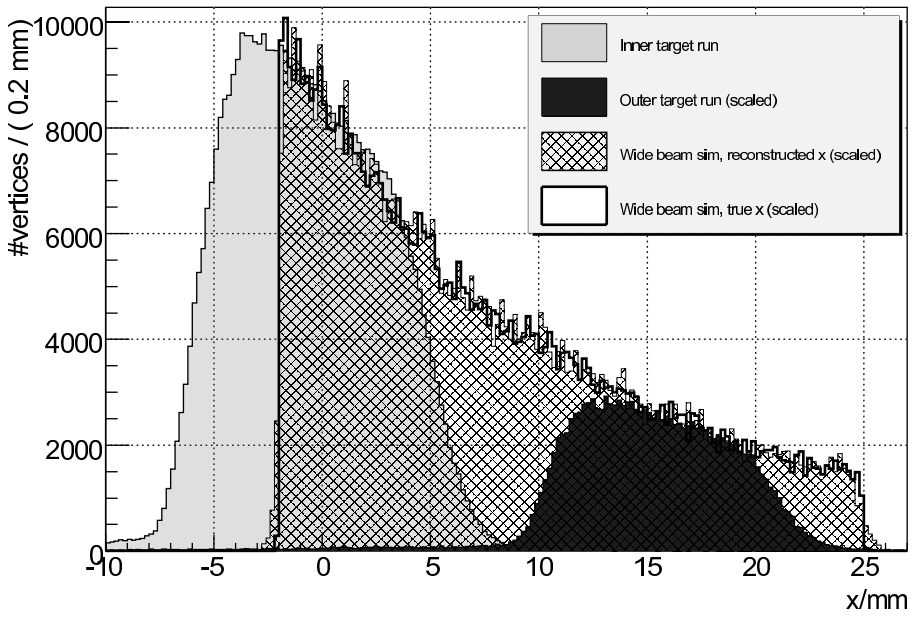

Figure 4.22: *An illustration of the geometrical acceptance function using the simulated "Wide beam" dataset. The x-position of the reconstructed vertices from interactions between a beam that is uniform is the region* $-2 \leq x \leq 25$mm *and the vacuum vessel is plotted (hatched fill pattern) together with the corresponding true x-positions (thick line, no fill). The vertices where selected with a z-cut. The reconstruction efficiency drops at higher x, leading to an exponential looking shape. Vertices from the vacuum vessel for the Inner HP4 (grey) and Outer HP4 (black) runs have been superimposed, and all the distributions have been rescaled relative to Inner HP4.*

of reconstructed vertices in the vacuum vessel from the uniformly generated beam is drawn with a hatched fill pattern. As is seen, the distribution is not uniform (as it was

generated), but drops exponentially with increasing x. To rule out that this is due to erroneous reconstruction, the true[12] x-position of the vertices is plotted (thick line, no fill) on top of the reconstructed distribution. Their overlap is almost total, meaning that there is no reconstruction effect. It is the geometrical acceptance function of the detector that causes the observed exponential distribution. On top of the simulated beam profile, the real HP4 Inner (grey) and Outer (black) vertex x-distributions are drawn. After rescaling, the real data clearly line up with the simulation, which indicates that their shape can be explained by the same effect; the geometrical acceptance function. The small discrepancy that remains between simulated and real data can be attributed to the fact that the real beam is not as perfectly uniform in x as the simulated one, and that the simulation does not include the acceptance of the scintillator trigger.

The composite target model

Even though the geometrical acceptance depends exponentially on the x-coordinate, it can be well approximated by a first order polynomial over the surface of the target. The target model (equation 4.19) is therefore modified by a linear component. It acts as a collective term which accounts for the beam profile, the geometrical acceptance (in the case of the x-dimension) as well as for the effects of target imperfections. The composite model for the distribution of the reconstructed vertices from interactions in a target becomes:

$$P = F\left(x, x_{low}, \sigma_{low}, x_{high}, \sigma_{high}\right) \times G\left(x, k, m\right) = \left[Erf\left(\frac{x - x_{low}}{\sqrt{2}\sigma_{low}}\right) - Erf\left(\frac{x - x_{high}}{\sqrt{2}\sigma_{high}}\right)\right] \cdot \left(kx + m\right). \tag{4.20}$$

and contains one observable (x), which comes from the data, and six free parameters of which two (k,m) are not of any interest for analysis of the target positions and vertex resolution. This PDF is used in the fits described in the following section.

4.9.3 Fitting procedure

The vertices for the one-dimensional slices of the targets are selected in two steps. In the case of an "x-slice"(see figure 4.19b), the procedure is as follows:

1. To estimate the centre of a target, fit a Gaussian function to the y-distribution of all vertices in a target and use the mean of the fit as the centre, y_c.

2. Select all vertices in the range $y_c \pm 0.15\,\text{mm}$ in the inner target datasets and $y_c \pm 0.5\,\text{mm}$ in the outer target datasets. The width of these slices have been chosen on the criteria that they have to be big enough to contain sufficiently many vertices, but small enough to suppress effects from the curved shape of the target edge. The large radius of the outer targets motivates the larger slice size than that of the inner targets.

The procedure is identical for a y-slice with the substitution $y \rightarrow x$.

In the next step, the dataset is fitted with equation 4.20 using the RooFit [97] package for ROOT [80], which in turn uses Minuit [82] for the function minimisation. The fit is

[12] The "true" position is the vertex position from the Monte Carlo information.

done using the unbinned maximum likelihood (ML) method in which for a given PDF $P(x, \vec{p})$ and data points x_i the Likelihood function

$$L(\vec{p}) = \prod_i P(x_i, \vec{p}) \tag{4.21}$$

is maximised (or equivalently: $-log(L(\vec{p}))$ is minimised) with respect to the parameters $\vec{p} = (x_{low}, \sigma_{low}, x_{high}, \sigma_{high}, k, m)$. The PDF is automatically normalised by RooFit.

The advantage of the unbinned ML-fit over the more common χ^2 -fit is that it can be applied for distributions with low statistics while avoiding biased fit parameters. The main disadvantage of the ML-method is that it does not provide a straightforward goodness-of-fit measure.

The slices from Inner target 2, HP2 (figure 4.19b) together with the fitted functions are shown in figure 4.23. The full collection of target slices with their respective fits can be found in Appendix E. The centre of the target is inferred from the arithmetic mean of x_{low} and x_{high} with the error

$$\delta_{centre} = \sqrt{\frac{\delta_{low}^2 + \delta_{high}^2}{2}} \tag{4.22}$$

where δ_{low} and δ_{high} are the errors on x_{low} and x_{high} from the fit.

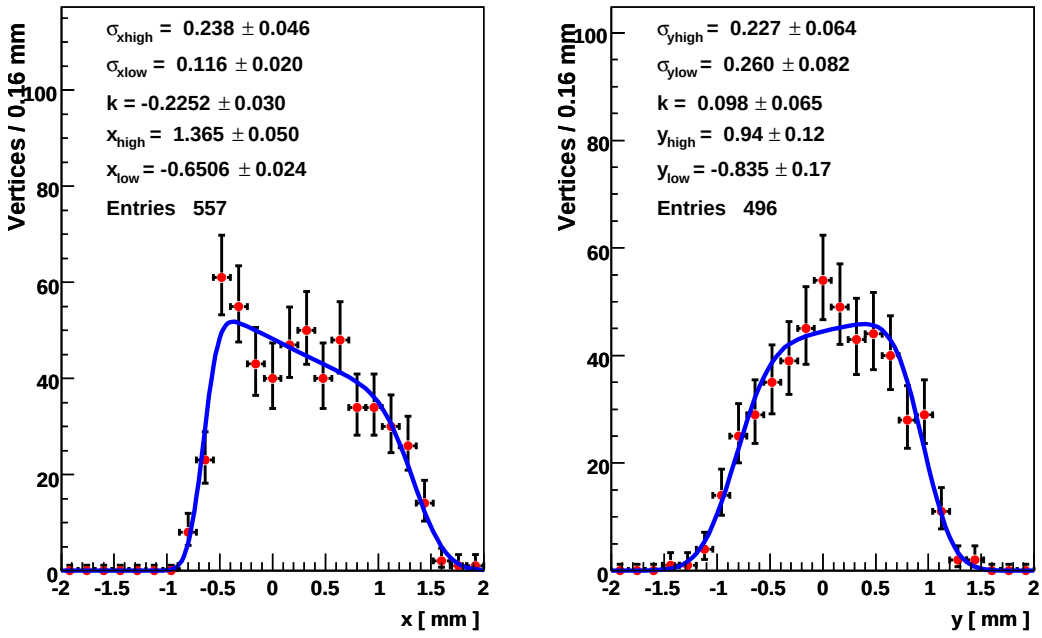

Figure 4.23: *The central x- and y-slices from the xy-distribution of Inner target 2 HP2, with the results of the fit.*

4.9.4 Fit validity and sensitivity

To validate the fit method, 250 toy distributions with 750 vertices each are generated according to equation 4.20 with $x_{low} = -1$, $x_{high} = 1$, $\sigma_{high} = \sigma_{low} = 0.2$, $k = 0$ and $m = 1$. The edge and resolution parameters are chosen to mimic the distributions of reconstructed vertices from an inner target with 1 mm radius and 0.2 mm vertex resolution, e.g. see Fig 4.23. Each of the 250 distributions is fitted with equation 4.20 using an unbinned ML-fit. From the 250 fits, two pull distributions are formed. The parameters of the low edge (x_{low}, σ_{low}) are chosen to represent the edge and resolution parameters x_{edge} and σ and the pulls are defined as

$$Pull_{edge} = \frac{x_{edge} - x_{true}}{\delta_{edge}} \tag{4.23}$$

$$Pull_{\sigma} = \frac{\sigma - \sigma_{true}}{\delta_{sigma}} \tag{4.24}$$

where $x_{true} = -1$ and $\sigma_{true} = 0.2$ are the values from the generation of the toy distributions and δ_{edge} and δ_{sigma} are the errors from the fits. The pull distributions are then fitted with Gaussian functions. If the target model fits are unbiased and have correct fit errors, the pull distributions should have a mean of 0 and an RMS of 1. Figures 4.24a and b show the pull distributions.

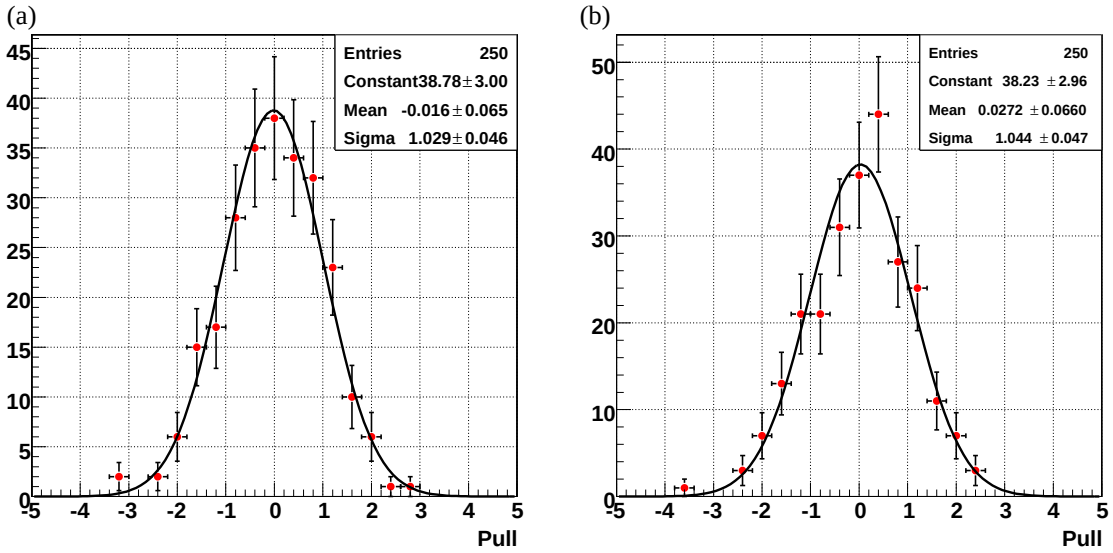

Figure 4.24: *Pull distributions from a toy study of the target model for the edge (a) and resolution (b) parameters.*

For both parameters, the mean and RMS fulfil these requirements, demonstrating the validity of the model.

The sensitivity of the fit at different sample sizes (number of vertices) is assessed by studying the Gaussian RMS of the distributions of fitted parameters while varying the sample size. This is done by generating 250 distributions with 250, 500, 1000, 1500 and 2000 data points each.

For each sample size, the distributions of the fitted values of the edge and resolution parameters (x_{edge} and σ) are formed. These distributions are fitted with Gaussian functions, and their RMS is plotted versus the sample size. The result is figure 4.25. The

RMS gives an estimate of how well the target fit corresponds to the true value for a given number of vertices. A low RMS indicates a high fit sensitivity. The sensitivity scales proportionally to $1/\sqrt{N_{vertices}}$ With an average sample size of 500 vertices in the real data used in this analysis the sensitivity is 45 μm for the edge parameters and 35 μm for the resolution parameters. These values indicate the intrinsic uncertainty of the fit method.

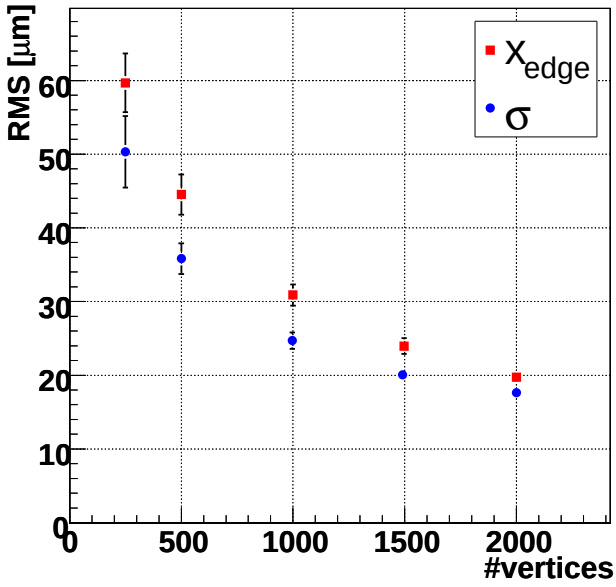

Figure 4.25: *The sensitivity of the edge (x_{edge}) and resolution (σ) parameters for various sample sizes. The spread (RMS) of the fitted parameter values from 250 fits is interpreted as the sensitivity.*

4.9.5 Internal consistency

The two major subsets of collected data are the HP2 and HP4 datasets. As they were obtained with some days difference (during which the experimental setup was moved at several occasions) and with a different set of modules, a comparison between the two is well-suited for a check of the internal consistency of the measurements, reconstruction and fitting model. Figure 4.26 shows the difference of the fitted edge values between HP2 and HP4.

Due to lack of sufficient statistics, no comparison could be made for the outer targets and inner target 4. Both the x and y measurements are consistent within errors with no difference between HP2 and HP4. This demonstrates the reproducibility of the experiment and shows the internal consistency between separate datasets.

Figure 4.27 shows the fitted edges of the targets in x and y for HP4 data versus HP2 data. The diagonal line indicates the points where HP2 = HP4 (i.e. a perfect correlation). As can be seen, the data points deviate somewhat from the design values of target positions and size, which should give data points at $(x, y) = (-1, -1)$ and $(x, y) = (1, 1)$. As will be shown in section 4.9.7, this is not because the reconstructed target positions are wrong. On the contrary, figure 4.27 shows the actual deviations from the design values.

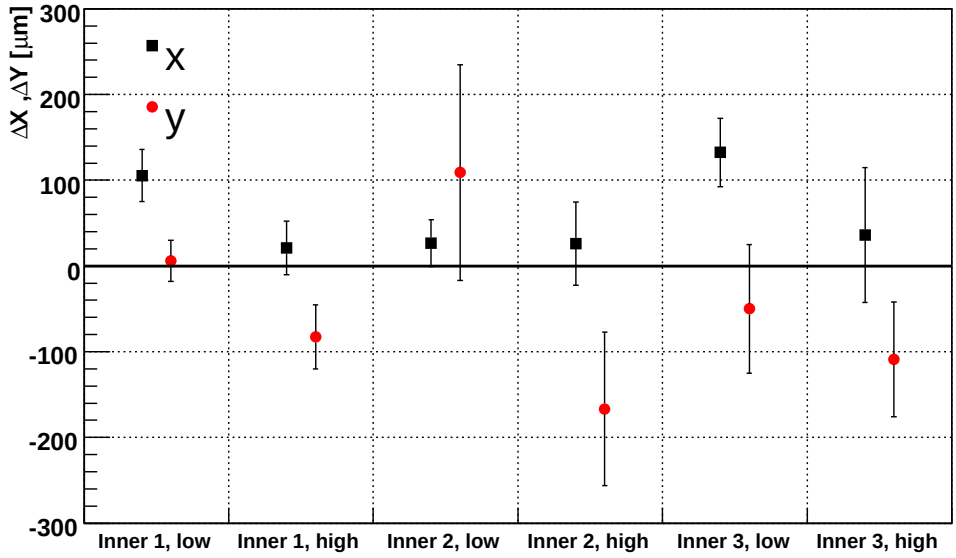

Figure 4.26: *Difference of the fitted values of the target edges between the HP2 and HP4 datasets. The error bars show the errors of the HP2 and HP4 measurements added in quadrature.*

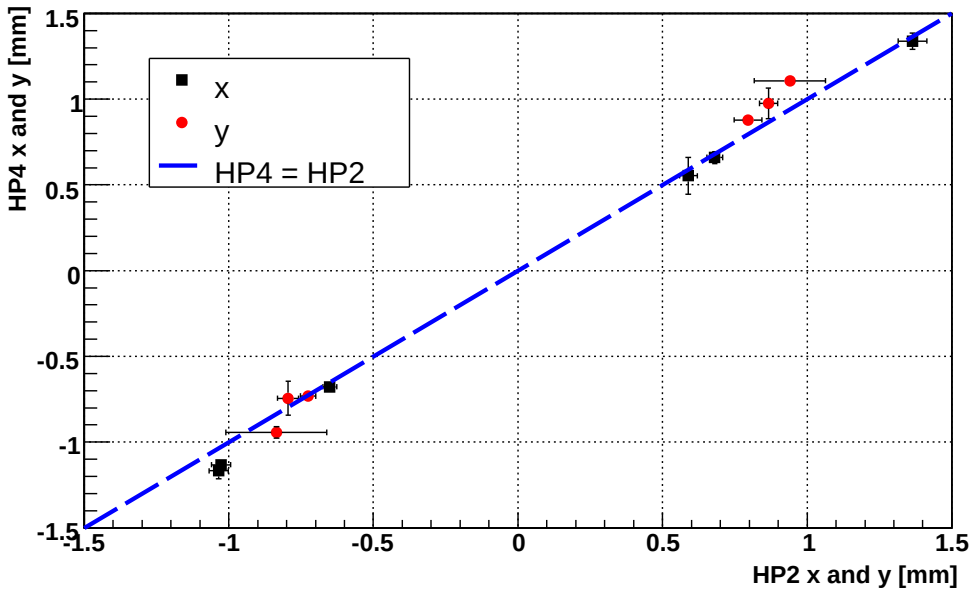

Figure 4.27: *Fitted values to the reconstructed target edge positions for HP4 (y-axis) and HP2 (x-axis). The error bars correspond to the errors of the fitted values. Only the inner targets 1, 2 and 3 are included.*

4.9.6 Comparison with simulation

To compare the vertex resolutions between data and simulation the values σ_{low} and σ_{high} from the fits are used. In figure 4.28, the correlation between simulation and data are

plotted for x and y, together with the line of perfect correlation at $\sigma_{data} = \sigma_{sim}$. The error bars show the errors from the fits.

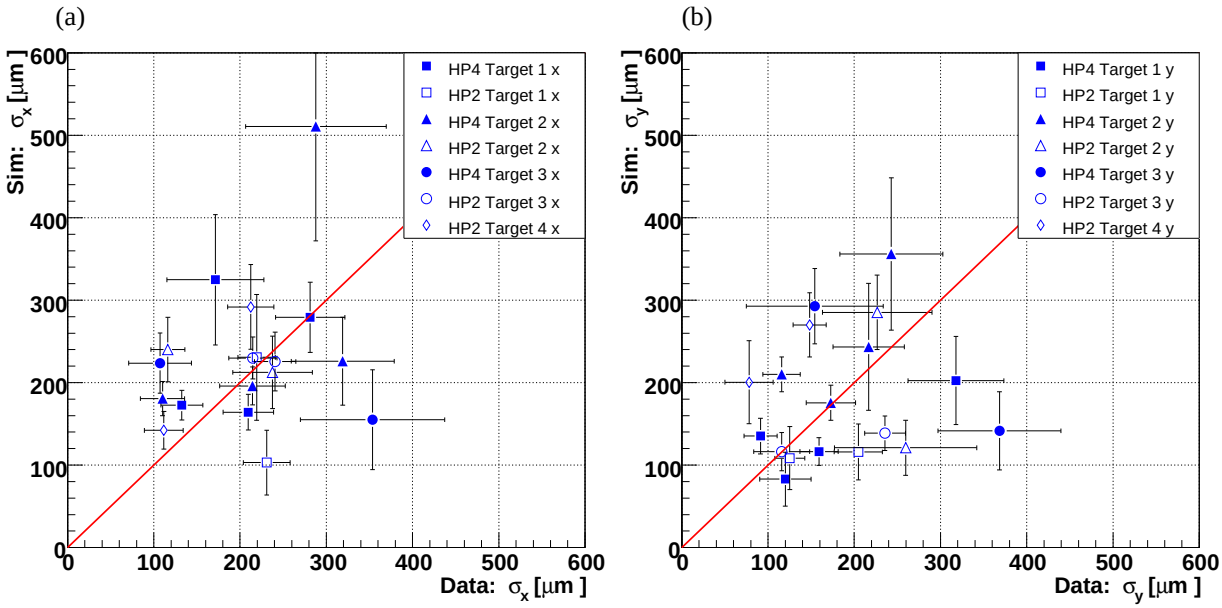

Figure 4.28: *Fitted resolutions ($\sigma_{low}, \sigma_{high}$) of x (a) and y (b), simulation versus data. Data points from inner and outer targets at the same z-position and cable configuration are drawn with the same marker type.*

The bulk of the resolution measurements from the data are in the range 100 μm−300 μm for both x and y.

It is observed that the distribution of values from data and simulation does not show strong correlation. Only 33% of the x points and 28% of the y points are within 1 σ from complete agreement. With the small sample sizes in the data the sensitivity is too low to allow for precise statements about the agreement between data and simulation. By studying the pull distributions of the data points, where the pull has been defined to be

$$pull = \frac{\sigma_{data} - \sigma_{sim}}{\sqrt{\delta^2_{data} + \delta^2_{sim}}} \tag{4.25}$$

for the x and y resolutions (figure 4.29) one sees that the distribution is centred around 0 and the Gaussian fits to the data do not indicate a significant bias in either direction, for neither x nor y. The fact that the RMS of the distributions are both larger than 1 suggests that the target model underestimates the errors.

4.9.7 Comparison with metrology

The target positions were determined in an optical survey by the CERN metrology laboratory. The base plate correction discussed in section 4.3 was applied. Furthermore, the error of the metrology measurement is estimated to be 109 μm (section 4.3). Figure 4.30 shows the difference in x and y between the true positions of the target centres and those inferred from the fits. The true position is defined as the metrology measurement for the

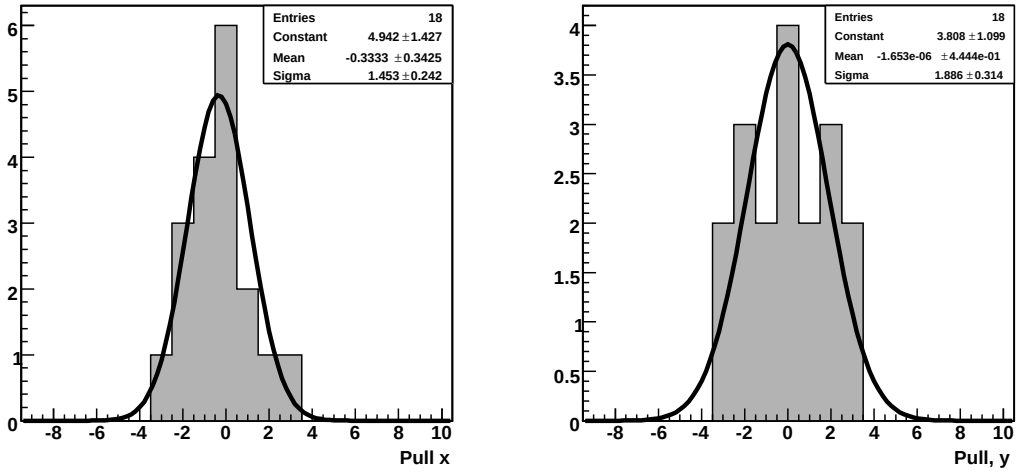

Figure 4.29: *Pull distribution of the data points (x left, y right) in figure 4.28, with Gaussian fit.*

real data and as the generated target position for the simulated data. For the real data points, the estimated metrology uncertainty is included as a grey error band.

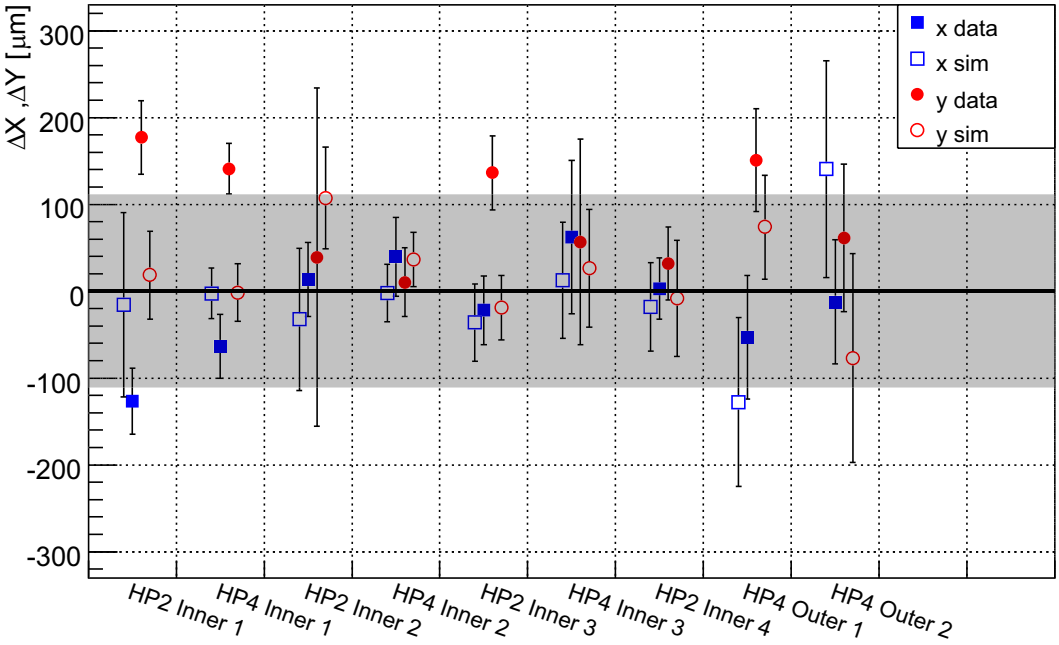

Figure 4.30: *Difference between metrology measurement (or simulated position) and fitted target edge position, for all available real and simulated data. The grey error band is the estimated metrology error.*

Table 4.6 shows the deviations from perfect agreement for the four sets of data points. The simulated values are not significantly different from 0. From this the general conclu-

Table 4.6: *Weighted average of the deviations from the metrology measurement/simulated value. The estimated contribution of the metrology error is included for the real data.*

Dataset	*Weighted average [μm]*
Data Δx	-27.8±15.1 ±109
Data Δy	104.8±15.8 ±109
Sim Δx	-10.4±16.6
Sim Δy	19.5±15.6

sion can be drawn that the vertex reconstruction and target fitting procedures reproduces the true position on average rather well. For the real data x is negatively biased and y is positively biased. However, neither of these deviations are significantly different from 0, due to the large errors on the metrology measurement.

The base plate correction was made under the assumption that the mock-up base used for the target metrology is perfectly flat. As this was never measured it leaves a potential source of systematic errors.

4.9.8 Target analysis conclusion

The internal consistency and reproducibility between different datasets as demonstrated in section 4.9.5 gives confidence that the method used is valid. The outcome of the comparison between data and simulation in section 4.9.6 shows no clear indication that simulation is doing better or worse than "reality" for tracks in the energy region around a few hundred MeV within the sizeable uncertainties in the measured vertex resolution. It should however be noted that the agreement between data and simulation is modest. It is difficult to assess the importance of this result due to the limited sensitivity of the target fit for the sizes of the data samples. The measured vertex resolutions are measured to be in the range 100 μm−300 μm in x in y. Due to big differences in effects of multiple scattering in the sensors expected from the high momentum tracks in the LHC as well as differences in the detector setup[13], the study can not be used directly to predict the performance of the VELO at LHC energies..

As was demonstrated in section 4.9.7 the reconstructed target centres from simulation are in agreement with the "true" values, showing that the vertex reconstruction gives the correct results. For real data, discrepancies from metrology are observed but they are within the experimental errors of the setup. A great source of uncertainty is the bad quality of the targets. Their uneven edges and non-circular shapes made it difficult to obtain precise metrology measurements. Without the well-defined points of reference from metrology, it is hard to draw firm conclusions. Particularly the discrepancy observed for the vertex y-measurement indicates a potential bias, but it is not in the power of this analysis to make a statistically significant statement about that. For that reason it is recommended that the vertex reconstruction performance is investigated further during the commissioning of the detector with the LHC beams.

[13]Mainly the absence of the RF-foil in the ACDC3 setup.

4.10 Summary

The ACDC3 test beam experiment achieved its goals. A partial detector half was commissioned successfully in a charged particle beam from the SPS using mostly final components, and nearly 90 million events were collected. The functionality and readiness of the alignment procedure [74] was tested extensively with the collected beam data [57] and used in the data analyses.

This chapter has presented three analyses based on the ACDC3 data: a S/N study, a single hit resolution study and a vertex performance study.

The S/N of the sensors was shown to be in the range $21.4 - 23.9$ for R-sensors and $23.9 - 29.5$ for the Φ-sensors. This is in good agreement with measurements of the S/N of prototype VELO sensors, and better than the requirements. The good sensor performance provides the possibility to optimise the Beetle sampling time such that the pulse pre-spill and spill-over are minimised.

The single hit resolution for particles with 0° incidence angle was shown to be in the range $8.5\,\mu$m$-21.5\,\mu$m for an R-sensor in the pitch range $40\,\mu$m$-90\,\mu$m. The resolution can be expressed as a function of the strip pitch by $8.5 + 0.26 \times (pitch - 40)\,\mu$m.

In the vertex performance study the beam was aimed at a set of lead targets rendering tracks from secondary particles through the detector. These tracks were combined into vertices and studied. By developing a model for the target distributions, the edges of the targets and the vertex precision could be successfully extracted from the data. The reconstructed edges agree with the metrology measurements within errors. The precision of the analysis was set by the low statistics, the effects of multiple scattering due to low momentum tracks, and the uncertainty in the metrology measurements caused by the uneven edges of the targets. The resolution, which is expected to be considerably worse than for the LHC conditions, was measured to be in the range $100 - 300\,\mu$m for x and y.

5 Commissioning of the VELO detector

After the ACDC3 beam test the detector was transported back to the assembly lab at the CERN Meyrin site. The remaining 32 VELO-modules were installed and their performance integrity verified through an examination of the value of their leakage currents, the amplitude of the noise levels and the frequency of dead strip occurrence. The fully assembled detector halves were surveyed at the CERN metrology laboratory and transported to the experimental site for installation in the VELO-vessel and subsequent commissioning. In parallel with the assembly process, other parts of the VELO detector, as for example the vacuum, motion and cooling systems and electronics chain were installed and commissioned in their final positions around interaction point 8 of the LHC.

This chapter covers the commissioning of the DAQ system and the sensors. The software tools used are presented in section 5.1. In section 5.2 the various DAQ tests are reported. The remainder of the chapter is devoted to the noise performance of the sensors (section 5.3) and the reconstruction of first tracks from an LHC beam seen by the VELO (section 5.4).

5.1 Test tools

A common set of analysis tools was employed during the DAQ and sensor commissioning. The collected test data were first processed with dedicated software algorithms executed from the Vetra program, and later analysed with the ROOT package. These tools are described here.

5.1.1 Sensor snapshot

The study of the pedestal and noise spectra of a sensor is a convenient way of finding problems with the sensor or somewhere along the readout and control chain. In the so-called "sensor snapshot", a low-level analysis tool, the pedestal and noise spectra are visualised for interpretation and checking.

The noise is calculated using the monitoring software package, *VeloDataMonitor*, in which the noise is defined as the RMS value of the distribution of ADC values of a given channel. In the commissioning 6000 values per channel were used. To allow for the study of non-zero-suppressed (NZS) data before and after common mode correction (CMC), the TELL1 emulator is used. The emulator performs pedestal subtraction, channel reordering and the linear CMC. See section 2.5.1 for details. In the noise studies, the first channel of each link of 32 channels is suppressed to remove the contribution from header cross-talk (for an example of header cross-talk, see figure 2.10). As unit of noise, ADC counts are used. The equivalent noise charge of one ADC count varies slightly between modules due to gain differences; a typical value for the most probable energy deposition of a MIP is 50 ADC counts (see beam test results, section 4.7) corresponding to an expected 22000

induced electron-hole pairs (section 2.1). The conversion factor can be estimated to be 440 electrons per ADC count.

5.1.2 The cable test

Each silicon sensor is read out with four data cables. An automated procedure is used to test the cables and their connections to the TELL1 and repeater boards. In this test procedure a special bit pattern is encoded in the analogue links using the test pulse of the Beetle chip. By splitting each link of 32 channels into blocks of eight channels, four 8-bit numbers can be stored. The four 8-bit numbers are used to store two copies of the link number and hybrid serial number. The redundancy measure of storing the numbers in two copies makes the test more robust against noisy or dead channels. For further robustness, the link number is encoded as $2 \times (link + 1)$. The addition of 1 ensures that link 0 also has a test pulse pattern, and the multiplication by 2 removes the influence of header cross-talk by not using the first channel of the link.

After taking data with the bit patterns present, the 8-bit numbers of each link are decoded. If the decoded link and hybrid numbers are not in agreement with the number of the link and hybrid that they are decoded from, there is an error in the cabling. Figure 5.1 shows a correlation plot between the read out link (the link number that the analysis software thinks it is reading out) and the encoded link number, for a wrongly cabled and a properly cabled case.

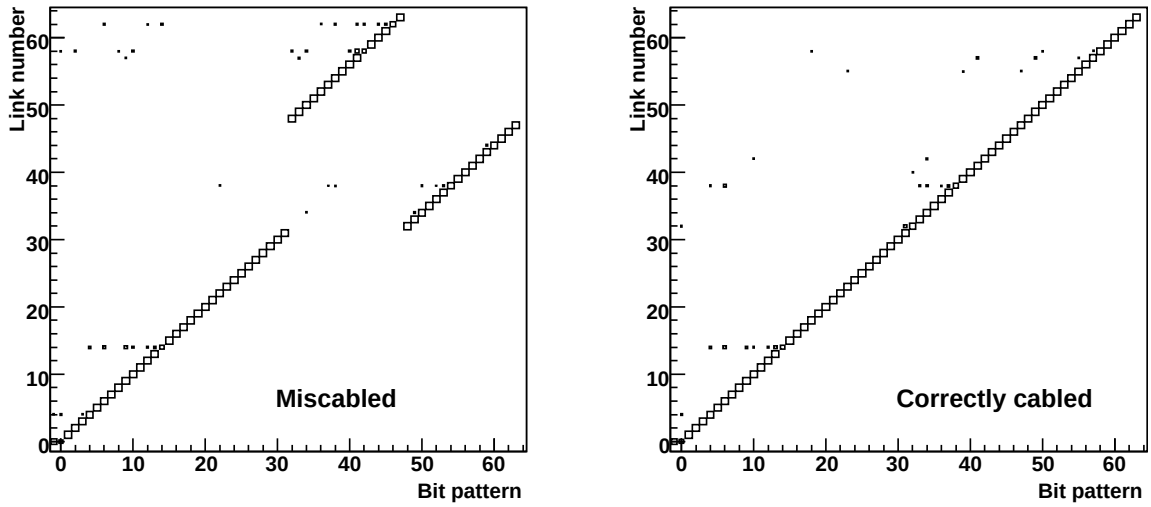

Figure 5.1: *Typical correlation plots from the cable test, for a wrongly cabled (left) and properly cabled (right) TELL1. In the wrongly cabled TELL1 case, the cables that read out links 32-47 and 48-63 have been swapped, which causes the pattern that can be seen in the plot. The outliers from the main band are a consequence of the noise in the system, which sometimes causes errors when decoding the bit pattern.*

5.1.3 ADC digitisation delay scan

There are several delay circuits on the Control and TELL1 boards that can be used to adjust the sampling points in the Beetle FE-chips and ADC cards, and to time-align the readout of the VELO with respect to the LHC clock. The pulse height of the channels in one link are transmitted serially from the detector to a TELL1, with 25 ns time spacing between the channels. A delay on the TELL1 controls the ADC digitisation point in time: it can be changed in coarse steps of clock cycles (25 ns) and fine steps, phases, of 1/16th of a clock cycle.

For an (approximately) box shaped signal, the sampling is optimally done at a point well separated from the rising and falling edges. To find the delay settings that fulfill this condition, a test pulse is injected into a given channel for the 16 possible phase settings, and the pulse height is determined at each setting. The pulse height is plotted as a function of ADC digitisation delay in figure 5.2. An automated analysis procedure is used to determine a suitable sampling point, indicated by the dashed line in the figure.

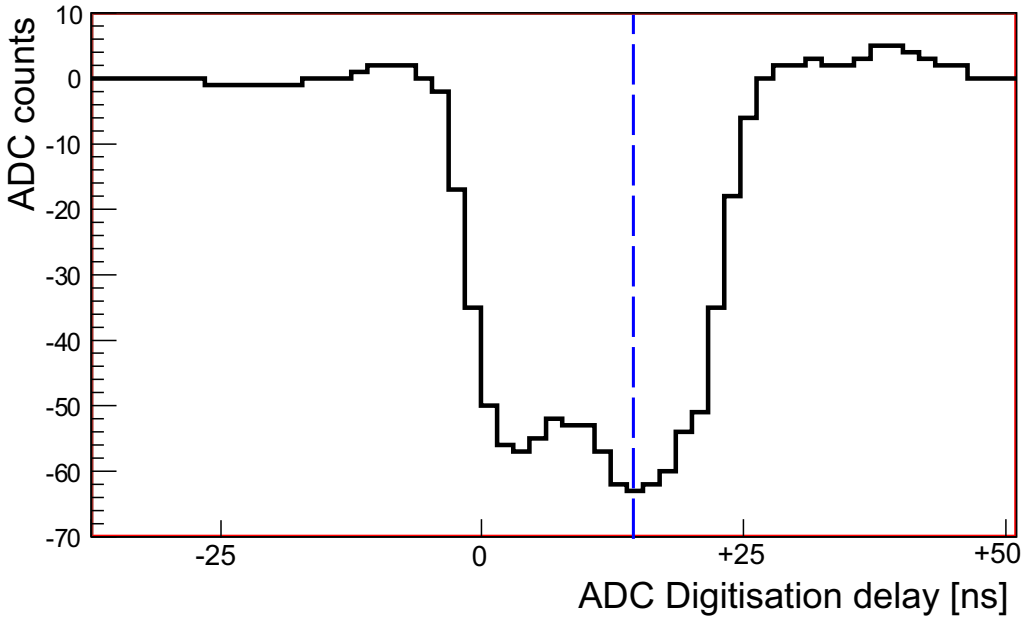

Figure 5.2: *Example of a ADC digitisation delay scan on a channel in TELL1 201, link 64 for a test pulse of negative polarity. The dashed line shows a suitable sampling point as determined from an automated analysis. The x-axis indicates different delay settings.*

It is possible to tune the ADC digitisation cycle and phase of the analogue links individually, but as the main source of difference between the signal shapes can be attributed to differences in data cable length, the same settings can be applied for all links sharing a data cable.

5.2 DAQ commissioning

The VELO data acquisition system (see section 2.5) is complex as it contains many interacting components. During commissioning, problems were encountered in hardware (TELL1s, control boards, ARx cards, etc), firmware (running on the TELL1 FPGAs),

and the PVSS experimental control software. The tests described in this section were designed to locate hardware problems, but they also uncovered bugs in the firmware as well as in the software.

5.2.1 ARx card test

As a first step, the ARx cards of the TELL1 boards were thoroughly tested. A 1 MHz sine wave with an amplitude close to the full dynamic range of the ADCs was injected into each link of the ARx cards. With a period of 1 μs, it almost matches the total time of the pulse train containing the header and channel information of a given link (4 header bits and 32 channels sent with 25 ns give a pulse train length of 900 ns). The result is a digitised sine wave that almost extends over a full link (see figure 5.3). By comparing the data and a sine function fitted to it, several malfunctioning ARx cards were found and subsequently repaired. A full report can be found elsewhere [98].

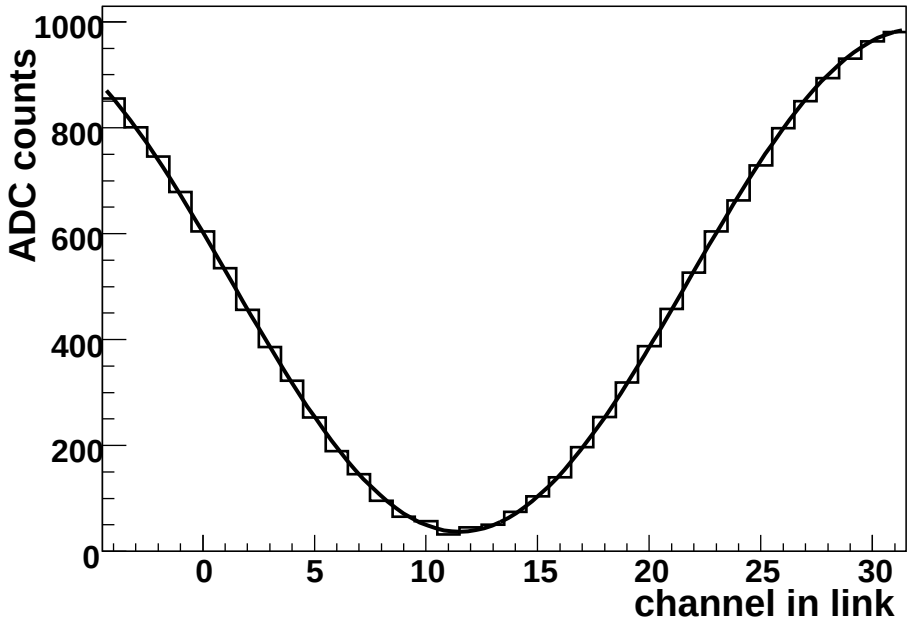

Figure 5.3: *An example of a digitised sine wave from the ARx card test. The x-axis shows a full analogue link (32 channels) and its preceding four header bits.*

5.2.2 The TELL1 uniformity test

In the test of the full readout chain, the uniform behaviour of the TELL1 boards was investigated using a test setup consisting of a dummy module, a repeater board, a control board and a set of one control and four data cables[1]. The dummy module had a fully populated hybrid but no silicon sensor. The main purpose of the test was:

- to find problematic TELL1s.

[1] Control board 9, control cable 1878, data cables 1740, 1741, 1742, 1743.

- to investigate differences in noise contribution between the ARx cards. Using the same module and data cables for all TELL1s, a large difference in noise between two TELL1s can be attributed to the ARx cards.

- to compare the pedestal levels of the ARx cards. Large deviations from 512 ADC counts (the half value in the range of the 10-bit ADC) reduce the available dynamic range.

Out of the 84 VELO TELL1 boards that were included in the uniformity test, 67 could be read out correctly. The remaining 17, about 20% of the boards, had various problems that prevented data taking and were repaired later. It was found that some of the boards had a problem with the vias[2] which caused them to behave unstably or break when thermally cycled.

The test setup was connected to each TELL1 board and 10000 noise events were recorded. The first 4000 events were used for the pedestal calculation and the remaining 6000 for the noise calculation. As the relative RMS error, $\delta(\mathrm{RMS})/\mathrm{RMS}$, of the noise can be approximated with $1/\sqrt{2N}$ [13], this renders a precision of 1%, which typically corresponds to 0.02 ADC counts for a VELO sensor. Since the same dummy module and cables were used all of the time, any variations between measurements should come from the TELL1 itself, especially from the ARx cards. To spot variations, a reference TELL1 was used for comparison. In practise, five reference TELL1s were used, one for each of the five crates that hold the TELL1s in the counting house.

Examples of two raw noise spectra can be seen in figure 5.4, for a good TELL1, and one with problematic links. The plots show the noise of the TELL1 under test, the noise of the reference TELL1, and the difference between the two. For all well-behaving channels the difference is close to 0. This means that the differences in noise contribution between ARx cards are minute. The total raw noise contribution is typically in the range 1.5-1.6 ADC counts.

To compare the pedestal variations, the pedestal values of each channel in the tested TELL1s are plotted in figure 5.5. As can be seen, the distribution of pedestal values is narrow (6.5 ADC counts in RMS) compared to the full dynamic range of the ADCs (1024 ADC counts). Out of the 135168 channels tested, 720 entries (0.5%) are in the over- and underflow bins. They belong to channels read out with problematic ARx cards. With the results from this uniformity test, these problems were spotted and subsequently corrected.

5.2.3 Control board uniformity test

The TELL1 uniformity test was followed by a similar investigation of the uniformity of the control boards. The test setup used the same dummy module, repeater board and cables as the TELL1 uniformity test, and a fixed TELL1 (#162). Noise data and test pulse data were recorded with the 84 ports[3] of the 14 control boards. The results of this test, which showed a good uniformity and no hardware problems, have been reported elsewhere [99].

[2] Through-connections between different layers of the TELL1 printed circuit board.
[3] One port per VELO sensor.

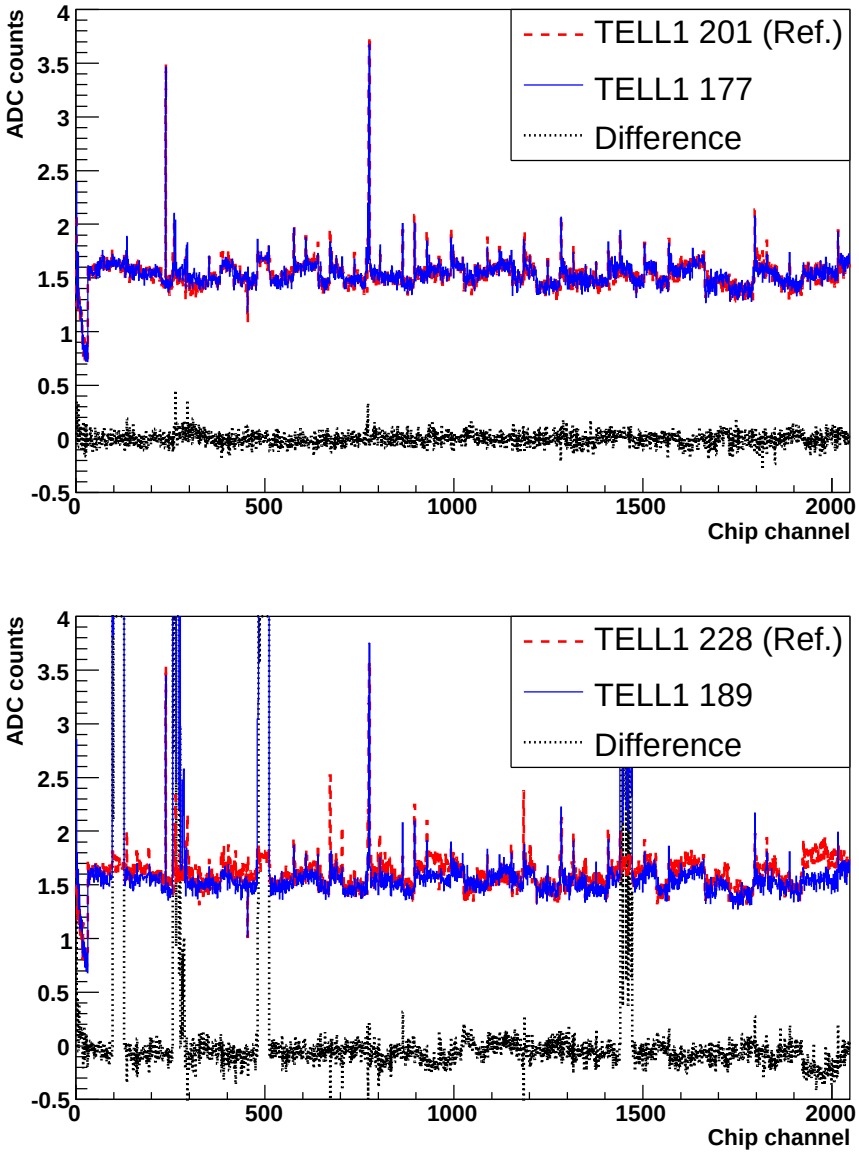

Figure 5.4: *Raw noise spectra for a good (top) and a problematic TELL1 (bottom). A reference spectrum (dashed) is subtracted from the noise spectrum (solid) and any problems can be spotted in the resulting curve (dotted).*

5.2.4 The slice test

The final test was the slice test. The expression *slice* refers to the full readout chain of one sensor, i.e. a "slice of the DAQ". With the dummy module and repeater board connected to each of the TELL1 and control board ports, the integrity of each slice was evaluated.

The test components were:

1. Adjust the timing by performing an ADC digitisation delay scan.
2. Perform the cable test to find wrongly connected or mislabelled cables.
3. Take a "sensor snapshot", i.e. collect data with and without test pulses to study

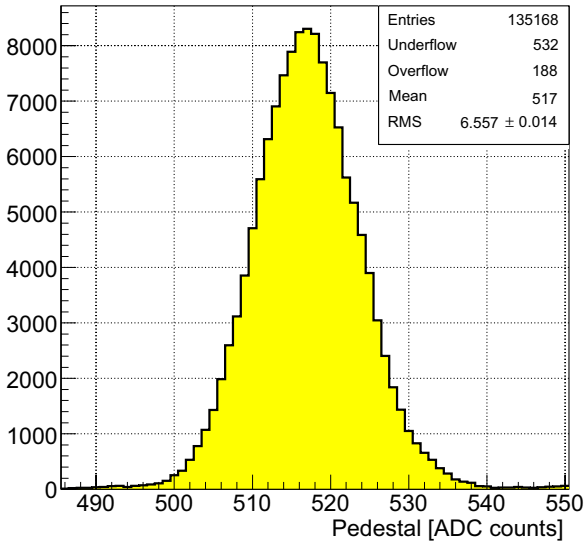

Figure 5.5: *Pedestal values of all channels of all TELL1s under test.*

the noise and pedestals.

In the test, a total of 64 slices out of 84 showed no problems (fig. 5.6). Out of the other slices, 7 were found to have problematic links. This was traced to problems with ARx cards, data cables or control cables. The remaining 13 slices could not be tested for various reasons, mainly due to TELL1 hardware problems. Some of these problems could be traced to an error related to the TELL1 front-end emulator [100]. The faulty TELL1s were sent for repair and replaced with spares.

5.3 Sensor commissioning

While validating the readout and controls system in the slice test, the low and high voltage systems had been fully installed and commissioned. The detector had reached a readiness such that tests could be performed with real modules, including the cooling and vacuum systems. Initially, a single module (M36) was powered up. This was the first time a module was powered after the transport from the assembly lab to the LHCb pit. With the VELO vessel filled with ultra-pure neon, the module was kept at a temperature of 27°C at the silicon[4]. The performance integrity of the module was evaluated and found to be good by comparing the I-V behaviour and noise spectrum with the measurements made in the assembly lab about a year earlier. The CMC noise spectra of the sensors of module M36 before and after power-up are shown in figure 5.7. The noise of the unbiased sensors is considerably higher. As the noise depends on the capacitive load of the detector on the Beetle chip, this observation is explained by a change of strip capacitance; the width of the depletion zone in an unbiased sensor is smaller than the that of a depleted (biased) sensor, and hence the capacitance of the unbiased sensor is higher, making it noisier. The increasing trend of noise versus strip number seen in figure 5.7a is explained by the linear

[4]Equivalent to a set-point of 8°C on the cooling system.

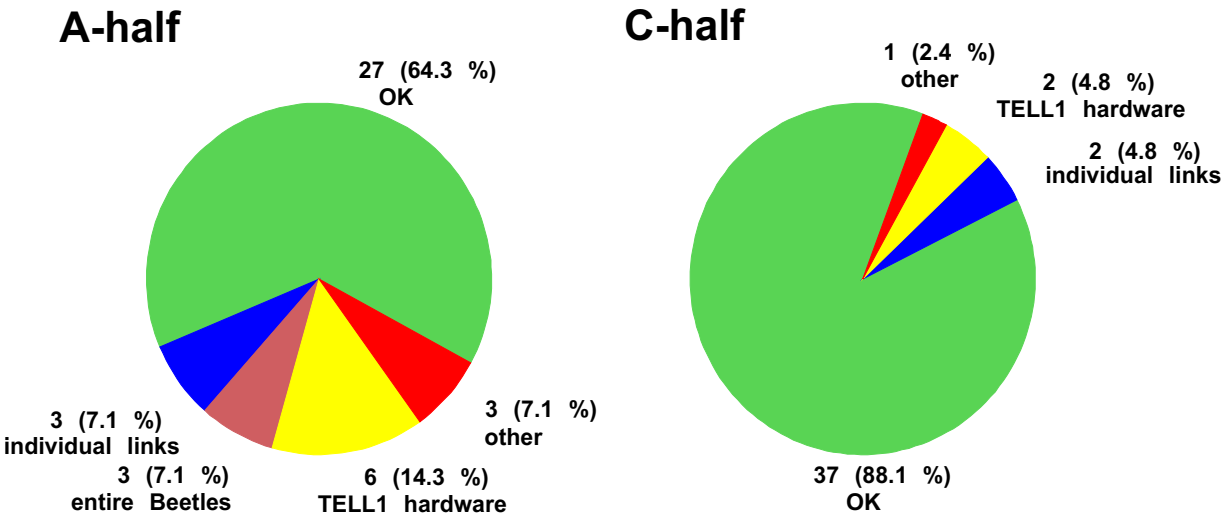

Figure 5.6: *A breakdown of the results from the slice test at the end of March 2008. The faulty TELL1s were replaced with spares and sent for repair. The label "other" includes problems with Beetle configuration (1 slice), TELL1s that cannot see triggers (1 slice), and PVSS communication problems (2 slices).*

dependence between capacitance and strip length; long strips at high radius have higher capacitance than short strips at low radius. An R-sensor has four sectors of 512 strips each, in which the strip radius increases with strip number. For the biased sensors the capacitive load of the strips is lower. This weakens the dependence between noise level and strip length.

Following the successful single module power-up, the remaining sensors with functioning TELL1s boards were powered individually and evaluated with I-V and noise measurements. In the next step the detector volume was evacuated to a pressure of 10^{-5} mbar, the sensors were cooled to a temperature of 14°C [5] and all modules of the detector were powered up simultaneously. The VELO was operated under these conditions over a period of two weeks, during which further tests took place. During one of these tests, all modules of the detector were read out simultaneously for the first time. The remainder of this section contains studies of the noise performance of the sensors using the data collected both during the operation in neon atmosphere and with the detector under vacuum. The difference in temperature conditions between these two data runs is not expected to cause any significant difference in noise levels.

[5] Equivalent to a set-point of −5°C on the cooling system.

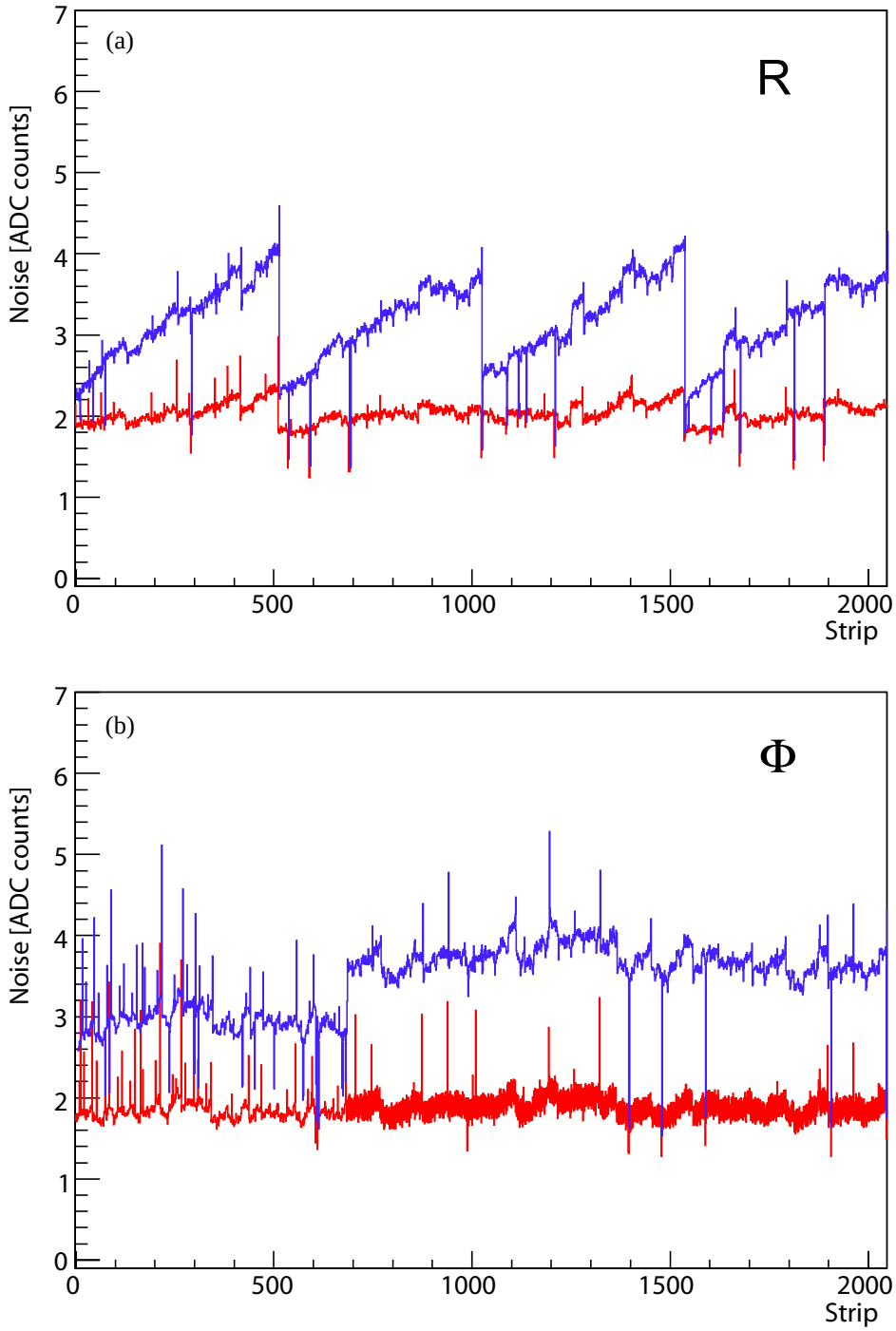

Figure 5.7: *The CMC noise spectrum of the first module (M36) to be powered after the installation of the VELO in the LHCb pit, R-sensor (top) and Φ-sensor (bottom). The upper curve of each plot shows the noise of the unbiased sensor and the lower curve shows the noise after a reverse bias voltage of 100 V was applied.*

5.3.1 Noise performance

To investigate the noise performance of the VELO sensors, non-zero suppressed data[6] from 80 sensors (40 R, 40 Φ) were collected. Four VELO sensors could not be read out due to TELL1 problems. The pressure in the detector was 10^{-5} mbar, the sensor bias was 100 V and the silicon temperature was 14°C. As in the uniformity and slice tests, the first 4000 events are used to calculate the pedestals, and the following 6000 events to calculate the noise.

The average (arithmetic mean) CMC noise of the strips in a sensor is calculated and presented for each detector slot in figures 5.8 (R) and 5.9 (Φ). Appendix B shows the positions of the slots in the detector. The error bars represent the RMS of the noise distribution for each sensor. The vertical thick line indicates the average noise. As usual, the first channel of each analogue link is removed from the calculation to avoid the cross-talk contamination from the header (see section 2.5.1). Channels that are considered noisy or have unphysical values (due to bad links, bad Beetles, etc.) are excluded; a noise criterion of $1.2 < \text{noise} < 2.8$ ADC counts yields 1.26% rejected channels.

[6] Run 26834, 15/07/2008.

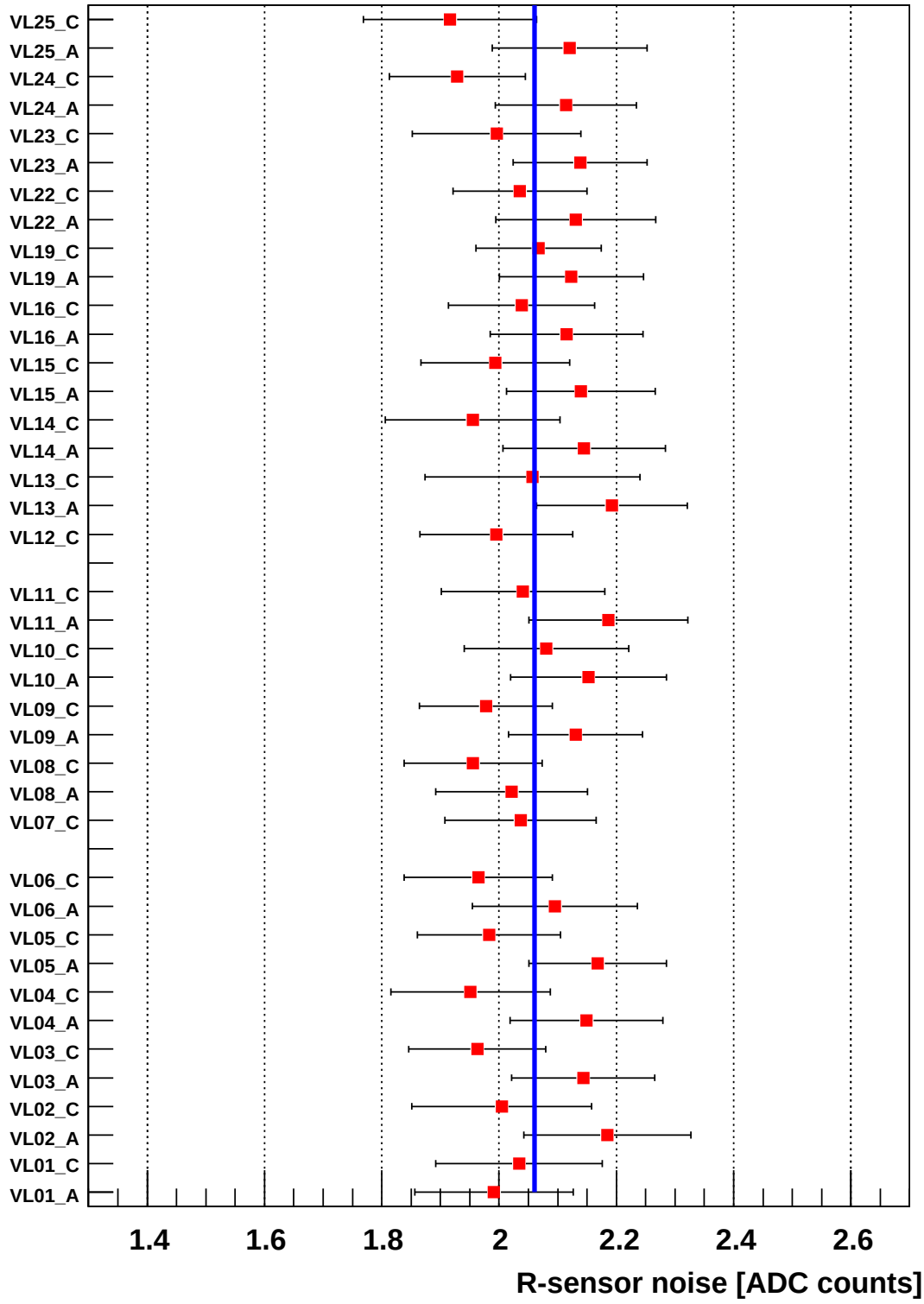

Figure 5.8: *Average CMC noise per R-sensor, labelled with the slot number in which the module is installed. The error bars show the standard deviation of the noise distribution of the strips.*

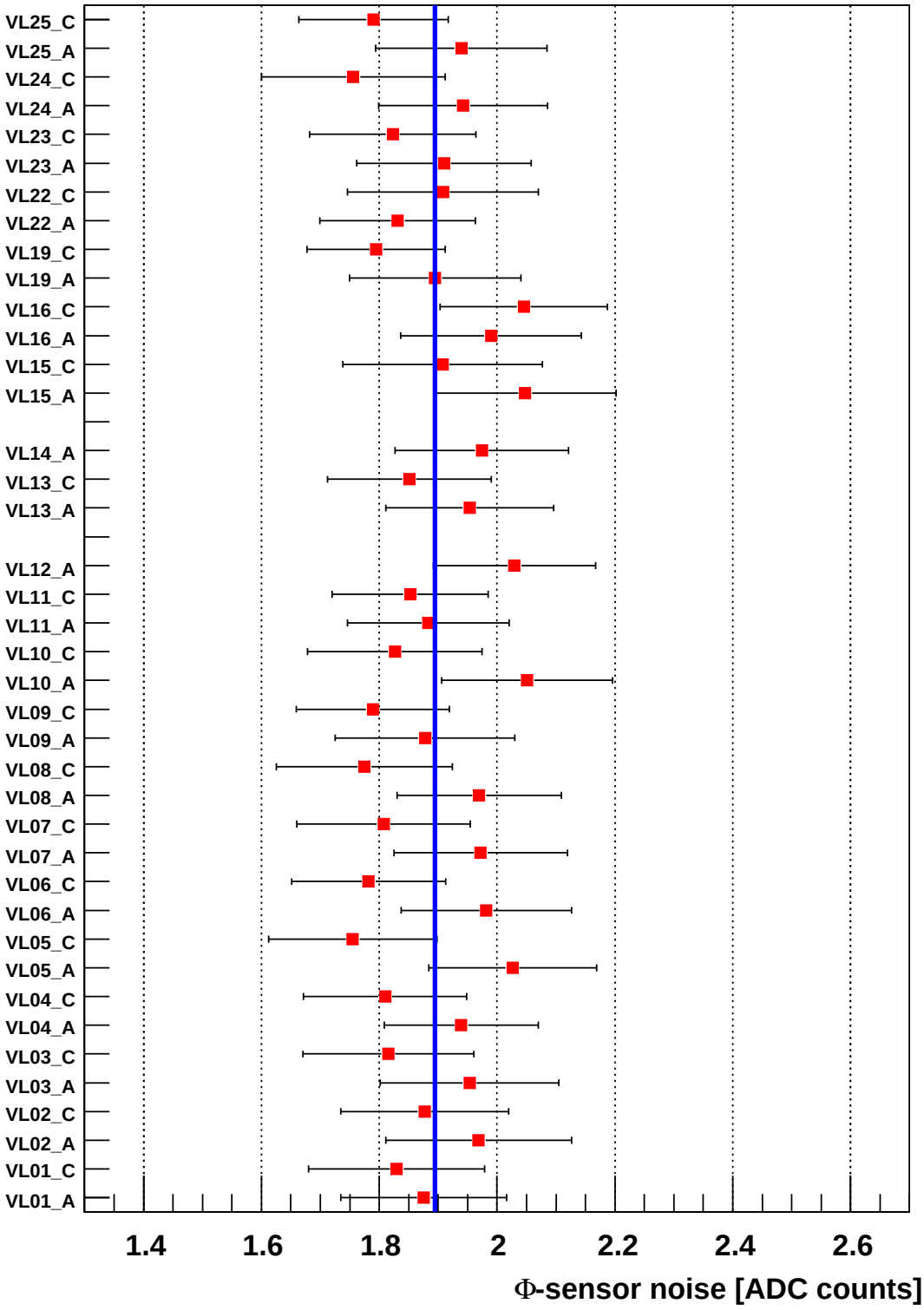

Figure 5.9: *Average CMC noise per Φ-sensor, labelled with the slot number in which the module is installed. The error bars show the standard deviation of the noise distribution of the strips.*

Figure 5.10 displays the CMC noise values in four groups: A- or C-half, R- or Φ-sensor. Besides the already observed difference in noise between sensor types, a systematic difference is seen between the two detector halves. As can be seen from table 5.1, which lists the average raw and CMC noise for the four groups, the sensors of the A-half have $0.10 - 0.13$ ADC counts higher raw and CMC noise than those of the C-half. This holds for both sensor types. The reason for this remains unclear. The effect is not present in the data taken during the detector assembly, where each sensor was thoroughly tested and characterised. The hypothesis that the sensors on the A-side were exposed to an external source of noise that did not affect the C-side at the time of data taking can be excluded based on the similarity in raw and CMC noise difference between A- and C-half. This issue deserves to be re-investigated.

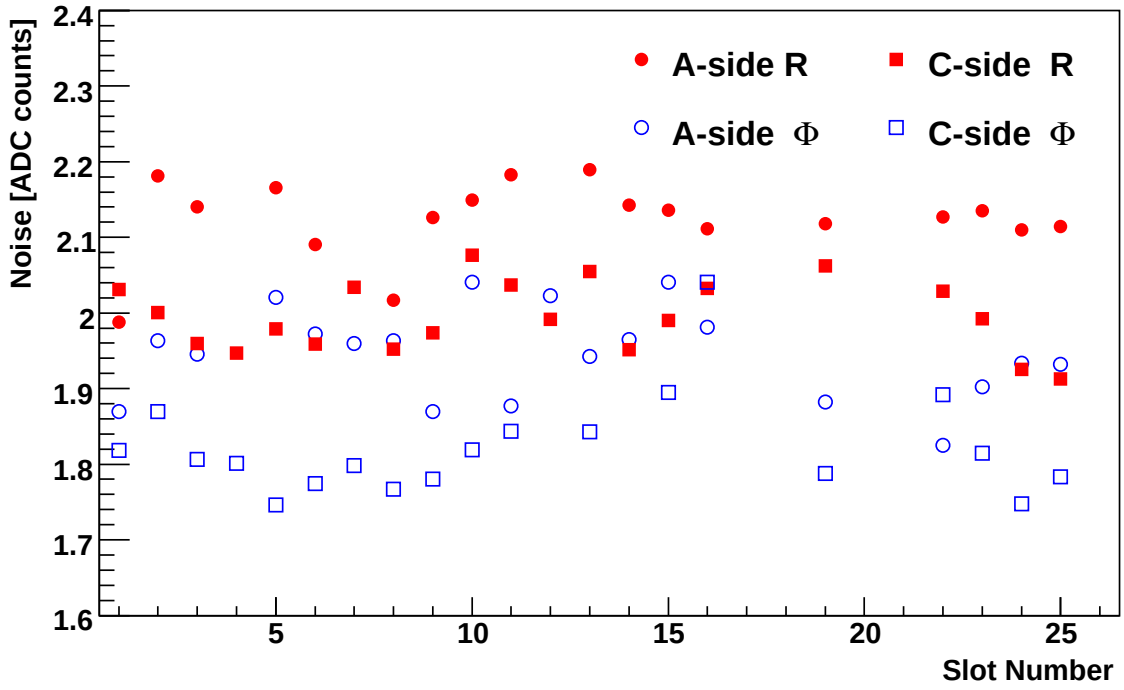

Figure 5.10: *Average CMC noise as a function of detector slot, split into four groups depending on detector half and sensor type. The standard deviation of the mean is assigned as errors to the points. They are too small to be seen at the scale used in the plot.*

Table 5.1: *Average raw and CMC noise for the R and Φ-sensors of the two detector halves.*

Sensor type	*Half*	*Mean raw noise*	*Mean CMC noise*
R	A	2.495 ± 0.001	2.128 ± 0.001
	C	2.366 ± 0.001	1.998 ± 0.001
Φ	A	2.224 ± 0.001	1.952 ± 0.001
	C	2.125 ± 0.001	1.827 ± 0.001

The CMC noise distributions of the 80 tested sensors are summarised in figure 5.11. The noise levels are comparable to those observed in the ACDC3 test beam experiment, cf. section 4.7.2.

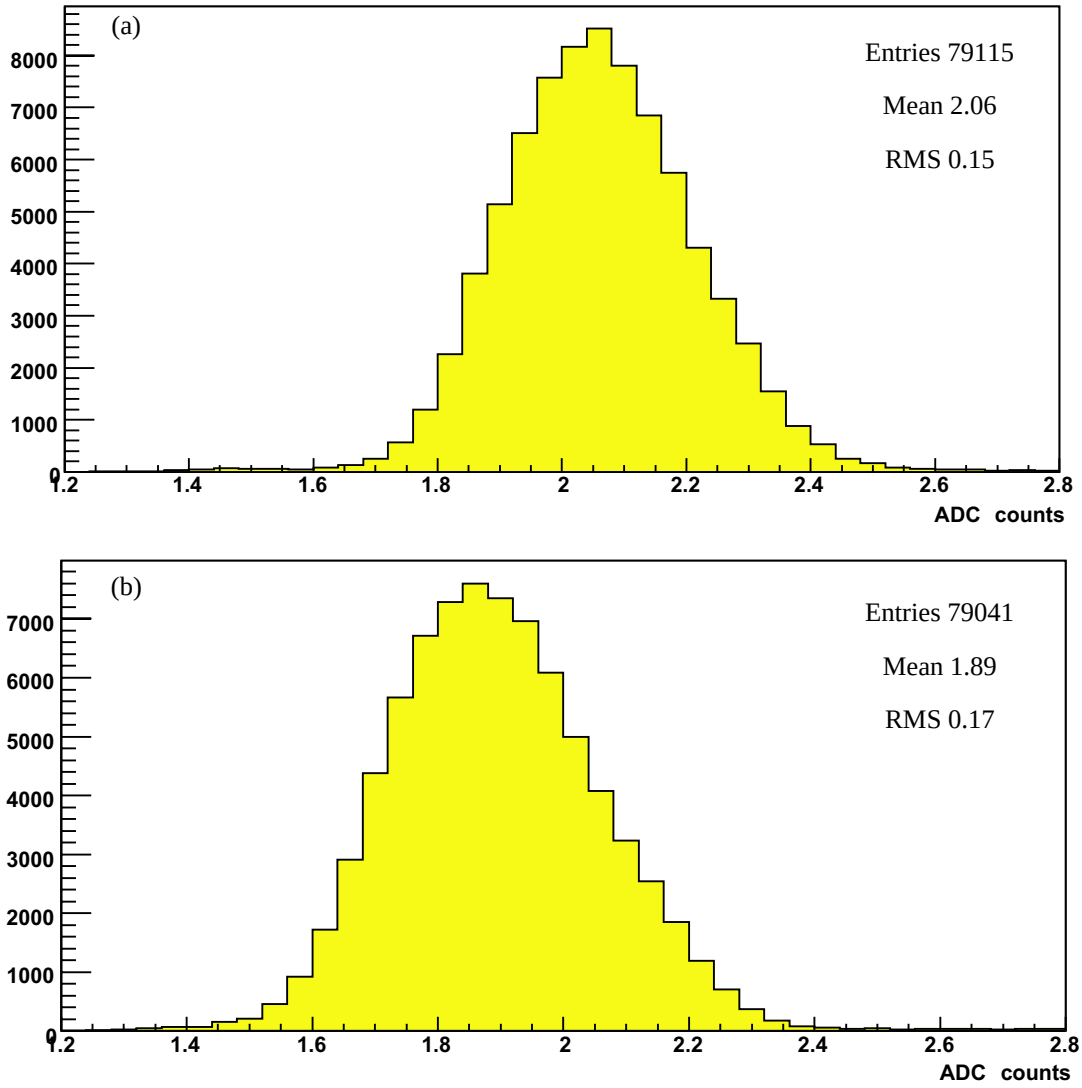

Figure 5.11: *Distribution of CMC noise from all strips in all R-sensors (a) and Φ-sensors (b).*

To further visualise the noise characteristics of the R- and Φ-sensors, figure 5.12 shows the average CMC noise for the R-sensors as a function of strip radius, and the CMC noise distributions of the three strip categories of a Φ-sensor. The noise of the R-sensors increases with the summed length of the strip and routing line, which increases with radius. The strip categories of a Φ-sensor (Inner, Outer Even and Outer Odd) are defined and explained in section 4.7. Table 5.2 summarises the average noise of the different strip types.

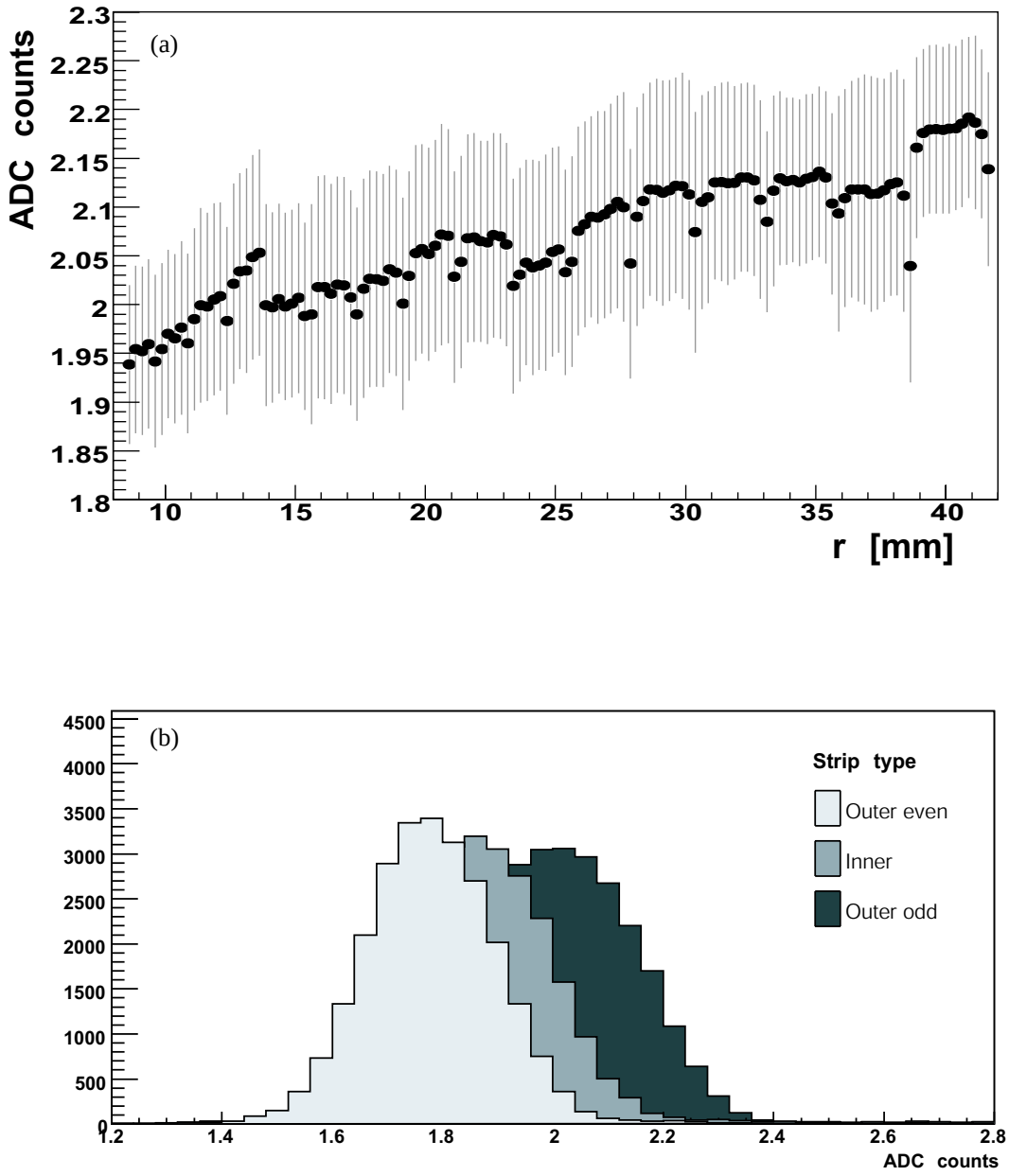

Figure 5.12: *Average CMC noise of all sensors, for:*
a) R-sensors, noise as a function of strip radius (RMS used for error bars)
b) Φ-sensors, split into the three different strip categories.

Table 5.2: *Average CMC noise and RMS of all sensors, for different strip types.*

Strip type	*Mean*	*RMS*
R	2.06	0.15
Φ total	1.89	0.17
- inner	1.88	0.15
- outer even	1.78	0.13
- outer odd	2.01	0.14

5.3.2 Individual versus collective power-up

For 68 of the sensors two snapshot datasets were collected: one taken when the module was individually powered and read out, and one when the module was powered and read out simultaneously with all the other modules. To investigate whether the noise performance of the modules deteriorates when they are collectively powered, the difference in noise between the two cases,

$$\Delta\text{noise} \equiv \text{noise}_{collective} - \text{noise}_{individual} \,,$$

is calculated. The average differences in raw and CMC noise are listed in table 5.3. The CMC noise values of the two cases are plotted versus each other for each sensor in figure 5.13. A clear correlation between the datasets can be seen and only small differences exist between the two cases. For the module with the biggest change in noise, the difference is 0.045 ADC counts, or 2.3%. From this it is concluded that no increase in noise is observed when all modules are powered simultaneously. On the contrary, it is observed that on average the raw noise is 0.01 ADC count higher for individually than collectively powered modules. This stable noise behaviour is attributed to the grounding method for all electronic devices (e.g. HV, LV, repeater boards, TELL1s). Moreover, due to the short distance between sensors and the RF-foil (1 mm), there is a risk of cross-talk between sensors in different modules occurring with the presence of beams. To reduce this, the hybrid ground plane is kept at the same potential as the RF-foil. Each hybrid ground plane is tied to the module support with a silver-plated copper grounding strap.

Table 5.3: *Average raw and CMC noise difference between individually and collectively powered modules.*

Sensor type	*Raw*	*CMC*
$\langle\Delta\text{noise}_R\rangle$	-0.0119 ± 0.0002	-0.0019 ± 0.0002
$\langle\Delta\text{noise}_\Phi\rangle$	-0.0111 ± 0.0002	-0.0056 ± 0.0002

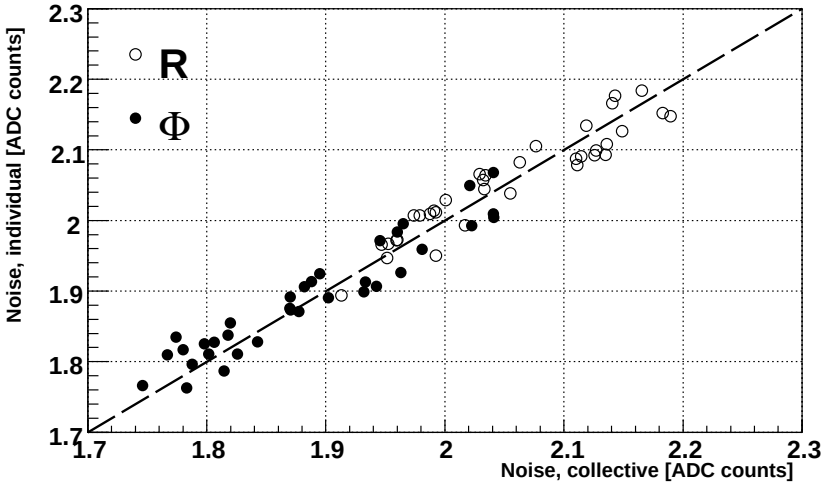

Figure 5.13: *Average CMC noise per sensor from a collective and an individual module power-up. Each data point represents a sensor.*

5.4 First tracks in the VELO

On August 22, 2008, the first so-called synchronisation test of the counter-clockwise LHC beam took place. A 450 GeV proton beam was injected from the SPS into the LHC ring at injection point TI8, directed for point 7 (fig. 5.14). As part of the test, the "TED" beam stopper, a 4.3 m long iron and copper bullet-shaped slab of approximately 20 ton weight, was inserted into the beam line. The interaction of the protons with the TED produced a shower of secondary and tertiary particles in the direction of LHCb. By using the SPD[7] as L0-trigger, the different sub-detectors of LHCb had the opportunity to trigger their readout and see events.

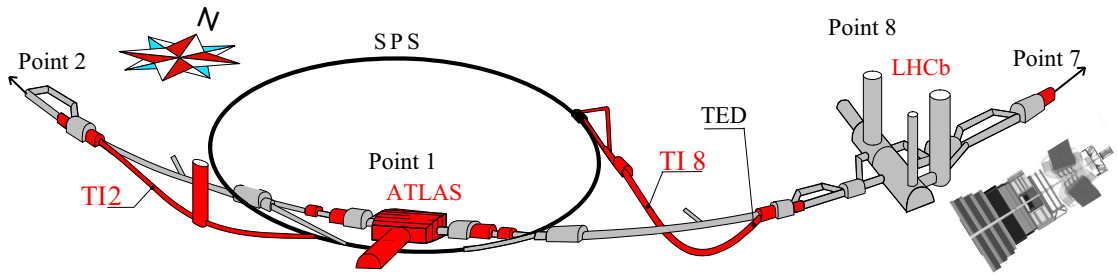

Figure 5.14: *Schematic overview of the SPS to LHC injection area around points 1 and 8. The beam was injected through TI8, directed for point 7. The shower of particles induced by the beam as it was dumped into the TED continued in the direction of point 8 and was detected by the LHCb detector. The orientation of the spectrometer is shown by the figure of the detector next to point 8, c.f. figure 1.5.*

To time-align the VELO with respect to the SPD trigger, a delay in the TTCrx chip on the control boards was used. The TTCrx chip receives timing, L0 trigger and fast control signals from the Readout Supervisor (see section 2.5). The delay affects all signals simultaneously. An initial delay setting was estimated based on the total length of the signal chain from the SPD to the VELO, taking into account the decision time of the Readout Supervisor, and the time of flight of the traversing particles. Data were taken in a run with 15 consecutive triggers: 7 time samples (of 25 ns each) before the central trigger, and 7 samples after. If the estimated delay was correct within ±150 ns, the particles should be visible in the data. Hence, by studying the cluster charge distribution in a sensor as a function of time sample, the optimal time sample could be found. To increase the probability of seeing particles, the Beetle settings were tuned to maximise the signal amplification and broaden the pulse shape. Additionally, the cluster thresholds in the TELL1 were set to be lower than nominal. Figure 5.15 shows the result, where time sample 7 is the initial estimate. The pulse shape can be seen to extend over time samples 5 to 8. The highest cluster charge distribution is found at time sample 6, one clock cycle away from the initial estimate.

Figure 5.16 shows an event display picture of one of these first events to be recorded. The 21 modules of the C-half are drawn, with the sensor hits and the reconstructed tracks.

[7]The Scintillator Pad Detector, a part of the LHCb calorimeter.

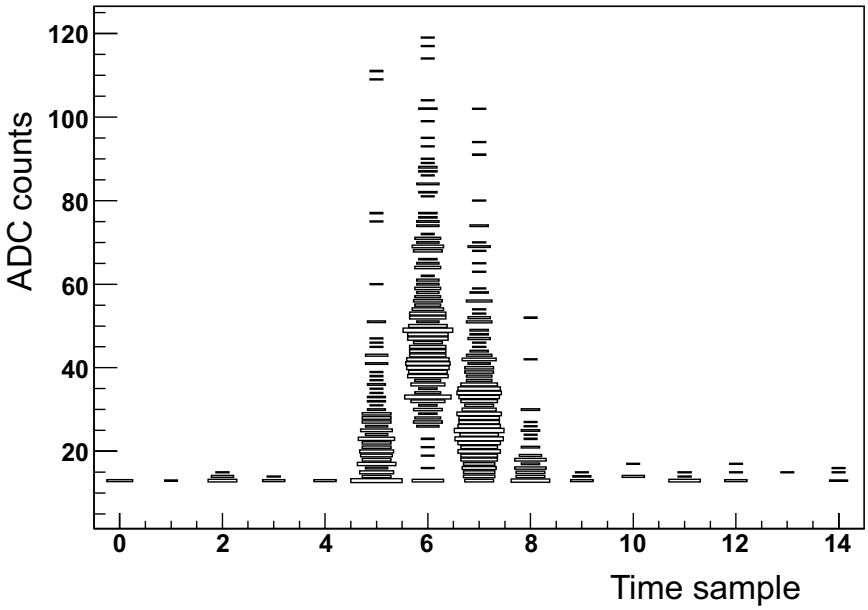

Figure 5.15: *Cluster charge as a function of time sample, for 15 consecutive samples. The estimated delay corresponds to time sample 7.*

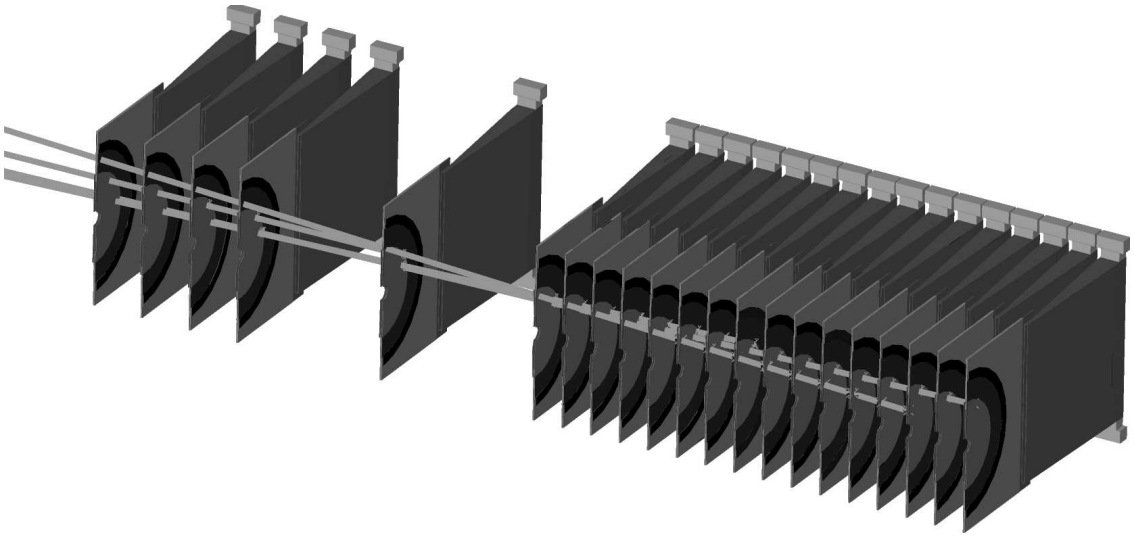

Figure 5.16: *Event display of one of the first LHC-induced events recorded with a fully powered VELO (run 32474). The C-half modules are drawn together with the sensors hits and the reconstructed tracks.*

5.5 Summary

This chapter has reviewed tests performed in the process of commissioning the VELO, with emphasis on the DAQ and the sensors. Software tools were introduced, and their use during the uniformity and slice tests was demonstrated. With these tests, problems with hardware, firmware and software were found and repaired.

As part of the commissioning, the performance integrity of the sensors was verified by an examination of their noise characteristics. The results of this analysis yielded an average CMC noise of 2.06 and 1.89 ADC counts for the R- and Φ-sensors respectively. A small systematic difference in raw and CMC noise between the detector halves is measured, but no good explanation for this is found. Furthermore, an investigation to determine differences in raw and CMC noise levels between individually and collectively powered modules showed no effects of significance.

The final section briefly described results from the first injection of a counter-clockwise beam into the LHC. By taking data with 15 consecutive triggers the VELO could be properly time-aligned with respect to the L0-trigger supplied by the SPD, and tracks through the detector were successfully reconstructed for the first time after the VELO was installed.

A Impact parameter resolution

This appendix describes a model to parameterise the impact parameter resolution in the VELO[1]. The plots shown are based on Monte Carlo simulated data from the so-called DC04 production.

A.1 Definition

The *three-dimensional* impact parameter d_0 is the shortest distance from the primary vertex to a reconstructed track. The d_0 mismatch r is defined as the absolute difference between the reconstructed and the true impact parameter. The impact parameter resolution σ_{d_0}, as presented in e.g. figure 1.11 and references [24, 27], is defined as the average mismatch, $\sigma_{\mathrm{d}_0} \equiv \langle r \rangle$.

To relate σ_{d_0} to the *two-dimensional* impact parameter resolution σ_{IP}, it is assumed that σ_{IP} is equal to the uncertainty in the x and y components of reconstructed impact parameter, i.e. $\sigma_{IP} = \sigma_x = \sigma_y$. It is also assumed that the errors are Gaussian. The distribution of the d_0 mismatch is then described by:

$$F(r) = re^{-0.5r^2/\sigma_{IP}^2}\,, \tag{A.1}$$

The three-dimensional impact parameter resolution is obtained by

$$\sigma_{\mathrm{d}_0} = \langle r \rangle = \frac{\int_0^\infty rF(r)\mathrm{d}r}{\int_0^\infty F(r)\mathrm{d}r} = \sqrt{\frac{\pi}{2}}\sigma_{IP}\,. \tag{A.2}$$

This equation defines the relation between the two- and three-dimensional impact parameter resolution.

A.2 The model

The impact parameter resolution depends on the multiple scattering of the particles, the hit resolution and the geometry of the tracking detector. By using the formulation of the two-dimensional impact parameter resolution introduced in [29,101], $\sigma^2_{\mathrm{d}_0}$ can be expressed as

$$\sigma^2_{\mathrm{d}_0} = \frac{\pi}{2}\sigma^2_{IP} = \frac{\pi}{2}\left[\frac{\Delta^2_{0n}\sigma_1^2 + \Delta^2_{01}\sigma_n^2}{\Delta^2_{1n}} + \theta_0^2\Delta^2_{01}\right]\,. \tag{A.3}$$

The model assumes that the track parameters are effectively determined with only two measurement planes, the first plane ($n = 1$) and the nth plane counting downstream. The length of this lever arm, and consequently the value of n, depends on the momentum of the particle. The first term is the contribution from the single hit resolution of the

[1] The section contains minor corrections with respect to the printed version.

two measurements (σ_1, σ_n), the distances from the measurements to the interaction point (Δ_{01}, Δ_{0n}), and the distance between the measurements (Δ_{1n}).

The second term is the contribution from the multiple scattering, where θ_0 is the projected average multiple scattering angle. It is assumed that all the scattering takes place in the first measurement plane.

A.2.1 The resolution term

The single hit resolution of the VELO scales linearly with the radius[2] so the term can be rewritten using $\sigma_n = \sigma_1 \frac{\Delta_{0n}}{\Delta_{01}}$ and by introducing the extrapolation factor $f = \Delta_{0n}/\Delta_{1n}$:

$$\frac{\Delta_{0n}^2\sigma_1^2 + \Delta_{01}^2\sigma_n^2}{\Delta_{1n}^2} = 2f^2\sigma_1^2\,. \tag{A.4}$$

For low momentum tracks the multiple scattering in the silicon planes is large. Due to this scattering, the sensor resolution contribution to the impact parameter resolution mainly comes from the two first measurements of the track, i.e. $n = 2$. For tracks of higher momentum, the scattering decreases and the more planes contribute to the effective lever arm of the track measurement. If the discussion is limited to the region of the VELO with 30 mm spacing between the modules (up to $z = 290$ mm, see appendix B) the average displacement due to multiple scattering that is experienced by a particle travelling between two modules is [13]

$$d = \frac{0.0136}{p}\sqrt{x/X_0}[1 + 0.038\ln(x/X_0)] \times 30\text{ mm} = \frac{0.032}{p}\text{ mm}\,, \tag{A.5}$$

where the material contribution of a VELO module is 0.64% of a radiation length X_0. With an expected sensor resolution of 8.5 μm (see section 4.8), the contribution of the multiple scattering to the total error becomes smaller than the resolution contribution for tracks with $p > 4$ GeV/c. For such tracks it is assumed that the effective measurement lever arm extends to $n > 2$. Consequently, the relevant detection layer in the effective lever arm is determined by $n = 2 + p/4$ where p is in GeV. Furthermore, the extrapolation factor f depends on the angle of track. The angular dependence is illustrated by plotting f as a function of inverse transverse momentum $1/p_{\mathrm{T}}$. Figure A.1 shows f and $f(1/p_{\mathrm{T}})$ for three datasets corresponding to separate momentum ranges. The extrapolation factor is implemented in the resolution term (equation A.4) as a linear function $f = A + B/p_{\mathrm{T}}$ where the coefficients A and B are extracted from a linear fit to the data. These fits are included in figure A.1.

A.2.2 The multiple scattering term

The average projected scattering angle can be expressed as

$$\theta_0 = \frac{13.6}{p}\sqrt{x/X_0}\,[1 + 0.038\ln(x/X_0)]\,, \tag{A.6}$$

[2] As demonstrated in section 4.8.

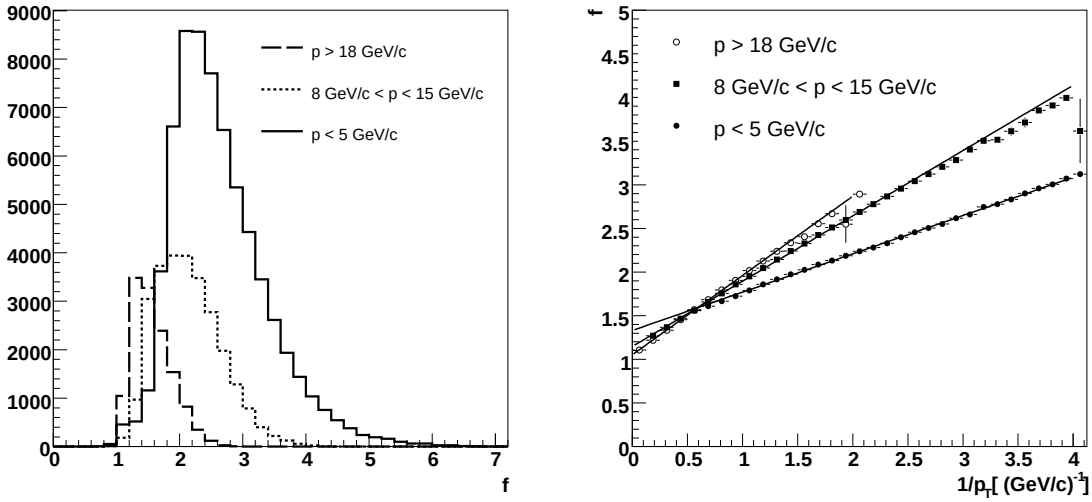

Figure A.1: *Left: The distribution of extrapolation factors f for tracks in a low, a medium and a high momentum range. Right: Extrapolation factor as a function of inverse transverse momentum, for the three momentum ranges. A linear fit to each of the datasets is also shown.*

where p is the particle momentum and x/X_0 is the amount of material traversed before the second measurement, expressed as a fraction of a radiation length X_0.

The multiple scattering term is reformulated in terms of p_{T} and the radius to the first measurement (r_1) using $p_{\mathrm{T}} = p\frac{r_1}{\Delta_{01}}$. This yields:

$$\theta_0^2\Delta_{01}^2 = \frac{r_1^2}{p_{\mathrm{T}}^2}\left\{0.0136\sqrt{x/X_0}\,[1+0.038\ln(x/X_0)]\right\}^2 . \tag{A.7}$$

A.3 Results

The complete three-dimensional impact parameter resolution squared now reads:

$$\sigma_{\mathrm{d_0}}^2 = \pi(A+B/p_{\mathrm{T}})^2\sigma_1^2 + \frac{\pi r_1^2}{2p_{\mathrm{T}}^2}\left\{0.0136\sqrt{x/X_0}\,[1+0.038\ln(x/X_0)]\right\}^2 . \tag{A.8}$$

The model is tested in three momentum ranges which have been arbitrarily selected to separate particles with low, medium and high momentum. Figure A.2 shows $\sigma_{\mathrm{d_0}}$ of as a function of $1/p_{\mathrm{T}}$ and fitted with equation A.8. The fit parameters are the resolution σ_1 and material factor x/X_0. The radius of the first measurement r_1 is fixed to 9 mm. As mentioned above, the parameterisation of f is performed separately by a linear fit of f as a function of $1/p_{\mathrm{T}}$. The results are:

- The low momentum range ($p < 5$ GeV/c)
  $f = 1.33 + 0.44/p_{\mathrm{T}}$
  $\sigma_1 = 8.5 \pm 0.2$ μm and $x/X_0 = 2.6 \pm .1\%$.
- The medium momentum range (8 GeV/c $< p <$ 15 GeV/c)
  $f = 1.15 + 0.75/p_{\mathrm{T}}$

$\sigma_1 = 7.8 \pm 0.2$ μm and $x/X_0 = 3.2 \pm 0.1\%$.

- The high momentum range ($p > 18$ GeV/c)
  $f = 1.1 + 0.91/p_{\mathrm{T}}$
  $\sigma_1 = 8.6 \pm 0.2$ μm and $x/X_0 = 3.2 \pm 0.4\%$.

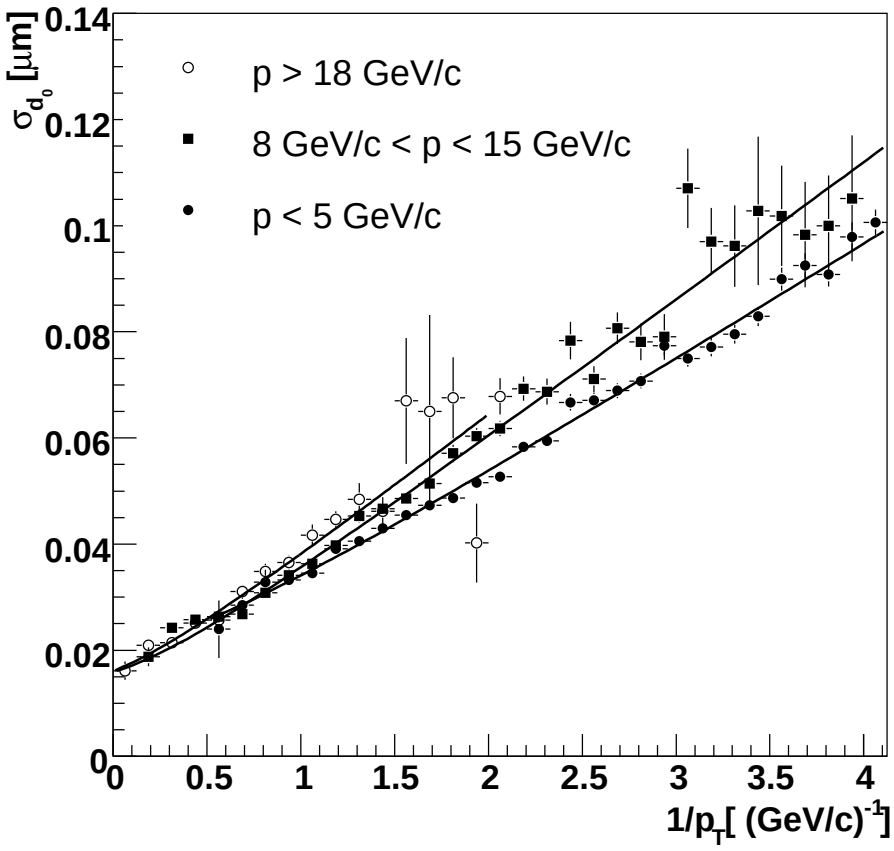

Figure A.2: *The fits of equation A.8 to the three-dimensional impact parameter resolution for data from tracks in three momentum ranges.*

A.4 Conclusion

The three-dimensional impact parameter resolution is linear in $1/p_{\mathrm{T}}$, but the interpretation of the curve in terms of scattering, measurement resolution and detector geometry is not straightforward. The number of VELO modules that contribute effectively to the measurement of the track parameters depends on the multiple scattering in the detector and therefore on the momentum of the track. In the model presented here, this is dealt with by splitting the tracks into three distinct momentum ranges and by parameterising the effective track lever arm in terms of track momentum. The results show that the observed impact parameter resolution is consistent with a single hit resolution of 8.5 μm and that the amount of scattering corresponds to about 3% of a radiation length, which is in agreement with the detector design [102].

B VELO and Pile-Up module positions

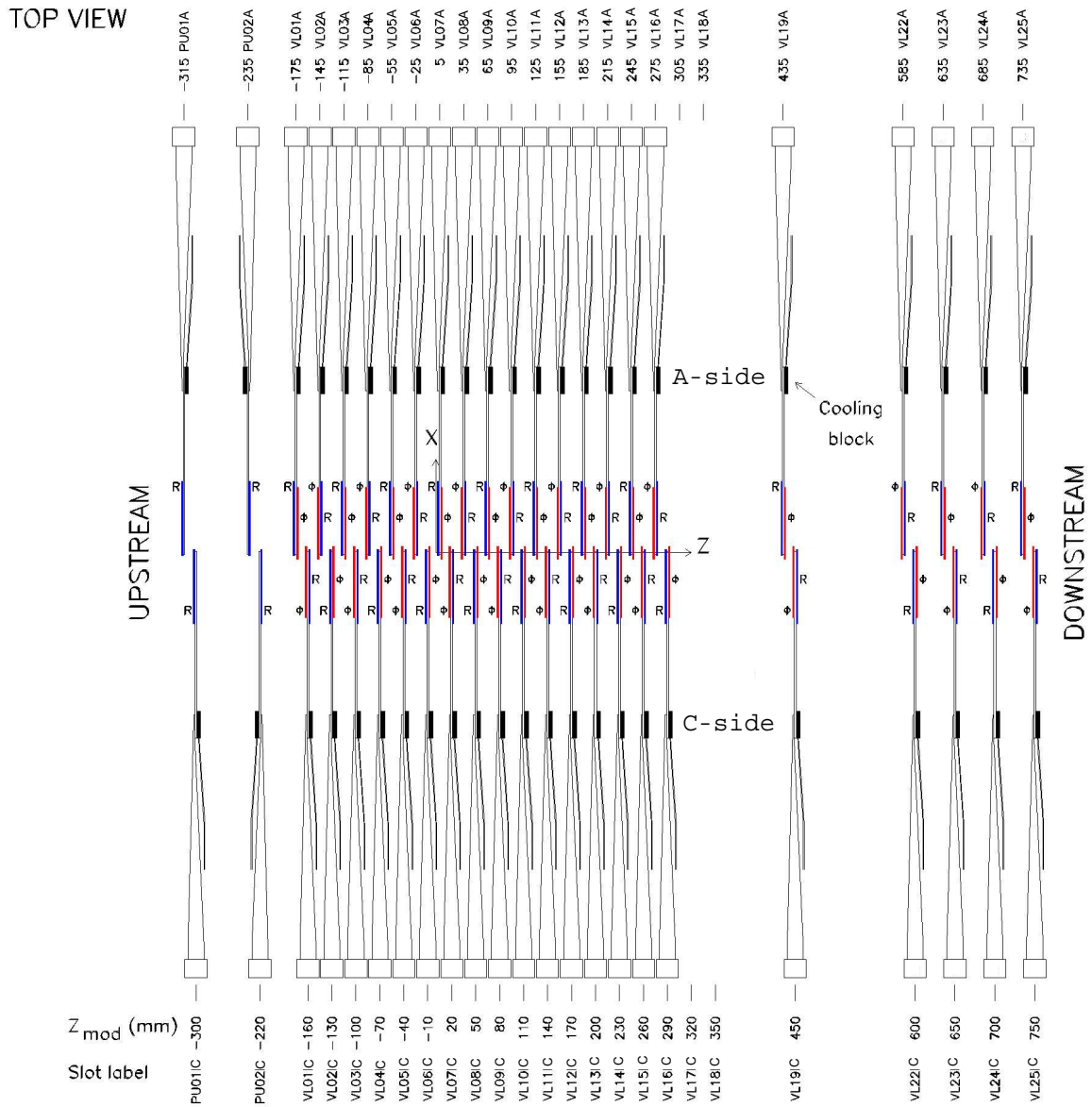

Figure B.1: *Top view sketch of PU and VELO module arrangement on detector halves. The coordinate system origin is at the nominal interaction point. The module Z position z_{mod} is defined for the centre plane of the module base (the XY plane that symmetrically cuts the module base). The slot labels are indicated next to the Z-positions.*

C ACDC3 Cable Configuration

Table C.1: *Cable configurations in ACDC3.*

Module serial no.	Sensor type	Software sensor no.	TELL1 no. HP1	HP2	HP3	HP4	Sensor z [mm]	Slot	sensor bias [V]	Depletion voltage [V]
M26	R	3	21	-	21	-	-161.15	VL01C	150	100
	Φ	67	30	-	30	-	-158.85	VL01C	140	90
M29	Φ	89	29	21	29	29	198.85	VL13C	100	50
	R	25	62	30	62	62	201.15	VL13C	100	50
M23	R	27	61	-	61	-	228.85	VL14C	120	70
	Φ	91	23	-	23	-	231.15	VL14C	110	60
M31	Φ	93	51	29	51	51	258.85	VL15C	100	30
	R	29	50	62	50	50	261.15	VL16C	100	20
M30	R	31	49	-	49	49	288.85	VL16C	100	50
	Φ	95	27	-	27	27	291.15	VL15C	100	50
M21	Φ	97	-	-	-	-	448.84	VL19C	110	60
	R	33	-	-	-	-	451.15	VL19C	100	50
M37	R	35	-	61	-	61	598.85	VL22C	100	30
	Φ	99	-	23	-	23	601.15	VL22C	100	30
M27	Φ	101	-	51	25	25	648.85	VL23C	100	50
	R	37	-	50	24	24	651.15	VL23C	100	50
M24	R	39	-	49	-	21	698.85	VL24C	100	20
	Φ	103	-	27	-	30	701.15	VL24C	100	30
M28	Φ	105	25	25	-	-	748.85	VL25C	100	20
	R	41	24	24	-	-	751.15	VL25C	100	20

D Target metrology

This section contains close-up photographs of the targets used in the ACDC3 setup, as described in section 4.3. The photographs were taken by the CERN metrology laboratory. Figure D.1 shows one of the target holders mounted on the mock-up baseplate during the survey.

The photographs in figure D.2 show the eight targets glued on mylar foil. The targets were machined and glued with tight time constraints, which is reflected in their non-circular shape, their unsmooth surfaces and the visible glue residue around them. This caused problems for the metrology measurement, and reduced the accuracy of the measurement.

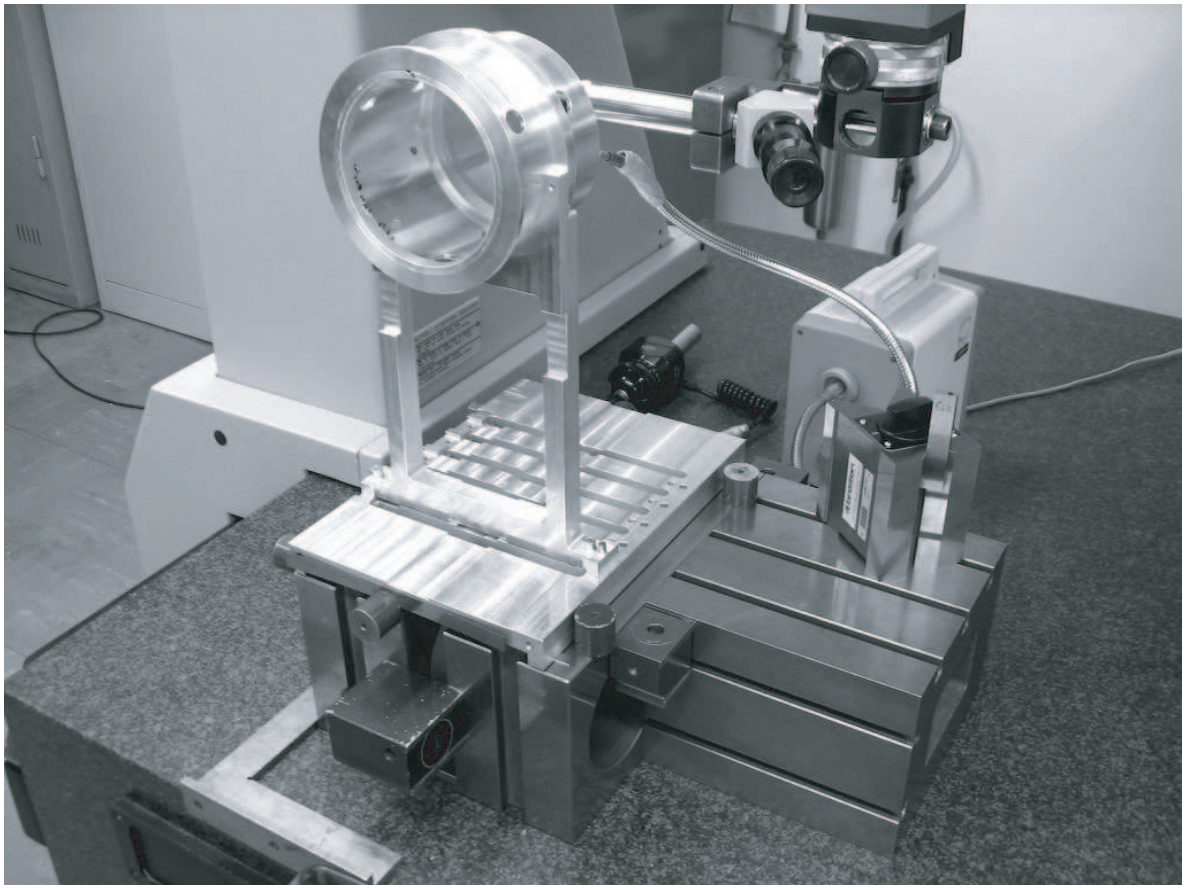

Figure D.1: *The metrology setup, with a target holder on the mock-up baseplate and the Ferranti coordinate measurement machine.*

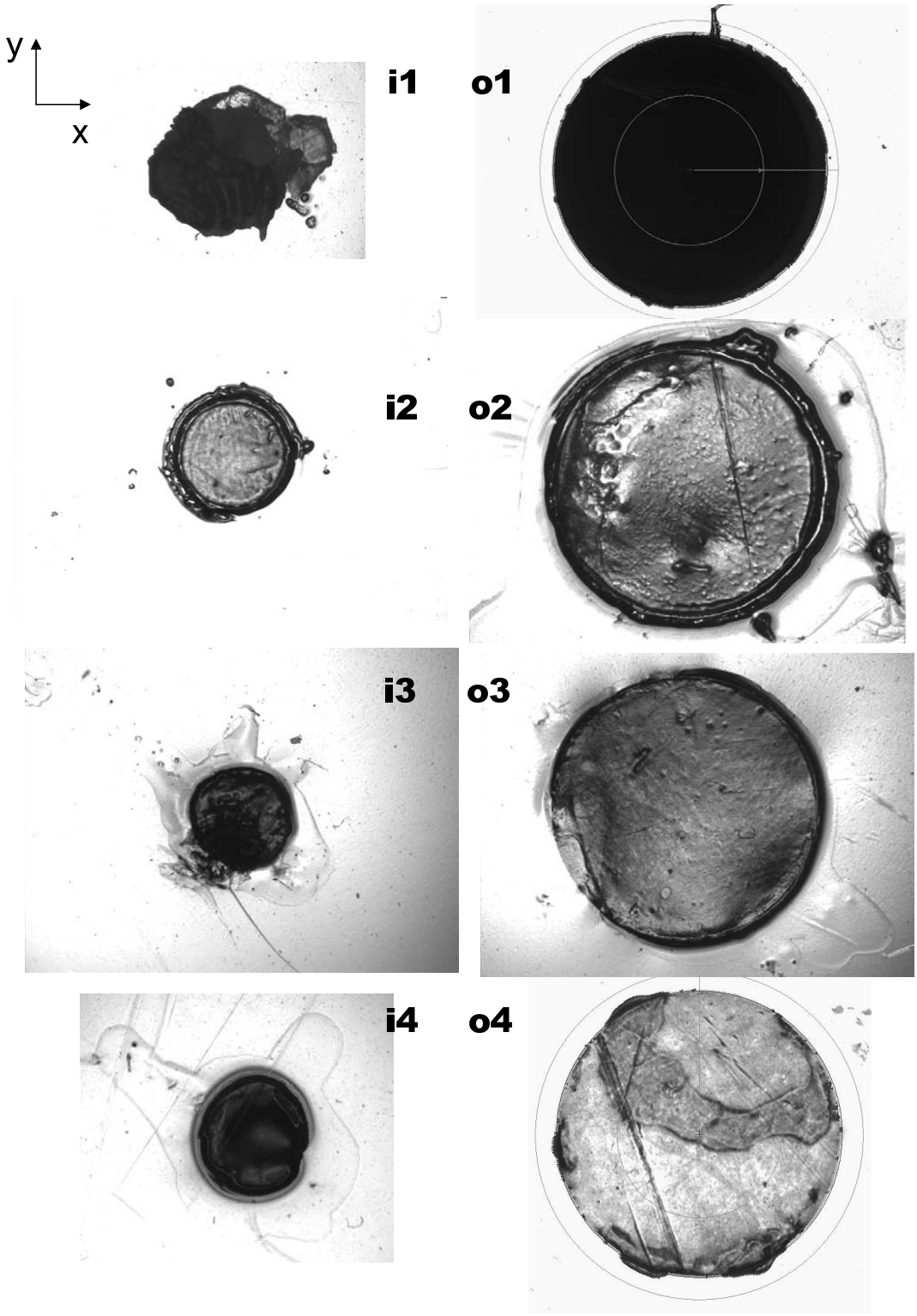

Figure D.2: *Photographs of the eight targets in the ACDC3 setup. The inner targets (denoted with 'i') are in the left column and the outer (denoted with 'o') are in the right column. Targets 1 are in the first row, and targets 2,3 and 4 follow in the rows below.*

E Reconstructed vertex distributions

This section contains the fits to the target slices in x (left column) and y (middle column) as described in section 4.9.3. The right column shows the 2-dimensional view of the target, with markers for the fitted edges, the therefrom induced target centre (square), and the target centre from the metrology measurements (solid circle).

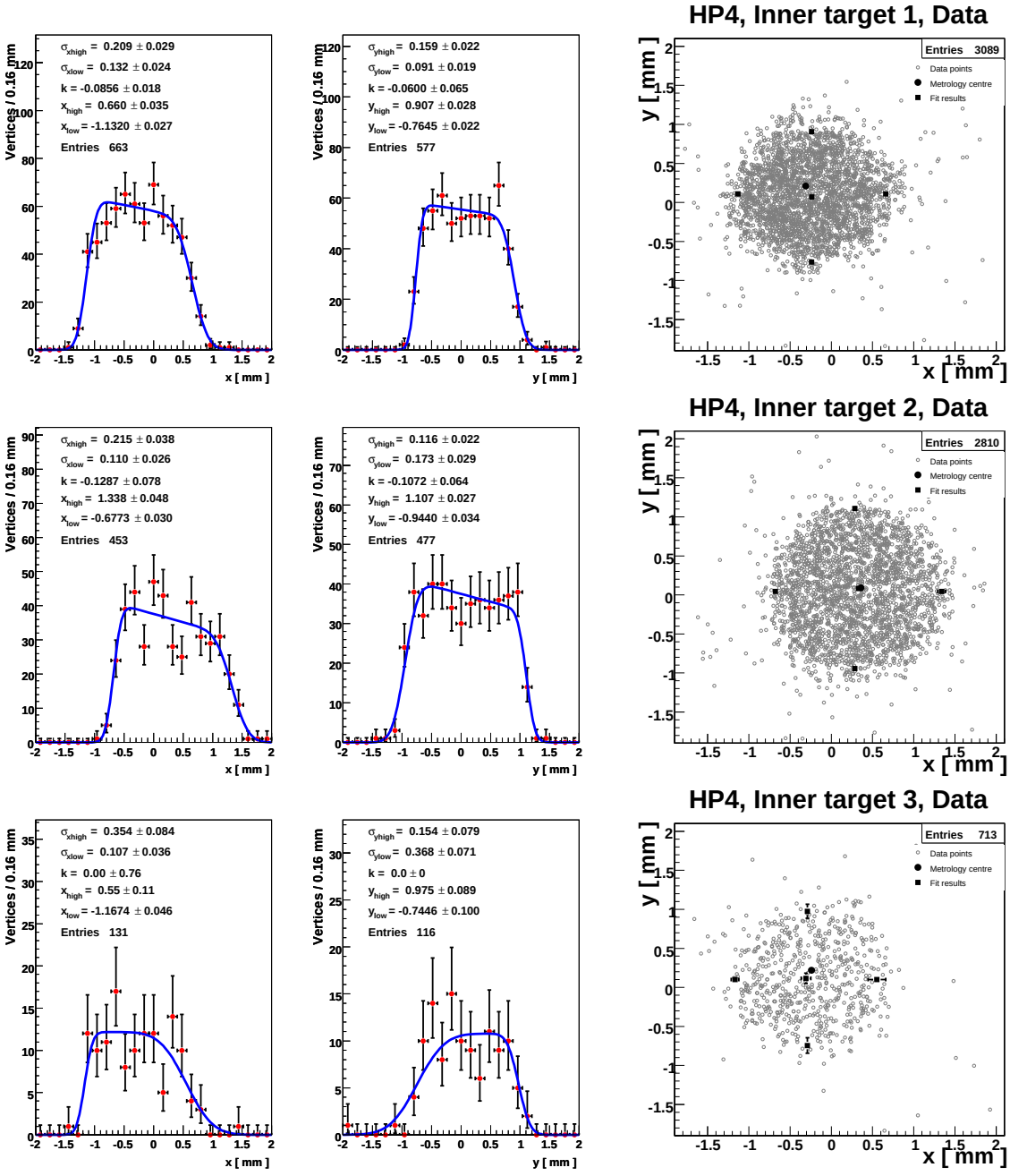

Figure E.1: *HP4 Inner targets, Data.*

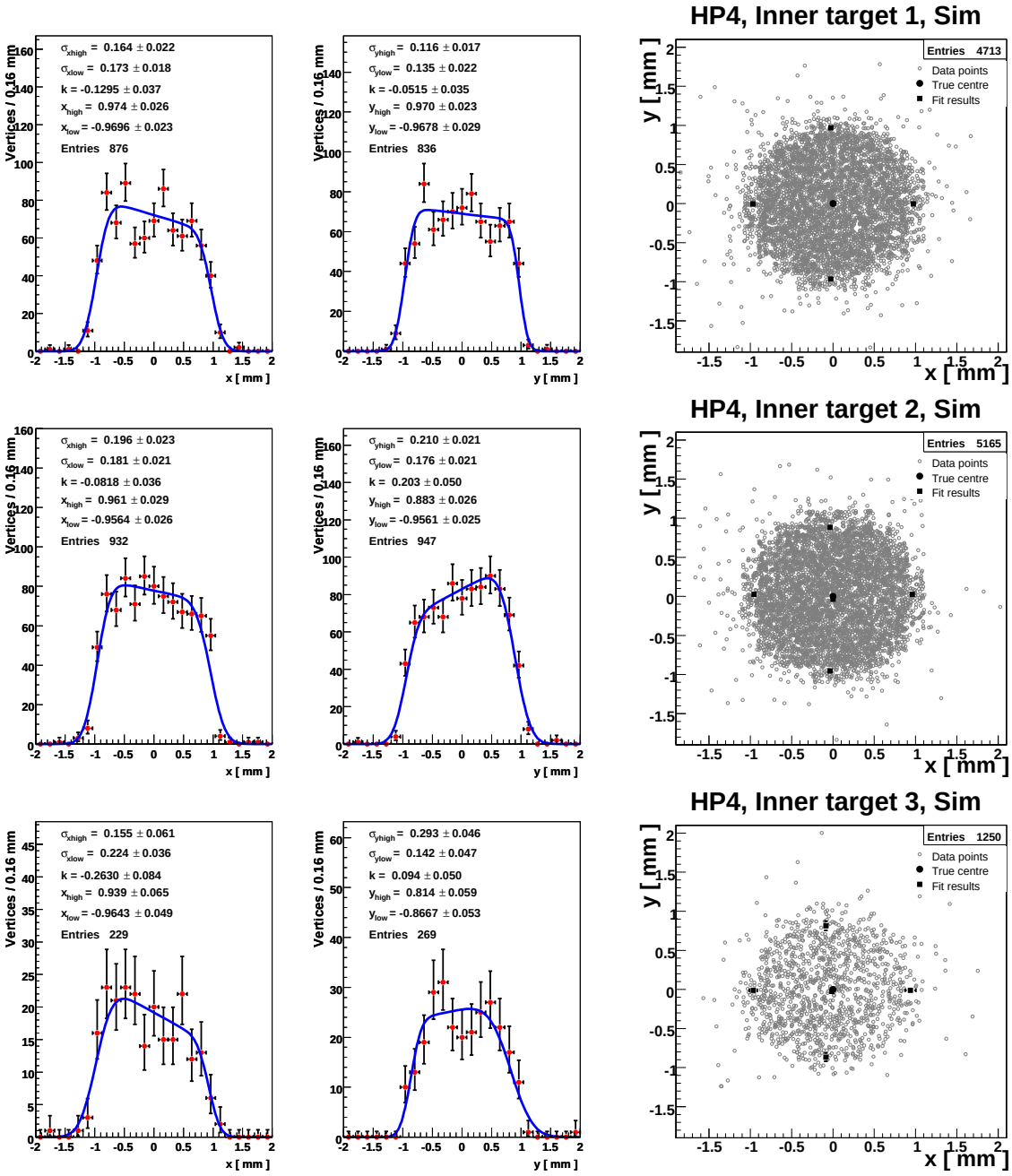

Figure E.2: *HP4 Inner targets, Simulation.*

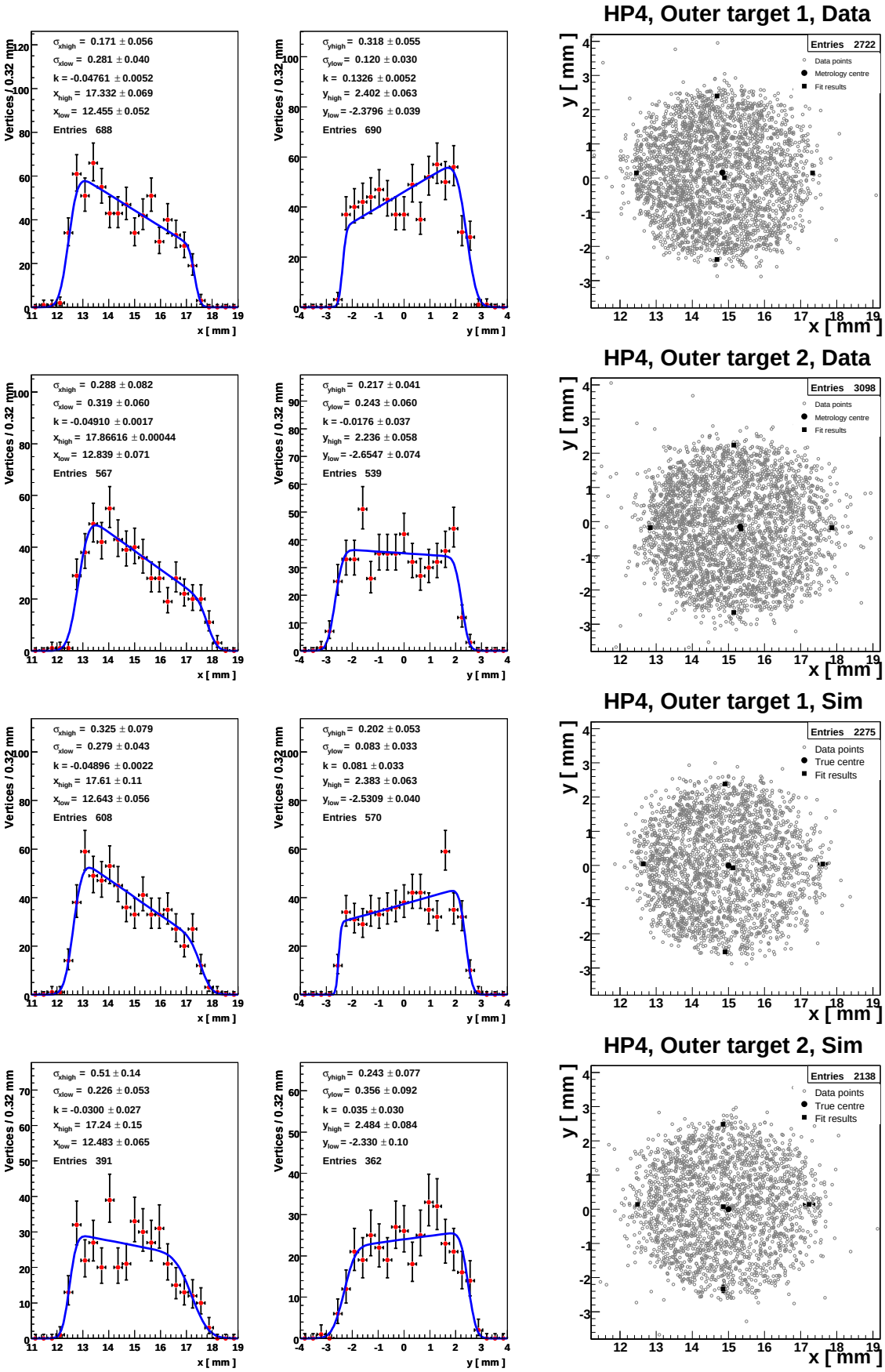

Figure E.3: *HP4 Outer targets, Data and Simulation.*

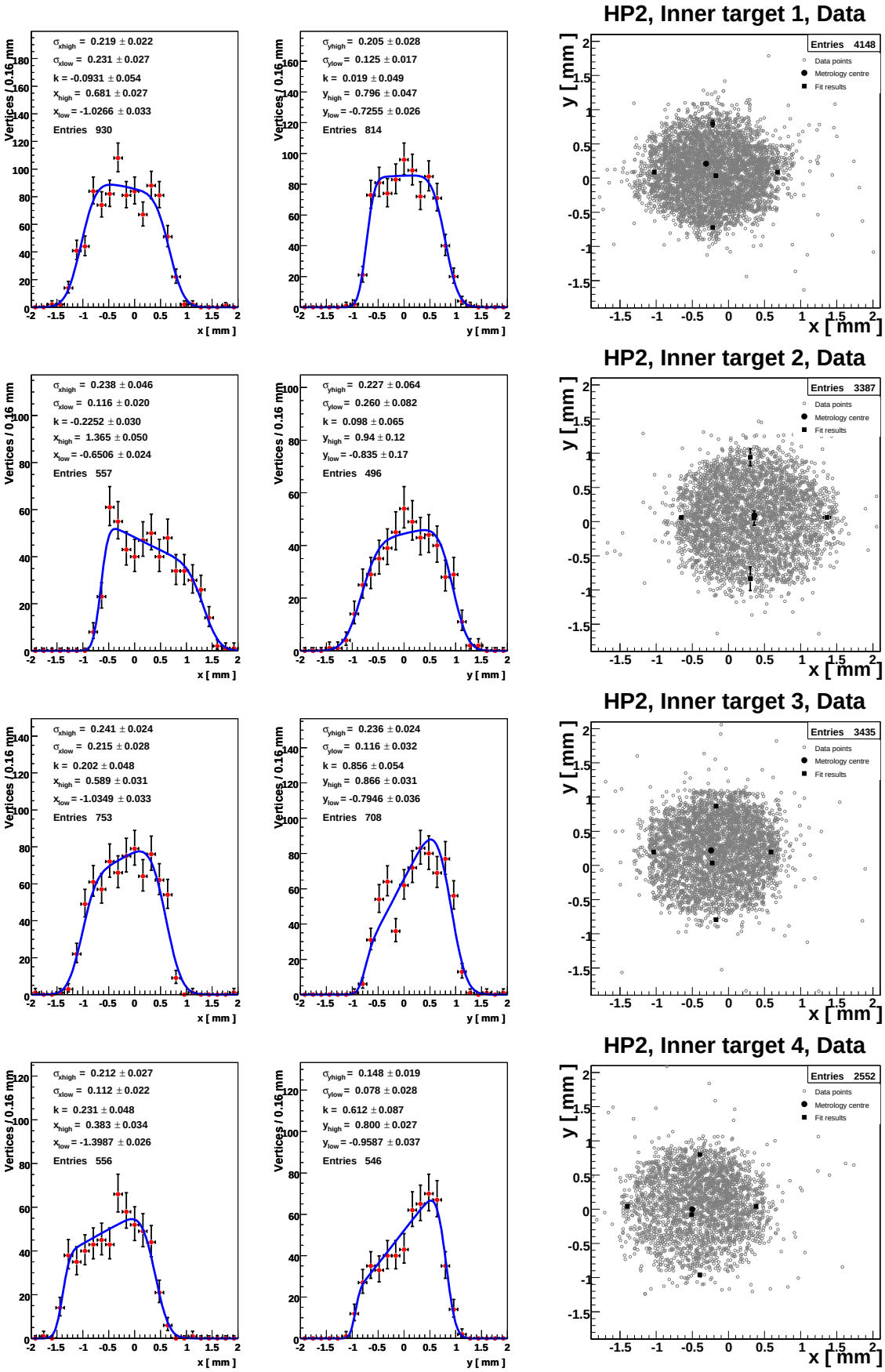

Figure E.4: *HP2 Inner targets, data.*

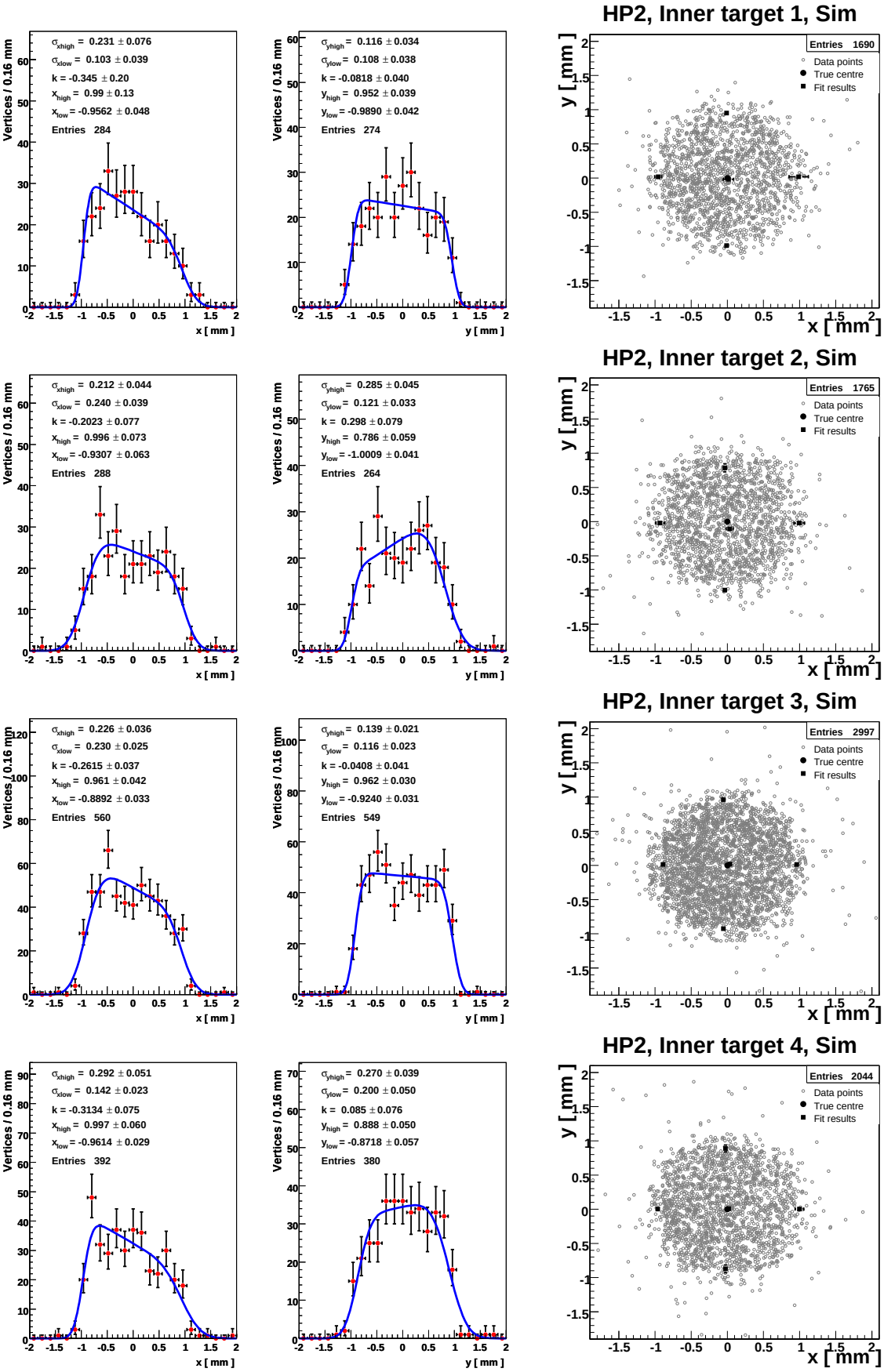

Figure E.5: *HP2 Inner targets, Simulation.*

F Alignment in ACDC3

Figures F.1 and F.2 show the mean[1] of the unbiased residuals for R and Φ-sensors, for all modules read out in cable configuration HP4. The R-sensor residuals are plotted versus strip pitch, and are well centred around 0. This indicates a good alignment. The Φ-sensor residuals are plotted versus ϕ-angle, and all display a "banana shape". As explained in section 4.6, this is related to the misalignment of the Φ-sensor relative to the R-sensor in a module. It can not be corrected for by the software alignment but requires a special procedure that was not yet developed at the time of this analysis [57].

[1] The mean from a Gaussian fit performed on y-projections of the data.

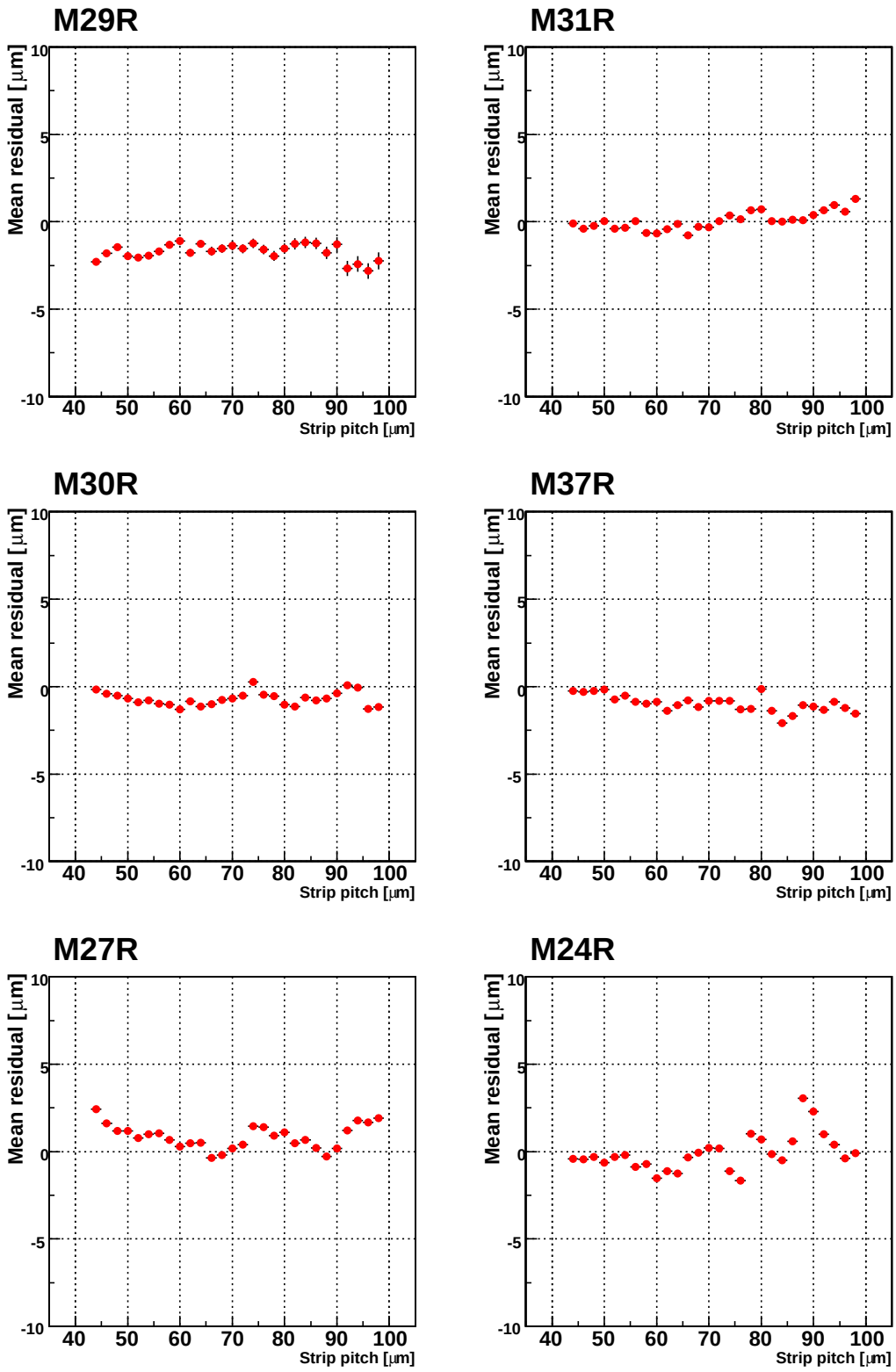

Figure F.1: *Fitted mean of unbiased track residuals versus strip pitch for R-sensors in the HP4 cable configuration.*

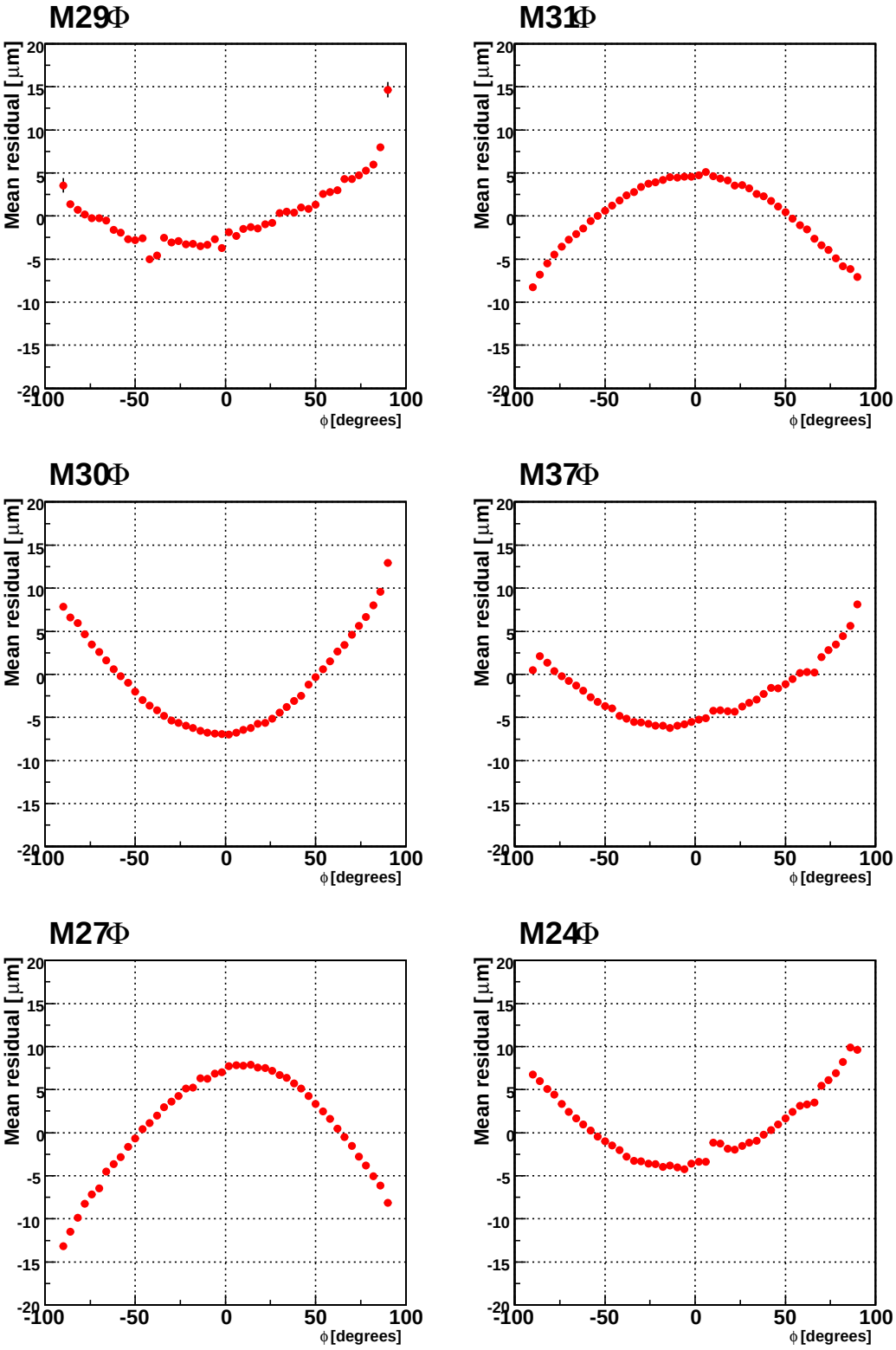

Figure F.2: *Fitted mean of unbiased track residuals versus polar angle ϕ for Φ-sensors in the HP4 cable configuration.*

Bibliography

[1] T. Maskawa and M. Kobayashi, "CP-Violation in the Renormalizable Theory of Weak Interaction", *Prog. Th. Phys*, vol. 49, p. 652, 1973.

[2] S. W. Herb *et al.*, "Observation of a Dimuon Resonance at 9.5 GeV in 400-GeV Proton-Nucleus Collisions", *Physical Review Letters*, vol. 39, no. 5, pp. 252–255, 1977.

[3] A. D. Sakharov, "Violation of CP invariance, C asymmetry, and baryon asymmetry of the universe", *Eksp. Teor. Fiz*, vol. 5, p. 32, 1967.

[4] K. Abe *et al.*, "Observation of Large CP Violation in the Neutral B Meson System", *Physical Review Letters*, vol. 87, no. 9, p. 91802, 2001.

[5] B. Aubert *et al.*, "Observation of CP Violation in the B_0 Meson System", *Physical Review Letters*, vol. 87, no. 9, p. 91801, 2001.

[6] UTfit Collaboration, M. Bona, *et al.*, "First Evidence of New Physics in b $\leftrightarrow$ s Transitions", 2008, http://arxiv.org/abs/0803.0659.

[7] L. Evans and P. B. (editors), "LHC Machine", *Journal of Instrumentation*, vol. 3, no. 08, p. S08001, 2008.

[8] The ATLAS Collaboration, G. Aad, *et al.*, "The ATLAS Experiment at the CERN Large Hadron Collider", *Journal of Instrumentation*, vol. 3, no. 08, p. S08003, 2008.

[9] The CMS Collaboration, S. Chatrchyan, *et al.*, "The CMS experiment at the CERN LHC", *Journal of Instrumentation*, vol. 3, no. 08, p. S08004, 2008.

[10] The ALICE Collaboration, K. Aamodt, *et al.*, "The ALICE experiment at the CERN LHC", *Journal of Instrumentation*, vol. 3, no. 08, p. S08002, 2008.

[11] E. Fernandez *et al.*, "Lifetime of Particles Containing b Quarks", *Physical Review Letters*, vol. 51, no. 12, pp. 1022–1025, 1983.

[12] N. S. Lockyer *et al.*, "Measurement of the Lifetime of Bottom Hadrons", *Physical Review Letters*, vol. 51, no. 15, pp. 1316–1319, 1983.

[13] Particle Data Group, C. Amsler, *et al.*, "Review of Particle Physics", *Phys. Lett. B*, vol. 667, no. 1, 2008.

[14] H. Albrecht *et al.*, "Observation of B^0-$\overline{B}^0$ mixing", *Physics Letters B*, vol. 192, no. 1-2, pp. 245–252, 1987.

[15] J. H. Christenson, J. W. Cronin, V. L. Fitch, and R. Turlay, "Evidence for the 2π Decay of the K_2^0 Meson", *Physical Review Letters*, vol. 13, no. 4, pp. 138–140, 1964.

[16] V. M. Abazov *et al.*, "Combined D0 measurements constraining the CP-violating phase and width difference in the B_s^0 system", *Phys. Rev.*, vol. D76, p. 057101, 2007.

[17] UTfit collaboration, M. Bona, *et al.*, "The unitarity triangle fit in the standard model and hadronic parameters from lattice QCD: A reappraisal after the measurements of Δm_s and BR($B \to \nu_\tau$)", *JHEP*, vol. 10, p. 081, 2006.

[18] The CDF collaboration, T. Aaltonen, *et al.*, "Search for $B_s \to \mu^+\mu^-$ and $B_d \to \mu^+\mu^-$ Decays with 2fb^{-1} of $p\bar{p}$ Collisions", *Phys. Rev. Lett.*, vol. 100, p. 101802, 2008.

[19] A. Buras, "Relations between $\Delta M_{s,d}$ and $B_{s,d} \to \mu\overline{\mu}$ in models with minimal flavour violation", *Physics Letters B*, vol. 566, no. 1-2, pp. 115–119, 2003.

[20] G. V. Ybeles Smit, *Probing new physics using AFB at LHCb.* PhD thesis, VU University, Amsterdam, 2009.

[21] L. Camilleri, "CP violation and search for new physics in LHCb", *International Journal of Modern Physics A*, vol. 22, no. 31, p. 5973, 2007.

[22] M. Honda, M. Nagano, S. Tonwar, K. Kasahara, T. Hara, N. Hayashida, Y. Matsubara, M. Teshima, and S. Yoshida, "Inelastic cross section for p-air collisions from air shower experiments and total cross section for p-p collisions up to $\sqrt{s} = 24$ tev", *Phys. Rev. Lett.*, vol. 70, pp. 525–528, Feb 1993.

[23] P. E. T. Sjöstrand, C. Friberg, L. Lönnblad, G. Miu, S. Mrenna, and E. Norrbin, "PYTHIA 6.154", *Computer Phys. Commun*, vol. 135, p. 238, 2001.

[24] The LHCb Collaboration, "LHCb Reoptimized Detector Design and Performance Technical Design Report", CERN-LHCC/2003-030, CERN, Sept 2003.

[25] E. Norrbin and T. Sjöstrand, "Production and hadronization of heavy quarks", *The European Physical Journal C-Particles and Fields*, vol. 17, no. 1, pp. 137–161, 2000.

[26] J. van Tilburg, *Track simulation and reconstruction in LHCb.* PhD thesis, VU University, Amsterdam, 2005.

[27] The LHCb Collaboration, A. Augusto Alves, Jr, *et al.*, "The LHCb Detector at the LHC", *Journal of Instrumentation*, vol. 3, no. 08, p. S08005, 2008.

[28] The LHCb Collaboration, "LHCb Magnet Technical Design Report", CERN-LHCC/2000-007, CERN, Jan 2000.

[29] The LHCb Collaboration, "LHCb VELO Technical Design Report", CERN-LHCC/2001-011, CERN, May 2001.

[30] The LHCb Collaboration, "LHCb Inner Tracker Technical Design Report", CERN-LHCC/2002-029, CERN, Nov 2002.

[31] The LHCb Collaboration, "LHCb Outer Tracker Technical Design Report", CERN-LHCC/2001-024, CERN, Sept 2001.

[32] R. M. Van der Eijk, *Track reconstruction in the LHCb experiment.* PhD thesis, VU University, Amsterdam, 2002.

[33] L. B. A. Hommels, *The Tracker in the Trigger of LHCb.* PhD thesis, University of Amsterdam, 2006.

[34] P. Vankov, *Study of the B-Meson Lifetime and the Performance of the Outer Tracker at LHCb.* PhD thesis, VU University, Amsterdam, 2008.

[35] D. Hutchcroft, "VELO Pattern Recognition", LHCb-2007-013, CERN, Geneva, Mar 2007.

[36] T. Lastoviicka, "Generic VELO Pattern Recognition", LHCb-2007-002, CERN, Geneva, Feb 2008.

[37] R. E. Kalman, "A new approach to linear filtering and prediction problems", *Journal of Basic Engineering*, vol. 82, no. 1, pp. 35–45, 1960.

[38] R. Frühwirth, "Application of Kalman Filtering to Track and Vertex Fitting", *Nuclear Instruments and Methods in Physics Research, A*, vol. 262, pp. 444–450, 1987.

[39] E. Rodrigues, "Tracking definitions", LHCb-2007-006, CERN, Geneva, Feb 2007.

[40] E. Bos, *Reconstruction of particle paths through the LHCb detector.* PhD thesis, VU University, Amsterdam, 2009.

[41] M. Krasowski, M. Kucharczyk, W. Männer, G. Polok, and M. Witek, "Primary vertex reconstruction", LHCb-2007-011, CERN, Geneva, Sept 2007.

[42] S. Amato, J. R. T. De Mello-Neto, and C. Nunes, "Constrained and unconstrained vertex fitting tools for LHCb", LHCb-2004-038, CERN, Geneva, May 2004.

[43] The LHCb Collaboration, "LHCb RICH Technical Design Report", CERN-LHCC/2000-037, CERN, Sept 2000.

[44] The LHCb Collaboration, "LHCb Calorimeter Technical Design Report", CERN-LHCC/2000-036, CERN, Sept 2000.

[45] The LHCb Collaboration, "LHCb Muon Technical Design Report", CERN-LHCC/2001-010, CERN, May 2001.

[46] The LHCb Collaboration, "LHCb Addendum to the Muon System Technical Design Report", CERN-LHCC/2003-002, CERN, 2003.

[47] The LHCb Collaboration, "LHCb Second Addendum to the Muon System Technical Design Report", CERN-LHCC/2005-012, CERN, 2005.

[48] R. W. Forty and O. Schneider, "RICH pattern recognition", LHCb-98-040, CERN, Geneva, Apr 1998.

[49] H. Terrier and I. Belyaev, "Particle identification with LHCb calorimeters", LHCb-2003-092, CERN, Geneva, Sept 2003.

[50] O. Deschamps, F. P. Machefert, M. H. Schune, G. Pakhlova, and I. Belyaev, "Photon and neutral pion reconstruction", LHCb-2003-091, CERN, Geneva, Sept 2003.

[51] W. R. Leo, *Techniques for Nuclear and Particle Physics Experiments.* Springer, 1994.

[52] L. Landau, "On the Energy Loss of Charged Particles by Ionization", *J. Physics*, vol. 8, p. 201, 1944.

[53] C. Leroy and P. G. Rancoita, *Principles of radiation interaction in matter and detection.* World Scientific, 2004.

[54] S. Hancock, F. James, J. Movchet, P. G. Rancoita, and L. Van Rossum, "Energy loss distributions for single particles and several particles in a thin silicon absorber", *Nuclear Instruments and Methods in Physics Research B*, vol. 1, p. 16, 1984.

[55] M. van Beuzekom, A. Van Lysebetten, and B. Verlaat, "CO2 cooling experience (LHCb)", *Proceedings of Science(Vertex 2007)009*, 2007.

[56] M. Ferro-Luzzi, "Definition of PU and VELO detector layout", CERN EDMS 719303, CERN, Geneva, 2006.

[57] M. Gersabeck, S. Viret, C. Parkes, *et al.*, "Performance of the LHCb Vertex Detector Alignment Algorithm determined with Beam Test Data", *Nuclear Instruments and Methods in Physics Research, A*, vol. 596, pp. 164–171, 2008.

[58] A. Papadelis *et al.*, "Performance studies of the Beetle1.3, 1.4 and 1.5 chips", LHCb-2005-044, CERN, Geneva, July 2005.

[59] J. P. Palacios *et al.*, "Pulseshape characteristics of a 300 μm PR03 R-measuring VELO sensor read out with a Beetle1.3 chip", LHCb-2004-068, CERN, Geneva, Jan 2005.

[60] J. Wang, "Vertex and Track Reconstruction and Luminosity Monitoring at LHCb", *Proceedings of Science(Vertex 2007)027*, 2007.

[61] J. Buytaert, P. Collins, D. Eckstein, K. Facius, and J. P. Palacios, "First measurement of the performance of a Beetle1.2 chip reading out a VELO sensor", LHCb-2003-133, CERN, Geneva, Oct 2003.

[62] J. B. Blanchard, "Analysis of the High Voltage scan data from the VErtex LOcator test beam", LHCb-2007-116, CERN, Geneva, Aug 2007.

[63] A. Papadelis, "Observations of sensor bias dependent cluster centroid shifts in a prototype sensor for the LHCb Vertex Locator detector", *Nucl. Instrum. Methods Phys. Res., A*, vol. 569, pp. 88–91. 6 p, Feb 2006.

[64] A. Affolder *et al.*, "LHCb-VELO module production with n-side read-out on n- and p-type silicon substrates", *Nucl. Instrum. Meth.*, vol. A583, pp. 18–22, 2007.

[65] S. Loechner and M. Schmelling, "The Beetle Reference Manual - chip version 1.3, 1.4 and 1.5", LHCb-2005-105, CERN, Geneva, Nov 2006.

[66] N. van Bakel, *The silicon vertex detector for LHCb: interaction with the LHC beams and the design of a reaction hard front-end chip.* PhD thesis, VU University, Amsterdam, 2004.

[67] S. Klous, *LHCb: Vertex detector and read out chip, Computing challange and $B_s \rightarrow J/\psi\phi$ analysis.* PhD thesis, VU University, Amsterdam, 2005.

[68] P. Koppenburg, "Effect of pulse overspill on the level 1 trigger", LHCb-2001-078, CERN, Geneva, May 2001.

[69] G. Haefeli *et al.*, "The LHCb DAQ interface board TELL1", *Nuclear Inst. and Methods in Physics Research, A*, vol. 560, no. 2, pp. 494–502, 2006.

[70] G. Haefeli, *Contribution to the development of the acquisition electronics for the LHCb experiment.* PhD thesis, EPFL Lausanne, Geneva, 2004.

[71] G. Haefeli and A. Gong, "LHCb VELO and ST clusterization on TELL1", CERN EDMS 690585, CERN, Geneva, 2006.

[72] N. Zaitsev, *Study of the LHCb pile-up trigger and $B_S \rightarrow J/\psi\phi$ decay.* PhD thesis, VU University, Amsterdam, 2000.

[73] M. Zupan and M. Ferro-Luzzi, "Pile-up system simulations", LHCb-2003-070, CERN, Geneva, Sept 2003.

[74] S. Viret, C. Parkes, and M. Gersabeck, "Alignment procedure of the LHCb Vertex Detector", *Nuclear Instruments and Methods in Physics Research, A*, vol. 596, pp. 157–163, 2008.

[75] V. Blobel and C. Kleinwort, "A New Method for the High-Precision Alignment of Track Detectors", *Arxiv preprint hep-ex/0208021*, 2002.

[76] S. Viret, C. Parkes, and M. Gersabeck, "LHCb VELO software alignment - PART II: the alignment of the VELO detector-halves", LHCb-2007-067, CERN, Geneva, July 2007.

[77] W. Baldini *et al.*, "LHCb Alignment Strategy", LHCb-2006-035, CERN, Geneva, June 2006.

[78] J. Buytaert, P. Collins, D. Eckstein, and J. P. Palacios, "Performance of a Beetle 1.2 chip reading out a Micron PR03 R measuring sensor", LHCb-2003-135, CERN, Geneva, June 2004.

[79] P. Bartalini *et al.*, "VELO telescope resolution and efficiency measurements", LHCb-2000-099, CERN, Geneva, Oct 2000.

[80] R. Brun, F. Rademakers, *et al.*, "ROOT-An Object Oriented Data Analysis Framework", *Proceedings AIHENP*, vol. 96, pp. 81–86, 1997.

[81] C. Parkes, "Track fit-vertex locator test-beam software description", LHCb-2001-038, CERN, Geneva, June 2001.

[82] F. James *et al.*, "MINUIT Function Minimization and Error Analysis", *CERN Program Library Long Writeup D*, vol. 506, 1998.

[83] S. Loechner, "First Results from the Engineering Run" Presented at 34th LHCb week, Beetle meeting, 2004,
http://indico.cern.ch/event/a044159.

[84] P. P. Allport, T. J. V. Bowcock, G. Casse, A. Greenall, J. N. Jackson, and P. R. Turner, "Charge collection efficiency studies with irradiated silicon detectors", *Nucl. Instrum. Methods Phys. Res., A*, vol. 501, no. 1, pp. 146–152, 2003.

[85] P. Riedler, W. Dabrowski, J. Kaplon, and P. Weilhammer, "Study of the performance of ATLAS prototype detectors using analogue LHC front-end electronics", *Nucl. Instrum. Methods Phys. Res., A*, vol. 477, no. 1-3, pp. 104–9, 2002.

[86] L. Eklund, "FIR experience from TB analysis" Presented in VELO group meeting 12/10/2005,
http://indico.cern.ch/event/a056573.

[87] G. Landi, "Problems of position reconstruction in silicon microstrip detectors", *Nuclear Inst. and Methods in Physics Research, A*, vol. 554, no. 1-3, pp. 226–246, 2005.

[88] S. F. Biagi. Private communication.

[89] K. Akiba *et al.*, "ACDC VELO phase-2 Testbeam Setup", LHCb-2008-007, CERN, Geneva, 2008.

[90] G. Patel, "Metrology of VELO C-side" Presented in VELO group meeting 14/03/2007,
http://indico.cern.ch/event/13279.

[91] D. Glaude, "Cible LHCb Velo", EMDS 807446, CERN, 2006.

[92] T. Szumlak and C. Parkes, "Description of the Vetra Project and its Application for the VELO Detector", LHCb-2008-022, CERN, Geneva, Feb 2008.

[93] G. Barrand *et al.*, "GAUDI - A software architecture and framework for building HEP data processing applications", *Computer Physics Communications*, vol. 140, no. 1-2, pp. 45–55, 2001.

[94] G. Casse, P. P. Allport, S. F. Biagi, T. J. V. Bowcock, A. Greenall, and P. R. Turner, "Charge collection and charge sharing in heavily irradiated n-side read-out silicon microstrip detectors", *Nuclear Inst. and Methods in Physics Research, A*, vol. 511, no. 1-2, pp. 112–117, 2003.

[95] G. D. Patel, "VELO Module Production - Quality and Process Control", LHCb-2007-088, CERN, Geneva, Nov 2007.

[96] A. Bates, L. Dwyer, F. Marinho, C. Parkes, A. Saavedra, and S. Viret, "VELO module characterisation: Results from the Glasgow LHCb VELO module burn-in", LHCb-2007-103, CERN, Geneva, July 2007.

[97] D. Kirkby and W. Verkerke, "The RooFit Toolkit for Data Modeling", *Statistical Problems in Particle Physics, Astrophysics And Cosmology: Proceedings of PHYSTAT05, Oxford, UK, 12-15 September 2005*, 2006.

[98] A. Noor, "A-rx card testing" Presented at VELO workshop 13/12/2007, http://indico.cern.ch/event/23825.

[99] R. Silva Coutinho, "Control Board Uniformity Test" Presented at 47th LHCb week, VELO session, 23/01/2008, http://indico.cern.ch/event/26113.

[100] O. Behrendt, "DAQ and Firmware" Presented in weekly VELO meeting 14/03/2008, http://indico.cern.ch/event/30380.

[101] T. J. V. Bowcock *et al.*, "VELO geometry optimisation", LHCb-2000-090, CERN, Geneva, Oct 2000.

[102] T. Ruf. Private communication.

Summary

The Large Hadron Collider (LHC) is a 27 km long circular proton accelerator outside Geneva, Switzerland. Protons are injected into the clockwise and anti-clockwise directions of the ring and accelerated to a momentum of 7 TeV/c. When filled, the LHC contains 3×10^{14} circulating protons, equivalent to a beam current of 0.584 A.

At four interaction points along the ring, the protons are brought to collision every 25 ns, i.e. 40 million times per second per interaction point. As the protons are smashed together at energies unprecedented in a laboratory the kinetic energy of the protons transforms into mass, and new particles can emerge that are heavier than the proton. These new particles are highly unstable, and decay within very short time spans.

One of these particles is the b-quark. It is an elementary particle of nature and a heavier type of quark than those that make up protons and neutrons. The b-quark decays within approximately 1.6 ps and during this period it travels about 1 cm from the point of production. By studying the decay products, fundamental questions about matter and antimatter may get an answer.

LHCb is one of the four experiments at the LHC. Its design is optimised for precision studies of the b-quark. One of the detectors of the LHCb experiment is the Vertex Locator (VELO), which measures the trajectories of b-quark decay products with micrometre precision using the technology of silicon strip sensors. The research described in this thesis focuses on the performance characterisation and commissioning of the VELO detector.

Chapter 3 describes a test of the performance of near-final prototype silicon sensors in a beam of charged particles. This was the last beam test in the R&D phase and the results were used as main input for the final design decisions. The Signal-to-Noise (S/N) ratio of the detector was investigated for three different versions of the Beetle front-end readout chip. It was found that the S/N of a 200 μm thick sensor was in the range 16.2 – 17.1. In another study systematic errors in the position measurement were investigated.

Chapter 4 gives a detailed report of a system test in which a quarter of the final detector was placed in a charged particle beam and read out with the final data acquisition system. The test was a first step of the commissioning of the VELO. The performance of the silicon sensors was investigated and the vertex reconstruction capability of the detector was put to test with a fixed target setup specifically designed to emulate a set of conditions present during LHC operation. The S/N of the 300 μm thick sensors was shown to be in the range $21.4 - 23.9$ for R-sensors and $23.9 - 29.5$ for the Φ-sensors. This is in good agreement with measurements of the S/N of prototype VELO sensors, and better than the requirements.

The resolution of the position measurement for particles with 0° incidence angle was shown to be in the range 8.5 μm$-$21.5 μm for an R-sensor in the pitch range 40 μm$-$90 μm. The resolution can be expressed as a function of the strip pitch by $8.5 + 0.26 \times (pitch - 40)$ μm.

In the vertex performance study the beam was aimed at a set of lead targets rendering tracks from secondary particles through the detector. These tracks were combined into vertices and used in a detailed analysis. By developing a model for the target distributions, the edges of the targets and the vertex precision could be successfully extracted from the data. The reconstructed edges were shown to agree with the metrology measurements within errors. The resolution, which was expected to be considerably worse than for the LHC conditions, was measured to be in the range $100 - 300\,\mu$m for x and y.

Chapter 5, documents the commissioning of the VELO and its readout system after the detector installation in the experimental area of LHCb. The chapter reviews the software tools that were developed for commissioning and data quality checking and describes the most important steps of the Data Acquisition System commissioning. As part of the commissioning, the performance integrity of the sensors was verified by an examination of their noise characteristics. The results of this analysis yielded an average noise of 2.06 and 1.89 ADC counts[2] for the R- and Φ-sensors respectively. Furthermore, an investigation to determine differences in raw and common mode corrected noise levels between individually and collectively powered modules showed no effects of significance.

The final section briefly describes results from the first injection of a counter-clockwise beam into the LHC. By taking data with 15 consecutive triggers the VELO could be properly time-aligned with respect to the L0-trigger supplied by the SPD, and tracks through the detector were successfully reconstructed for the first time after the VELO was installed.

[2]Corresponding to an equivalent noise charge of approximately 900 and 830 electrons.

Karakterisering en inbedrijfsstelling van de LHCb VELO detector

De *Large Hardon Collider* (LHC) is een cirkelvormige proton versneller met een omtrek van 27 km gebouwd onder de grond in de buurt van Genève in Zwitserland. In deze versneller worden protonen in tegengestelde richtingen geïnjecteerd en versneld tot een impuls van 7 TeV/c. Bij deze impuls hebben de protonen een snelheid van 99,9999991% van de lichtsnelheid. Als de LHC volledig gevuld is, bevat zij 3×10^{14} protonen.

Op vier punten langs de ring worden de protonen elke 25 ns tot botsing gebracht; er zullen dus 40 miljoen botsingen per seconde plaats zal plaats vinden op elk interactie punt. Deze botsingen gebeuren bij dusdanig hoge energieën dat de kinetische energie van de protonen omgezet zal worden in allerlei nieuwe deeltjes. Deze nieuwe deeltjes zijn instabiel en zullen binnen een zeer korte tijdsinterval vervallen.

Een van deze deeltjes is het b-quark. Dit is een elementair deeltje dat gezien kan worden als een zwaardere variant van de quarks die zich in protonen en neutronen bevinden. Het b-quark vervalt na ongeveer 1,6 ps en zal ongeveer 1 cm afleggen vanaf het punt waar het ontstaan is. Door de vervalsproducten van dit quark te bestuderen, is het mogelijk om fundamentele vragen over materie en antimaterie te kunnen beantwoorden.

LHCb is een van de vier experimenten bij de LHC. Het ontwerp van dit experiment is geoptimaliseerd om het b-quark te kunnen bestuderen. Een van de detectoren in LHCb is de *Vertex Locator* (VELO). Deze detector maakt gebruik van zogenaamde silicium strip sensoren en maakt het mogelijk om de afgelegde baan van de vervalsproducten van het b-quark met micrometer precisie te meten. Het onderzoek beschreven in dit proefschrift is gericht op de karakterisering van de eigenschappen en de inbedrijfstelling van de VELO detector.

Hoofdstuk 3 beschrijft een test van de gevoeligheid van het voorlaatste prototype silicium sensor in een bundel van geladen deeltjes. Dit werd de laatste bundeltest in de ontwikkelingsfase en de resultaten zijn gebruikt als uitgangspunt voor het uiteindelijke ontwerp. De signaal-ruis verhouding van de detector is onderzocht voor de drie verschillende versies van de Beetle front-end uitlees-chip. Het blijkt dat de signaal-ruis verhouding van een sensor met een dikte van 200 μm ligt tussen de 16,2 en 17,1.

Hoodfstuk 4 geeft een gedetailleerd verslag van een systeemtest waarin een kwart van de uiteindelijke detector in een bundel van geladen deeltjes werd geplaatst en uitgelezen was met het uiteindelijke data-acquisitiesysteem. Deze test kan gezien worden als de eerste stap in het opleveren van de VELO. De gevoeligheid van de silicium sensoren samen met de vertex reconstructienauwkeurigheid is onderzocht met een trefplaat-opstelling die ontworpen is om een aantal LHC condities zo goed mogelijk na te bootsen. De signaal-ruis verhouding van de 300 μm dikke sensoren bleek tussen de 21,4 en 23,9 voor de R-sensoren

en tussen de 23,9 en 29,5 voor de Φ sensoren te liggen. Dit is in goede overeenstemming met de metingen van de signaal-ruis verhouding uitgevoerd aan de prototype VELO sensoren.

De positie-resolutie voor deeltjes met een invalshoek van 0° blijkt tussen $8,5$ μm en $21.5\,\mu$m te liggen voor een R-sensor met steek tussen $40\,\mu$m en $90\,\mu$m. De resolutie kan worden uitgedrukt als functie van de strip steek als: $8.5 + 0.26 \times (steek - 40)\,\mu$m.

In de vertexprestatietest was de bundel gericht op een serie loden trefplaten zodat de secundaire deeltjes sporen achterlaten in de detector. Deze sporen werden gecombineerd tot vertices en verder geanalyseerd. Door een model voor de trefplaatdistributies te ontwikkelen, konden de randen van de trefplaten en de precisie van de vertices uit de data gehaald worden. De randen van de trefplaten blijken, binnen de fout, overeen te komen met optische precisiemetingen. De resolutie, waarvan werd verwacht dat die significant slechter zou zijn dan voor LHC condities, is volgens deze metingen tussen de 100 en $300\,\mu$m voor x en y.

Hoofdstuk 5 beschrijft de oplevering van de VELO en het uitleessysteem na de installatie in de experimenteerhal van LHCb. In dit hoofdstuk wordt de software beschreven die gebruikt is voor de inbedrijfstelling en voor het testen van de datakwaliteit. Ook worden hier de belangrijkste stappen van het opleveren van het data-acquisitiesysteem beschreven.

De prestaties van de sensoren zijn geverifieerd als deel van de oplevering van de VELO detector door de ruiskarakteristieken te onderzoeken. Verder heeft een onderzoek naar de verschillen in ruisniveaus tussen individuel en collectief gevoede modules geen significant effect opgeleverd.

Het laatste deel van dit hoofdstuk beschrijft de resultaten van de eerste injectie van een bundel in de LHC tegen de klok in. Door de data van 15 achtereenvolgende triggers te nemen, kon de VELO uitgelijnd worden in de tijd. Dit was de eerste keer sinds de installatie van de VELO dat sporen door de detector met succes gereconstrueerd konden worden.

Acknowledgements

Scientific research is rarely the product of a single person, and this thesis is certainly no exception. Firstly, Eddy Jans, my advisor and mentor during my Ph.D. studies, has always looked out for me and found time in his constantly crammed schedule to explain, discuss, read, listen and give feedback when I needed it. On a side note, his sometimes uncanny ability to predict future project delays has shown to me time after time the need to be conservative with time estimates. Likewise, Marcel Merk, my cunning thesis promoter, has been of enormous help, especially during the writing of this manuscript. His split second understanding of complex issues and physical intuition have been priceless to me and we have had good times both during and after working hours. Eddy and Marcel, I'm greatly indebted to you for all your support and good advice regarding my thesis.

The VELO group is full of bright people and it has always been a very inspiring environment to be in. As the VELO project is truly a team effort, I am very grateful to all the past and present Velonauts that I have the joy to work with. Just to mention a few out of the many, there was my office mate at CERN, Ann Van Lysebetten, who helped me navigate through French bureaucracy and always had a Delphi anecdote in store, and the good-hearted guru Kazu Akiba who was always worried sick about me. I honed my DAQ skills under the wing of Olaf Behrendt during endless sessions in the control room. Paula Collins has been an inspiration and a privilege to work with and Mark Tobin's never-ending catalogue of misadventures have been (and still are) a constant source of entertainment.

At NIKHEF I found good friends from day one. You are too many to mention here, but you know who you are. Thank you for the coffee breaks, the lunches, the physics/nerd banter, the dinners, the parties, the LaTeX tricks. To mention two people in particular, life in Amsterdam would not have been the same without the constant flow of sarcasms, cynicisms and BS from my brothers-in-arms, Sipho van der Putten and Patrick Motylinski. From those nights of the past with Big Mama at the Korsakoff to recent adventures in foreign lands, it has been a great ride all the way. Don't you ever take off your *lolbroeken* and *grapjassen*! I will miss you very much.

Together with Sipho, Gabriel Ybeles Smit made a very tangible contribution to this thesis: the translation of the dutch section. Thank you!

My 1.5 years at CERN passed incredibly fast, mainly because of the good times I had with the extraordinary posse of Swedes (real as well as honorary), Americans, Canadians, Spaniards, South-Africans, Dutch and Italians that I got to know there. Although we are far away from each other now I am sure we will keep our friendship alive!

Ett stort tack till mina nära och kära: mina fantastiska föräldrar Ilias och Anna för vilka jag har ALLT att tacka, mina underbara smarta systrar Karna och Elna,och min utökade familj: Mats, Marianne, Maja, Martina och Björn.

Last but not least I want to thank Malin, *min livskamrat* and astonishing wife who during my years of exile in the lowlands and in the alps has tolerated my vain pursuit of becoming a mad scientist. May we live happily ever after!

Aras Papadelis
Amsterdam, April 2009